

Nonequilibrium Shock-Layer Radiative Heating for Earth and Titan Entry

by

Christopher O. Johnston

Dissertation Submitted to the Faculty of the
Virginia Polytechnic Institute and State University
in partial fulfillment of the requirements for the degree of

Doctor of Philosophy

in

Aerospace Engineering

Dr. William H. Mason, Chair
Dr. Richard W. Barnwell
Dr. Brian R. Hollis
Dr. Joseph A. Schetz
Dr. Robert W. Walters

November 17, 2006

Blacksburg, Virginia

Keywords: Nonequilibrium Radiation, Viscous-Shock Layers, Aerothermodynamics

Copyright 2006, Christopher O. Johnston

Nonequilibrium Shock-Layer Radiative Heating for Earth and Titan Entry

Christopher O. Johnston

Dr. William H. Mason, Chairman
Virginia Polytechnic Institute and State University
Department of Aerospace and Ocean Engineering

(Abstract)

This thesis examines the modeling of the shock-layer radiative heating associated with hypersonic vehicles entering the atmospheres of Earth and Titan. For Earth entry, flight conditions characteristic of lunar-return are considered, while for Titan entry, the Huygens probe trajectory is considered. For both cases, the stagnation region flowfield is modeled using a two-temperature chemical nonequilibrium viscous shock layer (VSL) approach. This model is shown to provide results that are in agreement with the more computationally expensive Navier-Stokes solutions. A new radiation model is developed that applies the most up-to-date atomic and molecular data for both the spectrum and non-Boltzmann modeling. This model includes a new set of atomic-lines, which are shown to provide a significant increase in the radiation (relative to previous models) resulting from the 1 – 2 eV spectral range. A new set of electronic-impact excitation rates was compiled for the non-Boltzmann modeling of the atomic and molecular electronic states. Based on these new rates, a novel approach of curve-fitting the non-Boltzmann population of the radiating atomic and molecular states was developed. This new approach provides a simple and accurate method for calculating the atomic and molecular non-Boltzmann populations. The newly-developed nonequilibrium VSL flowfield and nonequilibrium radiation models were applied to the Fire II and Apollo 4 cases, and the resulting radiation predictions were compared with the flight data.

For the Fire II case, the present radiation-coupled flowfield model provides intensity values at the wall that predicted the flight data better than any other previous study, on average, throughout the trajectory for the both the 0.2 – 6.0 eV and 2.2 – 4.1 eV spectral ranges. The present results over-

predicted the calorimeter measurements of total heat flux over most of the trajectory. This was shown to possibly be a result of the super-catalytic assumption for the wall boundary condition, which caused the predicted convective heating to be too high. For the Apollo 4 case, over most of the trajectory the present model over-predicted the flight data for the wall radiative intensity values between 0.2 – 6.2 eV.

For the analysis of Huygens entry into Titan, the focus of the radiation model was the CN violet band. An efficient and accurate method of modeling the radiation from this band system was developed based on a simple modification to the smeared rotational band (SRB) model. This modified approach, labeled herein as SRBC, was compared with a detailed line-by-line (LBL) calculation and shown to compare within 5% in all cases. The SRBC method requires many orders-of-magnitude less computational time than the LBL method, which makes it ideal for coupling to the flowfield. The non-Boltzmann modeling of the CN electronic states, which govern the radiation for Huygens entry, is discussed and applied. The radiation prediction resulting from the non-Boltzmann model is up to 70% lower than the Boltzmann result. A new method for treating the escape factor in detail, rather than assuming a value equal to one, was developed. This treatment is shown to increase the radiation from the non-Boltzmann model by about 10%.

Acknowledgements

I would like to thank the members of my committee for their patience and time. Particularly, I would like to thank Dr. William H. Mason for being my advisor throughout my graduate student career and Dr. Brian R. Hollis for providing significant technical and administrative assistance to help me towards graduation. This dissertation would not have been possible without the guidance and expertise of Drs. Mason and Hollis. Also, it was my privilege to have Dr. Richard W. Barnwell on my committee and to be a student in four of his aerodynamics classes.

The help of Dr. Kenneth Sutton in learning the subject of shock-layer radiative heating was essential in completing this dissertation. His time and effort spent towards reviewing and discussing the present research resulted in numerous suggestions that greatly improved the quality of this work. This help is greatly appreciated.

The assistance of Dr. James N. Moss and Dr. Peter A. Gnoffo in developing the viscous-shock layer flowfield model is gratefully acknowledged. I would also like to thank Victor R. Lessard and Jettie W. Watts for their patience and time in answering my many computer-related questions, and Dr. Ramadas K. Prabhu for his help with the equilibrium chemistry program used in this work.

This work was funded by the NASA Langley Aerothermodynamics branch through the National Institute of Aerospace's "Rising Star" program.

Table of Contents

List of Figures **viii**

List of Tables **xiv**

Nomenclature **xvi**

Chapter 1	Introduction and Overview of Shock-Layer Radiative Heating	1
1.1	Introduction	1
1.2	Overview of Shock-Layer Radiative Heating Research	1
1.3	Review of the Main Shock-Layer Radiation Codes for Air.....	4
1.4	Review of Radiative Heating Predictions for Fire II	8
1.5	Review of Radiative Heating Predictions for Apollo 4	13
1.6	Review of Radiative Heating Predictions for Titan Entry and the Huygens Probe ...	15
1.7	Outline of the Dissertation.....	18
Chapter 2	The Viscous-Shock Layer Stagnation Line Flowfield	22
2.1	Chapter Overview	22
2.2	Governing Equations	23
2.3	The Species Continuity Equation	26
2.4	The Vibrational-Electronic-Electron Energy Equation	27
2.5	Solution Procedure.....	33
2.6	Shock-Slip Equations	33
2.7	The Equilibrium Viscous-Shock Layer	36
2.8	Application to Lunar-Return Shock Layers.....	37
2.9	Application to Huygens Entry Into Titan.....	45

Chapter 3	The Radiative Modeling of Equilibrium Air	50
3.1	Chapter Overview	50
3.2	Atomic Level Model	51
3.3	Basic Equations for Atomic Line Radiation	54
3.4	Assembling Data for Atomic Line Radiation.	57
3.5	A Method for Determining the Spectral Grid for Atomic Line Transport through a Nonequilibrium Shock-Layer.	65
3.6	Atomic Bound-Free and Free-Free Radiation	68
3.7	A Comparison of Various Approaches to Calculation Bound-Free Cross Sections . .	69
3.8	The Smeared Rotational-Band Method	78
3.9	Treatment of the Molecular Band Systems in Air	81
3.10	Summary of the Air Radiation Model in Equilibrium.	85
Chapter 4	Collisional-Radiative Modeling of N, O, N₂ and N₂⁺	89
4.1	Chapter Overview	89
4.2	Excitation and Deexcitation Mechanisms	90
4.3	The Master Equation	94
4.4	A Simple Method of Calculating ρ_l (with $k = 1$)	97
4.5	Non-Boltzmann Modeling of N and O.	99
4.6	The Approximate Atomic CR (AACR) Model	110
4.7	Non-Boltzmann Modeling for N ₂ ⁺ and N ₂	116
Chapter 5	Coupled Radiative Heating for Lunar-Return Shock-Layers	128
5.1	Chapter Overview	128
5.2	Radiation-Flowfield Coupling	129
5.3	Uncoupled Radiative Heating for Fire II	130
5.4	Coupled Radiative Heating for Fire II	132
5.5	Radiative Heating Analysis of Apollo 4	142
Chapter 6	Radiative Heating Methodology for the Huygens Probe	153
6.1	Chapter Overview	153
6.2	Spectral Modeling of CN Molecular Band Radiation.	154
6.3	Uncoupled and Coupled Radiative Heating Assuming a Boltzmann Distribution . .	160
6.4	Collisional-Radiative Modeling for Titan Entry	166

Chapter 7	Conclusions	172
7.1	Accomplishments	172
7.2	Future Work	174
 References		 175
 Appendix A	Atomic Line Data	195
 Appendix B	Photoionization Cross-Section Data	208
 Appendix C	Curve-Fit Coefficients for Calculating Electronic State Populations	212
 Appendix D	Line-By-Line Calculation of Molecular Band Radiation	217
 Appendix E	Derivation of the Escape-Factor for Molecular Band Radiation	220
 Appendix F	The Calculation of F_ν and q_ν in the Tangent-Slab Approximation	221
 Appendix G	Fundamental Concepts of Shock-Layer Radiative Heating	224
 Vita		226

List of Figures

1.1	Population of the electronic states of atomic nitrogen in nonequilibrium.	5
1.2	Comparison of past predictions with the Fire II total radiometer data throughout the trajectory	10
1.3	Comparison of past predictions with the Fire II total radiometer data from early in the trajectory	10
1.4	Comparison of past predictions with the frequency-integrated Fire II spectral radiometer data.	11
1.5	Comparison of past predictions with the Fire II calorimeter data.	12
1.6	A comparison of the various predictions for the radiation absorbed by the calorimeter.	13
1.7	A comparison of the various predictions for the Fire II convective heating.	13
1.8	Comparison of flight data and the predictions of past studies.	15
1.9	Comparison of the predicted radiative heating for Huygens entry.	17
2.1	Comparison of the VSL and LAURA stagnation line temperature profiles for the Fire 1634 case.	39
2.2	Comparison of the VSL and LAURA stagnation line species number density profiles for the Fire 1634 case	39
2.3	Comparison of the VSL and LAURA stagnation line temperature profiles for the Fire 1636 case.	40
2.4	Comparison of the VSL and LAURA stagnation line species number density profiles for the Fire 1636 case	40
2.5	Comparison of the VSL and LAURA stagnation line temperature profiles for the Fire 1643 case.	41
2.6	Comparison of the VSL and LAURA stagnation line species number density profiles for the Fire 1643 case	41
2.7	Wall directed radiative heat flux values predicted by the non-Boltzmann radiation models presented in Chapters 3 and 4 for the various flowfields	42

2.8	Comparison of T_{ve} between the nonequilibrium VSL, equilibrium VSL, and LAURA results for the 1643 s case	44
2.9	Comparison of the number densities predicted by the <i>equilibrium</i> VSL (E VSL) code and the LAURA code for the 1643 s case	44
2.10	Wall directed radiative heat flux values for the 1643 s case resulting from the NE VSL, E VSL, and LAURA flowfield models	45
2.11	Comparison of the VSL and LAURA temperature profiles for the t = 189 s case	46
2.12	Comparison of the VSL and LAURA CN number density profiles for the t = 189 s case	47
2.13	Temperature profiles predicted by the VSL method for the three peak-heating Huygens trajectory points	48
2.14	CN number density profiles predicted by the VSL method for the three peak-heating Huygens trajectory points.	48
2.15	Species number density profiles for the Huygens t = 189 s case predicted by the VSL method	49
3.1	Comparison of the line-shape functions proposed by Liu and Whiting	57
3.2	Comparison of the Stark broadening coefficients predicted by the various curve fits (Eqs. 3.14 – 3.15) with the detailed calculations of Griem and Wilson and Nicolet for nitrogen and oxygen	59
3.3	Radiative flux from a constant property slab of air at 10,000 K and 0.01 atm ; the “Total Spectrum” curve includes all the radiative mechanisms from all species; the other three curves are the accumulated flux values (W/cm ²) resulting from <i>only nitrogen</i> lines.	61
3.4	Radiative flux from a constant property slab of air at 10,000 K and 1.0 atm ; the “Total Spectrum” curve includes all the radiative mechanisms from all species; the other three curves are the accumulated flux values (W/cm ²) resulting from <i>only nitrogen</i> lines.	62
3.5	Comparison between the radiative flux spectrum from the nitrogen multiplet centered at 8.302 eV predicted by the individual and multiplet line models at 10,000 K	63
3.6	Comparison of the radiative flux from a constant property slab for an optically thick and optically thin line	67
3.7	Comparisons of the photoionization cross-sections obtained from the TOPbase, Hofsaess, and the hydrogenic approximation for a single level of nitrogen.	73

3.8	The bound-free and free-free frequency-dependent absorption coefficient (divided by the nitrogen number density) for nitrogen predicted by various models	73
3.9	The bound-free and free-free frequency-dependent radiative heat flux emitted from an equilibrium constant-property-slab of nitrogen.	74
3.10	The bound-free and free-free integrated radiative heat flux emitted from an equilibrium constant-property-slab of nitrogen.	74
3.11	The bound-free and free-free integrated radiative heat flux emitted from an equilibrium constant-property-slab of nitrogen.	75
3.12	Comparisons of the photoionization cross-sections obtained from the TOPbase, Hofsaess, and the hydrogenic approximation for a single level of oxygen.	76
3.13	The bound-free and free-free frequency-dependent absorption coefficient (divided by the oxygen number density) for oxygen predicted by various models.	76
3.14	The bound-free and free-free frequency-dependent radiative heat flux emitted from an equilibrium constant-property-slab of oxygen.	77
3.15	The bound-free and free-free integrated radiative heat flux emitted from an equilibrium constant-property-slab of oxygen.	77
3.16	The bound-free and free-free integrated radiative heat flux emitted from an equilibrium constant-property-slab of oxygen.	78
3.17	(a) Details of the constructing the SRB spectrum using Eq. (3.40) through (3.43). (b) A comparison of a small spectral region, predicted by the SRB and LBL methods, of the radiative flux resulting from the N_2^+ first-negative band system in a 4-cm slab of equilibrium air at 1 atm and 10,000 K.	79
3.18	(a - c) Molecular band emission coefficients divided by the upper-state number density, assuming a rotational and vibrational temperature of 10,000 K	84
3.19	Molecular band radiative spectrum from a 4-cm constant property slab of air at 10,000 K and 1 atm. The dark green line is the accumulated flux from only the molecular bands.	84
3.20	Frequency-integrated emission coefficients for molecular band systems in equilibrium air at 1 atm	85
3.21	Total emission coefficient (0 – 18 eV) for air at 1 atm predicted by various models.	87
3.22	Comparison of the emission coefficient contributions from the 0 – 6 eV spectral region from equilibrium air at 1 atm.	87
3.23	Integrated radiative flux components (divided by $2\pi\Delta z$) emitted from constant property slabs of various thicknesses in equilibrium air at 1 atm.	88

4.1	(a - e) Comparisons of the various approximate electron-impact excitation cross sections with detailed calculations. The two numbers in the top left hand corner refer to the transition $i - j$ with the levels defined in Table 3.1.....	104
4.2	(a - e) Comparisons of the various approximate electron-impact excitation cross sections with detailed calculations. The two numbers in the top left hand corner refer to the transition $i - j$ with the levels defined in Table 3.2.....	108
4.3	Influence of the various atomic CR models on the total wall-directed radiative flux for the Fire 1634 s case, the molecules are treated in all cases with the non-Boltzmann model presented later in this Chapter.....	112
4.4	Number densities of nitrogen levels for the $z = 4$ cm point predicted by the various models.....	114
4.5	Atomic line emission from nitrogen levels for the $z = 4$ cm point predicted by the various CR models.....	114
4.6	Number densities of nitrogen levels for the $z = 2$ cm point predicted by the various models.....	115
4.7	Atomic line emission from nitrogen levels for the $z = 2$ cm point predicted by the various CR models.....	116
4.8	Comparison of electron-impact excitation rates for populating the $N_2^+(B)$ state.....	119
4.9	The ratio of $N_2^+(B)$ inflow for various process for the Fire II 1634 s case, using the Table 4.7 rates.....	121
4.10	The ratio of $N_2^+(B)$ outflow for various process for the Fire II 1634 s case, using the Table 4.7 rates.....	121
4.11	The ratio of $N_2^+(B)$ inflow ratio minus the outflow ratio for each process corresponding to Figures 4.9 and 4.10.....	122
4.12	Comparison of the electronic state number densities predicted by the Boltzmann and CR Model along the stagnation line for the Fire II 1634 s case.....	123
4.13	Wall directed radiative flux profiles for the Fire II 1634 case for different treatments of the $N_2^+(B)$ state population.....	123
4.14	The ratio of $N_2(B)$ inflow for various process for the Fire II 1634 s case, using the Table 4.9 rates	125
4.15	The ratio of $N_2(B)$ outflow for various process for the Fire II 1634 s case, using the Table 4.9 rates	126
4.16	The ratio of $N_2(B)$ inflow ratio minus the outflow ratio for each process	

corresponding to Figures 4.14 and 4.15	126
4.17 Comparison of the electronic state number densities predicted by the Boltzmann and CR Model along the stagnation line for the Fire II 1634 s case.	127
5.1 Uncoupled and coupled values for the convective and radiative heat flux along the Fire II trajectory.	133
5.2 Partial wall intensity values (0.2 – 6.2 eV) predicted by the coupled and uncoupled application of the NE and E VSL flowfield models	134
5.3 Uncoupled and coupled stagnation-line temperature profiles for $t = 1643$ s	135
5.4 Wall-directed radiative flux profiles resulting from the coupled and uncoupled cases for $t = 1636$ s	136
5.5 Radiative flux spectrum at the wall for $t = 1636$ s resulting from uncoupled and coupled flowfield models.	136
5.6 Wall-directed radiative flux profiles resulting from the coupled and uncoupled cases for $t = 1643$ s	137
5.7 Radiative flux spectrum at the wall for $t = 1643$ s resulting from uncoupled and coupled flowfield models.	137
5.8 Comparison of the measured partial intensity (0.2 – 6.2 eV) with various predictions, including the results of the present radiation model applied to the NE and E VSL codes.	139
5.9 The same comparison as shown in Figure 5.8, except that it is focused on the early trajectory points for clarity.	139
5.10 Comparison of the partial intensity (2.2 – 4.1 eV) measured by the Fire II spectral radiometer with the present results and previous predictions.	140
5.11 Comparison of the present results, assuming a catalytic and non-catalytic wall, with the Fire II calorimeter data. These are coupled values from the nonequilibrium VSL flowfield	142
5.12 Uncoupled and coupled stagnation-line temperature profiles for $t = 10$ s	143
5.13 <i>Uncoupled</i> stagnation-line number density profiles for $t = 10$ s.	143
5.14 Uncoupled and coupled stagnation-line temperature profiles for $t = 32$ s	144
5.15 Uncoupled stagnation-line number density profiles for $t = 32$ s	144
5.16 Uncoupled and coupled values for the convective and radiative heat flux along the Apollo 4 trajectory obtained from the NE VSL model.	146
5.17 Cooling factors derived from the present Apollo and Fire results	146

5.18	Partial wall intensity values (0.2 – 6.2 eV) predicted by the coupled and uncoupled application of the NE and E VSL flowfield models	147
5.19	Wall-directed radiative flux profiles resulting from the different flowfield models, and treatment of the electronic state populations, for the $t = 10$ s case.	148
5.20	Wall-directed radiative flux profiles resulting from the different flowfield models, and treatment of the electronic state populations, for the $t = 32$ s case.	148
5.21	Radiative flux spectrum at the wall for the $t = 10$ s case.	149
5.22	Radiative flux spectrum at the wall for the $t = 32$ s case.	150
5.23	Comparison of the measured partial intensity (0.2 – 6.2 eV) with various predictions, including the results of the present model.	151
5.24	Influence of the updated atomic line model on the intensity between 0 and 6 eV . .	151
6.1	Comparison of the LBL and SRB predictions for the <i>CN violet</i> integrated emission coefficient.	156
6.2	Comparison between the various spectrum models for the radiative flux spectrum from a constant property slab of CN at 7000 K. The spectral range shown illustrates the (0-0) and (1-1) band heads	157
6.3	Comparison of the radiative flux from a constant property slab for different spectral models.	159
6.4	The contributions from the various radiative mechanisms to the wall directed radiative flux profile for the $t = 189$ uncoupled case	161
6.5	The CN violet spectrum at the wall as predicted by the SRBC method for the $t = 189$ coupled case.	162
6.6	Comparison between the coupled and uncoupled temperature profiles for the $t = 189$ case.	163
6.7	Comparison between the coupled and uncoupled CN number density profiles	163
6.8	Comparison of the mass rate of formation of CN molecules by various reactions for the uncoupled and coupled cases at $t = 189$ s.	164
6.9	Comparison between the coupled and uncoupled wall directed radiative flux profiles.	165
6.10	Values of the escape factor calculated for the three trajectory points compared with an approximate curve fit	169
6.11	The influence of various excitation mechanisms on the CN(B) number density for the $t=189$ case.	170

List of Tables

1.1	Trajectory points for Fire II cases.	7
1.2	Summary of previous Fire II studies.	8
1.3	Apollo 4 Trajectory Points.	14
1.4	Maximum heat-rate trajectory points for Huygens entry into Titan.	16
3.1	Energy Level Model for Atomic <i>Nitrogen</i> .	53
3.2	Energy Level Model for Atomic <i>Oxygen</i> .	54
3.3	Radiative flux (W/cm^2) emitted from <i>nitrogen atomic lines</i> at the edge of a 4-cm constant-property slab of equilibrium air at 10,000 K.	62
3.4	Radiative flux (W/cm^2) emitted from <i>oxygen atomic lines</i> at the edge of a 4-cm constant-property slab of equilibrium air at 10,000 K.	62
3.5	Comparison of the strongest lines for atomic <i>nitrogen</i> .	64
3.6	Comparison of the strongest lines for atomic <i>oxygen</i> .	65
3.7	Molecular band systems treated for air in the present model.	82
4.1	Summary of Approximate Equations for Electron Impact Excitation Rates.	101
4.2	Selection of Electron-Impact Excitation Rates for Nitrogen.	105
4.3	Selection of Electron-Impact Excitation Rates for Oxygen.	106
4.4	Level Groupings for the AACR Model.	111
4.5	Conditions for two points in the Fire 1634 s shock-layer.	113
4.6	N_2^+ electronic levels treated in the present model.	118
4.7	Non-Boltzmann rate model for N_2^+ .	118
4.8	N_2 electronic levels treated in the present model.	124
4.9	Non-Boltzmann rate model for N_2 .	124
5.1	<i>Uncoupled</i> convective and radiative heat-flux values (W/cm^2) and radiative intensities ($\text{W}/\text{cm}^2\text{-sr}$) for the Fire II vehicle.	131

5.2	<i>Coupled</i> convective and radiative heat-flux values (W/cm^2) and radiative intensities ($\text{W}/\text{cm}^2\text{-sr}$) for the Fire II vehicle.	133
5.3	<i>Uncoupled</i> convective and radiative heat-flux values (W/cm^2) and radiative intensities ($\text{W}/\text{cm}^2\text{-sr}$) for Apollo 4.	145
5.4	<i>Coupled</i> convective and radiative heat-flux values (W/cm^2) and radiative intensities ($\text{W}/\text{cm}^2\text{-sr}$) for Apollo 4.	145
6.1	Intensity resulting from a 1-cm constant property slab of CN in equilibrium at 7000 K ($\text{W}/\text{cm}^2\text{ - sr}$).	157
6.2	Table 6.2. Breakdown of the radiative heat flux towards the wall (q_r) at $z = 0$ for the <i>uncoupled</i> case (W/cm^2).	161
6.3	Comparison of the <i>convective</i> heat flux for the uncoupled and coupled cases (W/cm^2).	164
6.4	Comparison of the <i>radiative</i> heat flux towards the wall at $z = 0$ for the uncoupled and coupled cases (W/cm^2).	166
6.5	Excitation reactions considered in the present study.	167
6.6	Transition probabilities for the CN radiative transitions.	168
6.7	Comparison of the radiative heat flux towards the wall at $z = 0$ for the various escape factor models (W/cm^2).	171

Nomenclature

a_0	= Bohr radius, equal to 0.529×10^{-8} cm
$A_{j'i'}$	= transition probability for a line with an upper level j' and a lower level i'
b_ν	= line-shape function
B_e	= Klein-Dunham coefficient defined in Eq. (D-3)
B_V	= function of the vibrational quantum number defined as the first term in brackets in Eq. (D-3)
B_ν	= Blackbody or Planck function written in terms of frequency
c	= velocity of light, equal to 2.997925×10^{10} cm/s
c_i	= mass fraction of species i
C_r	= function of rotational temperature used in the SRB model defined in Eq. (6.2)
C_p	= specific heat
E_J	= rotational term energy for a molecule (cm^{-1})
E_V	= vibrational term energy for a molecule (cm^{-1})
E_e	= electronic term energy for a molecule (cm^{-1})
E_i	= electronic term energy for an atomic level i (cm^{-1})
E_{ionize}	= ionization energy of an atomic level i
E_u	= energy of the upper electronic level for a bound-bound transition
E_I^H	= ionization energy of hydrogen, equal to $109,697 \text{ cm}^{-1}$
e	= electron charge, equal to $4.80298 \times 10^{-10} \text{ cm}^{3/2} \text{ g}^{1/2}/\text{s}$
F_ν	= incoming radiative intensity integrated over all directions (erg/cm^2)
$f_{ij'}$	= absorption oscillator strength for a line with an upper level j' and a lower level i'
g_x	= degeneracy of the <i>molecular</i> energy mode x , equal to either J , V , or e
g_i	= degeneracy for an atomic level i
h	= Planck's constant, equal to 6.6256×10^{-27} erg-s
h_x	= enthalpy of energy mode x
$I_{w, \nu}$	= frequency dependent radiative intensity ($\text{erg}/\text{cm}^2\text{-sr}$)
$I_{w, h\nu}$	= frequency dependent radiative intensity ($\text{erg}/\text{cm}^2\text{-s-eV}$)
j	= frequency integrated emission coefficient ($\text{erg}/\text{cm}^3\text{-s-sr}$)
j_ν	= frequency dependent emission coefficient ($\text{erg}/\text{cm}^3\text{-sr}$)

J	= rotational quantum number
J_i	= diffusion mass flux of species i
k	= Boltzmann constant, equal to 1.38054×10^{-16} erg/K
K	= thermal conductivity
$K_e(i,j)$	= electron impact excitation rate from level i to level j ; the presence of a d or c in parenthesis refers to a dissociated or ionized level, respectively.
$K_M(i,j)$	= heavy-particle impact excitation rate from level i to level j ; the presence of a d or c in parenthesis refers to a dissociated or ionized level, respectively.
l	= orbital quantum number
L	= total orbital angular momentum quantum number
m	= electron mass, equal to 9.1091×10^{-28} g
M_i	= molecular weight of species i (kg/kg-mol)
N_a	= number density of an atom
N_x	= number density of either a species or an electronic state specified by the subscript x (particles/cm ³)
N_i	= number density of an atomic level i (particles/cm ³)
N_+	= ion number density (particles/cm ³)
N_e	= electron number density (particles/cm ³)
n	= distance tangent to the body surface, equal to z along the stagnation-line in Chapter 3 and the principal quantum number in Chapter 4
n_s	= shock-standoff distance divided by the nose radius of the body
p	= pressure
Q_x	= partition function of the energy mode x (nondimensional)
q_r	= wall-directed radiative heat flux, calculated in units of erg/s/cm ² , but usually presented in units of W/cm ² (1×10^{-7} W/cm ² = 1 erg/s/cm ²)
$q_{r,hv}$	= wall-directed frequency-dependent (in terms of eV) radiative heat flux
q_c	= convective heat flux (W/cm ²)
r	= radius measured from axis-of-symmetry to a point on the body
\bar{r}_0	= vector defined in Eq. (4.24) for the Saha decrements in Eq. (4.23)
\bar{r}_{00}	= vector defined in Eq. (4.24) for the Saha decrements in Eq. (4.23)
\bar{r}_j	= vector defined in Eq. (4.24) for the Saha decrements in Eq. (4.23), where j represents a level less than or equal to the number of levels that the QSS assumption is applied to.

R_{univ}	= universal gas constant
S	= total spin quantum number
t	= time (s)
T_a	= dissociation temperature (K), equal to $(T_{tr}T_{ve})^{1/2}$
T_{tr}	= translational-rotational temperature (K)
T_{ve}	= vibrational-electronic temperature (K)
T_e	= electronic temperature (K), assumed equal to T_v and T_e
U	= velocity component tangent to the body surface
V	= vibrational quantum number
v	= velocity normal to the body surface
w	= wave number (cm^{-1}), equal to $1/\lambda$ or ν/c
x	= number of active electrons for an atomic level
z	= distance along the stagnation line or through a constant-property slab (cm)
$\Delta\lambda_G$	= Gaussian half-width at half-height (cm)
$\Delta\lambda_L$	= Lorentzian half-width at half-height (cm)
$\Delta\lambda_R$	= Resonance half-width at half-height (cm)
$\Delta\lambda_S$	= Stark half-width at half-height (cm)
$\Delta\lambda_{S,0}$	= Stark broadening coefficient, equal to $\Delta\lambda_S$ at 10,000 K and $N_e = 1 \times 10^{16}$ particles/cm ³
Δz	= thickness of a constant-property slab (cm)
ε	= Reynolds number parameter, equal to the inverse square root of the Reynolds #
κ	= body curvature in Chapter 2
$A_{j,i}$	= escape factor for the transition from i to j (nondimensional)
λ	= wavelength (cm)
μ	= viscosity
ν	= frequency (s^{-1})
$\nu_{V'V''}$	= frequency of a vibrational band head obtained from Eq (3.46) (s^{-1})
ρ	= refers to the gas density in Chapter 2
ρ_i	= refers to the Saha-decrement of level i , defined by Eq. (4.14), in Chapter 4
τ_i	= radiative lifetime for a transition with an upper state i (s)

Subscripts

CL	= indicates the centerline in the spectrum of an atomic or molecular line
e	= refers to the electronic energy mode
EQ	= assumes that Boltzmann and Saha equilibrium exists among the electronic levels

$h\nu$ = indicates a spectral dependence in terms of eV; note that the equations presented throughout this document are for the frequency dependence (ν), although most of the figures are presented in terms of $h\nu$. The conversion between these two forms requires the multiplication of the ν dependent variable by 2.4182×10^{14} to obtain the $h\nu$ dependent variable.

inf = refers to a free-stream value

i = refers to the lower electronic state of an atomic transition

j = refers to the upper electronic state of an atomic transition

J = refers to the rotational energy mode

M = refers to a general heavy particle

tr = refers to the translational-rotational energy mode

ve = refers to the vibrational-electronic energy mode

V = refers to the vibrational energy mode

ν = indicates frequency dependence

Superscripts

bb = indicates a bound-bound atomic transition

bf = indicates a bound-free atomic transition

$cp\text{-slab}$ = indicates values resulting from a constant property slab

DE = indicates dissociation equilibrium, as defined by Eq. (4.7)

ff = indicates a free-free atomic transition

SB = indicates Saha-Boltzmann equilibrium

$-$ = indicates the radiative flux or intensity directed towards the vehicle wall

$'$ = defines a value in the upper electronic state of a molecular transition, for atoms it indicates that the level is ungrouped.

$''$ = defines a value in the lower electronic state of a molecular transition

Abbreviations

eV = electron volts; the frequency in eV, labeled $h\nu$, is equal to $1.24 \times 10^4 \nu / c$

E VSL = refers to the equilibrium VSL method

NE VSL = refers to the nonequilibrium VSL method

VSL = viscous shock-layer

VUV = vacuum ultraviolet; refers to the spectral region above 6 eV

Chapter 1

Introduction and Overview of Shock-Layer Radiative Heating

1.1 Introduction

The objective of the present work is to develop accurate models for the prediction of shock-layer radiative heating to vehicles entering the atmospheres of Earth and Titan. A brief discussion of the fundamental concepts of this problem is presented in Appendix G. The present chapter reviews the past research on this subject and highlights the inadequacies in the current state-of-the-art models. Section 1.2 provides a historical overview of the past research while Section 1.3 reviews the most widely used radiative heating codes of the past 30 years. Sections 1.4 and 1.5 discuss the Fire II and Apollo 4 flight experiments, respectively, and compare the radiative heating flight data obtained in these experiments with past computational studies. Much of the discussion in these sections is focused on highlighting the disagreement, not only between the flight data and the most recent computational studies, but also between the various computational studies that applied similar models. Section 1.6 reviews the status of radiative heating predictions for Titan entry, and in particular, the Huygens probe. Finally, Section 1.7 provides an outline of the subsequent chapters, which are intended to provide advancement in the state-of-the-art for predicting shock-layer radiative heating.

1.2 Overview of Shock-Layer Radiative Heating Research

The radiative heating to a reentry vehicle resulting from the high temperature gas surrounding the vehicle has been the subject of significant research over the past 50 years. The progress of these studies has followed closely with the state-of-the-art flowfield and chemistry models being

applied at the time, as well as with NASA's space exploration goals and military applications. From the late 1950s through the 1960s the majority of this work focused on the heating for lunar return conditions. Comprehensive reviews of this research are presented by Zhigulev et al. [1963], Biberman [1964], Belotserkovskii et al. [1969], Goulard et al. [1969], and Anderson [1969]. Early shock-layer radiation research was also concerned with radiative heating of ballistic missiles (e.g. Camm et al. [1959], Hammerling et al. [1959], and Allen et al. [1962]). It was soon concluded, though, that radiation would not contribute significantly to ballistic missile heating because of the relatively low flight velocities, and so work in this area was abandoned. During the 1960s, the state-of-art went from approximate inviscid flowfields with transparent or gray-gas radiation (e.g. Kennet and Strack [1961], Yoshikawa and Wick [1961], and Goulard [1961]) to coupled viscous flowfields in chemical equilibrium with semi-detailed non-gray spectral models (e.g. Hoshizaki and Wilson [1966], Hoshizaki and Lasher [1968], and Rigdon et al. [1968]). Other notable studies of the late 1960s combined time-asymptotic inviscid flowfields with approximate spectral models (Callis [1969] and Barnwell [1969]), or applied perturbation methods to obtain insight into radiation-flowfield coupling (Goulard [1964], Thomas [1965], Cohen [1967], Jischke [1968], and Olstad [1968]).

Radiative heating research in the 1970s concentrated on Mars return conditions for Earth entry (Rigdon et al. [1970], Garrett et al. [1972], and Moss [1976]) and entry into other planets such as Venus and Mars (Page and Woodward [1972], Sutton and Falanga [1973], Sutton [1974], Moss et al. [1977]). The studies of Venus entry were mostly in support of NASA's Pioneer-Venus mission, which entered Venus in 1978 and had thermocouples embedded in the heat shield. The thermocouple data from this mission (Pitts and Wakefield [1980]) was later the subject of comparison with convective and radiative heating predictions (Park and Ahn [1999]). The majority of the shock layer radiation studies in the 1970s considered the viscous boundary layer, either through a boundary layer code or through the use of the viscous shock layer equations, and assumed chemical and thermodynamic equilibrium. A review and comparison of the main radiation codes at the time was presented by Suttles [1972]. He concluded that the RAD/EQUIL code (Nicolet [1970]) was more efficient and accurate than Lockheed's RATRAP code (Wilson [1967]) and McDonnell Douglas's MDAC code (Rigdon et al. [1970]). Grose and Nealy [1975] considered nonequilibrium chemistry for Venus entry and showed that the radiative heating nearly doubled relative to the equilibrium prediction. Also of interest in the 1970s was entry into the outer planets such as Jupiter, Saturn, and Uranus (Sutton [1976], Nicolet et al. [1977], Zoby et al. [1978], Tiwari et al. [1979], and Moss [1979]). The aerothermal environments for entry into these planets were predicted to be very severe and produce massive ablation. The influence of the

ablation products on the flowfield and radiation was accounted for in these studies and shown to have a significant effect. The state-of-the-art at this point involved equilibrium viscous shock layer flowfields (Moss [1974]) coupled to detailed equilibrium radiation codes, such as the RAD/EQUIL code. A significant amount of the outer planet entry research was focused on the design of the Galileo probe for entry into Jupiter, which wouldn't actually enter the planet until 1995. Data from thermocouples and sensors to measure the shape change of the heat shield due to ablation was obtained (Milos [1997]) and compared to both updated (Matsuyama et al. [2005]) and earlier predictions.

The early 1980s saw continued interest in outer planet entry (Zoby and Moss [1980], Tiwari et al. [1981, 1983, 1984], and Nelson [1983]) and the beginning of detailed studies of nonequilibrium radiation in air (Park [1984a, 1985b]). Thermodynamic and chemical nonequilibrium Navier-Stokes flowfield models became common in the late 1980s and early 1990s (Park [1988, 1989], Gnoffo et al. [1989]), which required the proper modeling of nonequilibrium radiation (Hartung [1992a, 1992b], Gally [1992], Sharma [1993, 1996]). The NEQAIR and LORAN codes, which will be discussed in detail in the next section, were both developed to treat nonequilibrium radiation. The driving interests for these studies of nonequilibrium air radiation were the proposed aeroassist orbital transfer vehicle (AOTV) concept (Walberg [1985]) and the aeroassist flight experiment (AFE) (Jones [1987]). Although these vehicles never actually flew, they were designed to decelerate in the high-altitude low density regime, which would have produced significant nonequilibrium conditions. Radiative heating flight data was obtained for relatively low velocities (\sim 3.5 km/s) in the bow-shock flight experiment conducted by Erdmann et al. [1993]. This data was compared to the predictions of Levin et al. [1993], who showed that many of the nonequilibrium models at these conditions, which mainly dealt with molecular band radiation, were inadequate. She later suggested alternative models, which improved the agreement with the data (Levin et al. [1994]). Also of interest in the 1990s and the early 2000s was the radiative heating for entry into Titan. A review of past research on this topic will be discussed in detail in Section 1.6.

The current goal of NASA to return humans to the moon, and eventually Mars, has led to the renewed interest in the prediction of shock-layer radiative heating for lunar return conditions. A review of recent research on this topic will be presented in Sections 1.4 and 1.5. These sections focus on comparing recent computational studies with the Fire II and Apollo 4 flight experiments, both of which obtained radiative heating measurements at conditions relevant to lunar return.

1.3 Review of the Main Shock-Layer Radiation Codes for Air

The three main codes that have provided the majority of the shock-layer radiative heating predictions over the past 35 years are the RAD/EQUIL, NEQAIR, and LORAN codes. The earliest of these codes, which is referred to in the literature as either RAD/EQUIL, RAD, or RADICAL, was developed by Nicolet [1970]. This code modeled the spectral shape of each atomic line based on the atomic line data compiled by Wilson and Nicolet [1967]. Not all of the atomic lines listed by Wilson and Nicolet were treated individually in the code. To reduce computational time, lines spaced closely in the spectrum were combined into composite lines, and weak lines were ignored. The atomic continuum and molecular bands were modeled as smooth curve fits, similar to those presented by Hoshizaki and Wilson [1966]. The radiative heating prediction capability of RAD/EQUIL was developed assuming chemical and thermodynamic equilibrium.

The second significant radiation code mentioned above is the NEQAIR code developed by Park [1984a and 1985a], based on the original code by Whiting et al. [1969]. This code modeled the spectral shape of each atomic line based on the atomic line data complied by Wiese et al. [1966] and Griem [1974]. Nearly four times more lines were treated in NEQAIR than in RAD/EQUIL. The molecular band systems were modeled in NEQAIR using the line-by-line approach presented by Arnold et al. [1967]. This is a significant difference between NEQAIR and RAD/EQUIL because of the large computational cost of applying the line-by-line approach relative to RAD/EQUIL's approximate curve-fit approach. Another significant difference between the two codes is the collisional-radiative (CR), or non-Boltzmann, modeling of the atomic and molecular electronic states present in the NEQAIR code (Park [1985b]), as opposed to the assumed Boltzmann distribution of electronic states applied by RAD/EQUIL. This is significant because in regions of chemical and thermodynamic nonequilibrium, the electronic states of atoms and molecules do not follow a Boltzmann distribution. The non-Boltzmann populations of electronic states are calculated in NEQAIR using the quasi-steady state (QSS) approach, which was refined by Park through the years and is based on the collisional-radiative modeling approach originated by Bates et al. [1962]. Figure 1.1 illustrates a typical population distribution of the electronic states for nonequilibrium atomic nitrogen. The populations were calculated using the CR model developed in the present work and presented in Chapter 4. In this figure, N_i is the number density of level i , g_i is the degeneracy of the level, and E_i is the term-energy of the level. Note that the CR model predicts much lower number densities for the highly excited states than predicted by the Boltzmann model. This is a characteristic of nonequilibrium conditions during compression, such

as those found behind a shock wave in hypersonic flow. The opposite is true for expanding nonequilibrium conditions, such as those found in a favorable pressure-gradient boundary layer with chemically reacting flow.

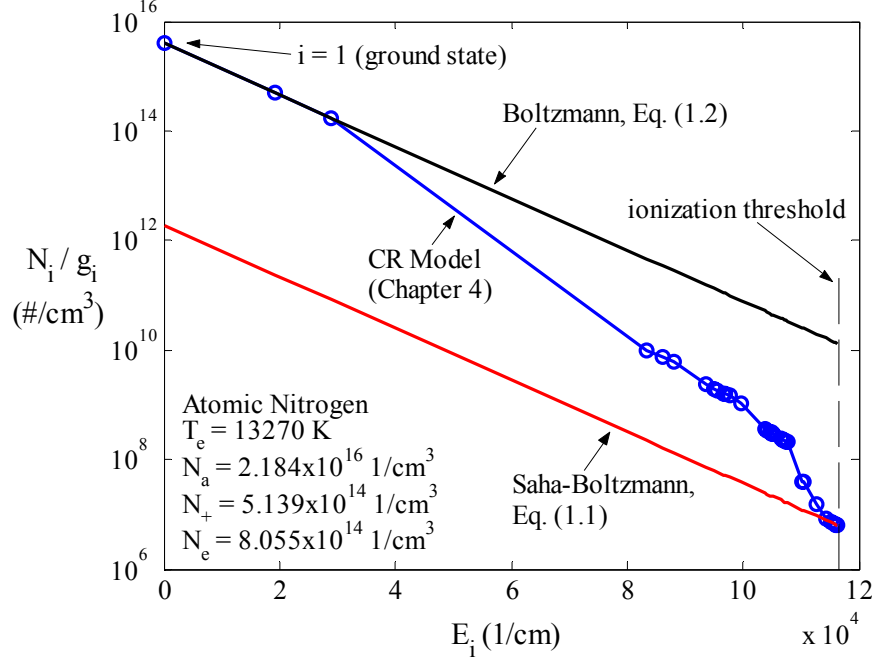


Figure 1.1. Population of the electronic states of atomic nitrogen in nonequilibrium

In the early 1990s, flowfield calculations that included chemical and thermodynamic nonequilibrium became standard. For these flowfields, the RAD/EQUIL code was inadequate because it assumed a Boltzmann distribution of the electronic states, which is incorrect in regions of nonequilibrium. Instead of resorting to the computationally intensive NEQAIR code for these situations, corrective procedures and major revisions to the RAD/EQUIL code were introduced. Gally et al. [1992 and 1993] developed two approximate correction methods, which were implemented in RAD/EQUIL, to account for the non-Boltzmann population of atomic electronic states. The first of these models, referred to as the 1st order local thermodynamic nonequilibrium (LTNE) model, was originally proposed by Carlson [1989]. It assumed that the excited atomic states were in equilibrium with the ions and electrons, instead of with the ground electronic state of the atom. The excited state number densities were therefore calculated using the Saha-Boltzmann equation as follows

$$N_i^{SB} = N_+ N_e \left(\frac{h^2}{2\pi m k T_e} \right)^{3/2} \frac{g_i \exp[-hc(E_i - E_{ionize})/kT_e]}{2Q_+} \quad (1.1)$$

instead of with the regular Boltzmann equation

$$N_i^B = N_a \frac{g_i \exp(-hcE_i / kT_e)}{Q_a} \quad (1.2)$$

On the other hand, the number densities for the ground states, which include three low-lying states for nitrogen and oxygen, *were* calculated using Eq. (1.2). The rationale for such a simple model is apparent from Figure 1.1, where the results of Eqs. (1.1) and (1.2) are compared with the detailed CR model results. It is seen that the three low lying states do follow a Boltzmann distribution closely, and the highly excited states do approach the Saha-Boltzmann population as the ionization limit is approached. The 1st order LTNE method is a very simple method for approximately accounting for the non-Boltzmann population of atomic states. It also shows the connection between chemical nonequilibrium and non-Boltzmann radiation. In regions of chemical equilibrium, Eqs. (1.1) and (1.2) are equivalent, by definition, because Eq. (1.1) is obtained by substituting Eq. (1.2) into the “law of mass action” equation (Anderson [2000]) for the following reaction



where A represents a neutral atom and A^+ represents its ion. In regions of chemical equilibrium, the flowfield solver will have enforced the law of mass action, which requires for the reaction in Eq. (1.3) that the neutral species, ion, and electron number densities are related as follows

$$N_a = N_+ N_e \left(\frac{h^2}{2\pi m k T_e} \right)^{3/2} \frac{Q_a}{2Q_+} \exp(hcE_{ionize} / kT_e) \quad (1.4)$$

Substituting this into Eq. (1.2) makes clear the equality of Eqs. (1.1) and (1.2) in regions of chemical equilibrium and explains why, in such a case, all three of the lines in Figure 1.1 would be the same. A procedure similar to the 1st order LTNE model was also outlined by Geendyke and Hartung [1991], although they applied the method exclusively to a step model representation of the spectrum. The 2nd order LTNE model, also presented by Gally et al. [1992], grouped together the excited states of an atom and treated them as a single species in the flowfield calculation. The populations of the various levels of the excited states were then distributed in a Boltzmann distribution, with the number density of the “excited” specie determined from the flowfield calculation. The 2nd order model was shown to result in slightly larger values than the 1st order model, with a difference of about 10% for the cases considered.

As an alternative to the RAD/EQUIL and NEQAIR codes, Hartung [1991] developed the code LORAN, which is composed essentially of the atomic spectral model and QSS model of NEQAIR along with a smeared rotational band model for the molecular bands. This avoids the computationally intensive line-by-line molecular band computation applied in NEQAIR. A

comparison of the LORAN and NEQAIR results was presented by Hartung [1992b], who showed that the two codes predicted wall radiative flux values that differed by only 6% for the cases considered.

1.4 Review of Radiative Heating Predictions for Fire II

The Fire II flight experiment was flown in 1965 to obtain radiating heating data for a capsule with a scaled-down Apollo-shaped forebody (Cauchon [1967]). Three non-ablating beryllium heat shields were attached on top of each other, with the top two being jettisoned at selected points in the trajectory prior to melting. Table 1.1 lists the flight conditions and wall temperature at various trajectory points along with the vehicle nose radius, which changes with the various heat-shields. Radiative heating data was obtained at the stagnation point with three different types of instrumentation. A *total* radiometer measured the radiative intensity behind a quartz window, which allowed the radiation in the spectral range of 0.2-6.2 eV to be measured. A *spectral* radiometer provided spectrally resolved intensity data in the spectral range of 2.2 to 4.1 eV with a resolution of about 0.04 eV and a reported uncertainty of $\pm 23\%$. The calorimeter measured the convective heating plus the *absorbed* radiative flux. The *absorbed* radiative flux refers to the component that is absorbed by the beryllium calorimeter over the entire spectrum. The spectral absorbtance of beryllium is reported by Cornette [1966].

Table 1.1. Trajectory points for Fire II cases

t (s)	Altitude (km)	Density (kg/m ³)	Velocity (km/s)	Temp. (K)	Wall Temp. (K)	Physical R_N (m)
1634.0	76.42	3.72×10^{-5}	11.36	195	615	0.935
1636.0	71.02	8.57×10^{-5}	11.31	210	810	0.935
1637.5	67.05	1.47×10^{-4}	11.25	228	1030	0.935
1640.5	59.62	3.86×10^{-4}	10.97	254	1560	0.935
1643.0	53.04	7.80×10^{-4}	10.48	276	640	0.805
1645.0	48.37	1.32×10^{-3}	9.83	285	1520	0.805
1648.3	41.60	3.25×10^{-3}	8.10	267	503	0.702

Many researchers have used the Fire II case as a benchmark for a new radiation code or flowfield solver. Table 1.2 lists those studies published since 1984, which are the most relevant to modern studies. Listed along with each researcher are the flowfield equations, chemistry model, radiation code, and method of obtaining the molecular and atomic state populations implemented in the particular study. All of the studies listed here include radiation-flowfield coupling, meaning the divergence of the radiative flux is included in the energy equation. Results from these studies will be compared with the flight data in the following paragraph.

Table 1.2. Summary of previous Fire II studies

Researcher	Flowfield Eqs. ¹	Chemistry ²	Radiation Code	State Populations ³
Sutton [1984]	Euler	E	RAD/EQUIL	B
Balakrishnan [1985]	VSL	E	RAD/EQUIL	B
Gupta [1987]	VSL	E	RAD/EQUIL	B
Bird [1987]	DSMC	NE	custom	NB
Carslon [1989]	VSL	E	8-step model	NB
Park [1989]	VSL	NE	NEQAIR	NB
Gally [1991]	VSL	NE	RAD/EQUIL	NB
Greendyke [1994]	NS	NE	LORAN	NB
Olynick [1994]	NS	NE	NOVAR	B
Park [2004]	VSL	NE	NEQAIR	NB

¹VSL = Viscous Shock Layer, DSMC = Direct Simulation Monte Carlo, NS = Navier Stokes

²E = Equilibrium, NE = Nonequilibrium

³B = Boltzmann, NB = Non-Boltzmann

The most widely analyzed data from the three measuring devices is the total radiometer data, which was presented in Figure 13 of Cauchon [1967] as the radiative intensity integrated between 0.2 and 6.2 eV. Figure 1.2 compares the intensity value predicted by many of the researchers listed in Table 1.2 with the flight data. Figure 1.3 presents a close-up of the early trajectory points, which are of particular interest because they are largely nonequilibrium. The results of Olynick [1994] compare best with the data, while the results of Gupta [1987] are also in good agreement throughout the trajectory. From Table 1.2, it is seen that Olynick applied the code NOVAR, which assumed a Boltzmann distribution of electronic states, to a Navier-Stokes nonequilibrium flowfield. The NOVAR code is reported to be essentially the same as LORAN, except that it is configured for computational efficiency and assumes a Boltzmann distribution of electronic states, instead of applying the QSS model used in LORAN and NEQAIR. It is interesting that Olynick's results compare so well for the early trajectory points, considering that a large percentage of the shock layer is in nonequilibrium, which should cause the Boltzmann assumption to over predict the radiation considerably (Greendyke [1993]). To check this, Olynick presented several cases that applied the QSS non-Boltzmann model. These results showed that the QSS and Boltzmann model agreed for the early trajectory points and then diverged with the later points, which should have been close to equilibrium. This trend is inconsistent with other studies (Greendyke and Hartung [1991]), which show that a Boltzmann distribution of electronic states is approached in regions of chemical equilibrium.

Another interesting feature of Figures 1.2 and 1.3 is the good agreement with the data obtained by Gupta [1987], who applied the RAD/EQUIL code to an equilibrium VSL flowfield. In a similar

study, Sutton [1984] also applied the RAD/EQUIL code to an equilibrium flowfield, although it was inviscid. Assuming that similar thermodynamic properties were used and that the radiation codes applied were actually the same, it would be expected that because of boundary layer absorption, Gupta's values should be lower than Sutton's. But, Figures 1.2 and 1.3 show the opposite trend throughout the trajectory. Furthermore, the results of Balakrishnan [1985] should agree very well with Gupta's, since they both applied the RAD/EQUIL code to an equilibrium VSL flowfield (although their VSL techniques were different). It is seen in Figures 1.2 and 1.3 that Gupta's and Balakrishnan's results do not compare well. Balakrishnan's values are significantly lower than both Gupta's and Sutton's, which indicates the expected influence of boundary layer absorption.

The most state-of-the-art studies presented in Figures 1.2 and 1.3 were those of Greendyke [1994] and Park [2004]. Although these studies agree reasonably well, they do not improve upon the results of older studies. A reason for this lack of improvement, especially for the early trajectory points, is the uncertainty in the nonequilibrium flowfield modeling (which was not an issue with the older equilibrium studies). This point is made clear in a study by Hartung et al. [1992a], who adjusted some of the unknown nonequilibrium flowfield parameters and studied their effect on the radiative heating for the Fire 1631, 1634, and 1637.5 second cases. It was shown that the intensity values for the 1634 and 1637.5 cases could vary from 1.8 to 4.4 and 11.0 to 20.0 W/cm²-sr, respectively, depending upon the nonequilibrium flowfield parameters chosen. Although recommended values for the parameters are provided in the literature (Park [1984b, 1988, 1989]), the evidence supporting these values is not overwhelming.

The frequency-integrated data from the spectral radiometer (between 2.2 and 4.1 eV), presented in Figure 13 of Cauchon [1967], has been the subject of comparison by a few researchers. The comparison between the data and predictions are shown in Figure 1.4. The two "Flight Data" lines represent the upper and lower limit of the data scatter. The predictions all agree reasonably well, although none stay within the data scatter throughout the entire trajectory. An interesting aspect of this comparison is the close agreement of the values predicted by Sutton and Balakrishnan, while in the Figures 1.2 and 1.3 the agreement between these two predictions is noticeably worse, especially near the peak heating point.

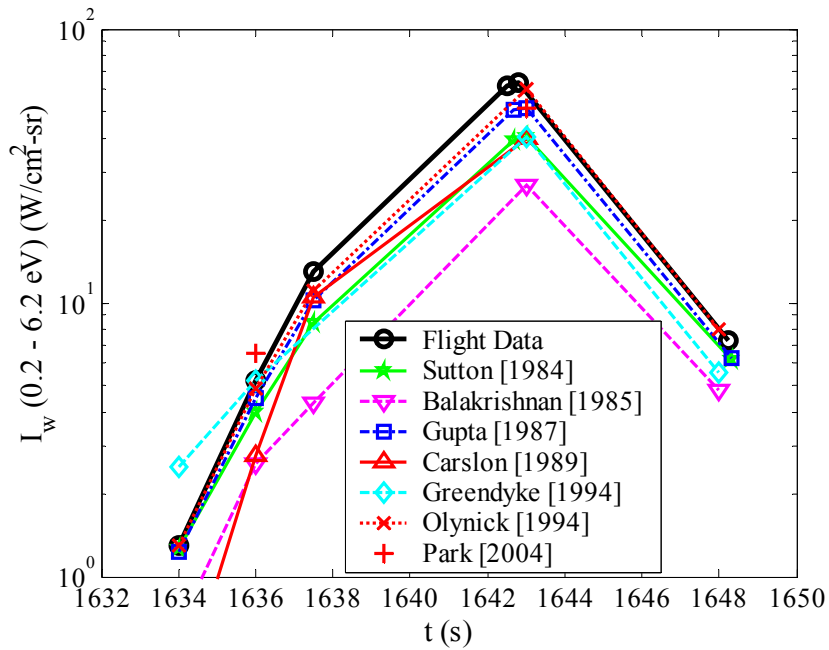


Figure 1.2. Comparison of past predictions for the partial intensity at the wall with the Fire II total radiometer data throughout the trajectory.

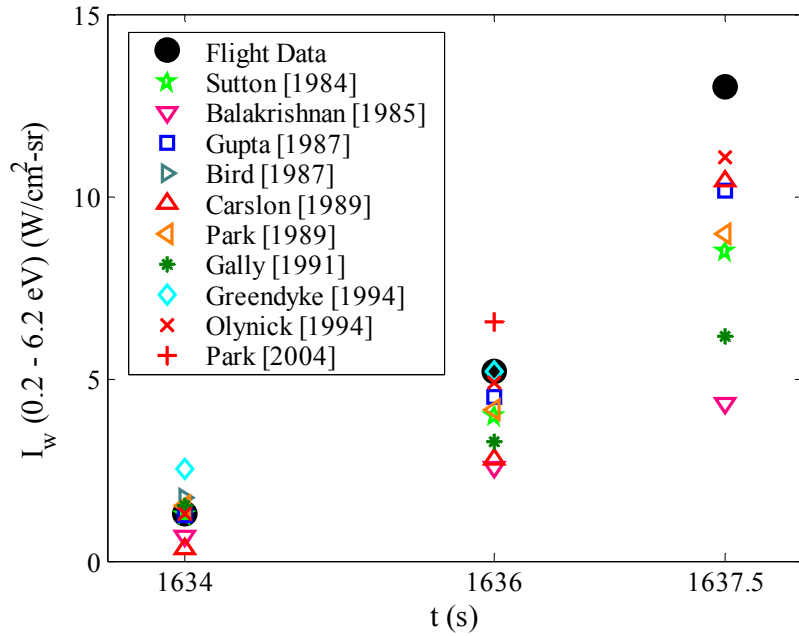


Figure 1.3. Comparison of past predictions for the partial intensity at the wall with the Fire II total radiometer data from early in the trajectory.

The only recent studies to present a comparison with the spectrally resolved data (Cauchon et al. [1967]) from the spectral radiometer were the studies of Park [2004] and Hartung et al. [1992a].

The study of Park [2004] presented, in *his* Figure 5, a comparison of his predicted spectrum with the measure spectrum for the 1643 s point. Although not shown here, the experiment and computed spectra agreed reasonably well, which is consistent with the decent comparison of the frequency-integrated values presented in Figure 1.4. Hartung et al. [1992a] compared their computed spectra obtained with the LORAN code, with the data for the 1631, 1634, and 1637.5 s trajectory points. The agreement for these nonequilibrium cases was not very good, although since they did not present values for the integrated intensity between 2.2 and 4.1 eV, it is difficult to quantify the disagreement. From Figure 5 of Hartung [1992b] and Figures 6 and 7 presented by Greendyke [1993], it is suspected that the non-Boltzmann modeling of N_2 and N_2^+ are likely responsible for this poor agreement with the data. The 2.2 to 4.1 eV region of the spectrum is dominated by the $N_2(1^+)$ and $N_2^+(1^-)$ bands, which emit strongly in the nonequilibrium region near the shock. The LORAN code applied by Hartung uses the same non-Boltzmann model (the QSS model) as NEQAIR.

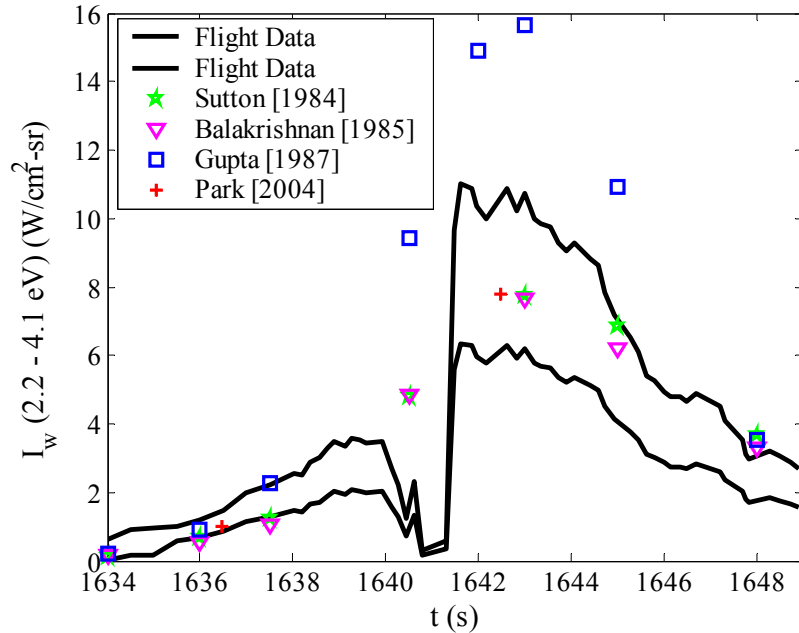


Figure 1.4. Comparison of past predictions with the frequency-integrated Fire II spectral radiometer data.

The Fire II calorimeter data presented by Cornette [1965] provide heating values that contain the convective heating plus the contribution of the radiative flux absorbed by the beryllium calorimeter. A comparison of the calorimeter data with various predictions, throughout the trajectory, is presented in Figure 1.5. Although the data cannot be separated into convective and radiative components, Figures 1.6 and 1.7 compare the calculated values of these components,

whose values add together to produce values shown in Figure 1.5. The best comparisons with the data in Figure 1.5 are the results of Olynick [1994], as was the case for the radiometer data in Figure 1.2. It is also seen in Figure 1.5 that the results of Sutton [1984] and Gupta [1987] are in close agreement with each other throughout the trajectory. This agreement is due to their offsetting differences in the radiative and convective components. Surprisingly, Sutton's radiative component is larger than Gupta's, which is the opposite of what was seen in Figure 1.2 for the 0.2 to 6.2 eV integrated intensity. This indicates that Sutton predicted a larger radiative contribution from the spectral region above 6.2 eV (the vacuum ultraviolet) than Gupta. This difference is likely due to boundary layer absorption, which influences the vacuum ultraviolet more than any other spectral region. The results of Greendyke [1994] provide the worst comparison with the data. It is seen that both the convective and radiative predictions are too low, especially near peak heating. Considering that Geendyke's analysis consisted of the most up-to-date models relative to the other studies, this result is not very encouraging. Note that the large difference in convective heating predicted by Greendyke and Olynick is present even though both studies applied a nonequilibrium Navier-Stokes flowfield with a super-catalytic wall boundary condition.

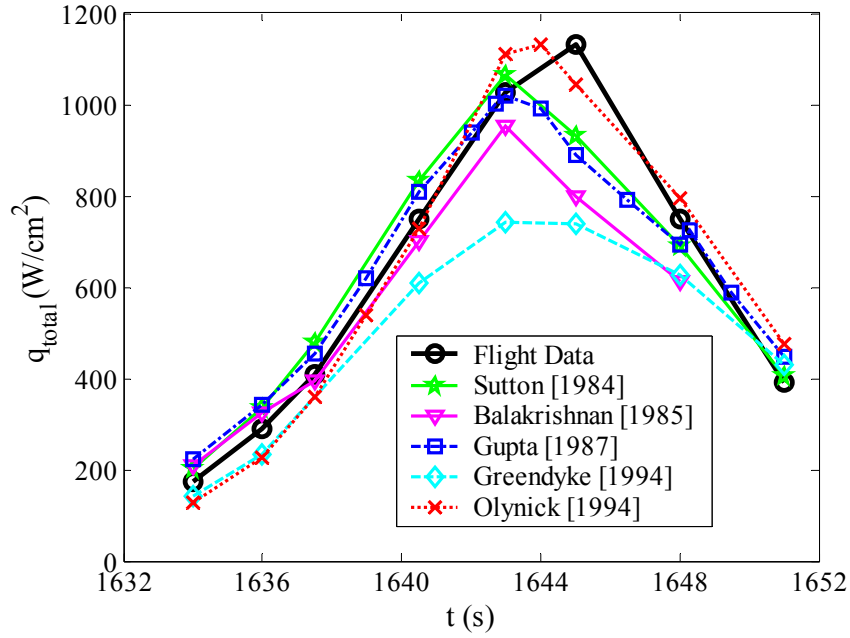


Figure 1.5. Comparison of past predictions for the total absorbed heat flux with the Fire II calorimeter data.

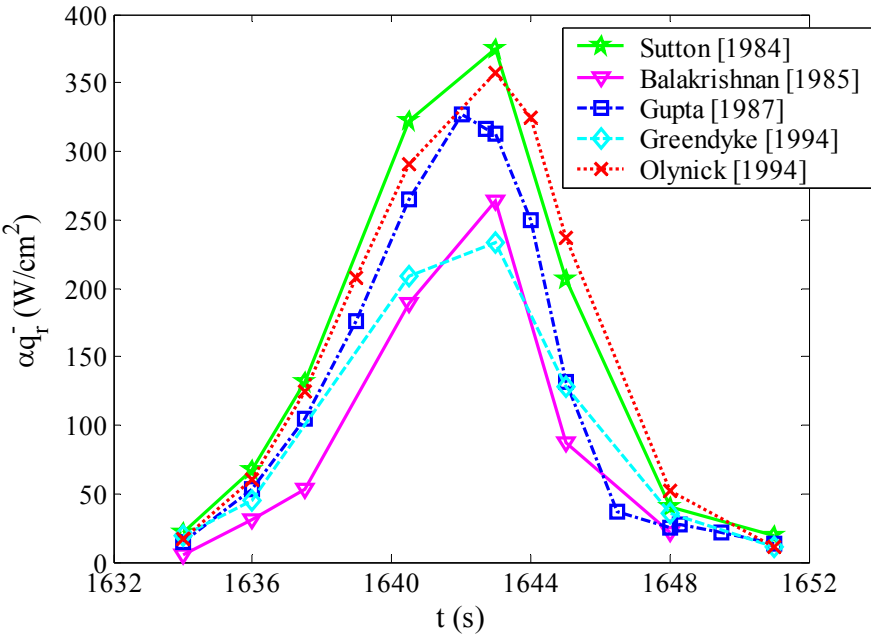


Figure 1.6. A comparison of the various predictions for the radiation absorbed by the calorimeter.

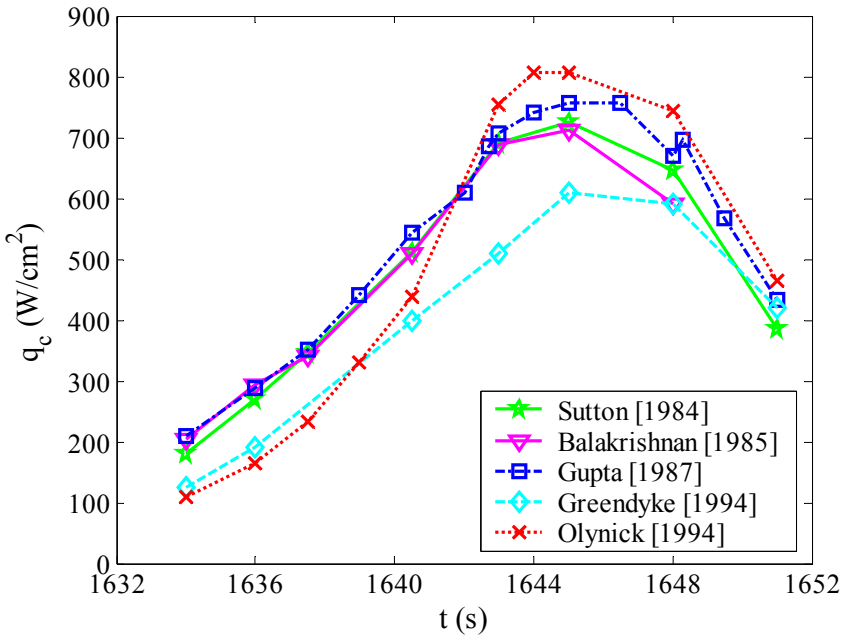


Figure 1.7. A comparison of the various predictions for the Fire II convective heating.

1.5 Review of Radiative Heating Predictions for Apollo 4

The Apollo 4 Command Module, an unmanned prototype equipped with a radiometer at the stagnation point, was flown in 1967. Successful measurements were made of the radiative intensity at the stagnation point throughout the trajectory (Reid et al. [1972]). The trajectory

points of interest are defined in Table 1.3, with t representing the time from launch past 30,000 s. The physical nose radius of the vehicle was 4.50 m, although since it was flown at an angle of attack of 25 degrees, an appropriate equivalent nose radius is required for a stagnation point analysis. Both Sutton [1984] and Balakrishnan [1985] chose a value of 3.05 m for the equivalent nose radius, while Park [2005] chose a value of 2.85 m.

Table 1.3. Apollo 4 Trajectory Points

t (s)	Altitude (km)	Density (kg/m ³)	Velocity (km/s)	Temp. (K)
10	75.98	3.59e-5	10.74	199.5
20	67.47	1.13e-4	10.64	229.0
24	64.55	1.74e-4	10.51	240.0
28	61.99	2.50e-4	10.38	251.0
32	59.79	3.41e-4	10.25	264.5
40	56.69	5.01e-4	9.80	271.0
44	55.89	5.51e-4	9.53	274.0
52	55.78	5.61e-4	9.02	278.0

A comparison of the most recent studies with the flight data is shown in Figure 1.8. The two lines labeled as “Flight Data” represent the upper and lower limits of the data. The details of the past studies are the same as those listed in Table 1.2. Hence, many of the explanations of the differences seen in the various studies are the same as those mentioned previously for the Fire II results. A significant difference between the Apollo 4 and Fire II flight experiments is that the Apollo 4 had an ablating heat shield, while the Fire vehicle did not. Park [2004] is the only study mentioned here that considered ablation, although the influence of ablation on the radiation was not made clear. In an earlier study by Park [2001], it was shown that the radiative intensity between 0.2 and 6.2 eV increased by as much as 25% due to the ablation products in the boundary layer. It was noted that the many of the important vacuum ultraviolet (VUV) molecular bands were not considered in this work. Park [2004] *did* consider the VUV bands, which was reported to be the only difference in the radiation model from the Park [2001] paper. The Park [2004] results show *no* increase in the radiative intensity between 0.2 and 6.2 eV due to the boundary layer. This discrepancy between the Park [2001] and Park [2004] result is difficult to explain because the added VUV bands are located above 6.2 eV, which means that they could not have directly effected the radiative intensity between 0.2 and 6.2 eV. Although it is possible that the added VUV bands influenced this spectral range indirectly through radiation-flowfield coupling, it is unlikely that this would have had such a large effect. Strong absorption in the boundary layer is shown by Park [2004] to occur because of the VUV bands, but again, this occurs above 6.2 eV. This absorption influenced the convective heating for the radiation-

flowfield coupled case considerably, increasing it by a factor of three above the uncoupled case. Park [2001] also showed a significant increase in the convective heating with the addition of coupling, which indicates that the observed increase is not due entirely to the absorption from the VUV bands.

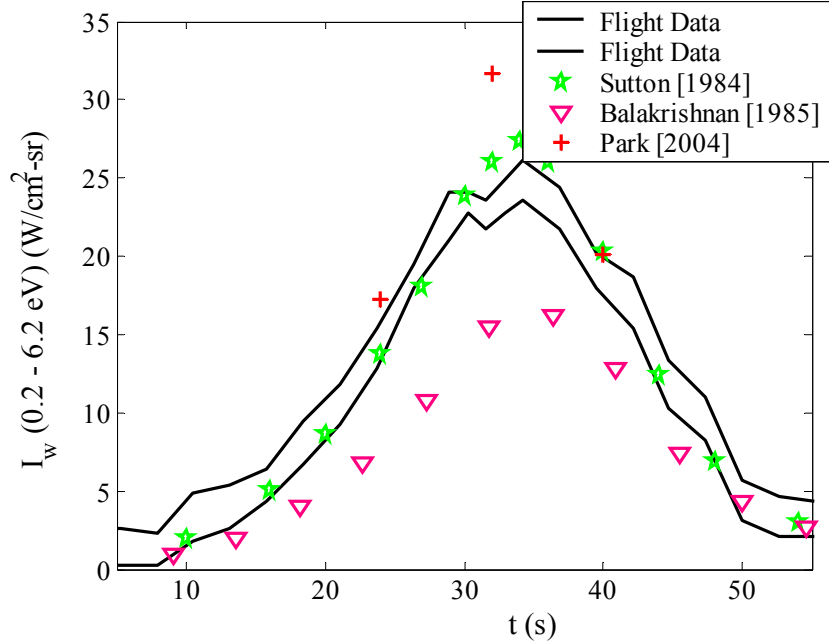


Figure 1.8. Comparison of flight data and the predictions of past studies

1.6 Review of Radiative Heating Predictions for Titan Entry and the Huygens Probe

Studies of the aerothermal environment for entry into Titan, a moon of Saturn, have been reported since the early 1980s. Tiwari et al. [1981] considered the use of Titan's atmosphere for braking into Saturn's orbit. An equilibrium viscous shock layer (VSL) analysis was used for the flowfield along with the RAD/EQUIL code for the radiation. The composition of Titan's atmosphere was unknown at the time of this study; so many different atmospheric compositions were considered. For cases where the CH₄ level was less than 10%, the radiative heating was shown to be insignificant relative to the convective heating for the trajectories considered. Park [1982] showed that the predicted radiation for Titan increases significantly when nonequilibrium chemistry is considered. Green et al. [1985] studied a deployable decelerator concept for Titan entry using an equilibrium VSL technique along with the RAD/EQUIL code.

The introduction of the joint NASA/ESA Huygens-Cassini mission in the early 1990s led to many studies concerning the radiative heating for Titan entry. The Huygens probe consisted of a 60 degree sphere-cone with a nose radius of 1.25 m. The predicted maximum heat rate trajectory is presented in Table 1.4 (Hollis [2005]). The first study of Huygens entry was conducted by Nelson et al. [1991], who introduced a set of chemical rates for CH₄-N₂-Ar mixtures, which are characteristic of the Titan atmosphere. The NEQAIR code was applied to nonequilibrium VSL flowfields along the stagnation line for a preliminary trajectory. Significant radiation from the CN violet and red molecular band systems was predicted. This radiation was significantly more than that of previous studies because of the nonequilibrium prediction of the CN molecule, which was under-predicted in previous studies. Park et al. [1996] compared the predictions of this model with experimental data obtained behind a shock at 2 Torr and 6 km/s. The predicted radiative flux compared well with the data, although it was for conditions not representative of the Huygens shock-layer, which has a pressure that is an order-of-magnitude lower. A similar experimental and computational study was conducted by Koffi-Kpante et al. [1997].

Table 1.4. Maximum heat-rate trajectory points for Huygens entry into Titan

<i>t</i> (s)	Altitude (km)	Density (kg/m ³)	Velocity (km/s)	Temp. (K)
169	367.9	3.64x10 ⁻⁵	6.05	171.3
177	328.5	7.20x10 ⁻⁵	5.89	175.8
185	291.1	1.83x10 ⁻⁴	5.49	177.0
189	273.2	2.96x10 ⁻⁴	5.13	176.6
193	257.8	3.79x10 ⁻⁴	4.71	175.8
201	230.5	7.43x10 ⁻⁴	3.66	173.4

Prior to the entry of the Huygens probe into Titan in January 2005, further computational and experimental studies of the radiative heating for Huygens were conducted to assure that the probe's heat shield was sufficient (Bose et al. [2005], Hollis et al. [2005], Raynaud et al. [2005], and Magin et al. [2005]). Since the successful completion of the Huygens mission, research has continued on this subject in an attempt to improve the prediction capability for future missions (Wright et al. [2006]). A topic of interest resulting from these studies is the disagreement between various computational studies and also with experimental data. A comparison of the predicted radiative heating values for Huygens entry is shown in Figure 1.9. The LAURA and DPLR results were taken from Hollis [2005]. It is seen that the two widely used radiation codes, NEQAIR and RAD/EQUIL, disagree by nearly a factor of two. Wright et al. [2005] have since shown agreement between the line-by-line approach of NEQAIR and other similar but independent line-by-line codes, which suggests that the lack of agreement shown by Hollis is due

to inadequacies in the molecular band modeling of the RAD/EQUIL code. The uncertainty in the spectral modeling is therefore small if the line-by-line approach is used. The drawback to this approach is that it is very computationally expensive, which makes it very difficult to apply to a coupled radiation-flowfield analysis. Therefore, although it models the spectrum accurately for given flowfield conditions, the inaccuracy due to ignoring coupling remains (which was the second source of uncertainty listed above). The coupling, or cooling, effect has been approximately treated in these past studies, which are shown as the approximately-cooled values in Figure 1.9, using a correction factor developed for Jupiter entry (Tauber and Wakefield [1971]). Unfortunately, this approximate method has not been validated for Titan entry with non-optically thin radiation.

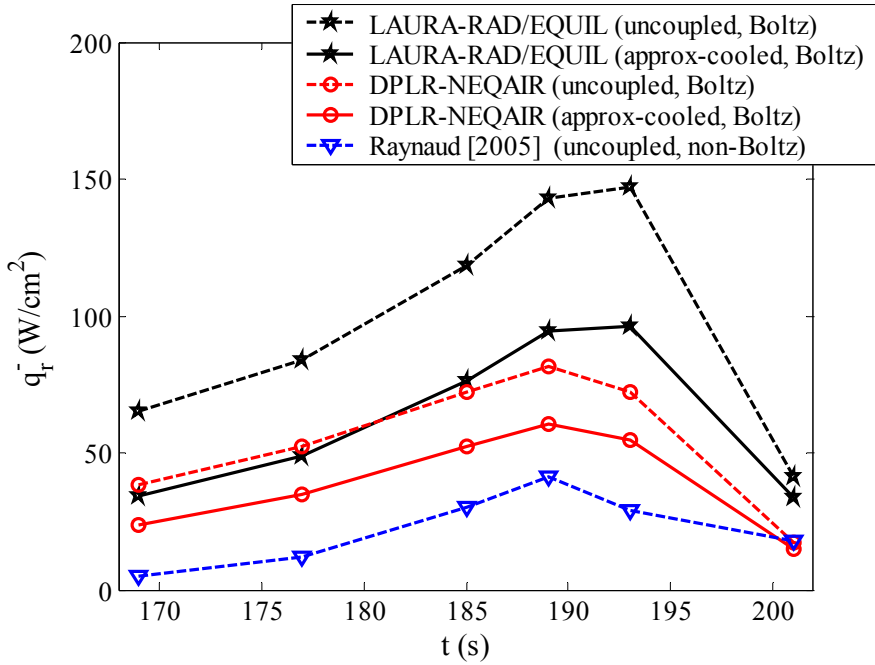


Figure 1.9. Comparison of the predicted radiative heating for Huygens entry

Although the experimental data of Park et al. [1996] and Koffi-Kpante et al. [1997] compared well with predictions, the experimental pressures are larger than those in a Huygens shock-layer near peak heating. The lower pressure data obtained by Bose et al. [2005], which was at conditions similar to a Huygens shock-layer near peak heating, showed radiation much lower than expected. This phenomenon was attributed to the non-Boltzmann population of the CN electronic states. Removing the Boltzmann assumption requires a kinetic scheme, similar to that used for nonequilibrium chemistry modeling, to calculate the CN excited state populations. Kinetics schemes for CN excitation have been proposed recently by both Raynaud et al. [2005] and Magin

et al. [2005] specifically for Titan. It has been shown that implementing these models reduces the radiative heating significantly. The influence of radiative absorption on the excitation calculation, as discussed by Bose et al. [2005], complicates the calculation further, especially if the spectrum is modeled using the line-by-line approach.

The unfortunate result that these various studies do not agree indicates that significant uncertainty exists in the prediction of shock-layer radiative heating for Titan entry. In summary, this uncertainty may be attributed to three primary sources: 1) the accuracy of the CN violet and red molecular band spectral representations (these band systems contribute the majority of the radiation at Huygens entry conditions); 2) the influence of radiation-flowfield coupling; 3) the accuracy of the kinetic scheme required for modeling the CN electronic state populations.

1.7 Outline of the Dissertation

The previous sections have shown disagreement between the results of various modern radiation models. These models have also been shown to disagree with available experimental data. The goal of this dissertation is to reconcile these differences for Earth and Titan Entry. This advancement in the state-of-the-art is accomplished through the development of detailed atomic and molecular spectral and state-kinetic models based on the most recent available data. Chapter 2 presents a viscous-shock layer (VSL) model for modeling chemical and thermodynamic nonequilibrium stagnation line flowfields. This provides an efficient and accurate flowfield model that allows for radiation-flowfield coupling to be accounted for with relative ease. The same chemical rates and thermodynamic properties are applied in the present study as used in NASA Langley's LAURA code (Gnoffo et al. [1989]), which makes comparisons between the results of the two methods more meaningful. The results of the present VSL method are compared with result from the LAURA code for the uncoupled Fire II and Huygens cases. The stagnation line flowfields from each are shown to compare well, for both equilibrium and nonequilibrium conditions. Furthermore, applying the same non-Boltzmann radiation code to both the LAURA and VSL flowfields is shown to produce wall radiative flux values that agree within 5%.

Chapter 3 presents a new set of models for the atomic radiation from nitrogen and oxygen, which are the major contributors to air radiation for most shock-layer conditions of interest. A set of atomic levels and atomic lines are chosen from the National Institute of Standards and Technology (NIST) online database (Ralchenko [2006]). Atomic bound-free cross sections for nitrogen and oxygen are collected from the Opacity project's TOPbase (Cunto et al. [1993]), which is also an online database that provides the most up-to-date values for the cross-sections. A

comparison of the new atomic model with previous models is made for equilibrium constant-property slabs. Radiation from the molecular band systems for Earth entry is reviewed (the molecular band systems for Titan are treated in Chapter 6), and their relative contribution to the total radiative heating is discussed.

Chapter 4 examines the collisional-radiative (CR) modeling for N, O, N₂, and N₂⁺. The CR model provides the non-Boltzmann population of the electronic states, which is shown to be important for the radiation calculation in regions of chemical and thermodynamic nonequilibrium. For each of the species treated, a new set of electronic-impact excitation rates are collected from the literature and compared with the values of previous models. A method of curve-fitting the detailed atomic and molecular models with electronic temperature and electron number density is developed, which provides a significant decreases in the computational burden associated with implementing the model.

Chapter 5 combines the flowfield model developed in Chapter 2, for *Earth* entry, with the radiation model developed in Chapters 3 and 4. This combination provides an efficient and accurate method for modeling coupled radiation-flowfield shock-layers. Predictions for the Fire II and Apollo 4 flight experiments are obtained from this model and compared with the flight data and previous theoretical predictions. For the Fire II cases, the present predictions provide, on average throughout the trajectory, a better comparison with data than any previous study. The comparison with Apollo 4 data is not as good, with the present model over predicting the data over most of the trajectory. The influence of the new radiation model, radiation-flowfield coupling, and non-Boltzmann radiation on the present results and the comparison with the data is discussed.

Chapter 6 investigates the radiative heating of the Huygens probe for entry into *Titan*. The majority of the shock-layer radiation for this case is a result of the CN violet molecular band system. The modeling of this band system for conditions relevant to a Huygens shock-layer is studied in detail. It is shown that a conventional smeared-rotational band (SRB) approach to the CN violet band is inadequate for the partially optically-thick conditions present in the Huygens shock-layer around the peak heating trajectory points. A simple modification is proposed to the SRB model that improves its accuracy in these partially optically-thick conditions. This modified approach, labeled herein as SRBC (smeared-rotational band *corrected*), is compared throughout this study with a detailed line-by-line (LBL) calculation and is shown to compare within 5% in all cases. The SRBC method requires many orders-of-magnitude less computational time than the

LBL method, which makes it ideal for coupling to the flowfield. The application of a collisional-radiative (CR) model for determining the population of the CN electronic states, which govern the radiation for Huygens entry, is discussed and applied.

Chapter 2

The Viscous Shock-Layer Stagnation Line Flowfield

2.1 Chapter Overview

To allow for an accurate calculation of shock layer radiation, the temperature and number densities of the radiating species must be known accurately throughout the shock-layer. The current state-of-the-art method for obtaining these values requires the solution of the Navier-Stokes equations. These solutions may be obtained with codes such as the LAURA code (Gnoffo [1990]). Unfortunately, the significant computational expense of such calculations, especially for coupled flowfield-radiation solutions, makes this approach undesirable for fundamental studies of shock-layer radiation. Since most entry-vehicles with significant radiative heating are capsule-like configurations, the nose radius is the main geometric dimension of the vehicle that governs the convective and radiative heating in the forebody stagnation region. Thus, a computationally efficient flowfield method that treats only the stagnation line of the vehicle (which is subsequently defined by its nose radius) is desired for the present study of radiation-flowfield coupled shock-layer. Such a method exists with the viscous shock-layer (VSL) method, which was developed by Davis [1970a] for a perfect gas flow, and was later extended to chemical nonequilibrium by Moss [1974] and multiple temperatures by Gally [1992] and Gupta [1996]. Although this method is also applicable to regions downstream of the stagnation line, it has the convenient property of being applicable to the stagnation line alone, without explicit consideration of the downstream flow.

The present chapter describes a method for calculating the stagnation-line flowfield properties of a two-temperature, chemical nonequilibrium, hypersonic viscous shock-layer using the VSL method. Based on the model outlined by Gupta [1996], the present approach extends this model by applying the most recent energy-exchange models and by allowing for the treatment of relatively high-temperature and highly-ionized conditions. The extension of this method to these high-temperature conditions ($T > 9,000$ K), allows it to be applied to the lunar-return shock layers of present interest. Section 2.2 presents the governing equations for a two-temperature thermochemical nonequilibrium viscous shock-layer and discusses the simplification of these equations for the analysis of the stagnation region. Sections 2.3 and 2.4 discuss the special treatment of the species continuity equation and vibrational-electronic-electron energy equation, respectively, which is required for an efficient solution procedure. The solutions of the other governing conservation equations are briefly described in Section 2.5. The shock-slip equations, which provide the boundary conditions for the governing conservation equations, are described in Section 2.6. The chemical-equilibrium VSL approach is briefly described in Section 2.7, and is later shown in Section 2.9 to provide a useful alternative to the nonequilibrium VSL approach for conditions where the majority of the shock-layer is in chemical equilibrium. Comparisons between the VSL and Navier-Stokes results are presented in Section 2.8 to validate the VSL method for lunar-return shock layers. This comparison, which has not been presented previously in the literature for a two-temperature nonequilibrium VSL method, provides valuable insight into the differences between the Navier-Stokes and VSL methods. The shock layers for Huygens entry into Titan are studied in Section 2.9 and compared with Navier-Stokes results.

2.2 Governing Equations

By writing the Navier-Stokes equations for a two-temperature chemical reacting flow in nondimensional form, and discarding terms that have an order greater than ε^2 , the following set of viscous shock-layer equations are obtained (Davis [1970a], Moss [1974]):

Species Continuity:

$$\rho \left(\frac{u}{1+n\kappa} \frac{\partial c_i}{\partial s} + v \frac{\partial c_i}{\partial n} \right) = \dot{w}_i - \frac{\varepsilon^2}{(1+n\kappa)(r+n\cos\theta)} \left\{ \frac{\partial}{\partial n} [(1+n\kappa)(r+n\cos\theta) J_i] \right\} \quad (2.1)$$

Vibrational-Electronic-Electron Energy:

$$\begin{aligned} \rho C_{p,ve} \left(\frac{u}{1+n\kappa} \frac{\partial T_{ve}}{\partial s} + v \frac{\partial T_{ve}}{\partial n} \right) &= Q_{e-t} + Q_{v-t} + Q_{e,ion} + Q_{v,dis} + Q_{rad} + \frac{p_e}{\rho} \left(\frac{u}{1+n\kappa} \frac{\partial \rho}{\partial s} + v \frac{\partial \rho}{\partial n} \right) \\ &+ \varepsilon^2 \left\{ \frac{\partial}{\partial n} \left[K_{ve} \frac{\partial T_{ve}}{\partial n} \right] + \left(\frac{\kappa}{1+n\kappa} + \frac{\cos \theta}{r+n \cos \theta} \right) K_{ve} \frac{\partial T_{ve}}{\partial n} - \sum_{i=1}^{N_s} J_i C_{p,ve}^i \frac{\partial T_{ve}}{\partial n} \right\} - \sum_{i=1}^{N_s} h_{ve,i} \dot{w}_i \end{aligned} \quad (2.2)$$

Total Energy:

$$\begin{aligned} \rho C_{p,tr} \left(\frac{u}{1+n\kappa} \frac{\partial T_{tr}}{\partial s} + v \frac{\partial T_{tr}}{\partial n} \right) + \rho C_{p,ve} \left(\frac{u}{1+n\kappa} \frac{\partial T_{ve}}{\partial s} + v \frac{\partial T_{ve}}{\partial n} \right) \\ - \left(\frac{u}{1+n\kappa} \frac{\partial p}{\partial s} + v \frac{\partial p}{\partial n} \right) = \varepsilon^2 \left\{ \frac{\partial}{\partial n} \left[K_{tr} \frac{\partial T_{tr}}{\partial n} + K_{ve} \frac{\partial T_{ve}}{\partial n} \right] + \left(\frac{\kappa}{1+n\kappa} + \frac{\cos \theta}{r+n \cos \theta} \right) \left(K_{tr} \frac{\partial T_{tr}}{\partial n} + K_{ve} \frac{\partial T_{ve}}{\partial n} \right) \right. \\ \left. - \sum_{i=1}^{N_s} J_i \left(C_{p,tr}^i \frac{\partial T_{tr}}{\partial n} + C_{p,ve}^i \frac{\partial T_{ve}}{\partial n} \right) + \mu \left(\frac{\partial u}{\partial n} - \frac{u\kappa}{1+n\kappa} \right)^2 \right\} - \sum_{i=1}^{N_s} h_i \dot{w}_i + Q_{rad} \end{aligned} \quad (2.3)$$

s-Momentum:

$$\begin{aligned} \rho \left(\frac{u}{1+n\kappa} \frac{\partial u}{\partial s} + v \frac{\partial u}{\partial n} + \frac{uv\kappa}{1+n\kappa} \right) + \frac{1}{1+n\kappa} \frac{\partial p}{\partial s} \\ = \varepsilon^2 \left\{ \frac{\partial}{\partial n} \left[\mu \left(\frac{\partial u}{\partial n} - \frac{u\kappa}{1+n\kappa} \right) \right] + \mu \left(\frac{2\kappa}{1+n\kappa} + \frac{\cos \theta}{r+n \cos \theta} \right) \left(\frac{\partial u}{\partial n} - \frac{u\kappa}{1+n\kappa} \right) \right\} \end{aligned} \quad (2.4)$$

Global Continuity:

$$\frac{\partial}{\partial s} [(r+n \cos \theta) \rho u] + \frac{\partial}{\partial n} [(1+n\kappa)(r+n \cos \theta) \rho v] = 0 \quad (2.5)$$

n-Momentum:

$$\rho \left(\frac{u}{1+n\kappa} \frac{\partial v}{\partial s} + v \frac{\partial v}{\partial n} - \frac{u^2 \kappa}{1+n\kappa} \right) + \frac{\partial p}{\partial n} = 0 \quad (2.6)$$

Equation of State:

$$p = \rho T_{tr} \left(\sum_{i=1, i \neq e}^{N_s} c_i \frac{R_{univ}}{M_i} \right) + \rho T_{ve} \left(c_e \frac{R_{univ}}{M_e} \right) \quad (2.7)$$

The nomenclature applied in these equations is consistent with that used by Davis [1970a and 1970b], Moss [1974], Gupta [1996], and most other VSL studies. These equations are for a two-dimensional axisymmetric flow with the coordinates n and s normal and tangential to the body, respectively. The one-dimensional stagnation-line solution is obtained from these equations by expanding the dependent variables in a Taylor series with respect to the nondimensional distance along the body ($\xi = s$) as follows

$$p(\xi, \eta) = p_1(\eta) + p_2(\eta)\xi^2 + \dots \quad (2.8)$$

$$u(\xi, \eta) = u_1(\eta)\xi + \dots \quad (2.9)$$

$$v(\xi, \eta) = v_1(\eta) + v_2(\eta)\xi^2 + \dots \quad (2.10)$$

$$n_s = n_{1s} + n_{2s}\xi^2 + \dots \quad (2.11)$$

The dependent variables T_{tr} , T_{ve} , ρ , and c_i are independent of ξ to first order, and are therefore not written here as an expansion for brevity. The geometric variables in the stagnation region may be expanded as

$$\theta = \pi/2 - \xi + \dots \quad (2.12)$$

$$\alpha = \frac{\pi}{2} + \xi \left(\frac{2n_{2s}}{1+n_{1s}} - 1 \right) + \dots \quad (2.13)$$

$$r = \xi + \dots \quad (2.14)$$

$$\kappa = 1 + \xi + \dots \quad (2.15)$$

By substituting these expansions into Eqs. (2.1 – 2.7), the partial differential equations are reduced to ordinary differential equations (with η as the independent variable). These equations are presented in Sections 2.3 and 2.4 for the species continuity equation and the vibrational-electronic-electron energy equation. The remaining stagnation-line conservation equations are the same as those presented by Moss [1974] and Miner and Lewis [1975]. As pointed out by Davis [1970a], the coupling of the stagnation-line solution to the downstream solution is represented entirely by the presence of n_{2s} in the stagnation-line tangential and normal momentum equations. This term, which is defined in Eq. (2.11), may be written in terms of the dimensional shock-wave radius of curvature at the stagnation line (R_S^*) as follows:

$$n_{2s} = 1 + n_{1s} - \frac{(1+n_{1s})^2}{(R_S^*/R_N^*)} + \dots \quad (2.16)$$

where R_N^* is the dimensional[†] nose radius of the body and n_{1s} is the shock-standoff distance at the stagnation-line, divided by R_N^* . In the original VSL solution procedure presented by Davis [1970a], an initial stagnation-line and downstream solution was obtained by assuming that n_{2s} was equal to zero. The n_{1s} and R_S^* values obtained from this initial solution were then applied to Eq. (2.16) to obtain a nonzero value for n_{2s} . Another solution was then calculated using this updated value. This “global iteration” procedure allows the weak elliptic nature of the VSL equations to be properly accounted for, and allows for the flowfield downstream of the

[†] Throughout this chapter, the ‘*’ superscript on a variable indicates that it is dimensional. This notation follows that used in most VSL studies.

stagnation-line to be obtained. Because only the stagnation line flowfield is of interest in the present study, a method of determining n_{2s} without having to apply this global iteration procedure, or obtaining a solution downstream of the stagnation-line, is desired. The effect of n_{2s} is restricted essentially to increasing the shock standoff distance (n_{1s}) by only about 5-10% relative to the case where n_{2s} is set to zero. Therefore, the precise calculation of n_{2s} is not essential, and it may be roughly approximated with little loss in the resulting flowfield accuracy. The approach used throughout this study is based on the shock-wave shape correlation presented by Billig [1967]. His expression for R_S^* may be written as

$$R_S^* / R_N^* = (1 + n_{1s}) \exp[0.54 / (M_\infty - 1)^{1.2}] \quad (2.17)$$

This expression is consistent with the early shock wave curvature measurements made by Sedney [1957]. Substituting this equation into Eq. (2.16) results in the following equation for n_{2s}

$$n_{2s} = (1 + n_{1s}) \left\{ 1 - \exp[-0.54 / (M_\infty - 1)^{1.2}] \right\} \quad (2.18)$$

This shows that as the free-stream Mach number (M_∞) increases, n_{2s} approaches zero, meaning the shock wave becomes concentric with the body. For the lunar-return conditions considered in the present study, this term had little impact on the solutions because of the high Mach numbers. Note that n_{2s} is the only term that couples the downstream flow to the stagnation-line even for truncated bodies, such as the Fire II vehicle. In the solution procedure discussed here, the physical nose radius is applied. The influence of the truncated body's shoulder radius on the stagnation-line flow is accounted for through n_{2s} , instead of using an equivalent nose radius (Zoby [1965]). This approach provides stagnation-line flowfields that are in excellent agreement with Navier-Stokes results, as will be shown in Sections 2.8. For the Huygens cases considered in the present study, the wide-angled sphere-cone body of the Huygens probe is not modeled well with Eq. (2.18). For these cases, an equivalent nose radius was used with n_{2s} set equal to unity. The radius was chosen by matching the VSL results with the shock-standoff distance predicted by the LAURA Navier-Stokes solutions. This resulted in a value of 1.35 m, which is only slightly larger than the physical value of 1.25 m. This small difference indicates that if no Navier-Stokes solution was available to determine the equivalent nose radius, the physical value could be applied with little loss in accuracy.

The following two sections discuss in detail the treatment of the species continuity equation and vibrational-electronic-electron energy equation, both of which require special attention for the multicomponent diffusion and two-temperature ionized flows considered in the present study.

2.3 The Species Continuity Equation

The stagnation-line expression for the mass conservation of species i may be written from Eqs. (2.1, 2.8 - 2.14) as follows

$$\frac{\rho v}{n_{1s}} \frac{\partial c_i}{\partial \eta} = \dot{w}_i - \frac{\varepsilon^2}{1 + n_{1s}\eta} \left(2J_i + \frac{1 + n_{1s}\eta}{n_{1s}} \frac{\partial J_i}{\partial \eta} \right) \quad (2.19)$$

The diffusion mass flux of species i present in this equation may be written in the following general form:

$$J_i = J_{A,i} \frac{\partial c_i}{\partial \eta} + J_{B,i} c_i + J_{C,i} \quad (2.20)$$

where the coefficients $J_{A,i}$, $J_{B,i}$ and $J_{C,i}$ depend on the chosen diffusion model. For a constant Lewis number (N_{Le}) model, these coefficients become

$$J_{A,i} = -\frac{K}{n_{1s} C_p} N_{Le}, \quad J_{B,i} = 0, \quad J_{C,i} = 0 \quad (2.21)$$

For the “approximate-corrected” multicomponent diffusion model proposed by Sutton and Gnoffo [1998], the coefficients become

$$J_{A,i} = -\frac{K}{n_{1s} C_p} D_{im}, \quad J_{B,i} = -\sum_{i=1}^{N_s} J_i^{old}, \quad J_{C,i} = 0 \quad (2.22)$$

where J_i^{old} is the J_i value calculated in the previous flowfield iteration. This approach will be used for modeling multicomponent diffusion instead of the “detailed” multicomponent treatment developed by Blottner [1969], which was subsequently applied by Moss [1974]. The Sutton and Gnoffo approach is simpler to apply, especially for ionized flows with 11 or more species, and has been shown to reproduce the results of the Stefan-Maxwell equations for a variety of chemical compositions (Gnoffo et al. [1999], Hollis et al. [2005]).

The mass rate of production of species i per-unit volume (\dot{w}_i) present in Eq. (2.19) may be written as

$$\dot{w}_i = \left(\frac{R_N^*}{\rho_\infty^* U_\infty^*} \right) M_i \sum_{r=1}^{N_r} (\beta_{i,r} - \alpha_{i,r}) (R_{f,r}^* - R_{b,r}^*) \quad (2.23)$$

where the first term in parentheses is for nondimensionalization. The forward and backward reaction rates may be written, respectively, as

$$R_{f,r}^* = 1000 \left[k_{f,r}^* (0.001 \rho^*)^{\sum_{i=1}^{N_s} \alpha_{i,r}} \prod_{i=1}^{N_s} \left(\frac{c_i}{M_i} \right)^{\alpha_{i,r}} \right] \quad (2.24)$$

$$R_{b,r}^* = 1000 \left[k_{b,r}^* (0.001 \rho^*)^{\sum_{i=1}^{N_s} \beta_{i,r}} \prod_{i=1}^{N_s} \left(\frac{c_i}{M_i} \right)^{\beta_{i,r}} \right] \quad (2.25)$$

which has the units of kg-mol/m³-s. Blottner [1969] suggested that linearizing \dot{w}_i improves convergence for highly dissociated flow. Following this suggestion, \dot{w}_i may be written as

$$\left(\frac{\dot{w}_i}{\rho} \right)^{k+1} = w_i^0 - w_i^1 c_i^{k+1} \quad (2.26)$$

where

$$w_i^0 = \left(\frac{\dot{w}_i}{\rho} \right)^k - \frac{\partial}{\partial c_i} \left(\frac{\dot{w}_i}{\rho} \right)^k c_i^k \quad (2.27)$$

and

$$w_i^1 = - \frac{\partial}{\partial c_i} \left(\frac{\dot{w}_i}{\rho} \right)^k \quad (2.28)$$

In these expressions, k indicates values obtained from the previous iteration. An upper limit of 25,000 K was applied for the temperature used to calculate the forward rate ($k_{f,r}^*$) and backward rate ($k_{b,r}^*$) for each chemical reaction. This was applied because most of the rates used for both Earth and Titan entry are not valid at temperatures above this value.

2.4 The Vibrational-Electronic-Electron Energy Equation

The equation for conservation of vibrational, electronic, and free-electron energy along the stagnation line may be written from Eqs. (2.2, 2.8 - 2.15) as

$$\begin{aligned} \frac{\rho C_{p,ve} v_1}{n_{1s}} \frac{\partial T_{ve}}{\partial \eta} &= \frac{p_e}{\rho} v_1 \frac{1}{n_{1s}} \frac{\partial \rho}{\partial \eta} + \varepsilon^2 \left\{ \frac{1}{n_{1s}^2} \frac{\partial}{\partial \eta} \left[K_{ve} \frac{\partial T_{ve}}{\partial \eta} \right] + \frac{2}{1+n_{1s}\eta} K_{ve} \frac{1}{n_{1s}} \frac{\partial T_{ve}}{\partial \eta} \right. \\ &\quad \left. - \sum_{i=1}^{N_s} J_i C_{p,ve}^i \frac{1}{n_{1s}} \frac{\partial T_{ve}}{\partial \eta} \right\} - \sum_{i=1}^{N_s} h_{ve,i} \dot{w}_i + Q_{e-t} + Q_{v-t} + Q_{e,ion} + Q_{v,dis} + Q_{rad} \end{aligned} \quad (2.29)$$

The proper modeling of the energy source terms ($Q_{e,ion}$, $Q_{v,dis}$, Q_{rad}) and relaxation terms(Q_{e-t} , Q_{v-t}) is key to calculating reasonable values of the vibrational-electronic-electron temperature (T_{ve}) from this equation. Since radiation is governed by T_{ve} , as will be discussed in Chapter 3, the proper treatment of this equation is essential for obtaining accurate shock-layer radiative heating values. The treatment applied in the present study for the energy source and relaxation terms is discussed in the following sub-sections.

a) Vibrational-Translational Energy Exchange: Q_{v-t}

For negligibly ionized flowfields, the vibrational-translational energy exchange term is the most important of the source and relaxation terms present in Eq. (2.29). Gnoffo et al. [1989] reviews the approach that has become the standard for treating this term. This approach is based on the Landau-Teller equation, which is written for the present model as follows

$$Q_{v-t} = \sum_{i=molec.} \rho_i \frac{e_{ve,i}(T_{tr}) - e_{ve,i}(T_{ve})}{\tau_i} F \quad (2.30)$$

where $e_{ve,i}(T_{tr})$ and $e_{ve,i}(T_{ve})$ represents the local equilibrium value and the physical value, respectively, of the vibrational-electronic-electron energy of species i . For situations where $e_{ve,i}(T_{tr})$ is larger than $e_{ve,i}(T_{ve})$, Eq. (2.30) shows that Q_{v-t} is positive, meaning that translational-rotational energy is being transferred to the vibrational energy mode. This tends to bring the two temperatures together. The rate at which the temperatures come together, or the rate of energy exchange between the two energy modes, depends on the relaxation time τ_i . This value is modeled using a combination of the Millikan and White correlation (τ_i^{MW}) and a correction introduced by Park (τ_i^P):

$$\tau_i = \tau_i^{MW} + \tau_i^P \quad (2.31)$$

The Millikan and White correlation is written as

$$\frac{1}{\tau_i^{MW}} = \left(\sum_{\substack{j=1 \\ j \neq e}}^{N_s} x_j \left\{ \left(\frac{U_\infty^*}{R_N^*} \right) \frac{101325}{p^*} \exp \left[A_i^* \left(T_{tr}^{*(1/3)} - 0.015 \left(\frac{M_i^* M_j^*}{M_i^* + M_j^*} \right)^{1/4} \right) - 18.42 \right] \right\}^{-1} \right) \left/ \sum_{\substack{j=1 \\ j \neq e}}^{N_s} x_j \right. \quad (2.32)$$

In this equation, x_i are the mole fractions, p^* is the pressure in N/m², T_{tr}^* is the translational-rotational temperature in Kelvin, and M_i^* is the specie molecular weight (kg/kg-mol). The A_i^* values are the correlation constants obtained by Milikan and White and presented in Table 1 of Gnoffo et al. [1989]. Park [1984] observed that the values predicted by Eq. (2.32) were too large for temperatures above 8000 K and suggested a correction of the following form

$$\tau_i^P = \left(\frac{U_\infty^*}{R_N^*} \right) \frac{1}{\sigma_i^* \bar{C}_i^* N_{total}^*} \quad (2.33)$$

where the average velocity of molecule i is written as

$$\bar{C}_i^* = \left(\frac{8 R_{univ}^* T_{tr}^*}{\pi M_i^*} \right)^{1/2} \quad (m/s) \quad (2.34)$$

and the total number density of the gas is

$$N_{total}^* = \sum_{i=1}^{N_s} N_i^* \quad (\text{particles / m}^3) \quad (2.35)$$

The limiting cross section required in Eq. (2.33) was estimated by Park [1989] using the following expression

$$\sigma_i^* = 10^{-21} \left(50,000 / T_{tr}^* \right)^2 \quad (\text{m}^2) \quad (2.36)$$

Other models for this term have been investigated by Hartung et al. [1992] and Greendyke [1993], although it was concluded in these studies that the treatment presented here is the most physically realistic. When applying Eq. (2.36) to a VSL flowfield, it was found necessary to place an upper limit on T_{tr}^* in order to obtain results consistent with shock capturing Navier-Stokes results. This is required for the discrete shock VSL calculation because of the very large T_{tr}^* values directly behind the shock, which are not present for the Navier-Stokes results. Although, Park [1989] states that Eq. (2.36) is valid up to 62,000 K, it is limited at 20,000 K for the present study. Increasing this limit increases the region of nonequilibrium behind the shock and influences the post-shock temperatures by changing the derivative terms in the shock-slip equations (which are presented in Section 2.6).

The function F in Eq. (2.30) was introduced by Park [1988] to account for the diffusion-like nature of the vibrational relaxation equation at high temperatures, and is written as

$$F = \left| \frac{T_{tr,sh} - T_{ve}}{T_{tr,sh} - T_{ve,sh}} \right|^{s-1} \quad (2.37)$$

where

$$s = 3.5 \exp \left(-5000 / T_{tr,sh}^* \right) \quad (2.38)$$

The temperature values with subscripts *sh* represents the post-shock values. To be consistent with current Navier-Stokes solvers that do not include this term, in particular the LAURA code, $F = 1$ is applied in the present study instead of Eq. (2.37). As discussed by Hartung et al. [1992], the main reason for not including this term is that it requires the definition of post-shock temperatures, which are not well defined for a shock capturing calculation. For the discrete shock approach used by the VSL method, this difficulty is not present and Eq. (2.37) can be included with no additional complexity. If it were included in the present study, which it is *not*, Eq. (2.37) would increase slightly the nonequilibrium region of the shock layer.

A common approximation to Eq. (2.30) that simplifies its evaluation is the following

$$Q_{v-t} = \rho \sum_{i=mol.} c_i \frac{C_{p,ve}^i (T_{tr} - T_{ve})}{\tau_i} F \quad (2.39)$$

Note that this term always contributes to bringing T_{tr} and T_{ve} together behind the shock. The smaller the relaxation time (τ_i), the larger this term becomes, and the quicker the two temperatures approach each other. The summation over the species in Eq. (2.39) only includes molecules. Because this term is proportional to the species mass fraction, when all the molecules are dissociated, and hence all the vibrational energy is gone, this term becomes zero. Also, as a result of their definition in the two-temperature model, the $e_{v,i}$ used in Eq. (2.30) or the $C_{p,ve}^i$ used in Eq. (2.39) contain the vibrational *as well as* electronic energy components. The inclusion of the electronic energy component is inconsistent with the physical meaning of this vibrational relaxation term. Fortunately, the error introduced by this approximate treatment is small because at high vibrational-electronic temperatures ($>8,000$ K) when the electronic energy of the molecules becomes important, the molecules are mostly dissociated. This is true for the nonequilibrium flow immediately behind the shock, where although the molecules have not had time to dissociate and the translational-rotational temperature is very high ($>20,000$ K), the vibrational-electronic temperature is very low ($<2,000$ K, if the frozen shock conditions are applied) and the corresponding electronic energy is low.

b) Electron-Translational Energy Exchange: Q_{e-t}

The electron-translational energy exchange term is the result of elastic collisions of electrons with neutral species and ions. The form of this term used in the present study was derived by Appleton and Bray [1964] for a monatomic ionized gas consisting of neutral species, ions, and electrons. Other notable discussions of this term are presented by Petschek and Byron [1957] and Sutton and Sherman [1965]. The dimensional form of this term is written as

$$Q_{e-t}^* = 3\rho_e^* R_{univ}^* (T_{tr}^* - T_{ve}^*) \sum_{i=1}^{N_s} \frac{v_{e,i}^*}{M_i^*} \quad (2.40)$$

where all the variables are dimensional. Dividing this by $\rho_\infty^* U_\infty^{*3} / R_N^*$, this term is defined in terms of nondimensional variables as

$$Q_{e-t} = 3\rho_e \left(\frac{R_{univ}^*}{M_{mix}^* C_{p,\infty}^*} \right) (T_{tr} - T_{ve}) \sum_{i=1}^{N_s} \frac{v_{e,i}}{M_i} \quad (2.41)$$

The collision frequency for collisions between ions and electrons is expressed as

$$v_{e,i} = \left(\frac{R_N^*}{U_\infty^*} \right) \frac{8}{3} \left(\frac{\pi N_A}{M_e^*} \right)^{1/2} \frac{N_i^* e^4}{(2kT_{ve}^*)^{3/2}} \ln \left(\frac{k^3 T_{ve}^{*3}}{\pi n_e^* e^6} \right) \quad (2.42)$$

where the first term in parenthesis makes this expression nondimensional. The collision frequency for collisions between neutrals and electrons is written as

$$v_{e,i} = \left(\frac{R_N^*}{U_\infty^*} \right) n_i^* \sigma_{e,i} \left(\frac{8kN_A T_{ve}^*}{\pi M_e^*} \right)^{1/2} \quad (2.43)$$

For the lunar-return shock-layers of present interest, the collisions between ions and electrons provide the dominant contribution to Q_{e-t} in Eq. (2.41). If these contributions are not considered, T_{tr} and T_{ve} will not equilibrate properly through the shock-layer. For coupled radiation-flowfield solutions, in fact, ignoring this term results in T_{tr} and T_{ve} having values that differ by more than 1,000 K in the chemical equilibrium region of the shock-layer. Note that Q_{e-t} has a similar influence on highly dissociated conditions in the process of ionizing that the vibrational-translational energy exchange term (Q_{v-t}) has on unionized conditions in the process of dissociating. In other words, Q_{e-t} governs the relaxation of the bound electronic and free-electron energy of atoms and molecules while Q_{v-t} governs the relaxation of the vibrational energy of the molecules. Note that this term requires ionization to be considered because it is proportional to the electron density. If ionized species are ignored, this term is zero, even though the bound-electronic energy of the atoms and molecules are included in the energy equation implicitly through the curve-fits used for the species enthalpies and specific heats. As a result, there is no mechanism for relaxation of the bound electronic energy with the translational-rotational energy modes.

c) Vibrational Energy Reactive Source Term: $Q_{v,dis}$

The vibrational energy reactive source term accounts for the energy created or destroyed through molecular dissociation or recombination. This term is written nondimensionally as

$$Q_{v,dis} = \sum_{i=molec.} \dot{w}_i \left(\frac{\hat{D}_i^*}{U_\infty^{*2}} \right) \quad (2.44)$$

where \dot{w}_i is defined in Eq. (2.23) and \hat{D}_i^* represents the vibrational energy created or destroyed at a rate \dot{w}_i . The \hat{D}_i^* term is defined empirically. Gnoffo et al. [1989] reviewed a couple of possible models for this term, although no model is recommended over another. Hartung et al. [1992] investigated the influence of these models on radiative heating for high velocity (>11 km/s) cases. It was shown that only models of the following form consistently resulted in non-negative temperature values near the shock

$$\hat{D}_i^* = c_{dis} e_{ve,i}^* \quad (2.45)$$

where c_{dis} is an unknown constant. Although there is not significant evidence to support the choice, it has become standard to set c_{dis} equal to one.

d) Electronic Energy Reactive Source Term: $Q_{e,ion}$

The electronic energy reactive source term accounts for the energy loss of free electrons due to the process of electron impact ionization. The precise definition of this term depends on how the free-electron and bound electronic energy modes are book-kept in solving the various energy equations. As previously mentioned, the bound electronic, free electron, and vibrational energy are grouped into one energy equation and solved for T_{ve} , while the total energy equation is solved for T_r instead of solving the translational-rotational energy equation explicitly. The grouping of the free electron with the bound electronic energy is actually uncommon in much of the past literature that discusses this term, so care must be taken when interpreting their discussions for use in the current model. The treatment of an independent electron energy equation is followed by Petschek and Byron [1957], Appleton and Bray [1964], Lee [1984], Carlson and Gally [1991], and Surzhikov et al. [2006], to name a few. Each of these studies provides a brief explanation of the electronic energy reactive source term in the context of an electron energy equation. Briefly, these explanations state that a free electron strikes a neutral particle and transfers energy from the translational energy of the free electron to the bound electronic states of the neutral atoms, therefore exciting the atoms. It is then assumed that all excited atoms are ionized, a process which requires a negligible amount of energy. The total energy lost by the electrons through this process, which is equal to the energy gained by the bound electronic states of the atom, is essentially the energy required to excite the atoms from the ground state, which is roughly equal to the ionization energy of the atom. Gnoffo et al. [1989] and Park [1990] present a similar discussion for this term even though they include it in a free-electron *plus* bound-electronic energy equation. Following Gnoffo et al. [1989], this term is written as

$$Q_{e,ion} = - \sum_{i=ions} \dot{w}_i \left(\frac{I_i^*}{U_\infty^{*2}} \right) \quad (2.46)$$

where I_i^* represents the energy required to ionize a species from an already excited state, which is equal to 4.05×10^8 J/kg-mol for atomic nitrogen and 4.30×10^8 J/kg-mol for atomic oxygen. The studies of Hartung et al. [1992] and Greendyke [1993] concluded that it was better to set I_i^* equal to the energy required to ionize a species from an already excited state, rather than from the ground state, as was suggested originally by Lee [1984]. This treatment was applied in the present study.

2.5 Solution Procedure

The total energy, n -momentum, s -momentum, and global continuity equations for the stagnation line are written similarly to Eqs. (2.19) and (2.29), and are presented in Appendix C of Moss [1974]. The solution of this set of equations is straightforward, and is similar to that presented by Moss [1974]. For the present solution procedure, a finite-difference grid using 150 points between the shock wave and body is applied. The points are spaced unevenly using the approach suggested by Lee and Gupta [1992]. The Thomas algorithm is used to solve each governing equation individually, and in the following order: species continuity for c_i (individually for each species), vibrational-electronic-electron for T_{ve} , total energy for T_{tr} , s -momentum for u , global continuity for n_{ls} and v , and n -momentum for p_1 and p_2 . The solution of these equations is repeated until convergence is reached. To avoid an unstable iteration procedure, an under-relaxation scheme is applied, which weights the most recently calculated value and the value from the previous iteration by 0.2 and 0.8, respectively. When obtaining a solution from scratch (i.e. *not* from a converged solution at a slightly different condition), values of 0.05 and 0.95 are required because of the highly nonlinear influence of the chemical reactions on the species number densities and the temperatures. The number of iterations required for a converged solution depends strongly on how close the shock layer is to chemical equilibrium. For conditions where less than 50% of the shock layer is in equilibrium, less than 100 iterations are required. For conditions where more than 90% is in equilibrium, up to 1000 iterations are required.

2.6 Shock-Slip Equations

The shock-slip equations provide the boundary conditions at the shock for the VSL solution procedure. These equations, introduced by Cheng [1962], are obtained by integrating the Navier-Stokes equations from the free-stream to the post shock state and retaining the first order normal derivative terms. It is also assumed that chemical production and energy exchange terms are negligible in the shock. The resulting shock-slip equations contain conduction and diffusion terms not present in the Rankine-Hugoniot equations. These additional terms are proportional to ε^2 , which is equal to the inverse of the free-stream Reynolds number, and the n -derivative of a flowfield parameter, depending on the equation. Much of the past interest in the shock-slip equations was to capture the effect of low Reynolds number, meaning ε^2 was large, although for the present work where ε^2 is small, the large n -derivative of the temperature and species mass fractions directly behind the shock for near equilibrium conditions causes the terms added shock-slip terms to be large. Not including shock-slip for cases where the shock-layer is near chemical

equilibrium results in an incorrect equilibrium shock-layer temperature, which can be differ by 1,000 K or more from the correct value (Gally and Carlson [1992]). The shock-slip equations presented by Gupta [1995] for thermochemical nonequilibrium may be solved for the post-shock stagnation-line variables. These equations are reviewed in the following subsections.

a) Global Continuity:

The global continuity equation is solved for the post-shock normal velocity as follows[‡]

$$v_s = -\frac{1}{\rho_s} \quad (2.47)$$

where ρ_s is the post-shock density. This equation does not contain any viscous terms, and is therefore not effected by slip.

b) *n*-Momentum:

The *n*-Momentum equation is solved for the post-shock pressure. To be consistent with Eq. (2.8), the post shock pressure is expanded in the following form

$$p_s = p_{1s} + \xi^2 p_{2s} \quad (2.48)$$

Substituting this into the *n*-Momentum shock-slip equations, the following expressions are obtained for the post-shock pressure

$$p_{1s} = p_\infty + \left(1 - \frac{1}{\rho_s}\right) + \varepsilon^2 \frac{4}{3} \left[\mu_s \frac{\partial v_s}{\partial n} \right] \quad (2.49)$$

$$p_{2s} = -\left(1 - \frac{2n_{2s}}{1+n_{1s}}\right) \left(1 - \frac{1}{\rho_s}\right) \quad (2.50)$$

c) *s*-Momentum:

The *s*-Momentum equation is solved for the post-shock tangential velocity gradient. The tangential velocity and tangential velocity gradient are related as

$$u_s = u_{1s} \xi + \dots \quad (2.51)$$

Substituting this into the *s*-Momentum equation results in the following equation for the post-shock tangential velocity gradient

$$u_{1s} = \left(1 - \frac{2n_{2s}}{1+n_{1s}}\right) - \varepsilon^2 \mu_s \frac{\partial u_{1s}}{\partial n} + \dots \quad (2.52)$$

d) Translational-Rotational Energy:

The shock-slip equation for the translational-rotational energy is written as

[‡] Note that v_s and ρ_s are nondimensionalized by their free-stream values.

$$h_{tr,\infty} - h_{tr,s} + \frac{1}{2} (1 + u_s^2 - v_s^2) = \varepsilon^2 K_{tr,s} \frac{\partial T_{tr,s}}{\partial n} + \varepsilon^2 \rho_s \left(\sum_{i=1}^{N_s} h_{tr,i} D_i \frac{\partial c_i}{\partial n} \right)_s + \frac{4}{3} \varepsilon^2 v_s \mu_s \frac{\partial v_s}{\partial n} \quad (2.53)$$

where the last term was not included by Gupta [1994]. To solve this equation in terms of the translational-rotational temperature, the following iteration formula proposed by Gupta is used

$$(h_{tr,i,s})^{k+1} = \left[\frac{(h_{tr,i,s} - \Delta h_i^f)}{T_{tr,s}} \right]^k T_{tr,s}^{k+1} + \Delta h_i^f \quad (2.54)$$

where k is the iteration number and Δh_i^f is the heat of formation of species i . Substituting Eq. (2.54) into Eq. (2.53) and solving for the translational-rotational temperature results in the following

$$T_{tr,s}^{k+1} = \frac{-h_{tr,\infty} + \varepsilon^2 K_{tr,s} \frac{\partial T_{tr,s}}{\partial n} - \varepsilon^2 \rho_s \sum_{i=1}^{N_s} D_i \Delta h_i^f \frac{\partial c_i}{\partial n} + \sum_{i=1}^{N_s} c_{i,s} \Delta h_i^f + \frac{4}{3} \varepsilon^2 v_s \mu_s \frac{\partial v_s}{\partial n} - \frac{1}{2} (1 + u_s^2 - v_s^2)}{- \left\{ \sum_{i=1}^{N_s} c_{i,s} \left[\frac{(h_{tr,i,s} - \Delta h_i^f)}{T_{tr,s}} \right]^k + \varepsilon^2 \rho_s \sum_{i=1}^{N_s} \left[\frac{(h_{tr,i,s} - \Delta h_i^f)}{T_{tr,s}} \right]^k D_i \frac{\partial c_i}{\partial n} \right\}} \quad (2.55)$$

e) Vibrational-Electronic-Electron Energy:

The shock-slip equation for the vibrational-electronic-electron energy is written as

$$h_{ve,\infty} - h_{ve,s} = \varepsilon^2 \left(K_{ve} \frac{\partial T_{ve}}{\partial n} \right)_s + \varepsilon^2 \left(\rho \sum_{i=1}^{N_s} h_{ve,i} D_i \frac{\partial c_i}{\partial n} \right)_s \quad (2.56)$$

Similarly to the translational-rotational enthalpy, the vibrational-electronic-electron enthalpy is written as

$$(h_{ve,i,s})^{k+1} = \left[\frac{h_{ve,i,s}}{T_{ve,s}} \right]^k T_{ve,s}^{k+1} \quad (2.57)$$

Substituting this into Eq. (2.56), the vibrational-electronic-electron temperature may solved to obtain the following equation:

$$T_{ve,s}^{k+1} = \frac{-\varepsilon^2 \left(K_{ve} \frac{\partial T_{ve}}{\partial n} \right)_s + h_{ve,\infty}}{\sum_{i=1}^{N_s} \left[\frac{h_{ve,i,s}}{T_{ve,s}} \right]^k + \varepsilon^2 \rho_s \sum_{i=1}^{N_s} \left[\frac{h_{ve,i,s}}{T_{ve,s}} \right]^k D_{i,s} \frac{\partial c_{i,s}}{\partial n}} \quad (2.58)$$

Application of this equation results in $T_{ve,s}$ values that range from 1,000 to 10,000 K, depending on the free-stream conditions. These values are significantly larger than the free-stream temperature, which is applied if the frozen-shock conditions are applied instead of the shock-slip conditions. These larger temperatures decrease the magnitude of the temperature gradients

located directly behind the shock. This decreases the stiffness of the species continuity and energy equations, which improves the convergence of these equations throughout the shock-layer.

2.7 The Equilibrium Viscous Shock-Layer

At the peak convective heating trajectory point of most lunar return vehicles, which occurs after the peak radiative heating point, the stagnation region shock-layer is in chemical and thermodynamic equilibrium throughout at least 90% of the shock-layer thickness. Although the two-temperature thermochemical nonequilibrium VSL formulation discussed in the previous sections is applicable in these situations, it becomes computationally inefficient because of the discrete shock formulation, which forces the flowfield variables to rapidly change from their frozen-shock values to their equilibrium values. This causes very large gradients directly behind the shock that tend to slow down the iteration solution procedure. This difficulty remains even when the shock-slip equations, discussed in the previous section, are applied. These problems may be avoided completely by applying the chemical equilibrium (and single temperature) formulation of the viscous shock layer, which was originally developed by Moss [1974] and has been widely applied since. The equilibrium shock conditions are used for this method, instead of the frozen or shock-slip conditions applied for the nonequilibrium case. The total energy equation (Eq. (2.3) with the chemical production term set to zero and T_{tr} and T_{ve} set equal to each other) is solved in terms of enthalpy, instead of temperature, and the species mass fractions are obtained by enforcing chemical equilibrium at each point in the shock-layer for a given enthalpy and density, instead of solving the species continuity equations. If binary diffusion is assumed, then the *elemental* mass fractions of N₂ and O₂ remain equal to their free-stream value (for Earth entry), which means that the solution of the elemental continuity equation is not required. The binary diffusion assumption is made in the present study for the equilibrium VSL solutions. Although multicomponent diffusion is applied for the nonequilibrium formulation, as discussed in Section 2.3, this has a negligible influence on the predicted radiative heating. A comparison between the equilibrium and nonequilibrium VSL methods will be made in the following section. The chemical equilibrium solver developed by Prabhu and Erickson [1988], which is specific to air, was incorporated in the present equilibrium VSL solver (the equilibrium VSL method was not applied to Titan entry in the present study). Note that although the equilibrium VSL method is many orders-of-magnitude faster than the thermochemical nonequilibrium VSL formulation, it is only accurate for the limited range of free-stream conditions and nose radii where the shock-layer is more than about 90% in equilibrium.

2.8 Application to Lunar-Return Shock-Layers

To validate the VSL model discussed in this chapter for lunar return conditions, comparisons were made with Navier-Stokes results produced by the LAURA code[§] for the Fire II cases discussed in Section 1.4. An effort was made to use the same kinetic models and thermophysical properties in the present VSL code as are applied in the LAURA code. The air model applied consists of the following 11-species: N_2 , N_2^+ , O_2 , O_2^+ , NO , NO^+ , N , N^+ , O , O^+ , and e^- . The forward chemical rates were taken from Park [1993], while the backward rates were obtained by applying detailed balancing; with the equilibrium constants calculated using curve-fits from McBride et al. [2002]. These curve-fits were also used to calculate the specific heat and enthalpy values for each species. The collision cross-sections required for the calculation of the diffusion, viscosity, and thermal conductivity coefficients were taken from Gupta et al. [1990]. Multicomponent diffusion was modeled using the “approximate-corrected” approach presented by Sutton and Gnoffo [1998] and discussed in Section 2.3. The constants required for the energy exchange terms in the vibrational-electronic-electron energy equation were discussed in Section 2.4, and are believed to be consistent with what is applied in the current version of LAURA. Note that the treatment of these terms is not consistent with that presented by Gnoffo et al. [1989] in the original documentation of the LAURA code.

The temperature and species number densities (relevant to the radiation calculation) predicted by VSL method and the LAURA code are compared in Figures 2.1 - 2.6 for the Fire II 1634, 1636, and 1643 s trajectory points, which were defined previously in Table 1.1. These three points were chosen because they represent a highly nonequilibrium condition (1634 s), a slightly nonequilibrium condition (1636 s), and an essentially equilibrium condition (1643 s). Note that the peak radiative and convective heating points were found in previous studies (see Figures 1.5 - 1.7) to occur near the 1643 s point. In Figures 2.1 - 2.6, the vehicle wall is located at $z = 0$, where z is the distance along the stagnation line. The consequence of the different treatments of the bow shock wave by the two methods is clearly shown in these figures. The “discrete shock” model of the VSL approach is seen in all cases to result in a larger translational-rotational temperature directly behind the shock, even with the application of the shock-slip equations. The T_{tr} values are seen to behave slightly different in the nonequilibrium region of the layer in all cases. This is another consequence of the discrete shock treatment, which results from T_{tr} beginning its relaxation process behind the shock at a higher temperature than for the LAURA case. The T_{ve}

[§]The LAURA results were provided by Dr. Brian Hollis of NASA Langley Research Center.

values, on the other hand, are in relatively good agreement in the nonequilibrium regions. This is fortunate because T_{ve} governs the radiation. The influence of the shock-slip equations, which were presented in Section 2.6, is seen most clearly in these figures with T_{ve} being significantly larger than the free-stream temperature, which it would equal if the “frozen shock” conditions were applied. The influence of shock-slip in this study is notably larger than that shown by Gally [1992], who implemented a similar three-temperature VSL model with shock slip. Although Gally does not present his shock-slip equations, the difference is likely due to the different treatments of the vibrational energy exchange in the shock-layer vibrational-electronic-electron energy equation. Unlike the present study, Gally applied the Park correction function represented by Eq. (2.37). Also, he did not report any upper limit on Eq. (2.36), which as mentioned in Section 2.4, was applied in the present study. Other than the differences near the shock, the temperature profiles shown in Figures 2.1 - 2.6 closely agree throughout the rest of the shock-layer. The locations at which the two temperatures equilibrate compare well between the methods, as do the values of the temperatures in the equilibrium regions of the layer, which agree within 1% for the cases shown. This close agreement in the equilibrium region of the shock-layer is required for the prediction of similar radiative emission values, because of the exponential T_{ve} dependence of the radiative emission. This exponential dependence is due to the Boltzmann distribution of the upper electronic state of the various radiative transitions, and hence is only true in the regions of chemical equilibrium where a Boltzmann distribution is approached, as will be shown in Chapter 4. Conversely to this exponential dependence on temperature, *most* of the radiative emission depends linearly on the species number densities (as shown in Section 3.6, the atomic bound-free emission has essentially a quadratic dependence). The disagreement in the equilibrium regions of no more than 5% is therefore regarded as sufficient. This disagreement, which is especially noticeable for atomic nitrogen, is caused by inaccuracies introduced by treating the shock discretely and by the expansion procedure used in Section 2.2 to obtain the stagnation line VSL equations. Specifically, the under prediction of the number densities for the VSL case indicates that the pressure, obtained from the n -momentum equation, is under predicted. For the stagnation line equations, the pressure was expanded in Eq. (2.8) using two terms. Applying more terms in this expansion, and introducing them appropriately in the governing conservation equations, including the shock-slip equations, would likely reduce the small differences shown in these figures.

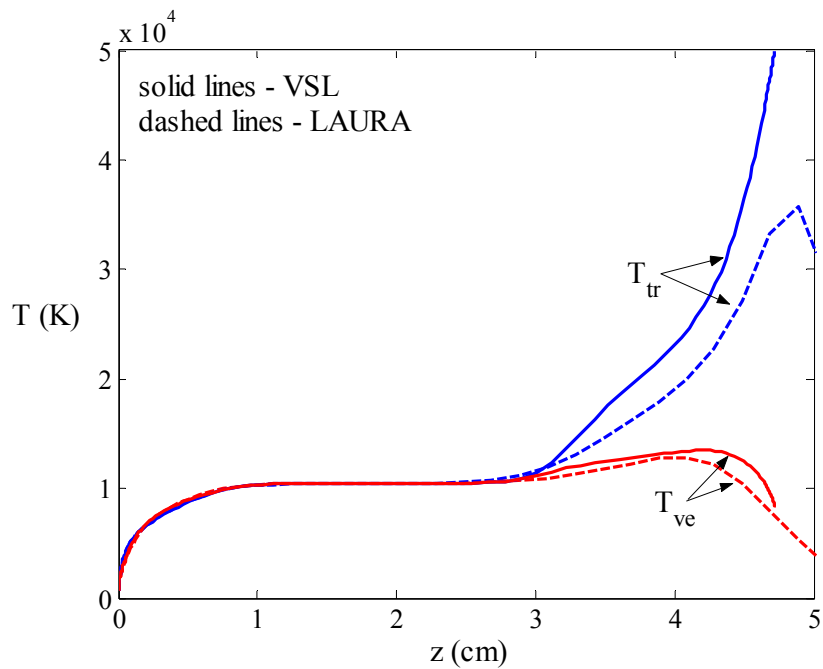


Figure 2.1. Comparison of the VSL and LAURA stagnation line temperature profiles for the Fire 1634 case

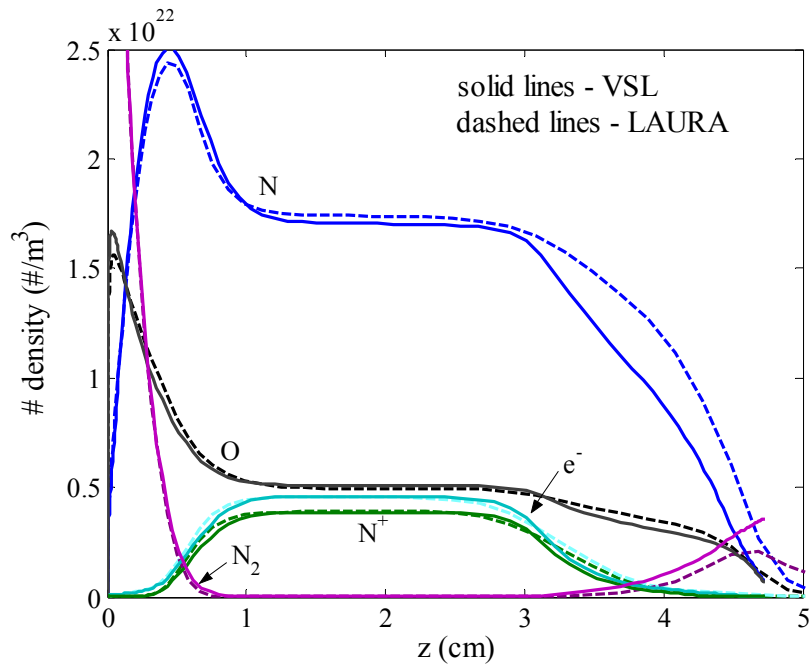


Figure 2.2. Comparison of the VSL and LAURA stagnation line species number density profiles for the Fire 1634 case

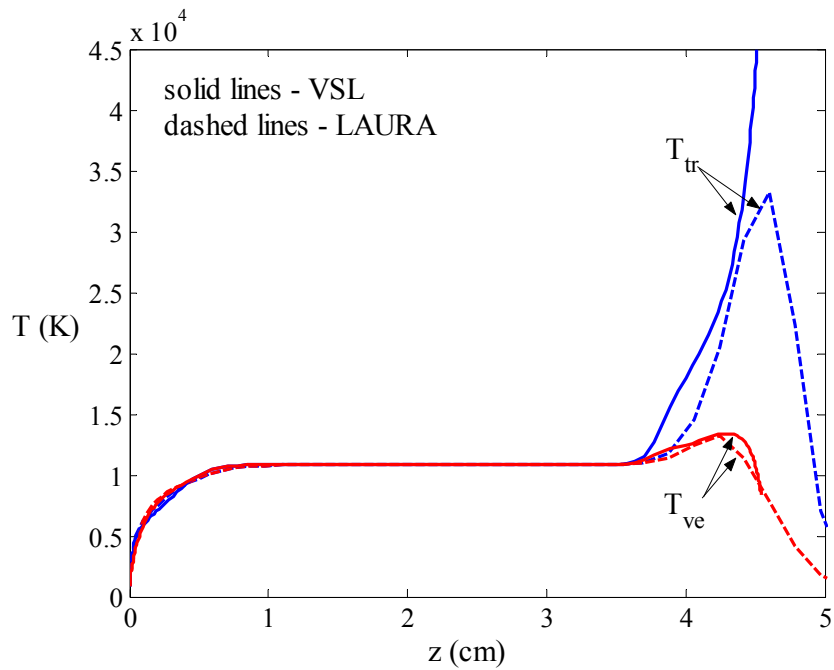


Figure 2.3. Comparison of the VSL and LAURA stagnation line temperature profiles for the Fire 1636 case

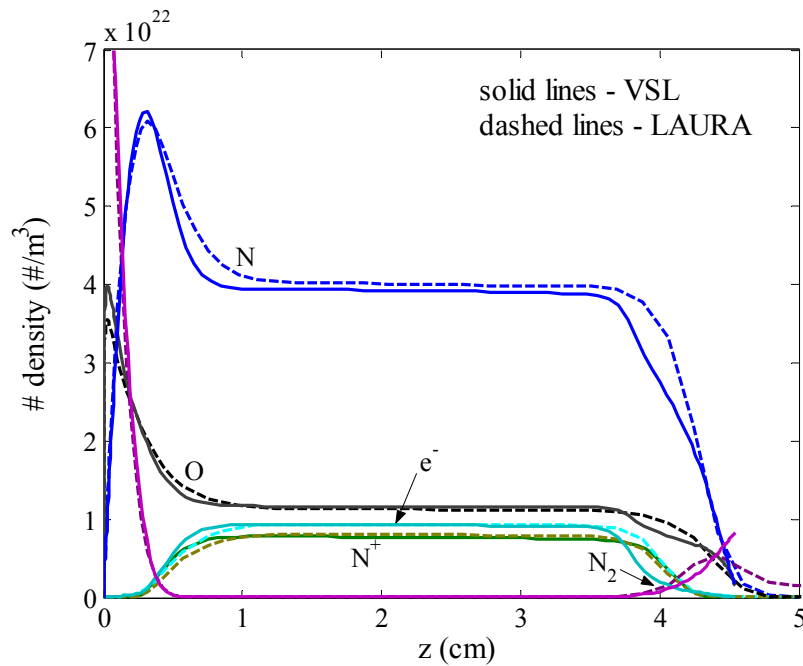


Figure 2.4. Comparison of the VSL and LAURA stagnation line species number density profiles for the Fire 1636 case

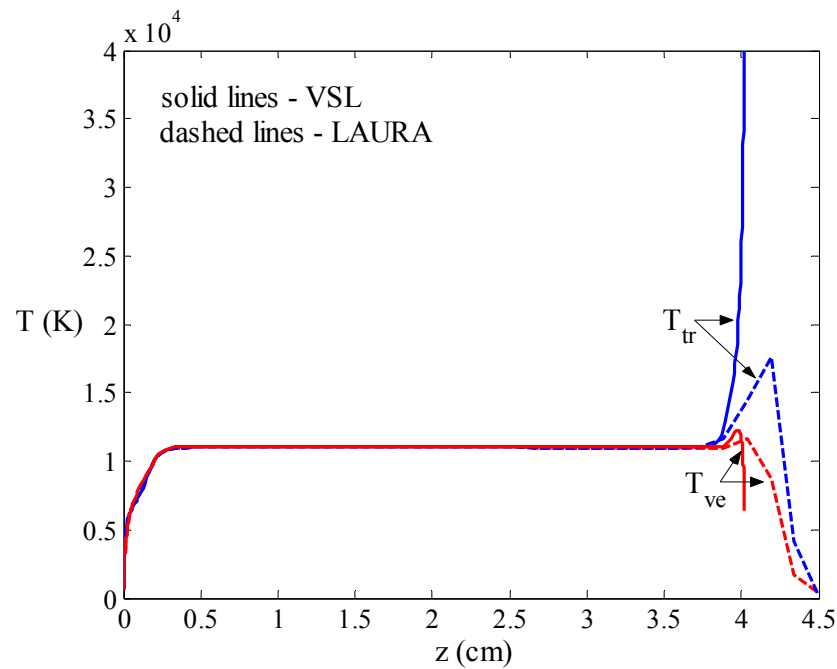


Figure 2.5. Comparison of the VSL and LAURA stagnation line temperature profiles for the Fire 1643 case

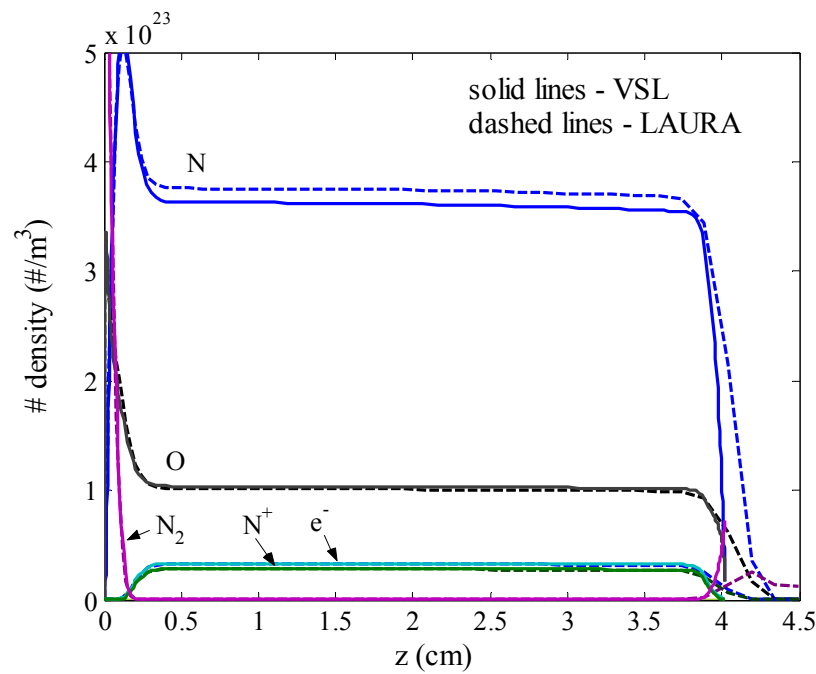


Figure 2.6. Comparison of the VSL and LAURA stagnation line species number density profiles for the Fire 1643 case

The good agreement between the VSL and LAURA flowfields was discussed in the previous paragraph, along with some discussion regarding the effect of the observed small differences on the radiative heating resulting from these two flowfield models. To make certain that the VSL method provides a sufficient flowfield model for predicting radiative heating, the radiation model to be discussed in Chapters 3 and 4 was applied to the flowfields studied in this section. The non-Boltzmann model for the atomic and molecular electronic states, presented in Chapter 4, was applied. Figure 2.7 presents the wall-directed radiative flux for the 1634 and 1636 s cases resulting from the VSL and LAURA flowfields presented in Figures 2.1 – 2.4. The values at the wall ($z = 0$) agree within 5% for the 1636 s case and 1% for the 1634 s case, while the values throughout the shock-layer agree closely as well. This agreement throughout the shock layer is required for the accurate modeling of radiation-flowfield coupling, which although not included here, is dependent on the wall-directed (and shock-directed) radiative flux at each point through the shock-layer, as will be discussed in Chapter 5. The agreement shown in Figure 2.7 is satisfactory, although even better agreement can be achieved for the more equilibrium 1643 s point, as will be discussed in the following paragraph.

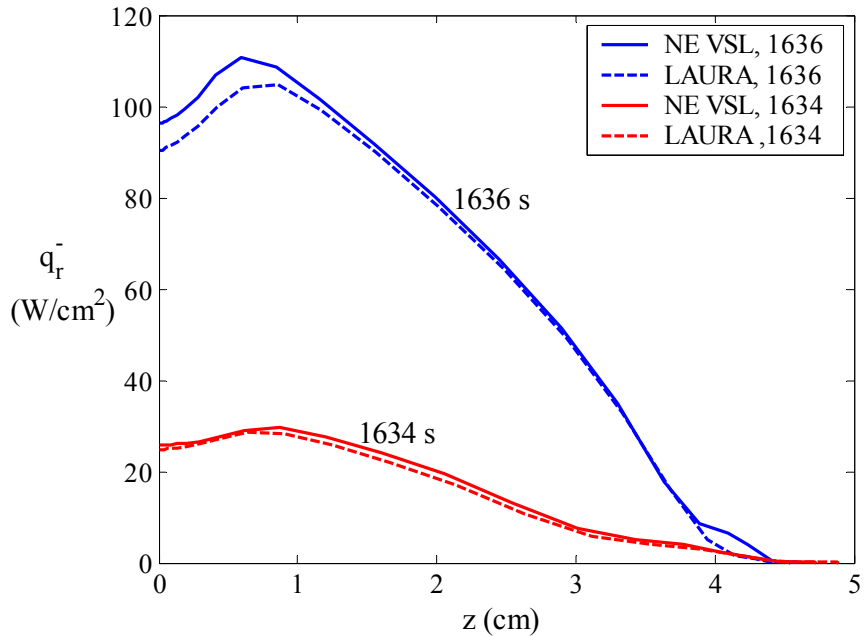


Figure 2.7. Wall directed radiative heat flux values predicted by the non-Boltzmann radiation models presented in Chapters 3 and 4 for the various flowfields.

For conditions where a majority of the shock-layer is in chemical equilibrium, such as for the Fire II 1643 s case presented in Figures 2.5 and 2.6, the nonequilibrium VSL approach becomes computationally inefficient. This inefficiency is a result of the large gradients directly behind the

shock, which directly effect the shock-slip equations and slow down the convergence of the iterative solution procedure. As discussed in Section 2.7, the *equilibrium* VSL approach (E VSL) provides the necessary alternative. Figure 2.8 compares T_{ve} predicted by the nonequilibrium VSL (NE VSL) model, E VSL model, and the LAURA model (this figure has a different y-axis than Figure 2.5 to highlight the differences between the results in the equilibrium region). Note that there is only a single temperature for the E VSL case, which for an accurate radiation calculation must closely model only T_{ve} . This is shown to be true in Figure 2.8, with the E VSL model agreeing better with the LAURA result than the NE VSL case. Although the small nonequilibrium region directly behind the shock is not modeled by the E VSL method, this has only a small effect on the resulting radiation, as indicated by the small radiative emission resulting from this region, as shown in Figure 2.7. The number densities predicted by the E VSL method are compared with the LAURA results in Figure 2.9 for the 1643 s case. Comparing this figure with Figure 2.6, it is seen that the number densities are predicted better (in the equilibrium region) by the E VSL method than the nonequilibrium method. This better agreement is a result of the equilibrium approach, which applies the chemical equilibrium shock conditions, avoids the inaccuracies associated with the large gradients behind the shock. The radiation resulting from these flowfield models are presented in Figure 2.10 for the 1643 s case. The nonequilibrium and equilibrium VSL methods provide wall flux values within 5% of the LAURA result. The majority of the difference for the NE VSL method comes from the slightly different number density and temperature predictions throughout the equilibrium region of the layer.

The conclusion reached in this section is that the NE VSL method provides a flowfield model for Earth entry sufficient for predicting radiative flux values that are consistent with those predicted by the LAURA code. Furthermore, for shock layers that are largely in equilibrium, the *E* VSL method provides both a more computationally efficient model than the *NE* VSL method, while being equally as accurate. These VSL models therefore provide an accurate stagnation-line flowfield model that can be used efficiently for radiation-flowfield coupling, instead of the computationally expensive LAURA code. The radiation-flowfield coupled solutions from these models will be presented and discussed in Chapter 5 for Earth entry.

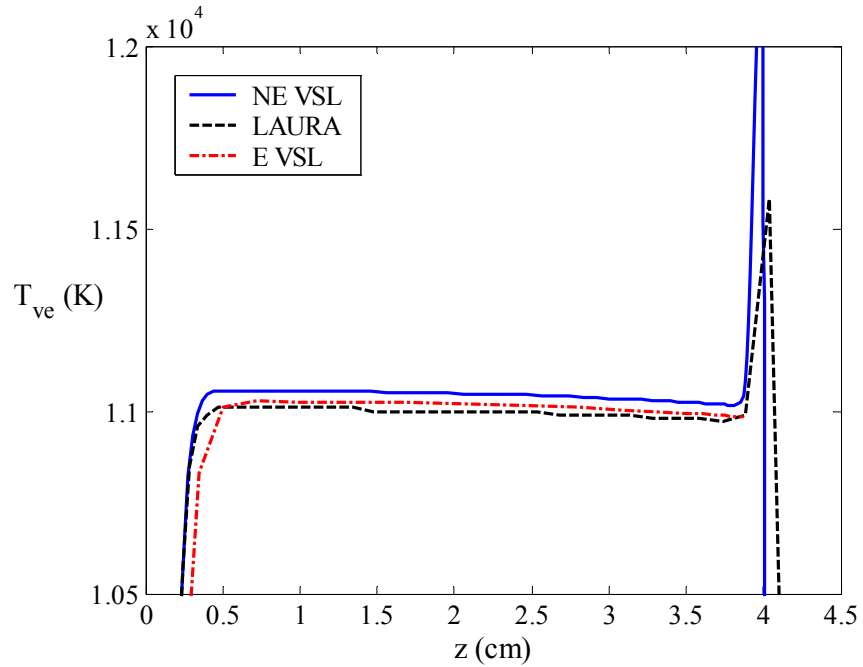


Figure 2.8. Comparison of T_{ve} between the nonequilibrium VSL, equilibrium VSL, and LAURA results for the 1643 s case (the T_{ve} axis was chosen so that the differences between the various models could be seen).

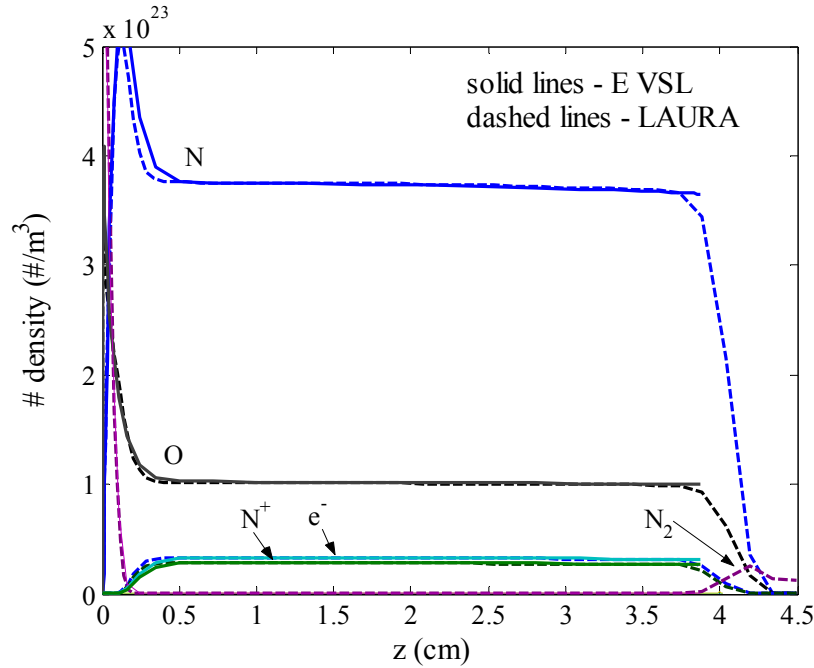


Figure 2.9. Comparison of the number densities predicted by the *equilibrium* VSL (E VSL) code and the LAURA code for the 1643 s case.

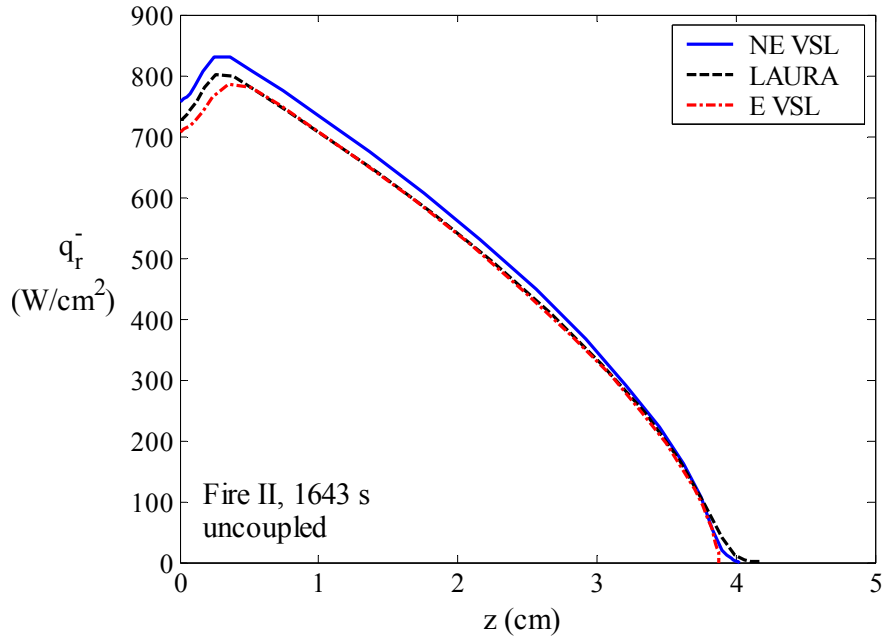


Figure 2.10. Wall directed radiative heat flux values for the 1643 s case resulting from the NE VSL, E VSL, and LAURA flowfield models.

2.9 Application to Huygens Entry into Titan

The application of the VSL code to Huygens entry is similar to the application to Earth entry discussed in the previous section. The most significant differences between these cases are the different composition of the Titan atmosphere, which requires a different kinetic model, and the fact that the Huygens probe traveled at much lower velocity at the peak heating points (relative to the Fire II cases), which results in negligible ionization. The kinetic model developed by Gocken [2004] was applied in the present study, with the reactions involving ionization being ignored. For this set of reactions, a model consisting of the following 14 species is required: Ar, C, CH, CH₂, CH₃, CH₄, CN, C₂, H, HCN, H₂, N, NH, and N₂. The chemical composition of the Titan atmosphere was assumed to consist of N₂, CH₄, and Ar in mole fractions of 0.9699, 0.0230, and 0.0071, respectively. An equivalent nose radius of 1.35 m was applied, which is slightly larger than probe's physical nose radius of 1.25 m. This value was shown to give good agreement with the shock standoff and convective heating predicted by previous analyses (Hollis et al. [2005]). A constant wall temperature of 2,000 K was chosen to approximately match the radiative equilibrium wall values obtained in previous studies. To be consistent with past studies, the wall was assumed to be super-catalytic, meaning that the species mass fractions at the wall were set

equal to their free-stream values. Table 1.4 defines the maximum heat-rate trajectory considered in this study.

To validate the present VSL code for application to Huygens entry cases, comparisons were made with the LAURA results obtained by Hollis et al. [2005], which used the same kinetic and thermophysical properties as used in the present VSL code. Figures 2.11 and 2.12 compare the temperature profiles and CN number density profiles predicted by these codes for the $t = 189$ s case. The temperature profiles are seen to compare well, even near the shock. Similarly, Figure 2.12 shows an excellent agreement for the CN number densities, which is impressive considering the number of species and reactions considered. Only the CN number densities are compared in this figure, for clarity, because they are the only species that radiate significantly. For the other species, the comparison is similar to that shown here for CN. These figures indicate that the VSL method is capable of reproducing the Navier-Stokes stagnation-line flowfields. Although not shown here, the radiative heating predicted by the two flowfields agree within 3% for this case. The comparisons for the other trajectory points are similar to those shown here. This VSL code will be applied in Chapter 6 as a computationally efficient method of obtaining radiation-flowfield coupled solutions. The following paragraph will discuss the basic characteristics of the peak-heating flowfields as they apply to the radiative heating.

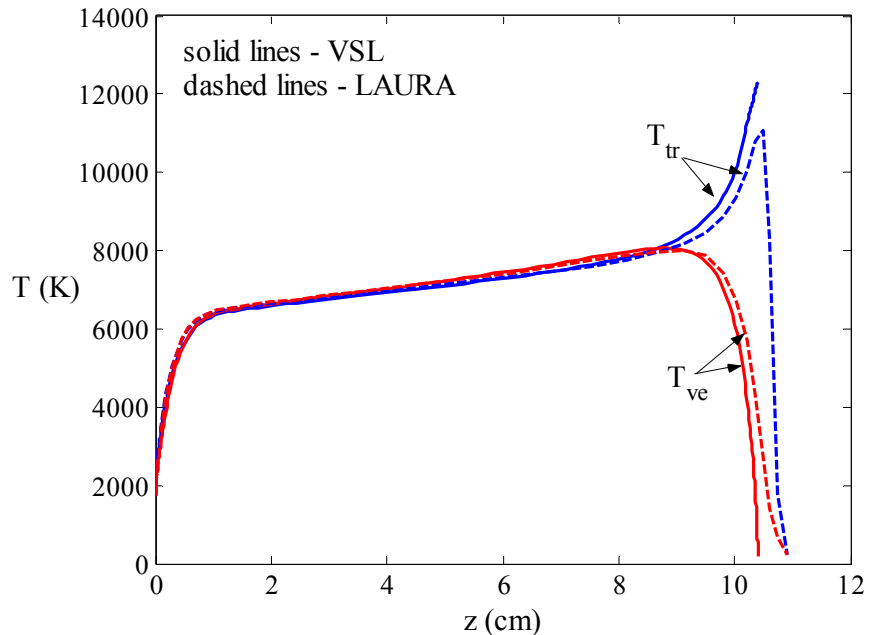


Figure 2.11. Comparison of the VSL and LAURA temperature profiles for the $t = 189$ s case.

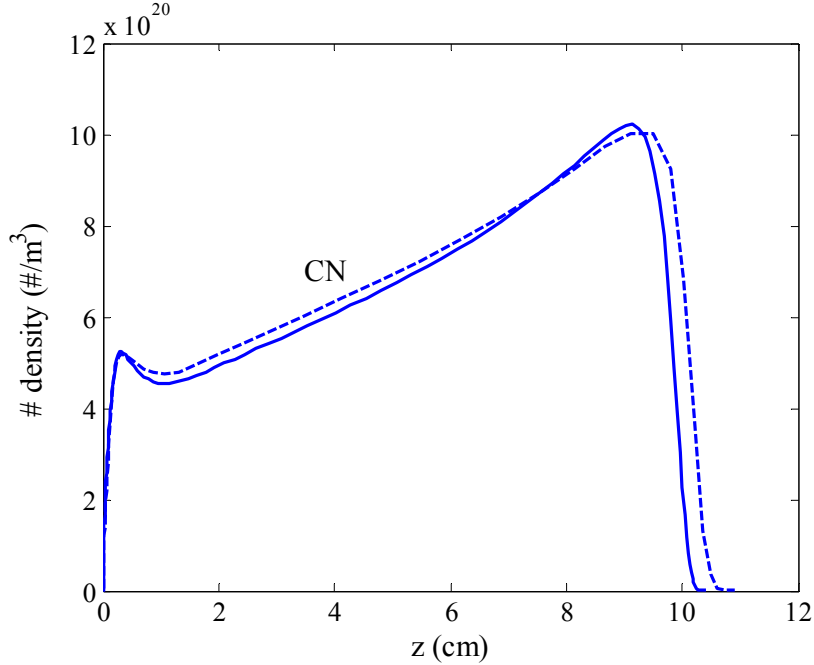


Figure 2.12. Comparison of the VSL and LAURA CN number density profiles for the $t = 189$ s case.

The temperature profiles for the three peak heating trajectory points, as defined by Hollis et al. [2005], are shown in Figure 2.13. These three cases are seen to have similar nonequilibrium behavior. For the later times, with the higher density, the profile becomes flatter as they approach equilibrium (although it is not reached here). The CN number density profiles for these cases are presented in Figure 2.14. Similar trends are seen for each case, although their magnitudes differ considerably. It will be shown in Chapter 6 that the opposite trends of the CN number density and shock-layer thickness increasing with increasing t , while the temperature decreases, results in the $t = 189$ case being the peak radiative heating case (assuming a Boltzmann distribution of the CN electronic states).

The complexity of the chemistry for these Huygens cases is illustrated in Figure 2.15, which presents the species number densities for all of the shock-layer species treated in the present model. While N_2 is no more than 15% dissociated throughout the layer, CH_4 is almost instantaneously dissociated behind the shock into CH_3 , CH_2 , and CH (note that CH_4 , CH_3 , and CH_2 are below the lower limit of the figure, except near the shock and near the wall).

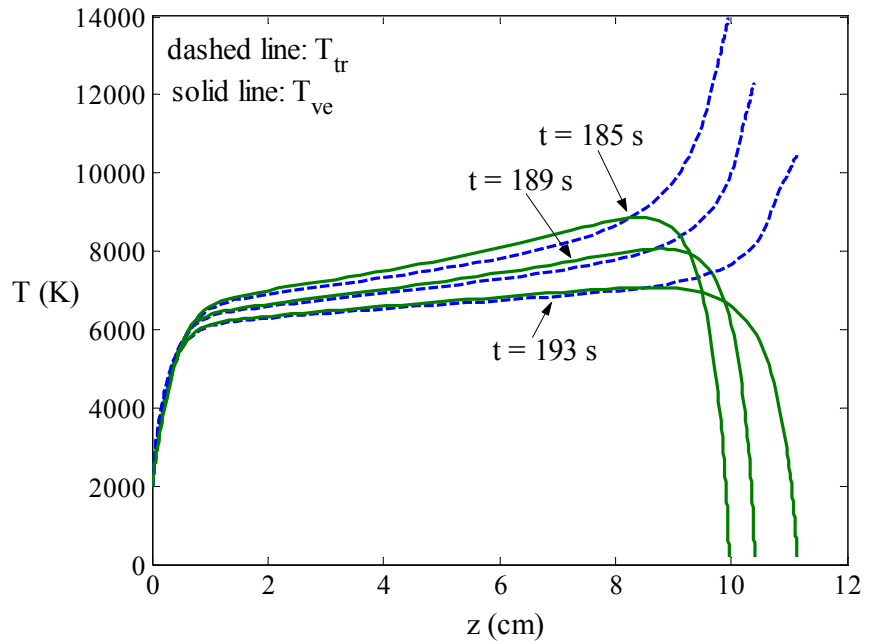


Figure 2.13. Temperature profiles predicted by the VSL method for the three peak-heating Huygens trajectory points.

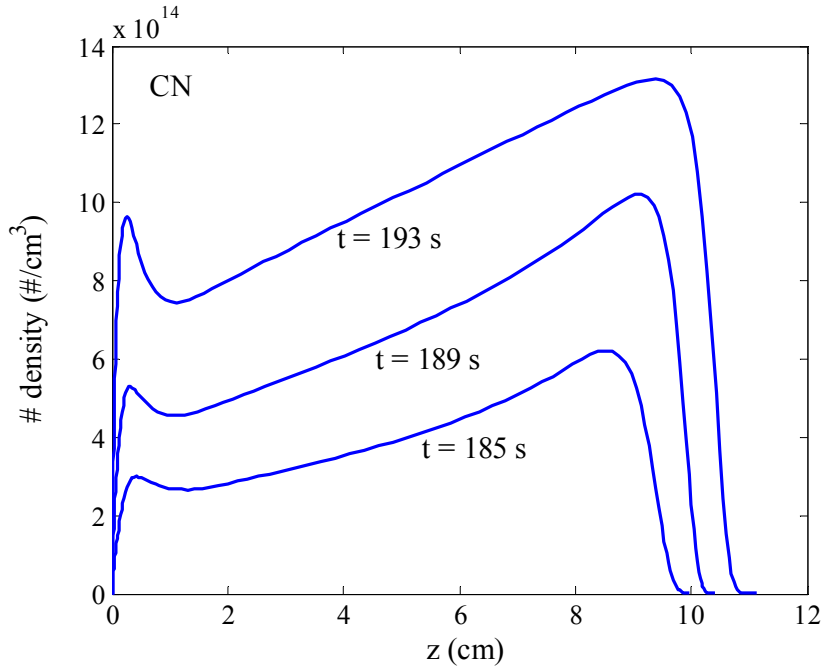


Figure 2.14. CN number density profiles predicted by the VSL method for the three peak-heating Huygens trajectory points.

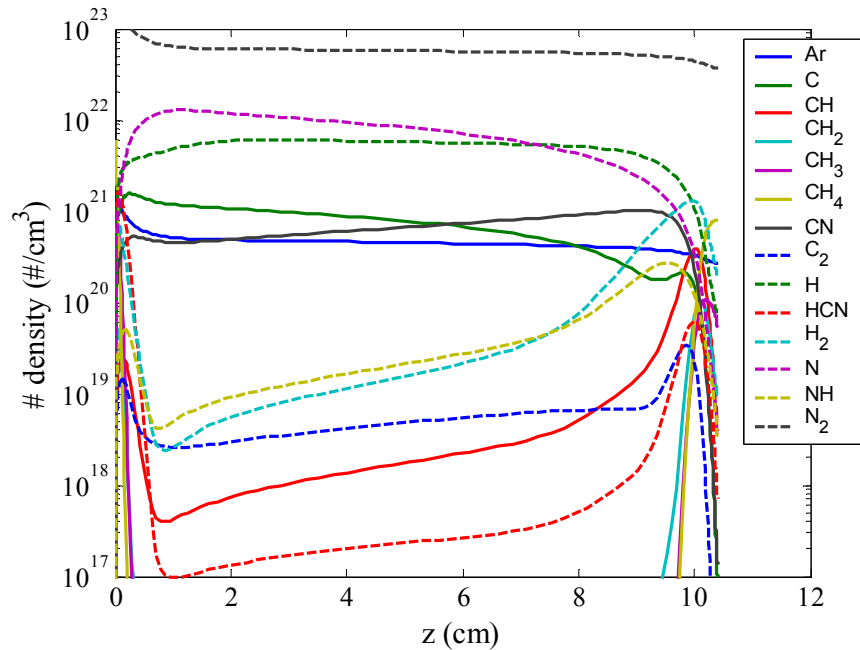


Figure 2.15. Species number density profiles for the Huygens $t = 189$ s case predicted by the VSL method.

Chapter 3

The Radiative Modeling of Equilibrium Air

3.1 Chapter Overview

This chapter presents a model for air radiation intended for the calculation of the radiative heating from lunar-return shock-layers ($7,000 < T < 13,000$ K, $0.01 < p < 2.0$ atm). This model is developed with the intention of applying it, in later chapters, to nonequilibrium chemistry, multiple temperature, and non-Boltzmann conditions. The ability to treat these nonequilibrium conditions is achieved by formulating the emission *and* absorption coefficient as a function of each radiative transition's upper and lower electronic state number density, respectively. Chapter 4 will address the problem of calculating the number densities of the atomic and molecular electronic states required for this radiation calculation. For the examples worked in this chapter, the assumptions of chemical equilibrium and Boltzmann electronic state populations are applied. Although these assumptions are restrictive, they are relevant to many of the shock layer conditions of present interest. The convenience of these assumptions is that they allow the number densities of the six radiating species, N, O, N₂, O₂, N₂⁺, and NO to be determined (assuming the equilibrium solver is accurate) by specifying only the temperature and pressure of the gas. The equilibrium chemical compositions applied in this work are obtained from the code developed by Prabhu and Erickson [1988].

The radiation from atomic nitrogen and oxygen will be discussed first, beginning with the presentation of the atomic level model in Section 3.2. The atomic level model specifies how the hundreds of detailed atomic states, listed in the NIST database (Ralchenko [2006]) for nitrogen

and oxygen, are organized into a reasonable number of “grouped” states. Although the model for the number densities of these grouped states (i.e. the atomic non-Boltzmann model) will not be developed until Chapter 4, the development of the atomic *line* and *continuum* models require this atomic level model *if* they are to be applied to non-Boltzmann conditions. Section 3.3 presents the equations required for the calculation of atomic line (bound-bound) radiation in non-Boltzmann conditions. The atomic line models for nitrogen and oxygen, based on atomic data from the NIST database and various sources for the Stark broadening half-widths, are presented in Section 3.4 and compared with previous models (Park [1985]). The difference between applying an individual or multiplet line model is investigated in this section as well, and the most important lines are highlighted and studied. A method for the systematic construction of a spectral grid, intended for the efficient transport of atomic line radiation through shock layers with widely varying temperatures and species number densities, is discussed in Section 3.5. The basic equations for modeling bound-free and free-free atomic radiation, which will be referred to as “continuum” radiation, are presented in Section 3.6. The continuum radiation resulting from various sources bound-free cross sections are compared in Section 3.7, with a final model being developed based on data from the TOPbase database (Cunto et al. [1993]). Section 3.8 discusses the implementation of the smeared rotational band (SRB) method for calculating molecular band radiation. This method is applied in Section 3.9 for the important molecular band systems of air, and the relative importance of each band system is studied. Section 3.10 applies the models developed throughout this chapter to equilibrium conditions relevant to lunar return shock layers, and provides a summary of the contributions from each of the discussed radiation mechanisms.

3.2 Atomic Level Model

The emission and absorption of an atomic line is proportional to the number density of the upper and lower electronic state of the defined transition, respectively. If the number density of these states are assumed to follow a Boltzmann distribution, and if the energy and degeneracy of the upper or lower states are defined for each atomic line, then there is no need for a separately defined set of atomic levels. This is true because the Boltzmann relationship and Plank function allow for the emission and absorption of each line to be determined. For the non-Boltzmann case, on the other hand, a separate model (this is the CR model, as will be defined in Chapter 4) is required for calculating the population of the electronic states of the radiating atom. The definition of each atomic state in this calculation must be related to the defined upper and lower state of each atomic line transition. Therefore, in preparation for the discussion of the atomic line model (Section 3.4) and the atomic non-Boltzmann model (Section 4.5), this section presents a

model for the atomic levels of nitrogen and oxygen suitable for the present hypersonic shock-layer applications.

There are few available guidelines for defining an adequate set of atomic levels for nitrogen and oxygen for the purpose of modeling the radiative heat flux from a chemical nonequilibrium shock-layer. Bourdon and Vervisch [1996] discussed the choice of an energy level model for atomic nitrogen. The focus of their study was the computation of the three-body recombination rate through the use of a CR model. They concluded that the 22 level model presented by Park [1990] and the 14 level model presented by Kunc and Soon [1989] were inadequate and proposed instead a 43 level model similar to that used by Park [1968]. Bourdon et al. [1998] reached a similar conclusion that 41 levels are required for atomic oxygen. Because the present study is focused on calculating the radiative flux from a shock layer, and not calculating the three-body recombination rate, the conclusion of Bourdon and Vervisch [1996] and Bourdon et al. [1998] that over 40 levels are required for nitrogen and oxygen is not directly applicable. Because no further guidance is available, the current model will be chosen as a compromise between the Bourdon studies and the widely used (for shock layer radiation) Park [1990] model. The new model is presented in Tables 3.1 and 3.2, with the energy levels ordered in terms of increasing energy. The data for these levels were obtained from the NIST database (Ralchenko [2006]); except for those that group all the levels of a single principal quantum number (n), which were taken from Park's work. For both nitrogen and oxygen, it is seen that none of the lower levels are grouped. This allows for maximum precision in the CR model calculation for these levels, which are the most important for the radiation calculation. It is likely, though, that it is unnecessary to treat some of these levels individually and that the total number of levels could be reduced by further grouping. Nevertheless, the present groupings will be maintained to provide benchmark results for assessing further simplifications. The relationship between the energy for a grouped level i and a set of ungrouped levels i' is:

$$E_i = \frac{\sum g_{i'} E_{i'}}{\sum g_{i'}} \quad (3.1)$$

and for the degeneracy is

$$g_i = \sum g_{i'} \quad (3.2)$$

where the summation is over all of the levels i' in the group i . The levels contained in a group are assumed to be populated in a local Boltzmann distribution, which allows the individual level number density ($N_{i'}$) to be related to the group number density (N_i) as follows

$$N_i = N_i \frac{g_i}{g_i} \exp \left[-\frac{hc}{kT_e} (E_i - E_i) \right] \quad (3.3)$$

This relationship is useful for relating data given in terms of the number density of the individual level (such as atomic line data and electron-impact excitation rates) to the number density of the appropriate grouped level.

Table 3.1. Energy Level Model for Atomic *Nitrogen*

Level Index <i>i</i>	<i>E_i</i> (eV)	<i>g_i</i>	<i>n</i>	<i>l</i>	<i>x</i>	<i>S</i>	<i>L</i>	Core ¹	Config.	Term
1	0	4	2	1	3	2	0	A	2p3	4S*
2	2.383962	10	2	1	3	1	2	A	2p3	2D*
3	3.575602	6	2	1	3	1	1	A	2p3	2P*
4	10.332297	12	3	0	1	2	1	B	3s	4P
5	10.686543	6	3	0	1	1	1	B	3s	2P
6	10.927030	12	2	1	4	2	1	C	2p4	4P
7	11.602633	2	3	1	1	1	0	B	3p	2S*
8	11.758386	20	3	1	1	2	2	B	3p	4D*
9	11.841712	12	3	1	1	2	1	B	3p	4P*
10	11.995575	4	3	1	1	2	0	B	3p	4S*
11	12.005823	10	3	1	1	1	2	B	3p	2D*
12	12.124904	6	3	1	1	1	1	B	3p	2P*
13	12.356713	10	3	0	1	1	2	B	3s	2D
14	12.856402	12	4	0	1	2	1	B	4s	4P
15	12.918660	6	4	0	1	1	1	B	4s	2P
16	12.972258	6	3	2	1	1	1	B	3d	2P
17	12.983572	28	3	2	1	2	3	B	3d	4F
18	12.999657	14	3	2	1	1	3	B	3d	2F
19	12.999948	12	3	2	1	2	1	B	3d	4P
20	13.019245	20	3	2	1	2	2	B	3d	4D
21	13.034976	10	3	2	1	1	2	B	3d	2D
22	13.201564	2	4	1	1	1	0	B	4p	2S*
23	13.244404	20	4	1	1	2	2	B	4p	4D*
24	13.268039	12	4	1	1	2	1	B	4p	4P*
25	13.294202	10	4	1	1	1	2	B	4p	2D*
26	13.321559	4	4	1	1	2	0	B	4p	4S*
27	13.342560	6	4	1	1	1	1	B	4p	2P*
28	13.676543	90	4	-	-	-	-	B	4d2P, 4d4F, 4d4D, 4d4F, 4d4P, 4d2D 4f4D, 4f4F, 4f4G, 4f2D, 4f2F, 4f2G	
29	13.697743	126	4	-	-	-	-	B	n = 5	
30	13.960947	450	5	-	-	-	-	B	n = 6	
31	14.170345	648	6	-	-	-	-	B	n = 7	
32	14.270642	822	7	-	-	-	-	B	n = 8	
33	14.335606	1152	8	-	-	-	-	B	n = 9	
34	14.380238	1458	9	-	-	-	-	B	n = 10	
35	14.412100	1800	10	-	-	-	-	B	n = 10	

¹A=2s2, B=2s2.2p2, C=2s

Table 3.2. Energy Level Model for Atomic *Oxygen*

Level Index <i>i</i>	<i>E_i</i> (eV)	<i>g_i</i>	<i>n</i>	<i>l</i>	<i>x</i>	<i>S</i>	<i>L</i>	Core ¹	Config.	Term
1	0.009668	9	2	1	4	1	1	A	2p4	3P
2	1.967364	5	2	1	4	0	2	A	2p4	1D
3	4.189746	1	2	1	4	0	0	A	2p4	1S
4	9.146091	5	3	0	1	2	0	B	3s	5S*
5	9.521363	3	3	0	1	1	0	B	3s	3S*
6	10.74064	15	3	1	1	2	1	C	3p	5P
7	10.98884	9	3	1	1	1	1	B	3p	3P
8	11.83761	5	4	0	1	2	0	B	4s	5S*
9	11.93039	3	4	0	1	1	0	B	4s	3S*
10	12.07863	25	3	2	1	2	2	B	3d	5D*
11	12.08703	15	3	2	1	1	2	B	3d	3D*
12	12.2861	15	4	1	1	2	1	B	4p	5P
13	12.35887	9	4	1	1	1	1	B	4p	3P
14	12.54019	15	3	0	1	1	2	B	3s	3D*
15	12.66086	5	5	0	1	2	0	B	5s	5S*
16	12.69747	3	5	0	1	1	0	B	5s	3S*
17	12.72847	5	3	0	1	0	2	B	3s	1D*
18	12.7537	25	4	2	1	2	2	B	4d	5D*
19	12.75902	15	4	2	1	1	2	B	4d	3D*
20	12.76644	35	4	3	1	2	3	B	4f	5F
21	12.76645	21	4	3	1	1	3	B	4f	3F
22	12.84802	15	5	1	1	2	1	B	5p	5P
23	12.87824	9	5	1	1	1	1	B	5p	3P
24	13.06612	25	5	2	1	2	2	B	5d	5D*
25	13.06905	15	5	2	1	1	2	B	5d	3D*
26	13.0731	35	5	3	1	2	3	B	5f	5F
27	13.07311	21	5	3	1	1	3	B	5f	3F
28	13.220803	288	6	-	-	-	-	B	n = 6	
29	13.337837	392	7	-	-	-	-	B	n = 7	
30	13.404041	512	8	-	-	-	-	B	n = 8	
31	13.448797	648	9	-	-	-	-	B	n = 9	
32	13.480535	800	10	-	-	-	-	B	n = 10	

¹A=2s2, B=2s3.2p2, C=2s

3.3 Basic Equations for Atomic Line Radiation

The equations required for the modeling of atomic-line (bound-bound) radiation are presented in this section. A more complete discussion regarding the fundamental concepts of this radiation mechanism, presented from both a classical theory and quantum theory perspective, may be found in the text by Zeldovich and Raizer [1966] (see pp. 283-298), among others. The major challenge in calculating atomic-line radiation is compiling the representative data for each individual line, as well as determining which lines should be modeled (since many lines have a negligible influence on the radiative heating and only increase the computational cost if included). This task will be discussed in Section 3.4.

The frequency-dependent absorption coefficient for a bound-bound atomic transition from an ungrouped lower level i' to an ungrouped upper level j' is written as follows (Hartung [1992]):

$$\kappa_{\nu,i'j'}^{bb} = \left\{ N_i \frac{g_{i'}}{g_i} \exp \left[-\frac{hc}{kT_e} (E_{i'} - E_i) \right] \right\} \frac{\pi e^2}{mc} f_{i'j'} b_\nu \quad (cm^{-1}) \quad (3.4)$$

where the term in brackets represents the number density of the level i' , which is written in terms of the number density of the corresponding grouped level i (which contains i'). The specification of grouped and ungrouped levels is required for *multiplet lines* if one of the levels of the transition is greater than $i = 28$ in Tables 3.1 and 3.2. For *individual lines*, this specification is required for all of the levels listed in Tables 3.1 and 3.2 because these levels are not separated by their spin quantum number. The grouping of individual lines into multiplet lines is discussed by Martin and Wiese [1996], and is essentially equivalent to assuming that the closely spaced lines lie on top of each other and that a Boltzmann distribution is present between the closely spaced atomic levels. The difference between applying multiplet and individual lines will be discussed in the next section. Similarly to the absorption coefficient, the frequency-dependent bound-bound emission coefficient is written as

$$j_{\nu,i'j'}^{bb} = \left\{ N_j \frac{g_{j'}}{g_j} \exp \left[-\frac{hc}{kT_e} (E_{j'} - E_j) \right] \right\} \frac{2\pi h e^2}{mc^3} \left(\frac{c}{\lambda_{CL}} \right)^3 \frac{g_{i'}}{g_{j'}} f_{i'j'} b_\nu \quad \left(\frac{erg \cdot s}{cm^3 \cdot sr} \right) \quad (3.5)$$

where j' is the ungrouped upper level and j is the grouped upper level that contains j' . Note that if N_i and N_j follow a Boltzmann distribution, then Eqs. (3.4) and (3.5) show that the emission and absorption coefficient are related as follows:

$$j_{\nu,i'j'}^{bb} = \frac{2h\nu_{CL}^3}{c^2} \kappa_{\nu,i'j'}^{bb} \exp(-h\nu_{CL}/kT_e) \quad \left(\frac{erg \cdot s}{cm^3 \cdot sr} \right) \quad (3.6)$$

which is the well-known Kirchoff's law. The frequency dependence of Eqs. (3.4) and (3.5) is contained entirely in the line-shape function, represented by b_ν in these equations. This function is defined by a Voigt profile, which is a convolution of Lorentzian and Gaussian profiles. An approximate equation is required for the Voigt profile because no exact analytic formula is available and it is too computationally intensive to perform the exact numerical integration procedure. The approximate formulas proposed by Whiting [1968] and Liu et al. [2001] are considered in the present work. The formula proposed by Whiting [1968] is written as

$$b_\nu = \frac{\lambda_{CL}^2}{2c\Delta\lambda_V [1.065 + 0.447(\Delta\lambda_L/\Delta\lambda_V) + 0.058(\Delta\lambda_L/\Delta\lambda_V)^2]} \left\{ \left[1 - \frac{\Delta\lambda_L}{\Delta\lambda_V} \right] \exp \left[-2.772 \left(\frac{\bar{\lambda}}{2\Delta\lambda_V} \right)^2 \right] \right. \\ \left. + \frac{\Delta\lambda_L/\Delta\lambda_V}{1 + (\bar{\lambda}/2\Delta\lambda_V)^2} + 0.016 \left(1 - \frac{\Delta\lambda_L}{\Delta\lambda_V} \right) \frac{\Delta\lambda_L}{\Delta\lambda_V} \left[\exp \left(-0.4 \left(\frac{\bar{\lambda}}{2\Delta\lambda_V} \right)^{2.25} \right) - \frac{10}{10 + (\bar{\lambda}/2\Delta\lambda_V)^{2.25}} \right] \right\} \quad (3.7)$$

where

$$\bar{\lambda} = |\lambda - \lambda_{CL}| \quad (3.8)$$

The formula proposed by Liu et al. [2001] is written as

$$b_\nu = C_1 \frac{\lambda_{CL}^2}{\pi c} \frac{\Delta\lambda_V}{\bar{\lambda}^2 + \Delta\lambda_V^2} + C_2 \frac{\lambda_{CL}^2}{c} \frac{\sqrt{\ln(2)}}{\Delta\lambda_V \sqrt{\pi}} \exp \left[-\frac{\ln(2)\bar{\lambda}^2}{\Delta\lambda_V^2} \right] \quad (3.9a)$$

$$C_1 = 0.68188 + (0.61293)d - (0.18384)d^2 - (0.11568)d^3 \quad (3.9b)$$

$$C_2 = 0.32460 - (0.61825)d + (0.17681)d^2 + (0.12109)d^3 \quad (3.9c)$$

$$d = \frac{\Delta\lambda_L - \Delta\lambda_G}{\Delta\lambda_L + \Delta\lambda_G} \quad (3.9d)$$

These equations are functions of the Voigt ($\Delta\lambda_V$), Gaussian ($\Delta\lambda_G$), and Lorentzian ($\Delta\lambda_L$) half-widths at half-height, or (half) half-widths. The Voigt (half) half-width is calculated from the approximation presented by Olivero and Longbothom [1977]:

$$\Delta\lambda_V = \left\{ -0.18121(1-d^2) - [0.023665 \exp(0.6d) + 0.00418 \exp(-1.9d)] \sin(\pi d) \right\} (\Delta\lambda_L + \Delta\lambda_G) \quad (3.10)$$

where d is given by Eq. (3.9d). Figure 3.1 compares the results of the two different line approximations of Eqs. (3.7) and (3.9) while applying Eq. (3.10) to both. Slight differences are seen in the outer region of the line with the large $\Delta\lambda_G$ value, which could possibly influence the flux from highly optically thick lines. This difference was found to have a negligible influence on the integrated radiative flux for the cases of present interest. The Whiting [1968] equation was used throughout the remainder of this work, except where otherwise specified.

The line shapes defined by Eqs. (3.7 – 3.10) are a function of the line half-widths resulting from various broadening mechanisms. The Lorentzian width is the sum of the Stark broadening ($\Delta\lambda_S$) and resonance broadening ($\Delta\lambda_R$) widths:

$$\Delta\lambda_L = \Delta\lambda_S + \Delta\lambda_R \quad (3.11)$$

The resonance broadening width may be calculated from the following equation

$$\Delta\lambda_R = 3\pi \left(\frac{g_{i'}}{g_{j'}} \right)^{1/2} \frac{e^2 f_{i'j'} \lambda_{CL}^3}{2\pi m c^2} \left\{ N_i \frac{g_{i'}}{g_i} \exp \left[-\frac{hc}{kT_e} (E_{i'} - E_i) \right] \right\} \quad (3.12)$$

where $g_{j'}$ and $g_{i'}$ are the degeneracies of the upper and lower ungrouped levels, respectively, and the term in brackets represents the number density of the lower ungrouped level. The Gaussian (half) half-width is dominated by Doppler broadening, which may be calculated as

$$\Delta\lambda_G = \Delta\lambda_D = \frac{1}{c\lambda_{CL}} \left(\frac{2kT_e \ln(2)}{m_s} \right)^{1/2} \quad (3.12b)$$

where m_s is the mass (g/particle) of the radiating species. The calculation of the Stark broadening width is not straightforward and will be discussed in the next section.

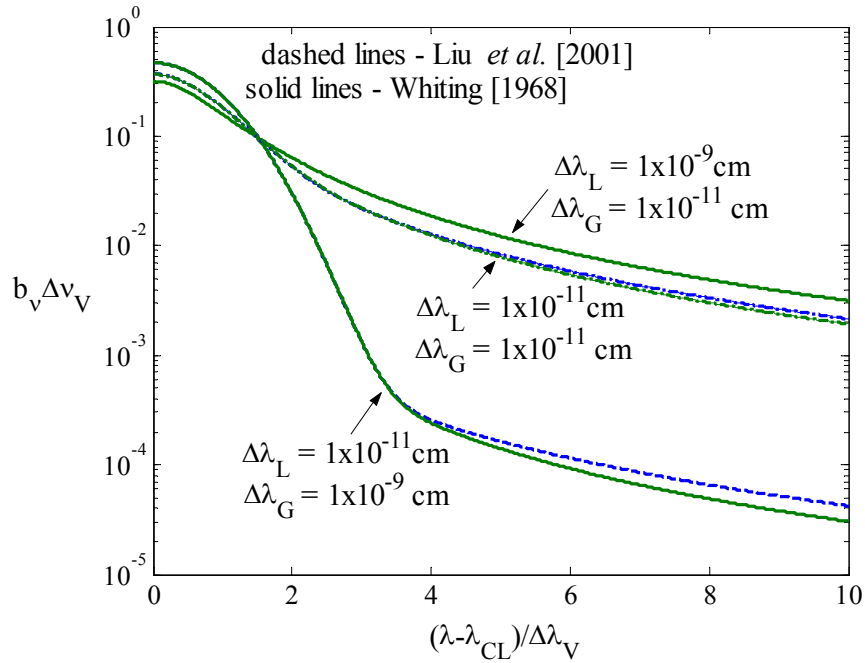


Figure 3.1. Comparison of the line-shape functions proposed by Liu and Whiting

3.4 Assembling Data for Atomic Line Radiation

The prime source of atomic line data for the present study was the NIST atomic line database (Ralchenko [2006]), which contains a comprehensive list of atomic line data for nitrogen and oxygen, among others. Note that the values listed in this database are nearly the same as those listed by Wiese et al. [1996]. The data required for each line are the specification of the upper and lower electronic state, the transition probability ($A_{j'i'}$) (or absorption oscillator strength ($f_{i'j'}$)), and the Stark broadening half-width at half-height ($\Delta\lambda_S$). The NIST database contains all of these data except for the $\Delta\lambda_S$ values, which were obtained from a variety of other sources, as will be

discussed in this section. The 1082 and 842 individual lines listed in the NIST database for nitrogen and oxygen, respectively, are too numerous to be practically applied (because of the computational burden associated with treating so many lines). The reduction of the number of lines treated, and the influence of this on the predicted radiation, will be discussed in this section, following the discussion of the Stark broadening half-widths.

Because of the large number of lines treated in this study, it was not practical to expect to find individually measured or calculated Stark broadening half-widths for each line. The approach used instead was to obtain all of the detailed values available in the literature, apply them to the lines that they were available for, and then form a correlation from these values for all of the remaining lines. The detailed Stark broadening half-widths at half-height ($\Delta\lambda_S$) used in the present work were obtained from the calculations presented by Griem [1974] and Wilson and Nicolet (WN) [1967]. These studies present values of $\Delta\lambda_S$ for an electron number density (N_e) of 1×10^{16} particles/cm³ and at various temperatures. The value of $\Delta\lambda_S$ at this N_e and a temperature of 10,000 K, which was a case considered by both Greim and WN, will be labeled $\Delta\lambda_{S,0}$ and referred to as the “Stark broadening coefficient”. The value of $\Delta\lambda_S$ at any other temperature and N_e may be approximately related to $\Delta\lambda_{S,0}$ through the following equation

$$\Delta\lambda_S = \Delta\lambda_{S,0} \left(\frac{T_e}{10000} \right)^n \left(\frac{N_e}{1 \times 10^{16} \text{ cm}^{-3}} \right) \quad (\text{cm}) \quad (3.13)$$

where the exponent n is chosen to fit the available data. For most nitrogen and oxygen lines, a value of 1/3 is acceptable (Park [1982]). Both Griem and WN treated multiplet lines, instead of individual lines. It was assumed that the width for each individual line was the same as its corresponding multiplet value. With this assumption, 277 lines for nitrogen and 216 lines for oxygen were assigned Stark broadening coefficients from those calculated by Griem and WN. To treat the remaining lines, the literature was searched for approximate models that would be simple to apply. The following approximate formula for the Stark broadening coefficient was derived by Cowley [1971] for atomic lines of neutral species

$$\Delta\lambda_{S,0} = \frac{9.27 \times 10^7 \lambda_{CL}^2}{(E_{ionize} - E_u)^2} \quad (\text{cm}) \quad (3.14)$$

where λ_{CL} in cm and E_{ionize} and E_u in cm⁻¹. Improvements to this equation have been proposed by Freudenstein and Cooper [1978] and Dimitrijevic and Konjevic [1986]. These improvements require knowledge of the upper state’s nearest interacting level, which makes them not nearly as

simple as Eq. (3.14). Interestingly, Arnold et al. [1979] obtained an empirical expression from carbon and silicon experimental data that is very similar to Cowley's result:

$$\Delta\lambda_{s,0} = \frac{4.20 \times 10^7 \lambda_{CL}^2}{(E_{ionize} - E_u)^2} \quad (cm) \quad (3.15)$$

Park [1982] showed that essentially the same formula agrees with the experimental data of argon lines. Figure 3.2 compares the detailed calculations of Griem and WN with Eqs. (3.14) and (3.15). Also shown in these figures is a least squares fit of the detailed calculations for both oxygen and nitrogen. The equation for this new fit is

$$\Delta\lambda_{s,0} = \frac{1.69 \times 10^{10} \lambda_{CL}^2}{(E_{ionize} - E_u)^{2.623}} \quad (cm) \quad (3.16)$$

This equation is applied in the present model, with a lower limit of 3.6 for $\log_{10}(E_{ionize} - E_u)$, beyond which the value of 3.6 is maintained. The limit at 3.6 prevents unrealistically large half-width values from being obtained for lines with upper levels very close to the ionization limit.

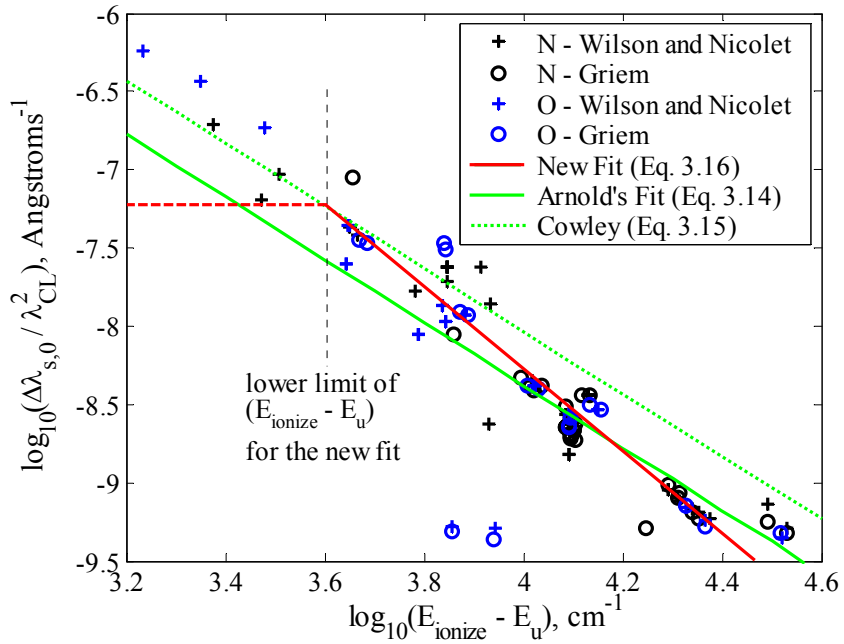


Figure 3.2. Comparison of the Stark broadening coefficients predicted by the various curve fits (Eqs. 3.14 – 3.15) with the detailed calculations of Griem and Wilson and Nicolet for nitrogen and oxygen.

The 1082 and 842 individual lines listed in the NIST database for nitrogen and oxygen, respectively, may be reduced to 263 and 176 multiplet lines. This is a manageable number of multiplet lines, although the approximations inherent in treating multiplet lines may prevent them

from predicting the radiative flux accurately. To quantify the difference between the multiplet and individual line models, the radiative flux from a constant-property slab of air at 10,000 K and various pressures was examined. Tables 3.3 and 3.4 present the radiative flux resulting from nitrogen and oxygen lines, respectively, for pressures ranging from 0.01 to 1.0 atm. The equilibrium number densities of nitrogen and oxygen at the given pressure and temperature are also listed in the tables. The contributions from the lines below and above 6.0 eV are presented separately, which emphasizes the fundamental difference between the two spectral ranges. In the region below 6.0 eV, or the visible and infrared region, the multiplet line model agrees within 5% of the individual line model for nitrogen, and within 9% for oxygen. For the spectral region above 6.2 eV, or the vacuum ultraviolet (VUV), the difference between the two line models is much greater, especially for the 0.01 atm case. For this low pressure case, these tables show that the VUV contributes a larger percentage of the total line radiation than at the higher pressure cases. This is a result of the blackbody limiting effect, which suppresses the VUV radiation for the high pressure cases more than it does for the low pressure cases. This phenomenon is explained by examining the governing radiation transport equation for a constant-property slab, which is written for the radiative flux at one end of the slab as follows

$$q_{r,\nu}^{cp\text{-}slab} = \pi B_\nu [1 - \exp(-2\kappa_\nu \Delta z)] \quad (3.17)$$

where the “blackbody”, or Planck function, is written as

$$B_\nu = 2h\nu^3c^{-2} \left[\exp\left(\frac{h\nu}{kT_e}\right) - 1 \right]^{-1} \quad (3.18)$$

The Planck function is only valid for cases where the radiating and absorbing species are populated by a Boltzmann distribution. For non-Boltzmann cases, the B_ν in Eq. (3.17) is replaced by the ratio of the emission and absorption coefficient. As the value of $\kappa_\nu \Delta z$ becomes large, Eq. (3.17) reduces to the following

$$q_{r,\nu}^{cp\text{-}slab} = \pi B_\nu + \dots, \text{ for } \kappa_\nu \Delta z \gg 1 \quad (3.19)$$

which represents the blackbody limit. Note that the value of this limit is independent of number density or the species, which means that it is the same for all of the cases listed in Tables 3.3 and 3.4. Thus, as the pressure increases and the temperature is held constant, κ_ν increases (because it is proportional to the number density) and the spectrum approaches the limit expressed in Eq. (3.19). Figures 3.3 and 3.4 present the complete spectrum, resulting from all radiating mechanisms of all species, for the 0.01 and 1 atm cases and applying the individual line model. The blackbody limit represented by Eq. (3.19) is plotted as the blue dotted line, which can only be seen on the right-hand side of these figures because of the upper-limit of the vertical-axis (which

was chosen to show the details in the VUV). In both of these cases, all of the lines above 6.0 eV reach the blackbody limit, while it is reached by none of the lines below 6 eV. When a spectral region is far from reaching the blackbody limit, it is commonly referred to as optically thin. The limiting form of Eq. (3.17) may be written for these cases as follows

$$q_{r,\nu}^{cp\text{-}slab} = 2\pi B_\nu \kappa_\nu \Delta z + \dots, \text{ for } \kappa_\nu \Delta z \ll 1 \quad (3.20)$$

where the product of B_ν and κ_ν represents the emission coefficient. The frequency integrated flux from Eq. (3.20) is directly proportional to the frequency integrated emission coefficient. Thus, because the multiplet and individual line models have essentially the same integrated emission coefficients, by definition, then the optically thin flux values predicted by the two models should be nearly equal. This is indeed the case for the 0–6 eV presented in Tables 3.3 and 3.4

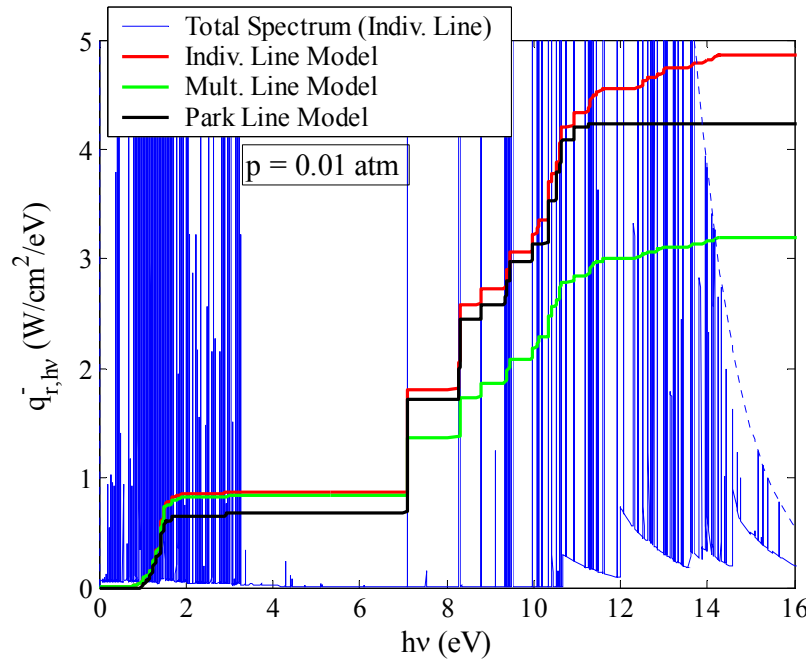


Figure 3.3. Radiative flux from a constant property slab of air at 10,000 K and **0.01 atm**; the “Total Spectrum” curve includes all the radiative mechanisms from all species; the other three curves are the accumulated flux values (W/cm^2) resulting from *only nitrogen* lines.

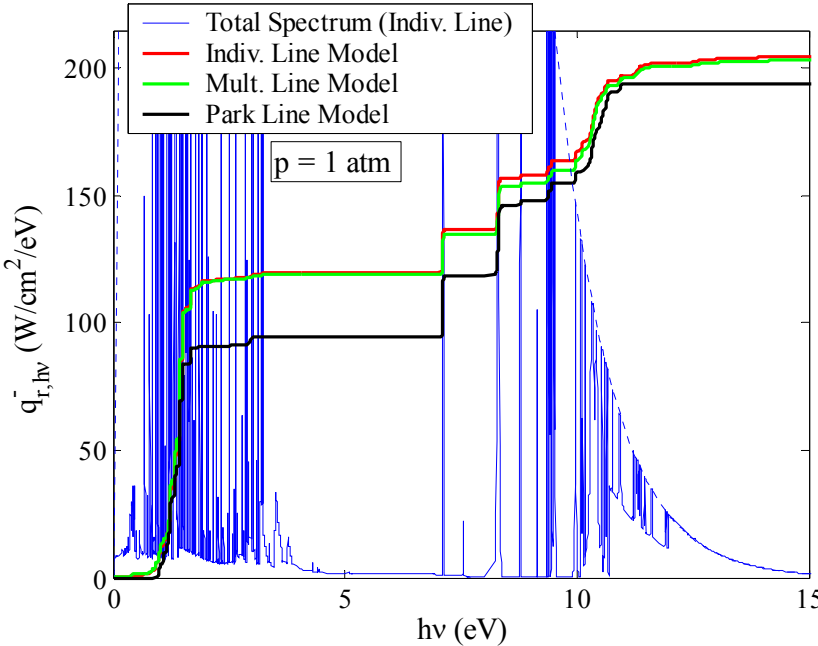


Figure 3.4. Radiative flux from a constant property slab of air at 10,000 K and **1.0 atm**; the “Total Spectrum” curve includes all the radiative mechanisms from all species; the other three curves are the accumulated flux values (W/cm^2) resulting from *only nitrogen* lines.

Table 3.3. Radiative flux (W/cm^2) emitted from ***nitrogen atomic lines*** at the edge of a 4-cm constant-property slab of equilibrium air at 10,000 K.

p (atm)	N_N (#/cm ³)	N_{e^-} (#/cm ³)	Indiv. Lines (0 - 6 eV)	Mult. Lines (0 - 6 eV)	% difference	Indiv. Lines (6 - 18 eV)	Mult. Lines (6 - 18 eV)	% difference
0.01	3.5e+15	1.4e+15	0.87	0.84	-3.49	3.99	2.35	-41.18
0.1	4.9e+16	5.2e+15	11.62	11.14	-4.18	15.15	11.97	-20.97
1	5.5e+17	1.7e+16	119.59	119.12	-0.47	84.60	84.11	-0.58

Table 3.4. Radiative flux (W/cm^2) emitted from ***oxygen atomic lines*** at the edge of a 4-cm constant-property slab of equilibrium air at 10,000 K.

p (atm)	N_O (#/cm ³)	N_{e^-} (#/cm ³)	Indiv. Lines (0 - 6 eV)	Mult. Lines (0 - 6 eV)	% difference	Indiv. Lines (6 - 18 eV)	Mult. Lines (6 - 18 eV)	% difference
0.01	1.0e+15	1.4e+15	0.25	0.25	-0.5	0.44	0.36	-17.44
0.1	1.4e+16	5.2e+15	3.00	2.96	-1.37	1.77	1.67	-5.68
1	1.6e+17	1.7e+16	29.13	31.59	8.45	9.10	8.28	-9.02

Figures 3.3 and 3.4 also present the accumulated radiative flux (W/cm^2), from left to right, resulting from *only nitrogen atomic lines* predicted by the individual, multiplet, and Park line models. The Park model will be discussed later, and is not of interest in the immediate discussion. The accumulated flux values shown in these figures illustrate which lines are causing the discrepancies to the frequency-integrated radiative flux values presented in Table 3.3 for nitrogen. Figure 3.3 shows that for 0.01 atm cases, a majority of the difference between the multiplet and

individual line models comes from the lines at 7.1 and 8.3 eV. The individual line model consists of four lines near 7.1 eV and 3 lines near 8.3 eV, while the multiplet model treats a single multiplet line at each of these locations. Figure 3.4 shows that at a pressure of 1 atm, the flux from these lines agree significantly better between the multiplet and individual line models. Figure 3.5 shows the details of the 8.3 eV lines predicted by the two models at 0.01 and 1.0 atm. This figure explains why the multiplet and individual line models agree better for the 1.0 atm case than for the 0.01 atm case. It is seen that the broader lines present at the higher pressure, resulting from the number density dependence in Eqs. (3.12) and (3.13), cause the single multiplet line at 1 atm to provide a reasonably accurate model of the three individual lines. On the other hand, at 0.01 atm the three individual lines are distinctly separate, and therefore not modeled accurately by the single multiplet line.

The conclusion reached from this comparison between multiplet and individual line models is that by applying individual lines for all lines above 6.0 eV, and multiplet lines for all lines below 6.0 eV, the computational expense may be reduced to a manageable level without compromising accuracy, even at the lower pressure conditions. The data for this line model is listed in Appendix A, which includes the transition probabilities and atomic levels from the NIST database, and the Stark broadening coefficients described previously in this section.

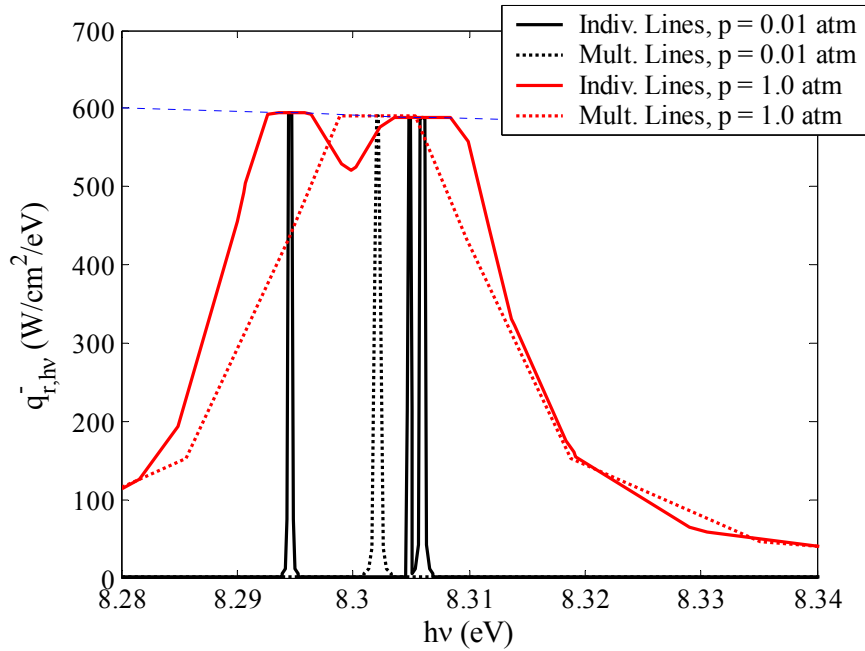


Figure 3.5. Comparison between the radiative flux spectrum from the nitrogen multiplet centered at 8.302 eV predicted by the individual and multiplet line models at 10,000 K.

The accumulated flux values from the Park model presented in Figures 3.3 and 3.4 provide insight into the difference between the old atomic line data of Park's model as used in NEQAIR and the most recent atomic data obtained from the NIST database (Wiese et al. [1996]), with the choice of Stark broadening half-widths discussed previously. The Park model (Park [1985], Whiting et al. [1996]) consists of the nitrogen and oxygen lines listed by Wiese [1966] and Stark broadening half-widths from an unspecified source. The two main conclusions that can be made from Figures 3.3 and 3.4 regarding the difference between the new model and Park's model is that Park's model under-predicts the radiation below 6 eV and over-predicts the contribution between 7 and 11 eV. This behavior can be explained by comparing the atomic line data applied for each model. To simplify this comparison, the largest contributors to the total flux were identified from the data presented in Figures 3.3 and 3.4. The chosen nine line multiplets, which contribute roughly 75% of the total radiative flux from nitrogen lines for the 1.0 atm case, are listed in Table 3.5. The multiplet identification number, transition probability ($A_{j'i'}$), line accuracy (Acc.), and Stark broadening half width are presented in this table for both models. Noting that line emission is proportional to $A_{j'i'}$ ($A_{j'i'}$ is related to $f_{ij'}$ through Eq. (A-1)), the previous observation that Park's model under-predicts the radiation below 6 eV and over-predicts the contribution between 7 and 11 eV is explained by the lower $A_{j'i'}$ values present in the Park model for the lines below 6 eV, and the larger values for the lines above 6 eV. For the important lines listed in Table 3.5, the $A_{j'i'}$ values applied by the present model all have better accuracy ratings than the Park model, with no lines having an uncertainty greater than 10%. The Stark broadening coefficients agree well for most of the lines listed, and for the present model, all the values listed here were obtained from Griem [1974].

Table 3.5. Comparison of the strongest lines for atomic **nitrogen**; $h\nu$ (eV), $A_{j'i'}$ (s^{-1}), $\Delta\lambda_{S,0}$ (Å)

Multiplet # ¹	<i>i</i>	<i>j</i>	$h\nu$	$A_{j'i'}$ Present ²	Acc. ⁴	$A_{j'i'}$ Park ³	Acc. ⁴	$\Delta\lambda_{S,0}$ Present	$\Delta\lambda_{S,0}$ Park
69 (34)	8	17	1.225	3.75E+07	B+	3.73E+07	B	2.21E-01	0
51 (23)	5	11	1.319	2.63E+07	B+	2.17E+07	C	7.15E-02	7.46E-02
46 (21)	4	8	1.426	2.47E+07	B+	1.90E+07	C	4.48E-02	4.51E-02
52 (25)	5	12	1.438	3.15E+07	B+	2.86E+07	C	7.28E-02	7.46E-02
47 (22)	4	9	1.509	3.11E+07	A	2.28E+07	C	4.42E-02	4.46E-02
48 (23)	4	10	1.663	3.77E+07	A	3.18E+07	C	4.77E-02	4.75E-02
29 (4)	3	5	7.110	1.39E+08	B+	2.00E+08	D	1.70E-03	2.23E-03
15 (3)	2	5	8.302	3.56E+08	B+	5.50E+08	D	1.25E-03	1.21E-03
1 (2)	1	4	10.332	4.00E+08	B+	5.40E+08	D-	6.90E-04	6.65E-04

¹The values *not* in parentheses refer to the multiplet number of the line, or lines, as defined by Weise et al. [1996], the value *in* parentheses refer to the multiplet number as defined by Weise [1966].

²The data for the present model is taken from Weise et al. [1996], which is the same as the online NIST database for the lines listed here.

³The data for the Park model was taken from Weise [1966].

⁴A, B, C, and D indicate uncertainties of 3, 10, 25, and 50%, respectively.

For atomic oxygen, the Park model was found to under-predict the radiation over the entire spectrum. As was done for nitrogen, the strongest lines were identified and the data for each was compared. It was found that four line multiplets contributed 90% of the atomic line radiation resulting from oxygen (note that for air, Tables 3.3 and 3.4 show that the oxygen line radiation is much less than that from nitrogen). These line multiplets are listed in Table 3.6 along with the $A_{j'i'}$ values from the present model and Park's model. It is seen that the $A_{j'i'}$ value for all of these lines is larger for the present model than for Park's model, which is consistent with the observation that Park's model under-predicted the oxygen line radiation. The Stark broadening coefficients for the lines listed here were obtained from Griem [1974], and are seen to agree well with the values applied by Park.

Table 3.6. Comparison of the strongest lines for atomic *oxygen*; $h\nu$ (eV), $A_{j'i'}$ (s^{-1}), $\Delta\lambda_{S,0}$ (\AA)¹

Multiplet #	<i>i</i>	<i>j</i>	$h\nu$	$A_{j'i'}$ Present	Acc.	$A_{j'i'}$ Park	Acc.	$\Delta\lambda_{S,0}$ Present	$\Delta\lambda_{S,0}$ Park
64 (28)	6	10	1.338	4.46E+07	A	4.19E+07	C	2.22E-01	2.14E-01
60 (12)	5	7	1.468	3.22E+07	B	2.80E+07	B	5.14E-02	5.28E-02
56 (11)	4	6	1.595	3.69E+07	A	3.40E+07	B	3.15E-02	3.27E-02
2 (2)	1	5	9.511	6.11E+08	A	3.80E+08	D	8.21E-04	7.84E-04

¹see Table 3.5 for further details on column definitions

3.5 A Method for Determining the Spectral Grid for Atomic Line Transport through a Nonequilibrium Shock-Layer

A crucial step in calculating line radiation is choosing a spectral grid with a resolution sufficient to model every atomic line at every spatial point through the shock-layer. For viscous flowfields with thermal and chemical nonequilibrium, this is difficult because the width of a single atomic line can vary by orders of magnitude through the layer. This is a result of the large electronic temperature and species number density variations, which cause the line widths to vary significantly.

The first step in determining the line grid is choosing the maximum and minimum spacing from the line center. Because we are interested in correctly predicting the radiative flux through the shock-layer, the grid should be chosen to accurately model the flux and not necessarily the absorption or emission coefficient. This statement is important when considering optically thick lines, because a large percentage of the radiative flux resulting from a single line comes from the line wings, $(\lambda - \lambda_{CL})/\Delta\lambda_\nu > 10$. An estimate of the maximum spacing required to correctly

model a single line at a single point in the shock-layer may be obtained by considering a constant property slab with the local flowfield properties and the shock-layer thickness. The radiative flux at one end of this slab, assuming a Boltzmann distribution of atomic states, may be obtained from Eq. (3.17). Figure 3.6 illustrates the importance of considering the optical thickness of a line when choosing the maximum distance from the centerline. In the cases shown, the absorption coefficient line shape is the same, except it is scaled up or down (by changing κ_{CL}) to produce the optically thin and thick cases. By considering a constant property slab, the problem of determining the maximum distance from the center of a single line at a single point in the layer is approximately reduced to solving the following equation for λ - λ_{CL}

$$q_{r,\nu,ij}^{cp-slab} / q_{r,CL,ij}^{cp-slab} = 0.01 \quad (3.21)$$

where the value in the numerator is the frequency (or wavelength) dependent flux for a single line emitted from the slab and the denominator is the centerline flux from the same line. The value of 0.01 is chosen as the point after which the percentage contribution to the total flux of the line is negligible. When solving Eq. (3.21), it is reasonable to assume that the line shape is Lorenztian by applying Eq. (3.9a) with $C_2 = 0$. This assumption is valid because the line wings are dominated by the Lorenztian profile and because Lorenztian broadening is usually larger than Gaussian. Equation (3.21) may now be solved analytically using Eqs. (3.4), (3.9a) with $C_2 = 0$, and (3.17) to obtain the following

$$\bar{\lambda}_{slab,ij}^z = \sqrt{-C_1 \frac{\Delta\lambda_\nu \lambda_{CL}^2}{\pi c} \left\{ N_i \frac{g_{i'}}{g_i} \exp\left[-\frac{hc}{kT_e} (E_{i'} - E_i)\right] \right\} \left[\frac{mc}{2\Delta\pi e^2 f_{i'j'}} \ln\left\{ 1 - \frac{q_{r,\nu,ij}^{cp-slab}}{q_{r,CL,ij}^{cp-slab}} [1 - \exp(-2\kappa_{CL,ij} \Delta z)] \right\} \right]^{-1} - \Delta\lambda_\nu^2} \quad (3.22)$$

where $\bar{\lambda}_{slab,ij}^z = |\lambda_{slab,ij}^z - \lambda_{CL,ij}^z|$ represents the distance from the centerline at which Eq. (3.21) is satisfied for the line with an upper level j and a lower level i at the location z in the shock-layer. Evaluating this equation at every point through the layer allows the minimum and maximum value of $\bar{\lambda}_{slab,ij}^z$ to be found, which are labeled $\bar{\lambda}_{\min,ij}$ and $\bar{\lambda}_{\max,ij}$, respectively. These values are treated as the minimum and maximum distance from the centerline required for the accurate modeling of the radiative flux resulting from the specified line. This provides guidance in choosing the minimum and maximum grid spacing for the line. Evaluating Eq. (3.22) at every point through the shock-layer is unnecessary, though, because the minimum will usually occur at the wall and the maximum will occur at the location of maximum T_e or $\Delta\lambda_\nu$. Therefore, Eq. (3.22) needs only to be evaluated at these three locations to find $\bar{\lambda}_{\min,ij}$ and $\bar{\lambda}_{\max,ij}$.

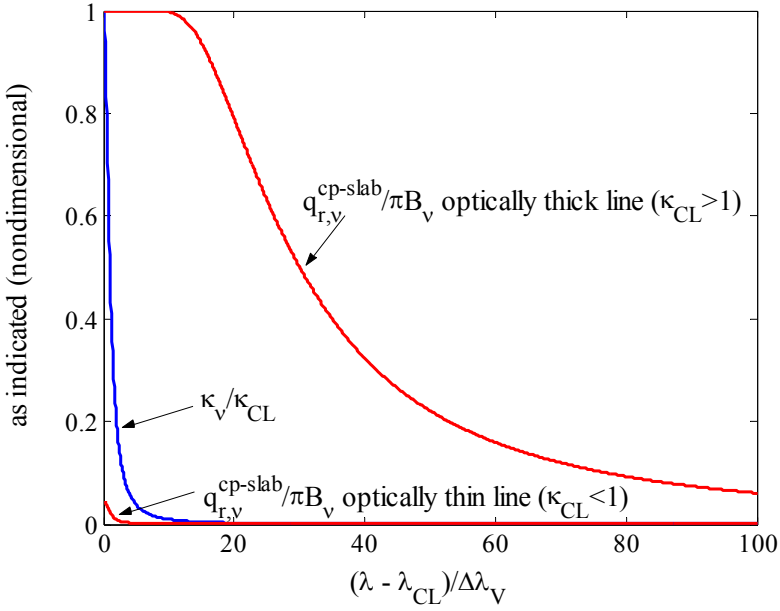


Figure 3.6. Comparison of the radiative flux from a constant property slab for an optically thick and optically thin line.

Once $\bar{\lambda}_{\min,ij}$ and $\bar{\lambda}_{\max,ij}$ are obtained, a method must be determined that spreads K points, where K is the number of points that model half of a line (not including the centerline point), between the centerline and $\bar{\lambda}_{\max,ij}$, with $\bar{\lambda}_{\min,ij}$ being the distance from the centerline to the first point away from the centerline. This is accomplished using the Roberts stretching formula (Tannehill et al. [1997]), which is written as

$$\frac{\bar{\lambda}_k}{\bar{\lambda}_{\max,ij}} = 1 - \beta \left[\left(\frac{\beta+1}{\beta-1} \right)^{1-\frac{k}{K}} - 1 \right] \left[\left(\frac{\beta+1}{\beta-1} \right)^{1-\frac{k}{K}} + 1 \right]^{-1} \quad (3.23)$$

In this equation, k is the grid index where $k = 1$ specifies the first point away from the centerline and $k = K$ indicates the furthest point. Note that Eq. (3.23) automatically enforces that $\bar{\lambda}_K = \bar{\lambda}_{\max,ij}$. The other requirement, which states that $\bar{\lambda}_1 = \bar{\lambda}_{\min,ij}$, is satisfied by the proper choice of the stretching parameter β , although this also depends on the number of points used to model each line. For $K = 8$ (meaning a total of 17 points were used to model each line), a value of 1.01 for β was found to provide excellent results over a wide range of conditions. This was applied throughout the present study.

3.6 Atomic Bound-Free and Free-Free Radiation

Bound-free radiation is the result of a bound electron being excited to an energy level above the ionization energy, which results in the bound electron becoming a free electron (Zeldovich and Raizer [1966], pp. 248-276). The absorption coefficient resulting from this process is written as

$$\kappa_{\nu,i}^{bf} = \sigma_{\nu,i}^{bf} N_i \quad (cm^{-1}) \quad (3.24)$$

where $\sigma_{\nu,i}^{bf}$ is the absorption cross section of level i and N_i is the number density of this level.

There is a lower limit for the frequency when applying Eq. (3.24). The frequency must be larger than a threshold value, which may be approximated as

$$\nu_{thresh,i} = (E_{ionize} - E_i) c \quad (s^{-1}) \quad (3.25)$$

For frequencies below this value, the contribution of level i to the bound-free spectrum is zero. The emission coefficient may be derived by assuming that it is proportional to the ion and electron number densities and a function ($\Phi_{\nu,i}$) that is independent of the atomic state populations and the ion or electron number densities:

$$j_{\nu,i}^{bf} = N_+ N_e \Phi_{\nu,i} \quad \left(\frac{erg \cdot s}{cm^3 \cdot sr} \right) \quad (3.26)$$

The function $\Phi_{\nu,i}$ can be related to $\sigma_{\nu,i}^{bf}$ by applying Kirchoff's law, which may be written as

$$j_{\nu,i,EQ}^{bf} = \frac{2h\nu^3}{c^2} \kappa_{\nu,i,EQ} \exp(-h\nu/kT_e) \quad \left(\frac{erg \cdot s}{cm^3 \cdot sr} \right) \quad (3.27)$$

where the subscript EQ indicates that the electron, ion, and atomic state number densities used in the emission and absorption coefficients satisfy the Saha-Boltzmann equation:

$$\left(\frac{N_+ N_e}{N_i} \right)_{EQ} = \frac{2Q_+}{g_i} \left(\frac{2\pi n k T_e}{h^2} \right)^{3/2} \exp[hc(E_i - E_{ionize})/kT_e] \quad (3.28)$$

The requirement that the Saha-Boltzmann equation be satisfied for Kirchoff's law to be applied implies that the atomic states are populated in a Boltzmann distribution and that chemical equilibrium exists among the atoms, ions, and electrons. This second requirement is only true for bound-free radiation. For bound-bound radiation, only a Boltzmann distribution of the atomic states is required to apply Kirchoff's law. Combining Eqs. (3.24), (3.26), (3.27) and (3.28) and solving for $\Phi_{\nu,i}$ results in the following

$$\Phi_{\nu,i} = \frac{2h\nu^3}{c^2} \frac{g_i}{2Q_+} \left(\frac{h^2}{2\pi n k T_e} \right)^{3/2} \sigma_{\nu,i}^{bf} \exp \left[\frac{hc(E_{ionize} - E_i) - h\nu}{kT_e} \right] \quad (3.29)$$

Note that, as was assumed previously, this function is independent of the electron, ion, and excited state number densities. This fact makes Eq. (3.29) valid regardless of whether there is chemical equilibrium or a Boltzmann distribution of excited states. Combining Eqs. (3.26) and (3.29), the bound-free emission coefficient from a single level i becomes

$$j_{\nu,i}^{bf} = N_+ N_e \frac{2h\nu^3}{c^2} \frac{g_i}{2Q_+} \left(\frac{h^2}{2\pi mkT_e} \right)^{3/2} \sigma_{\nu,i}^{bf} \exp \left[\frac{hc(E_{ionize} - E_i) - h\nu}{kT_e} \right] \quad \left(\frac{\text{erg} \cdot \text{s}}{\text{cm}^3 \cdot \text{sr}} \right) \quad (3.30)$$

The lower limit on frequency used for the absorption coefficient, which was obtained from Eq. (3.25), is used for Eq. (3.30). The calculation of the bound-free absorption cross section ($\sigma_{\nu,i}^{bf}$), which is required for both the emission and absorption coefficients (Eqs. (3.24) and (3.30)), will be discussed later.

Free-free radiation, also called bremsstrahlung emission, results from electrons being slowed down in the external electric field of positive ions. The loss of kinetic energy of each electron is accompanied by the emission of a photon of equal energy. The absorption coefficient for this process may be written as

$$\kappa_{\nu}^{ff} = \frac{4}{3} \left(\frac{2\pi}{3mkT_e} \right)^{1/2} \frac{Z^2 e^6}{hcm\nu^3} N_+ N_e \quad (\text{cm}^{-1}) \quad (3.31)$$

and the emission coefficient may be written as

$$j_{\nu}^{ff} = \frac{8}{3} \left(\frac{2\pi}{3mkT_e} \right)^{1/2} \frac{Z^2 e^6}{mc^3} N_+ N_e \exp \left(-\frac{h\nu}{kT_e} \right) \quad \left(\frac{\text{erg} \cdot \text{s}}{\text{cm}^3 \cdot \text{sr}} \right) \quad (3.32)$$

Due to the negative exponential dependence on ν , the free-free emission contributes significantly only in the low frequency region of the spectrum.

3.7 A Comparison of Various Approaches to Calculating Bound-Free Cross-Sections

The main difficulty in calculating the bound-free radiation is determining the bound-free absorption cross sections, $\sigma_{\nu,i}^{bf}$, for each atomic level as a function of frequency. The simplest approach is to apply the hydrogenic model, which may be corrected for non-hydrogen atoms by applying a correction factor, called a Gaunt factor (Biberman and Norman [1960]). The equation for the bound-free absorption cross-section using this approach is written by Chambers [1994] as

$$\begin{aligned}\sigma_{v,i}^{bf} &= \frac{128}{3\sqrt{3}} \frac{\pi^4 m Z^4 e^{10} Q_+}{v^3 c h^6 n_{eff,i}^3 g_i} \bar{G} \\ &= 5.64 \times 10^{29} \frac{Z^4 Q_+}{v^3 n_{eff,i}^3 g_i} \bar{G} \quad (cm^2)\end{aligned}\tag{3.33}$$

where $n_{eff,i}$ is the effective quantum number, \bar{G} is the Gaunt factor (which may be a function of frequency), and Z is the charge number of the species ($Z = 1$ for neutral atoms). The effective principle quantum number is calculated as

$$n_{eff,i} = \sqrt{\frac{E_H}{E_{ionize} - E_i}}\tag{3.34}$$

where E_H is the ionization energy of hydrogen. Equation (3.33) was derived by Chambers following the derivation by Zeldovich and Raizer [1966] (see pp. 261-272). The final equation presented by Zeldovich and Raizer includes the hydrogen relationships for the degeneracy ($g_i = 2n_{eff}^2$) and ion partition function ($Q_+ = 1$), which leads to the following

$$\begin{aligned}\sigma_{v,i}^{bf} &= \frac{64}{3\sqrt{3}} \frac{\pi^4 m Z^4 e^{10}}{v^3 c h^6 n_{eff,i}^5} \bar{G} \\ &= 2.82 \times 10^{29} \frac{Z^4}{v^3 n_{eff,i}^5} \bar{G} \quad (cm^2)\end{aligned}\tag{3.35}$$

Chambers removes these hydrogen-specific relationships with the reasoning that the accuracy for non-hydrogen atoms will then be increased because two assumptions regarding the non-hydrogen atom are being removed. Interestingly, a comparison of the results obtained with Eqs. (3.33) and (3.35) with detailed calculations available in the literature (which will be discussed later) show that Eq. (3.35) is actually more accurate for nitrogen and oxygen. The reason for this may be that the Gaunt factors used for this comparison are intended for use with Eq. (3.35). The Gaunt factors used for this comparison were obtained from Biberman and Norman [1960, 1961, and 1963]. One interesting aspect of Eq. (3.33) is that it implies a temperature dependence, which is uncharacteristic of photoionization cross sections, through Q^+ . Because of its favorable comparison with detailed cross-sections, Eq. (3.35) will be used throughout this study, instead of Eq. (3.33), when it is stated that the “hydrogenic model” is being used. It will be shown later in this section that although Eq. (3.35) is more accurate than Eq. (3.33), its accuracy is unsatisfactory when compared with detailed calculations. Assuming a Boltzmann distribution of electronic states, a simplified version of the hydrogenic model (developed by Biberman and Norman [1961]) was applied by Armaly [1979] for nitrogen and oxygen. The results of Armaly’s study are presented later in this section.

The most accurate approach available for determining the bound-free cross sections is to use tabulated results from detailed theoretical calculations. One of the most complete and up-to-date sources for these values is the Opacity Project’s online photoionization cross-section database, called the TOPbase (Cunto et al. [1993]). This database provides spectrally-resolved cross-sections for all the levels of all the atoms and ions of present interest. In fact, the spectral resolution is so great and requires so many frequency points (over 12,000 for nitrogen) that a method of approximating the data using fewer frequency points is required for the practical computation of radiative heat flux through a shock-layer. The method developed for this in the present study uses two different forms of approximation for modeling the cross-section frequency-dependence. The cross sections for the first three levels of oxygen and nitrogen are represented with a step-model consisting of enough steps to sufficiently model many of the “spikes” in the spectrum. The step models created for nitrogen and oxygen are listed in Appendix B. The cross sections for the remaining levels are approximated by the following function

$$\sigma_{v,i}^{bf} = \sigma_{thresh,i}^{bf} \left(\frac{hv_{thresh,i}}{hv} \right)^{\theta_i} \quad (cm^2) \quad (3.36)$$

where the parameters $\sigma_{thresh,i}^{bf}$, $hv_{thresh,i}$, and θ_i are chosen to give the best fit through the TOPbase data, and are listed in Appendix B.

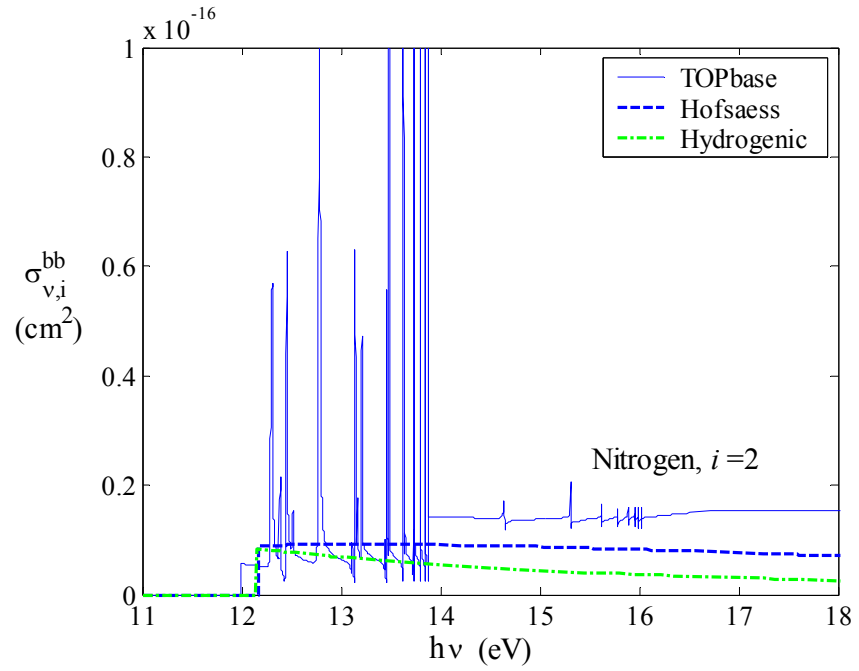
Another source of cross-sections that considers all of the atomic levels presently considered for nitrogen and oxygen is the theoretical study by Hofsaess [1979]. The data presented by Hofsaess has significantly less spectral resolution than the TOPbase data. For example, the Hofsaess data contains a total of 320 frequency points for the first 25 levels of nitrogen, which is significantly less than the approximately 12,000 required for the TOPbase data. A comparison of the Hofsaess and TOPbase data, along with the approximate hydrogenic model, are presented in the following paragraphs for nitrogen and oxygen.

a) Nitrogen

A comparison between the bound-free cross sections resulting from the second level of nitrogen, as predicted by the TOPbase, Hofsaess, and hydrogenic models, is presented in Figure 3.7. This comparison is representative of cross-sections resulting from most levels of nitrogen. It is seen that the hydrogenic and Hofsaess models predict values of the same order-of-magnitude as the TOPbase model. The spikes present in the TOPbase cross-sections resulting from only the first three levels of nitrogen and oxygen were found to influence the integrated radiative heat flux. For this reason, the cross-sections for only the first three levels were approximated as *detailed steps* in

the “TOPbase fit” model*. These detailed steps were chosen to model the spikes that noticeably influenced the integrated flux. The cross sections for the rest of the levels are represented in the “TOPbase fit” model by Eq. (3.36), which is a smooth function. Note that the “TOPbase fit” model is not shown in Figure 3.7 because it is indistinguishable from the TOPbase data, although for many of the upper levels the “TOPbase fit” values are only rough approximations of the actual TOPbase data. This inaccuracy is acceptable for nitrogen and oxygen levels greater than three, because the number density of the higher levels are orders-of-magnitude lower than the first three levels, which means they have only a small influence on the total emission and absorption coefficients. The frequency-dependent absorption coefficient, *accounting for only bound-free and free-free radiation from nitrogen*, is shown in Figure 3.8 for the various models. A Boltzmann distribution of excited states is assumed and the electronic temperature is 10,000 K. The corresponding frequency-dependent radiative heat flux from a constant-property-slab, with conditions identical to those of the 1 atm equilibrium air case studied in Section 3.4, is presented in Figure 3.9. The product of N_N (the number density of neutral nitrogen) and Δz (the thickness of the slab) is a similarity parameter that defines the optical thickness of the layer (along with the electronic temperature). Although the spikes in the TOPbase curve in the range of 4 – 10 eV are not modeled by the “TOPbase fit”, as shown in Figure 3.8, it is seen in Figure 3.9 that this portion of the spectrum does not contribute significantly to the radiative flux. This conclusion is true for most temperatures and number densities of interest for hypersonic shock layers. The integrated radiative heat flux values resulting from *only the bound-free and free-free nitrogen continuum* are shown in Figures 3.10 and 3.11 as a function of $N_N \Delta z$. The upper limit of the horizontal-axis in Figure 3.10 represents the conditions for the case shown in Figure 3.9. The 80 W/cm² contribution from the nitrogen continuum is not negligible relative to the 204 W/cm² atomic line contribution presented in Table 3.3. Note that the horizontal-axis of Figure 3.11 is two orders-of-magnitude lower than that for Figure 3.10 in order to show a different of optical thickness regime. Both Figures 3.10 and 3.11 show an excellent agreement between the TOPbase fit and the detailed TOPbase result. Similarly, the Hofsaess result agrees reasonably well with the TOPbase data in both figures, although less so than the TOPbase fit. The hydrogenic and Armaly models are seen to be accurate in one figure, but not in the other. Because of its accurate modeling of the TOPbase data and its simplicity, the TOPbase fit model will be applied throughout the remainder of this study.

* this approximate model is based on the TOPbase data and is listed in Appendix B



Figures 3.7. Comparisons of the photoionization cross-sections obtained from the TOPbase, Hofsaess, and the hydrogenic approximation for a single level of nitrogen.

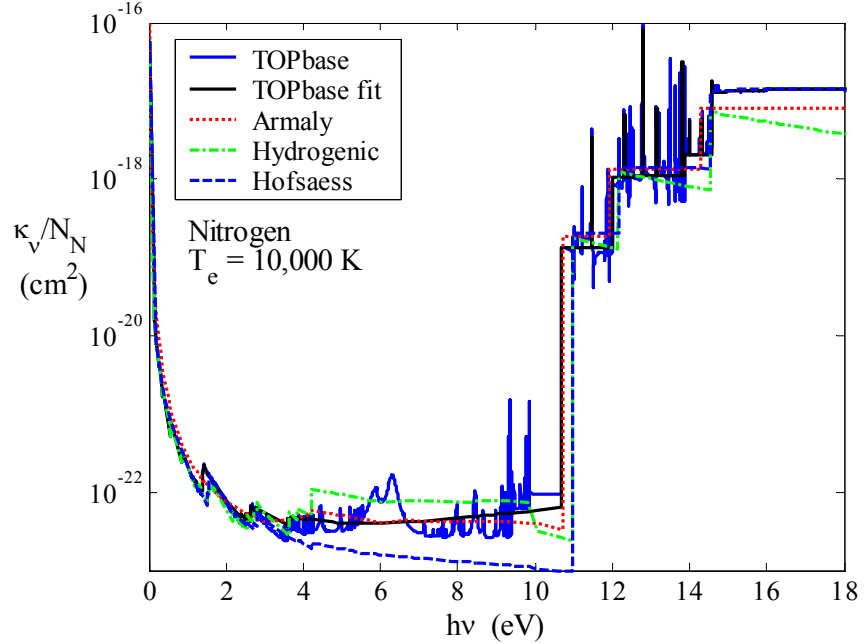


Figure 3.8. The bound-free and free-free frequency-dependent absorption coefficient (divided by the nitrogen number density) for nitrogen predicted by various models.

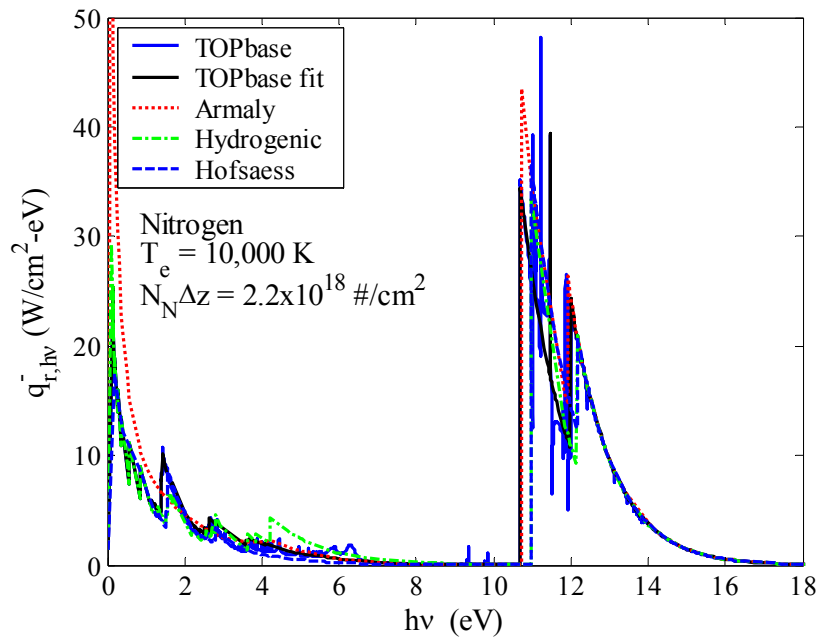


Figure 3.9. The bound-free and free-free frequency-dependent radiative heat flux emitted from an equilibrium constant-property-slab of nitrogen.

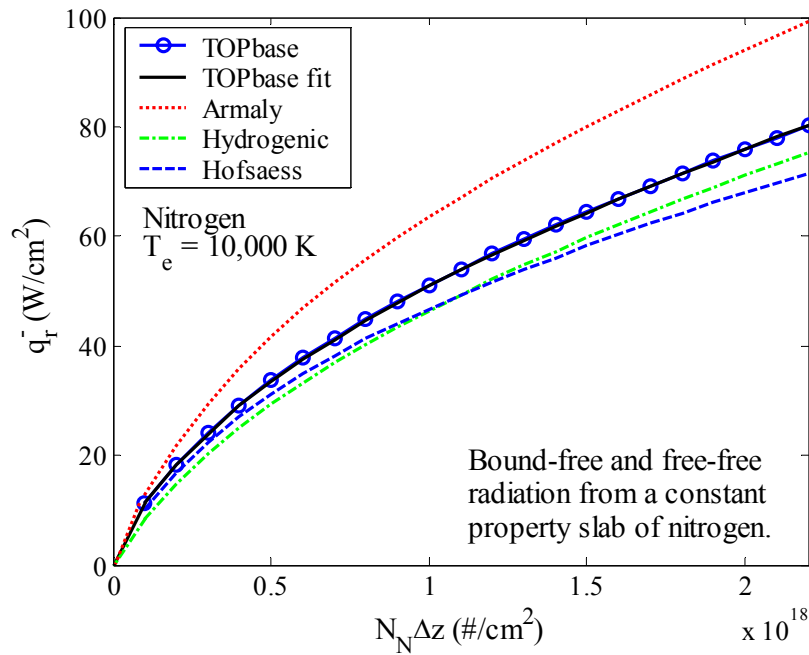


Figure 3.10. The bound-free and free-free integrated radiative heat flux emitted from an equilibrium constant-property-slab of nitrogen for values of $N_N\Delta z$ on the order of 10^{18}#/cm^2 .

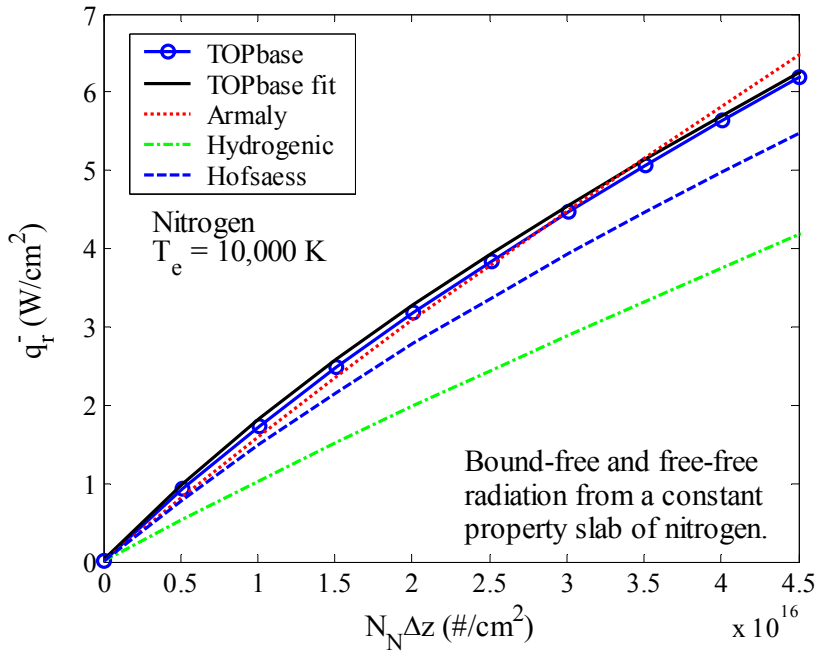
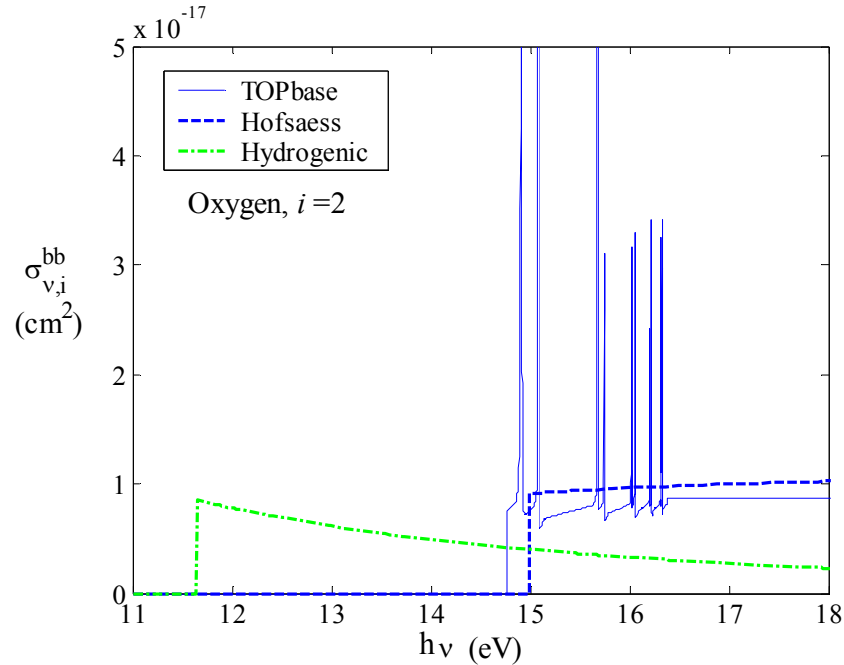


Figure 3.11. The bound-free and free-free integrated radiative heat flux emitted from an equilibrium constant-property-slab of nitrogen for values of $N_N \Delta z$ on the order of 10^{16}#/cm^2 .

b) Oxygen

The conclusions regarding the modeling of the bound-free and free radiation discussed above for nitrogen are not generally applicable to oxygen. The equivalent figures to those discussed above for nitrogen are presented in Figures 3.12 – 3.16 for oxygen. Figure 3.12 shows a major difference between the hydrogenic and detailed cross-sections resulting from the second level of oxygen, and although not shown, was also found for the third level. Specifically, the threshold frequency is seen to be significantly lower for the hydrogenic model than for the TOPbase and Hofsaess models. Figures 3.13 – 3.16 show the significance of this difference on the resulting radiative heat flux from the oxygen continuum. Note that in creating the Armaly model, Armaly applied the hydrogenic model to obtain the cross-sections for the low lying levels. It is then reported by Armaly, when comparing with the cross-sections predicted by previous studies, that the contribution from the second and third levels appeared to be missing from the previous studies. It is shown in Figure 3.12 that these levels appeared to be missing because their threshold frequency is shifted to about 15 eV, which is a spectral region that is dominated by the ground-level cross-section.



Figures 3.12. Comparisons of the photoionization cross-sections obtained from the TOPbase, Hofsaess, and the hydrogenic approximation for a single level of oxygen.

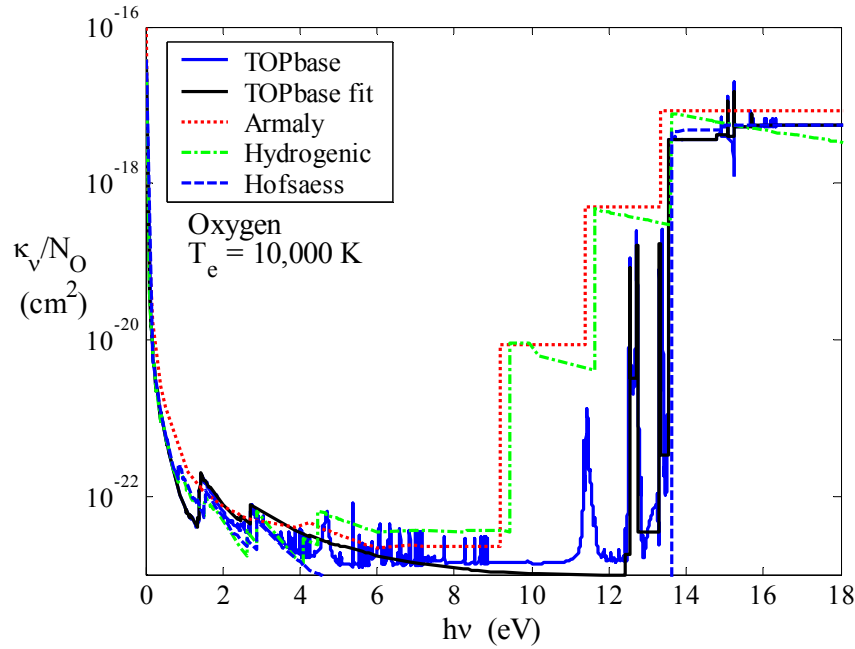


Figure 3.13. The bound-free and free-free frequency-dependent absorption coefficient (divided by the oxygen number density) for oxygen predicted by various models.

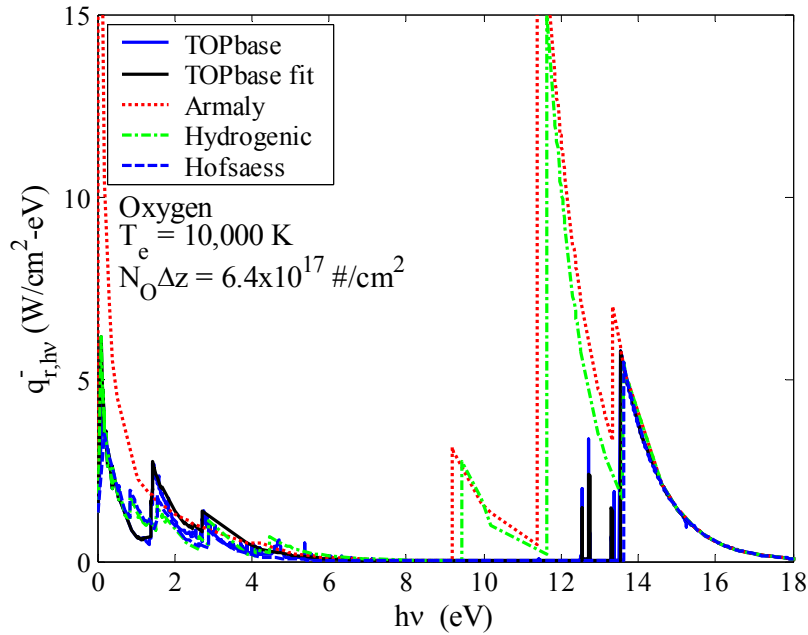


Figure 3.14. The bound-free and free-free frequency-dependent radiative heat flux emitted from an equilibrium constant-property-slab of oxygen.

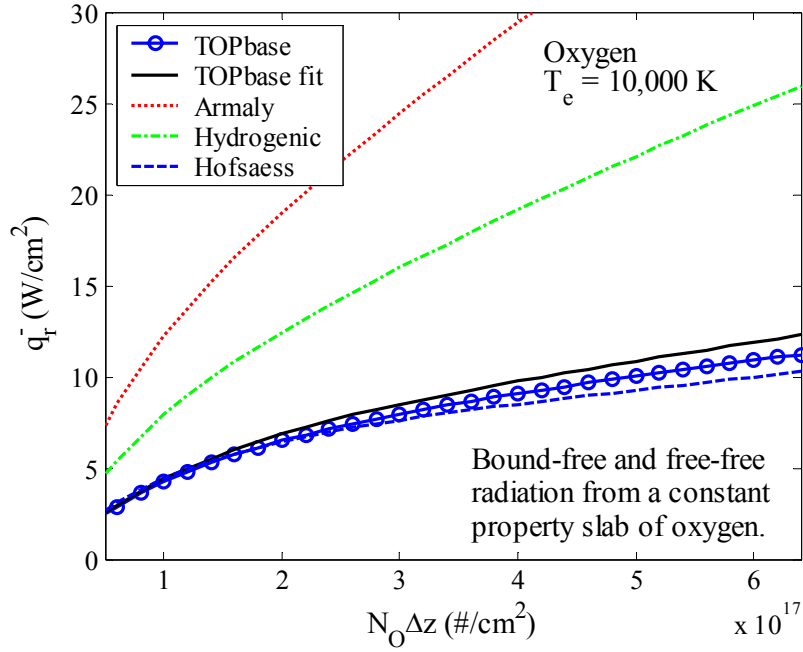


Figure 3.15. The bound-free and free-free integrated radiative heat flux emitted from an equilibrium constant-property-slab of oxygen for values of $N_O\Delta z$ on the order of 10^{17}#/cm^2 .

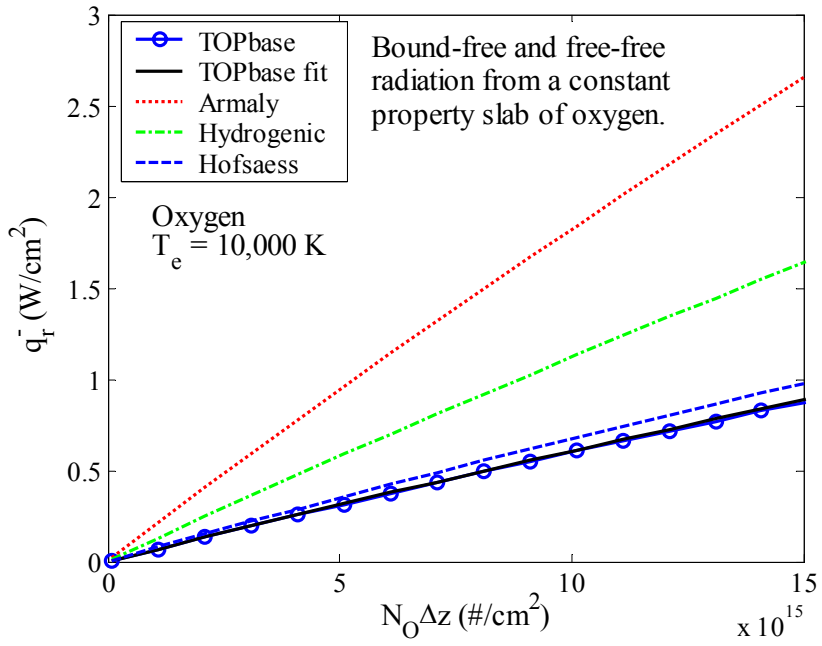


Figure 3.16. The bound-free and free-free integrated radiative heat flux emitted from an equilibrium constant-property-slab of oxygen for values of $N_O\Delta z$ on the order of 10^{16}#/cm^2 .

3.8 The Smeared Rotational Band Method

The radiation resulting from molecular species in equilibrium air at conditions relevant to lunar return shock-layers is usually no more than 7% of the total radiative flux. At *nonequilibrium* conditions, this contribution can increase slightly, depending on the shock-layer thickness and nonequilibrium region, but conditions where this is significant usually occur away from peak heating conditions, where the total radiative flux is relatively small. Because molecular band systems do not contribute significantly, it was desired to model them using a computationally inexpensive technique that provides reasonably accurate results. The “smeared rotational band” (SRB) method developed by Patch, Shackleford, and Penner [1962] was chosen for this purpose. This method was recently extended by Chambers [1994] to higher-order accuracy and multi-temperature conditions. From Chambers, the equations for the absorption and emission coefficients for a single molecular band system are written as follows

$$\kappa_v = N_{e''} \frac{\pi e^2}{mc^2} \sum_{V''} \sum_{V'} \frac{1}{|B_{V'} - B_{V''}|} \frac{f_{V''V'}}{Q_{J''} Q_{V''}} \exp\left(-\frac{hc}{kT_v} E_{V''}\right) \exp\left(-\frac{hc}{kT_r} E_{J''}\right) \quad (\text{cm}^{-1}) \quad (3.37)$$

$$j_v = N_{e'} \frac{2h\pi e^2}{mc^4} \frac{g_{e'}}{g_{e''}} \sum_{V''} \sum_{V'} \frac{v^3}{|B_{V'} - B_{V''}|} \frac{f_{V''V'}}{Q_J Q_{V'}} \exp\left(-\frac{hc}{kT_v} E_{V'}\right) \exp\left(-\frac{hc}{kT_r} E_J\right) \quad \left(\frac{\text{erg}}{\text{cm}^3 \cdot \text{sr}}\right) \quad (3.38)$$

The various terms in these equations are defined in Appendix D, except for the rotational energy, which is approximated as follows

$$E_J = \frac{B_e}{B_{e'} - B_{e''}} \frac{(v - v_{V'V''})}{c} \quad (cm^{-1}) \quad (3.39)$$

and the function B_V , which represents the first term in brackets in Eq. (D-3). Note that Eq. (3.39) ignores the second term in brackets in Eq. (D-3), which simplifies the evaluation of Eqs. (3.37) and (3.38), with minimal loss in accuracy. The simplicity of applying the SRB approach is seen by writing the absorption coefficient as follows

$$\frac{\kappa_v}{N_{e''}} = \phi(v) \sum_{n=1}^{NN} P_{V'V'',n} \quad v_{V'V'',n-1} \leq v \leq v_{V'V'',n} \quad (3.40)$$

where

$$P_{V'V'',n} = \frac{\pi e^2}{mc^2} \frac{1}{|B_{V'} - B_{V''}|} \frac{f_{V''V'}}{Q_{J''} Q_{V''}} \exp\left(-\frac{hc}{kT_v} E_{V''}\right) \exp\left(\frac{h}{kT_r} \frac{B_e}{B_{e'} - B_{e''}} v_{V'V''}\right) \quad (3.41)$$

and

$$\phi(v) = \exp\left(-\frac{h}{kT_r} v \frac{B_{e''}}{B_{e'} - B_{e''}}\right) \quad (3.42)$$

The limiting frequencies for Eq. (3.40) may be calculated for each $V'-V''$ transition as

$$v_{V'V'',n} = c \left[E_{e'} - E_{e''} + E_{V'} - E_{V''} - \frac{1}{4} \frac{(B_{V'} + B_{V''})^2}{(B_{V'} - B_{V''})} \right] \quad (3.43)$$

The last term in this equation, suggested by Golden [1967], improves the agreement between this method and the line-by-line approach. The subscript n on $P_{V'V''}$ and $v_{V'V''}$ is assigned by sorting the $v_{V'V''}$ values in ascending or descending order, depending on the sign of $B_{e'} - B_{e''}$ for the band system (ascending if positive, descending if negative). Figure 3.17(a) illustrates the construction of the spectrum using Eq. (3.40). The procedure for the emission coefficient is analogous.

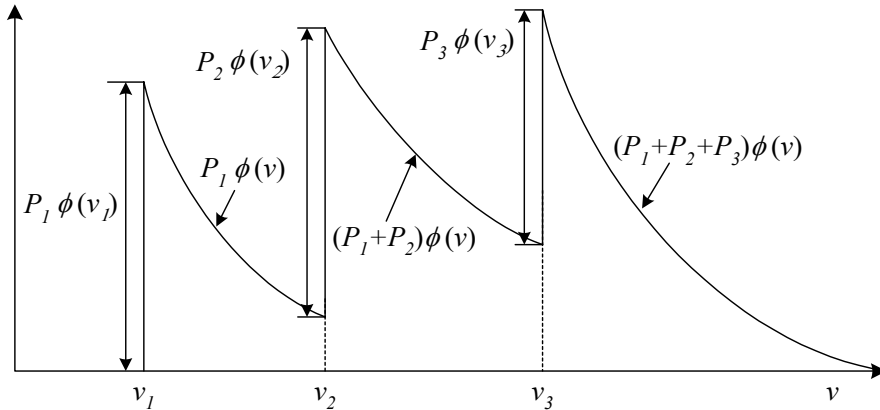


Figure 3.17(a). Details of constructing the SRB spectrum using Eq. (3.40) through (3.43).

The accuracy of the SRB method may be gauged relative to the results of the detailed line-by-line (LBL) method, which is described in detail in Appendix D for the simple case of a $^2\Sigma - ^2\Sigma$ transition. This case is of interest for the CN violet molecular band, which will be studied exclusively in Chapter 6 for Titan entry. For the Titan entry case, Chapter 6 will show, by comparing the SRB and LBL results, that the SRB method is insufficient because the spectrum is partially optically thick. The result of this is that the SRB method over-predicts the integrated flux by up to 40% relative to the LBL method (see Section 6.2). Fortunately, the most important band system for air (at conditions of present interest) will be shown in the next section to be the N_2^+ first-negative band system, which is also a $^2\Sigma - ^2\Sigma$ transition. Thus, the LBL method described in Appendix D may be applied to this band system and compared to the SRB results for conditions typical of a lunar-return shock-layer. For a 4-cm constant property slab of equilibrium air at 1 atm and 10,000 K, Figure 3.17(b) compares a limited region of the radiative flux spectrum predicted by the SRB and LBL methods. Although the two spectrums appear to be very different, they actually predict spectrally-integrated flux values that agree within 4% (resulting from integration over the entire spectrum, not just the range shown in the figure). The reason for this good agreement is that the spectrum is optically thin, which is indicated in the figure by the Planck function (B_{hv}) being significantly larger than any of the peaks in either the SRB or LBL spectrum (note that the B_{hv} curve shown has been divided 30 so that it is in the range of the figure's vertical-axis). As will be discussed in the next section, the derivation of the SRB method guarantees that it will reproduce the LBL-predicted integrated flux for optically thin conditions (i.e. they predict the same integrated emission). Thus, the conclusion that the most significant molecular band system is optically thin, as predicted by both the SRB and LBL models, implies that the SRB model will provide accurate integrated radiative flux values (the VUV molecular band systems discussed in the next section are actually optically thick, but they are weak emitters relative to the N_2^+ first negative band). This provides the justification necessary for the SRB method to the present air cases. For the Titan cases discussed in Chapter 6, this will not be the case.

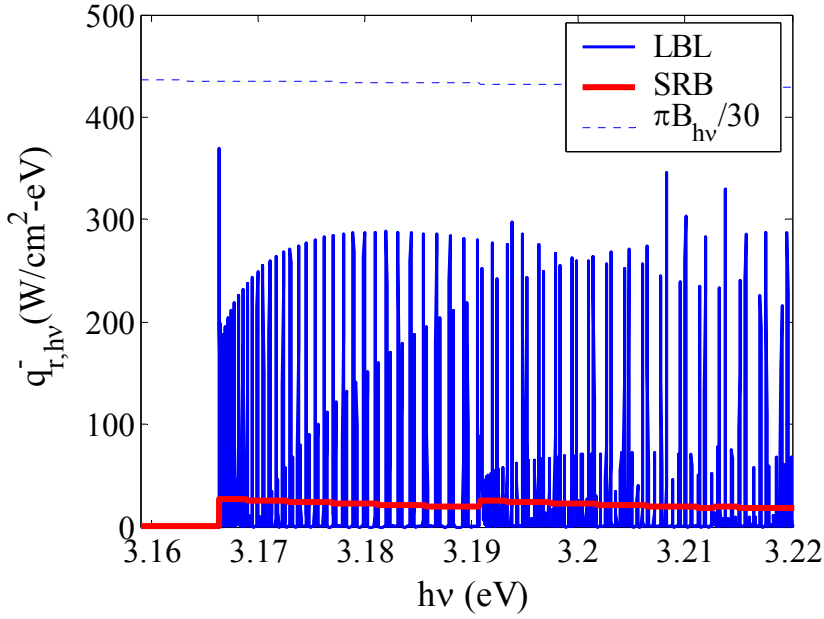


Figure 3.17(b). A comparison of a small spectral region, predicted by the SRB and LBL methods, of the radiative flux resulting from the N_2^+ first-negative band system in a 4-cm slab of equilibrium air at 1 atm and 10,000 K ($N_{\text{N}2+}\Delta z = 1.5 \times 10^{14} \text{ cm}^{-2}$).

To further reduce the computational burden of the modeling the molecular band systems, a step model representation of the molecular-band spectrum is applied for cases where the contributions of all radiating mechanisms are included (meaning atomic lines and the atomic continuum are also considered). This step model assumes constant values of the emission and absorption coefficient over specified frequency increments. The magnitude of the constant value is obtained for each frequency increment by analytically integrating the corresponding SRB equation. This guarantees that the integrated emission predicted by the step-model is the same as the actual SRB spectrum. Note that the spectrums presented in the following section do not apply this step model. An example of this step model representation of the molecular bands can be seen in Figure 5.24, where the N_2^+ first-negative is visible in the 2.5 to 4.0 eV range.

3.9 Treatment of the Molecular Band Systems in Air

The 15 molecular band systems treated for air are listed in Table 3.7. The data required to implement these band systems were taken mostly from Laux [1993], although for the vacuum ultraviolet (VUV) systems, various other sources were used, as indicated in the table. The last two columns in the table indicate whether the band system was accounted for in the NEQAIR (Park [1985a]) or RAD/EQUIL (Nicolet [1970]) codes. Note that the modeling of the band system in

these past codes was different than the smeared rotational band method applied here. The NEQAIR code applied a line-by-line calculation while the RAD/EQUIL code applied a curve-fit model, which was a smooth function of temperature and frequency.

Table 3.7. Molecular band systems treated for air in the present model.

Molec.	Transition	Name	Spectral Range (eV)	Ref.	In NEQAIR?	In RAD/EQUIL?	% of flux [#]
N ₂	B ³ P _g - A ³ S _u ⁺	1 ⁺ (1 st -positive)	0.2 - 2.5	1	yes	yes	0.77
N ₂	C ³ P _u - B ³ P _g	2 ⁺ (2 nd -positive)	2.7 - 4.7	1	yes	yes	3.65
N ₂	c ₄ 'S _u ⁺ - X ¹ S _g ⁺	Carroll-Yoshino	11.5 - 14.0	2,3,4	no	no	9.54
N ₂	c ₃ 'P _u - X ¹ S _g ⁺	Worley-Jenkins	11.5 - 14.0	2,3,4	no	no	3.92
N ₂	b ¹ P _u - X ¹ S _g ⁺	Birge-Hopfield I	7.0 - 13.1	3,5	no	yes	4.72
N ₂	b ¹ S _u ⁺ - X ¹ S _g ⁺	Birge-Hopfield II	7.6 - 14.0	2,3,4	yes	yes	4.65
N ₂	o ₃ ¹ P _u - X ¹ S _g ⁺	Worley	10.4 - 14.0	2,3,4	no	no	2.08
N ₂ ⁺	B ² S _u ⁺ - X ² S _g ⁺	1 ⁻ (1 st -negative)	1.2 - 4.6	1	yes	yes	53.83
NO	B ² P _r - X ² P _r	β (beta)	2.1 - 6.9	1	yes	yes	1.72
NO	A ² S ⁺ - X ² P _r	γ (gamma)	3.2 - 7.5	1	yes	yes	2.63
NO	C ² P _r - X ² P _r	δ (delta)	3.7 - 7.6	1	yes*	yes	4.80
NO	D ² S ⁺ - X ² P _r	ε (epsilon)	3.4 - 8.0	1	yes*	yes	4.57
NO	B ² Δ - X ² P _r	β' (beta-prime)	3.9 - 8.4	1	yes*	no	1.41
NO	E ² S ⁺ - X ² P _r	γ' (gamma-prime)	4.6 - 8.9	1	yes*	no	1.44
O ₂	B ³ S _u ⁻ - X ³ S _g ⁻	Schumann-Runge	2.6 - 7.0	1	yes	yes	0.27

¹Laux, C. O., Rept. T-288, Stanford University, 1993.

²Whang, T.J., Guoxing, Z., Stwalley, W.C., and Wu, C.Y.R., *Journal of Quantitative Spectroscopy and Radiative Transfer*, Vol. 55, pp. 335-344, 1996.

³Stahel, D., Leoni, M., and Dresslar, K., *Journal of Chemical Physics*, Vol. 79, pp. 2541-2558, 1983.

⁴Chauveau, S., Perrin, M.Y., Riviere, P., and Soufiani, A., *Journal of Quantitative Spectroscopy and Radiative Transfer*, Vol. 72, pp. 503-530, 2002.

⁵Generosa, J.I., Harris, R.A., Sullo, L.R., AFWL-TR-70-108, 1971.

*Included in the “NEQAIR 96” version, but not the original version from Park [1985].

[#]This column lists the percentage contribution of each band system to the total molecular-band flux from a 4-cm equilibrium constant-property slab of air at 1 atm and 10,000 K.

The spectral-emission coefficients, divided by the upper-state electronic state number densities, are plotted in Figure 3.18 (a - c) assuming a vibrational and rotational temperature of 10,000 K. Because each of these band systems has a different upper electronic state, no conclusion can be made from these figures about their relative magnitudes. The last column in Table 3.7 lists the percent contribution of each band system to the total molecular band radiative flux from a 4-cm thick constant property slab of air at 10,000 K and 1 atm. The resulting molecular band spectrum at this condition is presented in Figure 3.19 along with the resulting accumulated molecular band flux. The total molecular band flux is 18.3 W/cm² for this case, which is relatively insignificant relative to the atomic line and bound-free contribution presented in the previous sections for this condition.

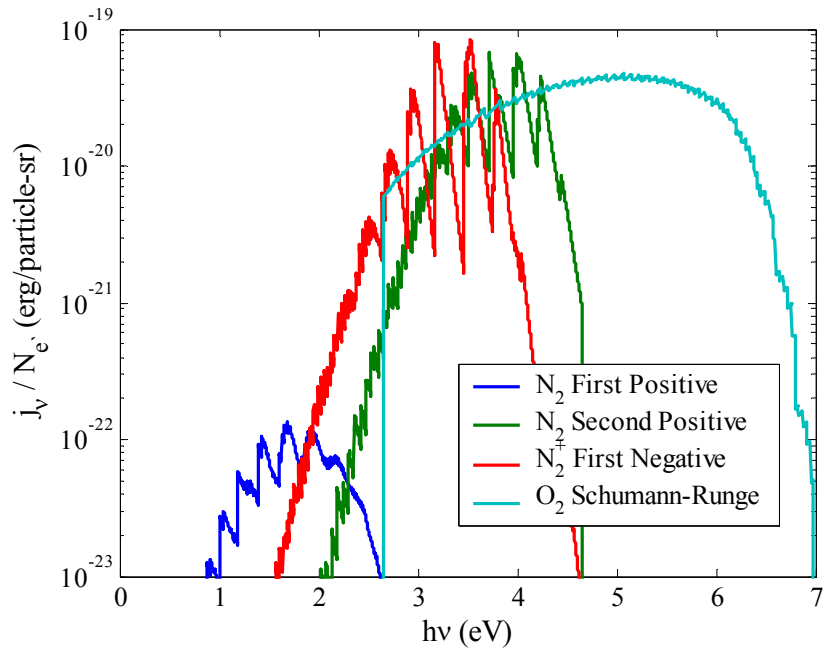


Figure 3.18(a). Molecular band emission coefficients divided by the upper-state number density, assuming a rotational and vibrational temperature of 10,000 K.

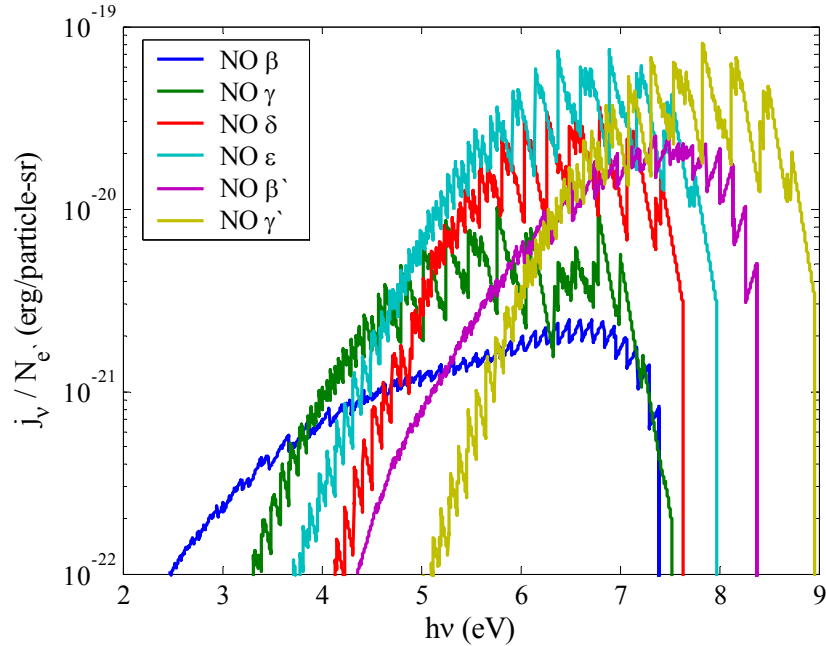


Figure 3.18(b). Molecular band emission coefficients divided by the upper-state number density, assuming a rotational and vibrational temperature of 10,000 K.

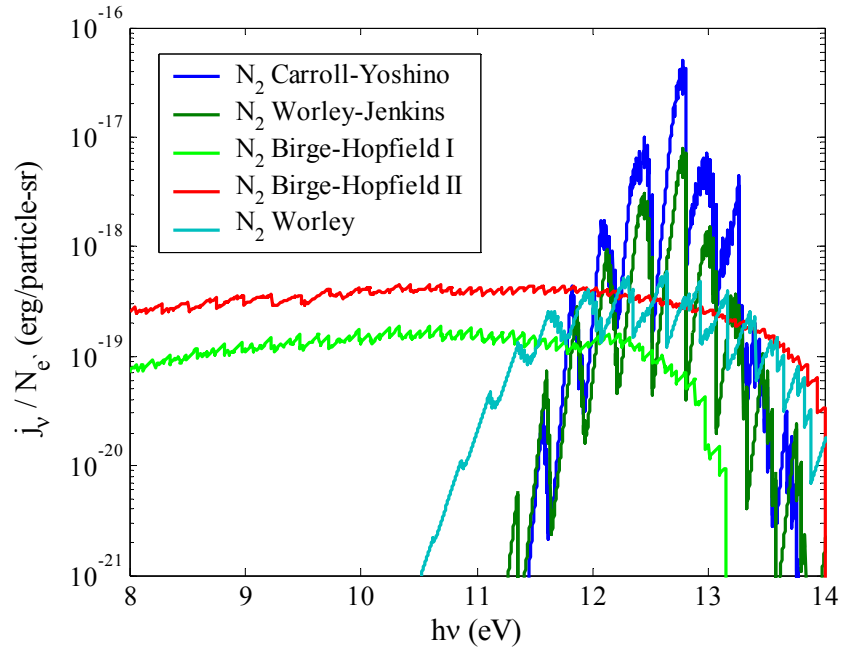


Figure 3.18(c). Molecular band emission coefficients divided by the upper-state number density, assuming a rotational and vibrational temperature of 10,000 K.

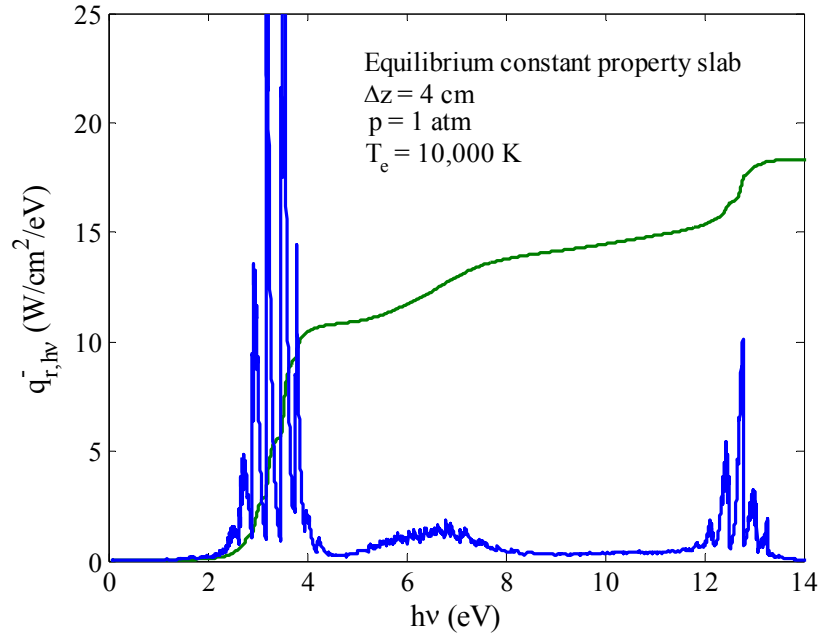


Figure 3.19. Molecular band radiative spectrum from a 4-cm constant property slab of air at 10,000 K and 1 atm. The dark green line is the accumulated flux from only the molecular bands.

As discussed in the previous section, the band systems located completely below 10 eV are optically thin for nearly all conditions of present interest. For these optically thin band systems,

the frequency-integrated radiative flux is related to the frequency-integrated emission coefficient through the following equation

$$q_v^{cp\text{-}slab} = 2\pi j \Delta z + \dots \quad (3.44)$$

where j is the frequency integrated emission coefficient and Δz is the thickness of the slab. As will be presented in Chapter 6 (Eq. (6.1)), the frequency-integrated emission coefficient may be obtained by analytically integrating Eq. (3.38). Figure 3.20 presents the values of j resulting from each of the optically thin band systems in equilibrium air at a pressure of 1 atm. The N_2^+ 1- system is seen to dominate for temperatures above 8,000 K, while the O_2 Shumann-Runge band is negligible for the entire range of temperatures shown here. The vacuum ultraviolet band (VUV) systems are not shown in this figure because they are optically thick for most length scales of present interest, and therefore their contribution to the radiative flux cannot be related to the emission coefficient using Eq. (3.44).

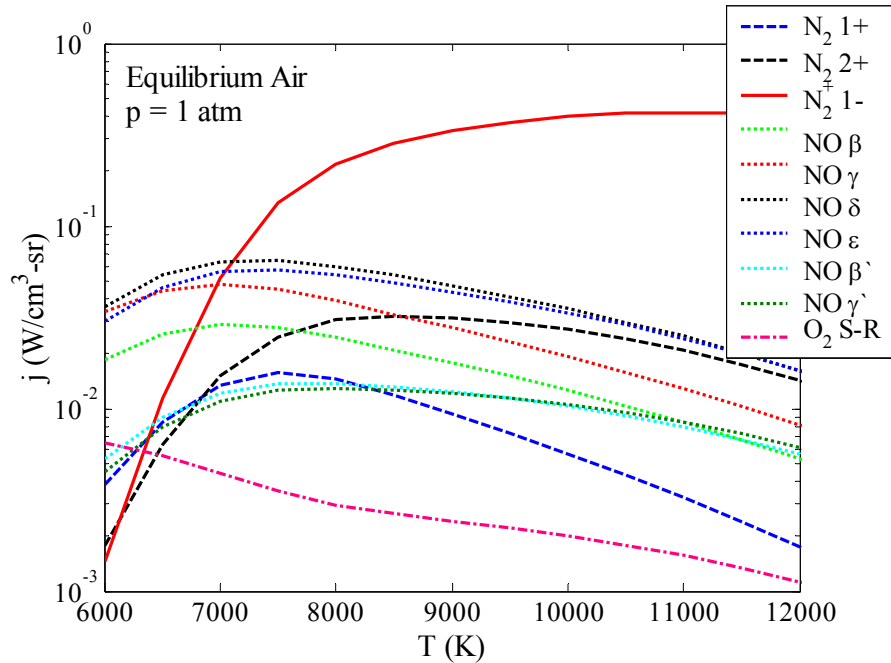
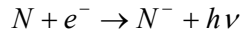


Figure 3.20. Frequency-integrated emission coefficients for molecular band systems in equilibrium air at 1 atm.

3.10 Summary of the Air Radiation Model in Equilibrium

To summarize the contributions from the atomic line, atomic continuum, and molecular band radiation models presented in the previous sections, the total emission coefficient from equilibrium air at 1 atm and a range of temperatures are compared in Figure 3.21 with the results of recent studies by Naghizadeh-Kashani et al. [2002] and Chauvaeu et al. [2003]. The excellent

agreement with the results of Chauvaeu is to be expected because the same source of atomic line data was applied (from the NIST database). Since atomic line emission from the VUV contributes 99% of the total integrated emission coefficient, this figure essentially verifies only that Eq. (3.5) is being implemented correctly in the present study. Note that the calculation of the integrated emission from atomic lines in the VUV is performed analytically using Eq. (3.5) because the spectral grid, which was constructed (see Section 3.5) to accurately model the radiative flux, does not model accurately the spectral emission coefficient for atomic lines in the VUV (see the discussion of Figure 3.6 for an explanation on why this is true). Figure 3.22, which presents the integrated emission coefficient from the 0 – 6 eV spectral region, provides a more meaningful comparison between the present model and that by Chauveau et al. [2003]. This spectral region (0 – 6 eV) is nearly optically thin for most conditions of present interest, and therefore the emission coefficient may be related to the radiative flux from a constant property slab using Eq. (3.20). A notable difference between the present model and that presented by Chauveau et al. is that they included the contribution from the photodetachment of N^- and O^- which is the result of the following process



The absorption and emission coefficients for this process are not well known, and it has not been confirmed that this process even occurs. It was proposed in the early 1960s to explain discrepancies between experimental measurements and theoretical predictions of the continuum radiation (Thomas and Menard [1967], Gruszczynski and Warren [1967]). It is possible, though, that these measurements of the *continuum* radiation also contained contributions from molecular band systems, resulting in the larger than expected continuum value. In Figure 3.22, the curve labeled “At. Cont. w/ neg.” contains this negative continuum contribution, as it was applied by Chauveau et al. [2003], while the curve labeled “At. Cont. no neg.” does not contain this component. The line labeled “Total” (for the present model), which is the sum of the atomic lines, atomic continuum, and molecular bands, does contain the negative continuum component. The agreement between the individual components predicted by the two models is very good if the negative continuum contribution is included, although even without the negative continuum, the total radiation is not significantly effected (considering the logarithmic vertical-axis), especially at the higher temperatures.

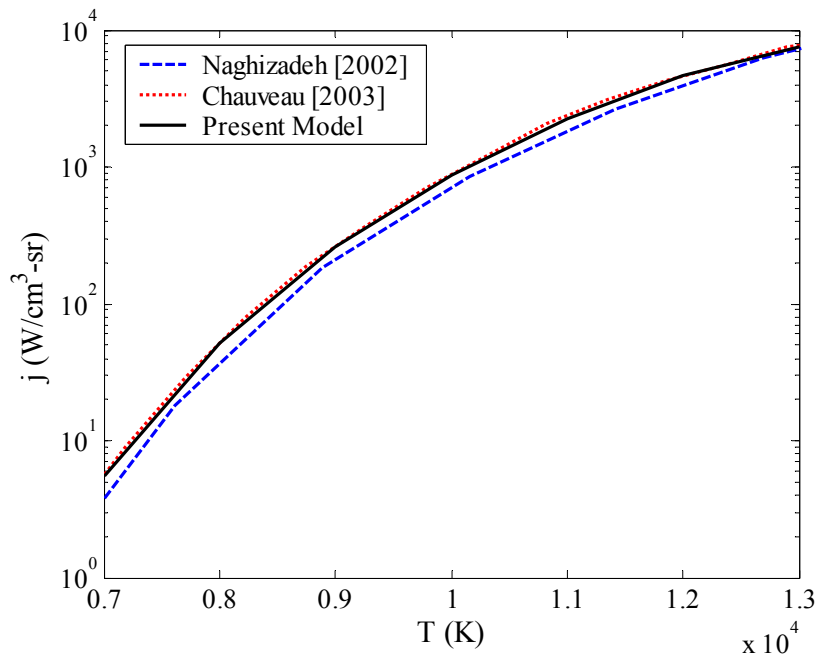


Figure 3.21. Total emission coefficient ($0 - 18$ eV) for air at 1 atm predicted by various models

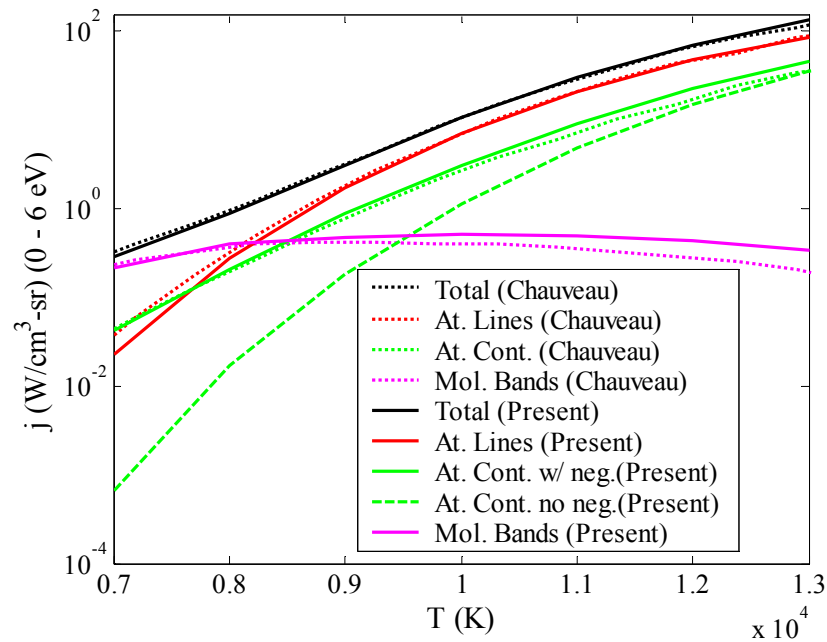


Figure 3.22. Comparison of the emission coefficient contributions from the $0 - 6$ eV spectral region from equilibrium air at 1 atm

The emission coefficients presented in Figures 3.21 and 3.22 do not indicate the influence of optical thickness on the radiation transport through the gas. For the present applications, we are interested in the radiation transport through shock-layers with thicknesses ranging from about 4-

cm (Fire II) to 20-cm (CEV). Figure 3.23 presents the radiative flux through constant-property slabs of various thicknesses. By dividing the flux values by $2\pi\Delta z$ (as they are in this figure), the influence of optical thickness may be assessed for the $\Delta z = 1$ and 10-cm cases by noting their decrease, for a fixed temperature, from the $\Delta z = 0$ case. In this figure, the contributions from the 0 – 6 eV and 6 – 18 eV spectral regions are considered separately because of their distinctly different transport characteristics. This difference is clearly shown by the similarity in the 0 – 6 eV cases for a fixed temperature, while values for the 6 – 18 eV cases differ by roughly two orders-of-magnitude. For the 10-cm slab, which is the most relevant to the shock-layers of present interest, the contributions from the 0 – 6 eV and 6 – 18 eV ranges are of equal orders-of-magnitude.

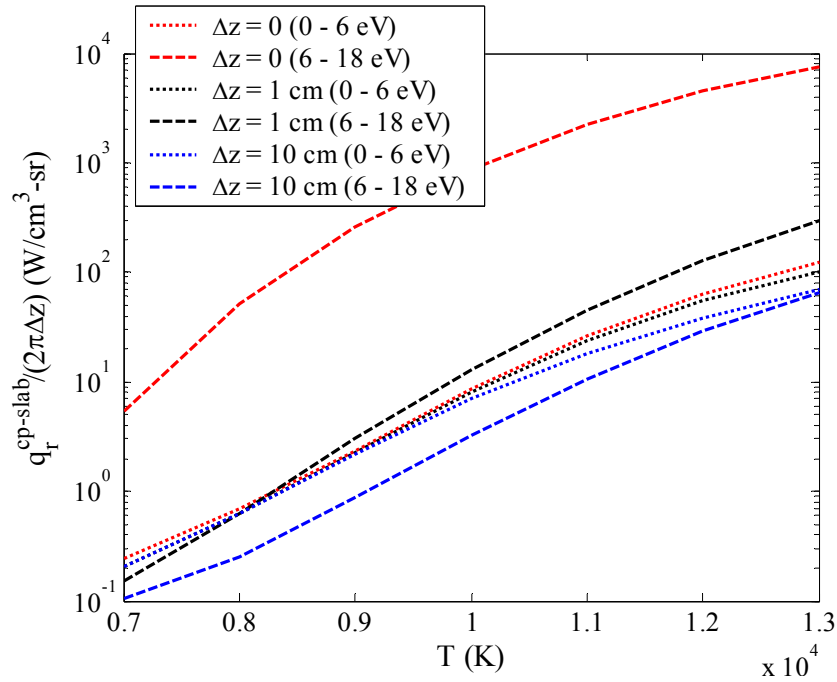


Figure 3.23. Integrated radiative flux components (divided by $2\pi\Delta z$) emitted from constant property slabs of various thicknesses in equilibrium air at 1 atm

Chapter 4

Collisional-Radiative Modeling of N, O, N₂, and N₂⁺

4.1 Chapter Overview

In the previous chapter, the calculation of the radiative emission and absorption was discussed for the various radiative processes of atoms and molecules. The magnitude of the emission and absorption coefficients from these various radiative processes are proportional to the number density of the emitting or absorbing electronic state. For all of the examples worked in Chapter 3, it was assumed that these electronic states were populated by a Boltzmann distribution. This assumption is accurate for chemical equilibrium conditions. As shown in Chapter 2, there are significant regions of chemical *nonequilibrium* in the lunar return (and Titan entry) shock-layers of present interest, which require that the non-Boltzmann electronic state populations be considered. The present chapter investigates the calculation of these non-Boltzmann electronic state populations for the significant radiating species present in air shock-layers at lunar return conditions. The species considered in this chapter include two atomic species, N and O, and two molecular species, N₂ and N₂⁺. Although it was shown in Chapter 3 that the NO and O₂ molecules contribute to the radiation at lunar-return conditions, it was found that they could be assumed to be populated in a Boltzmann distribution. This assumption is allowable because these molecules do not reach a peak in the nonequilibrium region of the shock layer (unlike the N₂⁺ molecule), so their nonequilibrium contribution is small.

The atomic and molecular electronic state-populations are modeled using a collisional-radiative (CR) model, which accounts for the repopulation and depopulation of the atomic and molecular states through collisional and radiative processes. These processes are discussed individually in

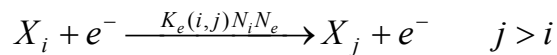
Section 4.2. In Section 4.3, the general formulation of the CR model's governing equation, called the Master Equation, is derived from the processes discussed in Section 4.2. A practical method of solving the Master Equation is presented in Section 4.4. The task of assembling the rates required for the atomic CR modeling of N and O is discussed in Sections 4.5. Excitation rates from several sources are compared and a final set of rates is compiled and presented. Based on this detailed rate model and the solution procedure for the Master Equation discussed in Section 4.4, an “approximate atomic CR” (AACR) model was developed, which allows for the efficient and accurate application of the atomic CR model. The AACR model is presented in Section 4.6, and is conveniently represented by curve fits presented in Appendix C. The non-Boltzmann modeling of the two molecular species, N_2 and N_2^+ , is discussed in Section 4.7. The influence of various collisional processes on these molecules is studied, and rates from several sources are compared. A recommended set of rates is proposed, and a set of curve fits (which are presented in Appendix C) are constructed for the radiating electronic states of these molecules. The non-Boltzmann modeling for entry into Titan at Huygens conditions, which requires the modeling of only CN, will be discussed in Chapter 6. The general discussion of the electronic state repopulation and depopulation mechanisms presented in Sections 4.2 and 4.3 are equally relevant to the Titan case.

4.2 Excitation and De-Excitation Mechanisms

As mentioned previously, the population of the radiating atomic and molecular electronic states required for the calculation of the radiative emission and absorption are calculated by solving the so-called Master Equation. The derivation of this equation requires the specification of the various repopulation and depopulation mechanisms of the atomic or molecular states. The present model will consider electron impact, heavy particle impact, and radiative processes. These processes are defined as follows:

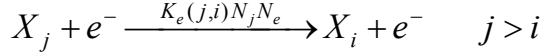
I. Electron-Impact Excitation and De-Excitation:

The process of electron-impact excitation is significant for both atoms and molecules in the hypersonic shock-layer applications of present interest. For the excitation of an electronic level i to a higher level j , this process may be written symbolically as



where X is the atom or molecule being excited and e^- represents the colliding electron. The rate of excitation of level j per-unit volume for this process is written as $K_e(i,j)N_iN_e$, where $K_e(i,j)$ is the electron-impact rate coefficient, N_i is the number density of level i , and N_e is the number density

of electrons. In writing $K_e(i,j)$, the first term in the parenthesis represents the initial state of the transition and the second term represents the final state. The reverse process of electron-impact de-excitation may be written similarly as



The de-excitation rate is related to the corresponding excitation rate through detailed balancing, which results in the following relationship

$$K_e(j,i) = K_e(i,j) \frac{g_i}{g_j} \exp\left[-\frac{hc}{kT_e}(E_i - E_j)\right] \quad (cm^3 s^{-1}) \quad (4.1)$$

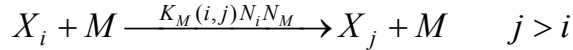
The net rate of excitation of level i per-unit volume due to electron impact excitation is obtained by summing over the populating and depopulating transitions from the m levels of the atom or molecule:

$$\left(\frac{\partial N_i}{\partial t}\right)_{elec-imp-ex} = \sum_{j=1}^m K_e(j,i)N_jN_e - \sum_{j=1}^m K_e(i,j)N_iN_e \quad \left(\frac{\text{particles}}{cm^3 - s}\right) \quad (4.2)$$

This component is one of the largest contributors to the total population and depopulation of level i , for both atoms and molecules.

II. Heavy Particle Impact Excitation and De-Excitation:

Transitions due to heavy particle collisions are similar in concept to electron-impact transitions, although they are significantly less important than electron-impact transitions for most applications.



where X is the atom or molecule being excited and M represents the colliding heavy particle. The rate of the reverse process is written as it is for electron-impact excitation in Eq. (4.1), except that T_e should be replaced with T_t , which is the governing temperature of the heavy particle translational model. The net rate of this process is written as

$$\left(\frac{\partial N_i}{\partial t}\right)_{hp-imp-ex} = \sum_{j=1}^m K_M(j,i)N_jN_M - \sum_{j=1}^m K_M(i,j)N_iN_M \quad \left(\frac{\text{particles}}{cm^3 - s}\right) \quad (4.3)$$

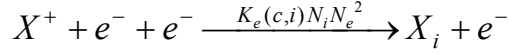
This process is negligible for atomic and molecular species in lunar-return shock layers. The small influence of this term will be shown in Section 4.7 for molecules. For the Titan shock-layers studied in Chapter 6, though, this process is the dominant contributor to the excitation of the strongly-radiating CN molecule.

III. Electron-Impact Ionization and Recombination

The process of electron-impact ionization is significant in most hypersonic shock-layer applications for atoms only. The ionization of level i through this process may be written symbolically as



where X^+ represents the ionized specie and $K_e(i,c)N_i N_e$ represents the rate of ionization of level i per-unit volume. The reverse process, or three-body recombination, is written as



The ionization and recombination rate coefficients are related as follows

$$K_e(c,i) = K_e(i,c) \frac{N_i^{SB}}{N_+ N_e} \quad (cm^6 s^{-1}) \quad (4.4)$$

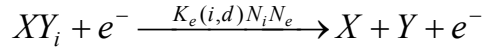
where N_+ is the ion number density and N_i^{SB} is the Saha-Boltzmann number density defined in Eq. (1.1). The net rate of excitation of level i due to this process may be written as

$$\left(\frac{\partial N_i}{\partial t} \right)_{elec-imp-ion} = K_e(c,i)N_+ N_e^2 - K_e(i,c)N_i N_e \quad \left(\frac{\text{particles}}{cm^3 - s} \right) \quad (4.5)$$

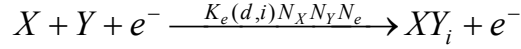
Note that this component is negligible for molecules at the shock-layer conditions of present interest.

IV. Electron-Impact Dissociation and Recombination:

The process of electron-impact dissociation of molecules contributes noticeably, for some cases, to the molecular state populations. The dissociation of level i of the molecule XY through this process may be written symbolically as



where X and Y represents the atomic species formed by dissociation and $K(d,i)N_i N_e$ represents the rate of dissociation of level i per-unit volume. The reverse process, or three-body recombination, is written as



The dissociation and recombination rate coefficients are related as follows

$$K_e(d,i) = K_e(i,d) \frac{N_i^{DE}}{N_X N_Y} \quad (cm^6 s^{-1}) \quad (4.6)$$

where N_i^{DE} is the number density of level i for the dissociation process in chemical equilibrium.

This may be written as

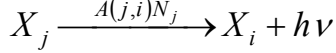
$$N_i^{DE} = N_X N_Y \frac{Q_{XY}}{Q_X Q_Y} \frac{g_{e,i}}{Q_{e,i}} \exp \left[\frac{hc}{kT_e} (E_{e,dis}^i - E_{e,i}) \right] \quad (4.7)$$

where Q_{XY} , Q_X , and Q_Y are the total partition functions for the particular species. Although the influence of dissociation is found to be non-negligible for some cases in Section 4.7, the recombination process is found to be negligible for all cases. The net rate of excitation of level i due to this process may be written as

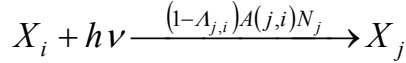
$$\left(\frac{\partial N_i}{\partial t} \right)_{elec-imp-dis} = K_e(d, i) N_X N_Y N_e - K_e(i, d) N_i N_e \quad \left(\frac{\text{particles}}{\text{cm}^3 \cdot \text{s}} \right) \quad (4.8)$$

V. Bound-Bound Radiative Transitions (Atomic Line Transitions):

The bound-bound radiative transitions are a result of the spontaneous emission of a photon, which is accompanied by a transition from an upper state j to a lower state i :



The rate of transition from level i to level j is written as product of the transition probability ($A(j,i)$) and the upper-state number density N_j . The reverse process to spontaneous emission is the process of photon absorption, which causes the excitation of an electron from the lower absorbing state to an upper state. This process is complicated because the absorption at a point is a function of the radiative intensity at that point, which is a function of the radiation emitted throughout the flowfield. As a result, this process is usually approximately treated using the escape factor concept, which assumes that the de-population of level i due to absorption is some fraction of the re-population of level i by emission. This fraction or escape factor, defined as $\Lambda_{j,i}$, may be interpreted as the fraction of radiation that escapes from a point. The radiation absorption process may therefore written symbolically as



If $\Lambda_{j,i}$ is set equal to unity, then all of the radiation escapes, meaning the gas is transparent and there is no re-population by absorption. Conversely, if $\Lambda_{j,i}$ is set equal to zero, then the re-population and de-population of a level i due to absorption and emission cancels out, which may be interpreted as no net “escaping” radiation. The net rate population of level i due to bound-bound radiative transitions may be written as

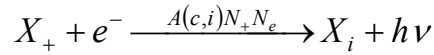
$$\left(\frac{\partial N_i}{\partial t} \right)_{rad-ex} = \sum_{j=i+1}^m \Lambda_{j,i} A(j,i) N_j - \sum_{j=1}^{i-1} \Lambda_{i,j} A(i,j) N_i \quad \left(\frac{\text{particles}}{\text{cm}^3 \cdot \text{s}} \right) \quad (4.9)$$

This excitation mechanism is equally important for molecules and atoms. For the atoms and molecules treated for air, the escape factors are set equal to one, which assumes that the gas is

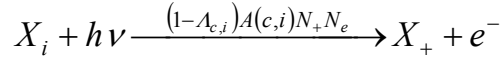
optically thin. This approximation is not consistent with the radiation transport calculation, which includes absorption. For the Titan shock-layers treated in Chapter 6, the escape factors were calculated in detail following Appendix G. This calculation was not practical for the air cases because of the number of molecular bands and atomic lines treated.

VI. Bound-Free Radiative Transitions:

The process of an electron and ion recombining to form a neutral species and emit a photon results in the population of level i of the neutral species. This process may be written symbolically as follows:



where the rate of population of level i is proportional to the recombination coefficient $A(c,i)$ and the ion and electron number densities. The reverse process of photoionization may be written as



The escape factor concept is used here as it was for the bound-bound transitions. The resulting rate of change of level i due to bound-free radiative transitions may be written as

$$\left(\frac{\partial N_i}{\partial t} \right)_{rad-ion} = A_{c,i} A(c,i) N_+ N_e \quad \left(\frac{\text{particles}}{\text{cm}^3 - \text{s}} \right) \quad (4.10)$$

This excitation mechanism is important in most cases only for atoms.

4.3 The Master Equation

As mentioned in the previous section, the Master Equation is the governing equation for the electronic state populations of atoms and molecules. This differential equation, which must be solved for every state of a radiating atom or molecule, equates the time-rate-of-change of a level's population with all of the populating and depopulating mechanisms discussed in the previous section. Therefore, from Eqs. (4.2, 4.3, 4.5, 4.8, 4.9, 4.10) the time-rate-of-change of the level i may be written as

$$\begin{aligned} \frac{\partial N_i}{\partial t} = & \left(\frac{\partial N_i}{\partial t} \right)_{elec-imp-ex} + \left(\frac{\partial N_i}{\partial t} \right)_{hp-imp-ex} + \left(\frac{\partial N_i}{\partial t} \right)_{elec-imp-ion} \\ & + \left(\frac{\partial N_i}{\partial t} \right)_{elec-imp-dis} + \left(\frac{\partial N_i}{\partial t} \right)_{rad-ex} + \left(\frac{\partial N_i}{\partial t} \right)_{rad-ion} \end{aligned} \quad (4.11)$$

or

$$\begin{aligned}
\frac{\partial N_i}{\partial t} = & \overbrace{\sum_{j=1}^m K_e(j,i)N_j N_e - \sum_{j=1}^m K_e(i,j)N_i N_e}^{elec-imp-ex} + \overbrace{\sum_{j=1}^m K_M(j,i)N_j N_M - \sum_{j=1}^m K_M(i,j)N_i N_M}^{hp-imp-ex} \\
& + \overbrace{K_e(c,i)N_+ N_e^2 - K_e(i,c)N_i N_e}^{elec-imp-ion} + \overbrace{K_e(d,i)N_X N_Y N_e - K_e(i,d)N_i N_e}^{elec-imp-dis} \\
& + \overbrace{\sum_{j=i+1}^m A_{j,i}A(j,i)N_j - \sum_{j=1}^{i-1} A_{i,j}A(i,j)N_i}^{rad-ex} + \overbrace{A_{c,i}A(c,i)N_+ N_e}^{rad-ion}
\end{aligned} \tag{4.12}$$

It will be convenient to replace $K_e(j,i)$, $K_e(c,i)$, and $K_e(d,i)$ in this equation with the detailed balancing relationships written in Eqs. (4.1), (4.4), and (4.6), respectively. Upon making these substitutions into Eq. (4.12) and dividing by N_e and N_i^{SB} , the following is obtained

$$\begin{aligned}
& \sum_{j=1}^{i-1} \left(K_e(i,j) + K_M(i,j) \frac{N_M}{N_e} \right) \rho_j \\
& - \left[\sum_{j=1}^m \left(K_e(i,j) + K_M(i,j) \frac{N_M}{N_e} \right) + K_e(i,c) + K_e(i,d) + \sum_{j=1}^{i-1} A_{i,j} \frac{A(i,j)}{N_e} \right] \rho_i \\
& + \sum_{j=i+1}^m \left(K_e(i,j) + K_M(i,j) \frac{N_M}{N_e} + A_{j,i}A(j,i) \frac{N_j^{SB}}{N_i^{SB} N_e} \right) \rho_j \\
& = \frac{1}{N_i^{SB} N_e} \frac{\partial N_i}{\partial t} - K_e(i,c) - K_e(i,d) \frac{N_i^{DE}}{N_i^{SB}} - A_{c,i}A(c,i) \frac{N_+}{N_i^{SB}}
\end{aligned} \tag{4.13}$$

where the population factor ρ_i is defined as

$$\rho_i = \frac{N_i}{N_i^{SB}} \tag{4.14}$$

Eq. (4.13) represents a set of m (which is defined as the number of electronic levels treated) differential equations for the m unknown ρ_i values. If it is assumed that $\partial N_i / \partial t$ is equal to zero, then this set of differential equations reduces to a set of linear algebraic equations for the ρ_i values. This is the quasi-steady state (QSS) assumption, which is known to be *invalid* for the low energy levels of atoms and molecules (Park [1984]). To accommodate this, the Master Equation may be solved using the QSS assumption for all of the levels above a specified minimum. The populations of the levels below this minimum value are then obtained by other means, as will be discussed in Section 4.4. Therefore, it is assumed that $\partial N_i / \partial t = 0$ for all energy levels above a given value of i , which will be labeled k . The solution of Eq. (4.13) may then be rewritten for all values of $i > k$ as follows

$$\begin{aligned}
& \sum_{j=k+1}^{i-1} \left(K_e(i, j) + K_M(i, j) \frac{N_M}{N_e} \right) \rho_j \\
& - \left[\sum_{j=1}^m \left(K_e(i, j) + K_M(i, j) \frac{N_M}{N_e} \right) + K_e(i, c) + K_e(i, d) + \sum_{j=1}^{i-1} A_{i,j} \frac{A(i, j)}{N_e} \right] \rho_i \\
& + \sum_{j=i+1}^m \left(K_e(i, j) + K_M(i, j) \frac{N_M}{N_e} + A_{j,i} A(j, i) \frac{N_j^{SB}}{N_i^{SB} N_e} \right) \rho_j \\
& = -K_e(i, c) - K_e(i, d) \frac{N_i^{DE}}{N_i^{SB}} - A_{c,i} A(c, i) \frac{N_+}{N_i^{SB}} - \sum_{j=1}^k \left(K_e(i, j) + K_M(i, j) \frac{N_M}{N_e} \right) \rho_j
\end{aligned} \tag{4.15}$$

Treating the values of ρ_i with $i \leq k$ as known, Eq. (4.15) can be written in matrix form as

$$[M] \bar{\rho}_{k+1,m} = \bar{P} + \bar{Q} \bar{\psi} + \sum_{j=1}^k \bar{R}_j \rho_j \tag{4.16}$$

where $\bar{\rho}_{k+1,m}$ is the vector of ρ_i values spanning $i = k+1$ to m and $\bar{\rho}_{1,k}$ spans the values from $i = 1$ to k . The terms in the vector $\bar{\psi}$ are defined as

$$\psi_i = \frac{N_i^{DE}}{N_i^{SB}} \tag{4.17}$$

The elements of these vectors and matrices are defined as

$$M(i, i) = - \left[\sum_{j=1}^m \left(K_e(i, j) + K_M(i, j) \frac{N_M}{N_e} \right) + K_e(i, c) + K_e(i, d) + \sum_{j=1}^{i-1} A_{i,j} \frac{A(i, j)}{N_e} \right] \tag{4.18}$$

$$\begin{aligned}
M(i, j) &= \left(K_e(i, j) + K_M(i, j) \frac{N_M}{N_e} + A_{j,i} A(j, i) \frac{N_j^{SB}}{N_i^{SB} N_e} \right) & j > i \\
M(i, j) &= \left(K_e(i, j) + K_M(i, j) \frac{N_M}{N_e} \right) & j < i
\end{aligned} \tag{4.19}$$

$$\bar{P}(i) = -K_e(i, c) - A_{c,i} A(c, i) \frac{N_+}{N_i^{SB}} \tag{4.20}$$

$$\bar{Q}_j(i) = -K_e(i, d) \tag{4.21}$$

$$\bar{R}_j(i) = - \left(K_e(i, j) + K_M(i, j) \frac{N_M}{N_e} \right) \quad 1 \leq j \leq k \tag{4.22}$$

It will be convenient to write the solution of Eq. (4.16) as follows

$$\bar{\rho}_{k+1,m} = \bar{r}_0 + \bar{r}_{00} \bar{\psi} + \sum_{j=1}^k \bar{r}_j \rho_j \tag{4.23}$$

where

$$\begin{aligned}\bar{r}_0 &= [M]^{-1} \bar{P} \\ \bar{r}_{00} &= [M]^{-1} \bar{Q} \\ \bar{r}_j &= [M]^{-1} \bar{R}_j\end{aligned}\quad (4.24)$$

With k set equal to one and $\bar{r}_{00} = 0$, Eq. (4.23) is equivalent to Eq. (20) presented by Bates et al. [1962]. Note that Eqs. (4.18 – 4.22) are functions of the following flowfield variables: N_X , N_Y , N_M , N_e , T_t and T_e (the T_e dependence is implied through the rate coefficients for the electron-impact processes and T_t for the heavy-particle processes). Although N_+ , N_i^{SB} , and N_i^{DE} appear in these equations, they may be reduced to a N_e , N_X , N_Y , T_b and T_e dependence using the Saha-Boltzmann equation (Eq. (1.1)) and Eq. (4.7). For atomic species, it is well known that the heavy-particle impact excitation does not contribute significantly, and since the dissociation processes are not considered for atoms, then Eqs. (4.18 – 4.22) are functions of only N_e and T_e . For molecular species, it will be shown that for the lunar-return shock layers of present interest, the heavy particle excitation and electron-impact recombination processes may be ignored. This results in Eqs. (4.18 – 4.22) also being a function of only N_e and T_e . The significance of these dependencies is that they result in the \bar{r}_0 and \bar{r}_j vectors (defined in Eq. (4.24)) being functions of only N_e and T_e , which means that they may be conveniently compiled in tables or curve fits in terms of these two variables. Thus, the costly matrix inversion required to calculate these vectors, shown in Eq. (4.24), may be avoided. This was recognized by Bates and Kingston [1963], who present tables of \bar{r}_0 and \bar{r}_1 for hydrogen plasmas with $0 \leq N_e \leq \infty$, $250 \leq T_e \leq 64000$, and $A_{j,i} = 0$ (optically thick) and 1 (optically thin). The present curve-fits developed for the atoms and molecules will be discussed in Sections 4.6 and 4.7, respectively.

4.4 A Simple Method of Calculating ρ_I (with $k = 1$)

The previous section presented a method of calculating the ρ_i values for energy levels above a specified level (k) by making the quasi-steady state approximation ($\partial N_i / \partial t = 0$). Equation (4.23) shows that these values can be represented as a linear combination of the ρ_i values for energy levels less than or equal to k . This section discusses a method of setting $k = 1$ and calculating ρ_I using the following equation

$$\sum_{j=1}^m N_j = N_a \quad (4.25)$$

which forces the sum of the individual state populations to equal the total number density of the species obtained from the flowfield. This approach, which was introduced by Park [1979], is used

in NEQAIR's QSS subroutine (Park [1984, 1985], Whiting [1996]). The reason for using Eq. (4.25) to obtain ρ_l is that it introduces a valid equation to replace Eq. (4.15), which as stated previously, is invalid for the ground state. The drawback to this approach is that no information is introduced regarding the rate-of-change of the species number densities through the shock-layer. Another drawback is that for nitrogen and oxygen, the 2nd and 3rd energy levels have relatively low energy values (they are often referred to as equivalent ground states), which means they are closely coupled with the ground level (see pp. 93 of Park [1990]). Thus, the assumption that the quasi-steady approach is invalid for the ground level should also apply to these levels. A study of the effects of these drawbacks has not been reported in the literature. It was found in the present study that setting $k = 3$ and assuming that the 2nd and 3rd levels were in a Boltzmann distribution with the 1st level resulted in essentially the same answer as setting $k = 1$, which is the approach discussed in this section.

The equations required for the application of this method will now be derived. Rewriting Eq. (4.25) in terms of ρ_i and separating ρ_l from the summation results in

$$\rho_1 \chi_1 + \sum_{j=2}^m \rho_j \chi_j = 1 \quad (4.26)$$

where χ_i is defined as

$$\chi_i = \frac{N_i^{SB}}{N_a} \quad (4.27)$$

Substituting Eq. (4.23) with $k = 1$ into this expression and solving for ρ_l results in the following

$$\rho_l = \frac{1 - \sum_{j=2}^m [\bar{r}_0(j) + \bar{r}_{00}(j)\bar{\nu}(j)]\chi_j}{\chi_1 + \sum_{j=2}^m \bar{r}_1(j)\chi_j} \quad (4.28)$$

In summary, the solution procedure for this approach involves the following:

- 1) Obtain the \bar{r}_0 , \bar{r}_{00} , and \bar{r}_1 vectors either by solving Eqs. (4.24) or from a previously prepared table or curve fit (recall that \bar{r}_0 and \bar{r}_1 contain m terms).
- 2) Calculate ρ_l from Eq. (4.28)
- 3) Calculate the ρ_i values from Eq. (4.23), which is written for this case as

$$\rho_i = \bar{r}_0(i) + \bar{r}_{00}(i)\bar{\nu}(i) + \bar{r}_1(i)\rho_l \quad (4.29)$$

As mentioned previously, the method outlined here is equivalent to that used by Park in the QSS subroutine of NEQAIR, although in the present case the equations have been formulated in terms of the \bar{r}_0 , \bar{r}_{00} , and \bar{r}_1 vectors.

4.5 Non-Boltzmann Modeling of N and O

This section presents rate models, specifically for atomic nitrogen and oxygen, for the significant excitation processes discussed in Section 4.2. The various rates were collected from all available experimental and theoretical published sources, compared, and a “best” value chosen. For some processes, no rates were available in the literature, and so approximate formulas were applied. The majority of the effort in constructing this model was obtaining electron-impact excitation rates for transitions between all of the levels of N and O. This effort will therefore receive the majority of the following discussion regarding the various excitation processes.

I. Electron-Impact Excitation:

The process of electron impact excitation was discussed in general in Section 4.2. The fact that there are electron-impact excitation processes between each atomic level results in a large number of rates being required. For the present study, the 35 levels for N and 32 levels for O listed in Tables 3.1 and 3.2 imply that there are 595 and 496 rates required for each species, respectively. Consequently, collecting this complete set of rates is a difficult and tedious task. The difficulty is compounded by the fact that there are a limited number of detailed calculations and experimental studies for N and O, which are furthermore limited to a relatively small number of transitions. Thus, extensive use of approximate analytic formulas is required to complete the set of rates for each species. These approximate formulas are discussed in the following paragraph, followed by a discussion of the available detailed rates for both N and O.

One of the simplest of the approximate formulas was presented by Van Regmoter [1962] and is valid for optically allowed transitions. This formula is written as follows

$$K_e(i,j) = \frac{g_{i'}}{g_i} \sum_{i',j'} \frac{2\pi^{1/2}}{ca_0^2} \left(\frac{hcE_1^H}{kT_e} \right)^{1/2} \frac{1.16 \times 10^4 g_{i'} f_{i'j'} P(y) \exp(-y)}{\Delta E_{i'j'}} \quad (cm^3 s^{-1}) \quad (4.30)$$

where $E_1^H = 109,697 \text{ cm}^{-1}$ is the ionization potential of the hydrogen atom, $y = hc\Delta E_{i'j'}/kT_e$, $\Delta E_{i'j'} = E_{j'} - E_{i'} (\text{cm}^{-1})$ and $P(y)$ is a function originally tabulated by Van Regmoter and later fitted by Kastner and Bhatia [1997] with the following expression

$$\begin{aligned}\log_{10} P(y) = & -0.94492 - 0.66652(\log_{10} y) - 0.047591(\log_{10} y)^2 \\ & + 0.024394(\log_{10} y)^3 + 0.0037309(\log_{10} y)^4\end{aligned}\quad (4.30b)$$

The summation in Eq. (4.30) is over all of the i' and j' individual levels present in the i and j grouped levels. Park [1973] suggests an approximate treatment for *forbidden* transitions that satisfy all of the allowed transition requirements *except* that $\Delta S = \pm 1$ instead of zero. For forbidden transitions that satisfy this requirement, Park [1973] suggests that K_e may be approximated as 2/5 of the rate for the corresponding allowed transition. This has been found to be the most accurate approximation for forbidden transitions between the lower levels ($i,j < 10$). Unfortunately, this approximation may only be applied to a limited number of forbidden transitions because a corresponding allowed transition is required. For a general optically forbidden transition, Allen's formula (Allen [1962]) may be applied:

$$K_e(i, j) = 5.465 \times 10^{-11} T_e^{1/2} \frac{1}{g_i} \left(\frac{E_1^H}{\Delta E_{ij}} \right) y [\exp(-y) - y \bar{E}_1(y)] \quad (cm^3 s^{-1}) \quad (4.31)$$

where $\bar{E}_1(y)$ is an exponential integral. A more involved approximation that is equally valid for allowed and forbidden transitions was presented by Gryzinski [1959]. This approach requires the calculation of the following cross sections as a function of the electron energy (E):

$$\sigma_{ij}(E) = \frac{4.2484 \times 10^{-6}}{\Delta E_{ij}^2} \left(\frac{E}{E_{ionize} - E_i + E} \right)^{3/2} \left\{ \frac{2}{3} \left[\frac{E_{ionize} - E_i}{E} + \frac{\Delta E_{ij}}{E} \left(1 - \frac{E_{ionize} - E_i}{E} \right) - \left(\frac{\Delta E_{ij}}{E} \right)^2 \right] \right\} \quad (4.32)$$

for $\Delta E_{ij} + E_{ionize} - E_i \leq E$

$$\begin{aligned}\sigma_{ij}(E) = & \frac{4.2484 \times 10^{-6}}{\Delta E_{ij}^2} \left(\frac{E}{E_{ionize} - E_i + E} \right)^{3/2} \left\{ \frac{2}{3} \left[\frac{E_{ionize} - E_i}{E} + \frac{\Delta E_{ij}}{E} \left(1 - \frac{E_{ionize} - E_i}{E} \right) - \left(\frac{\Delta E_{ij}}{E} \right)^2 \right] \right. \\ & \left. \times \left[\left(1 + \frac{\Delta E_{ij}}{E_{ionize} - E_i} \right) \left(1 - \frac{\Delta E_{ij}}{E} \right) \right]^{1/2} \right\} \quad (4.33)\end{aligned}$$

for $\Delta E_{ij} + E_{ionize} - E_i \geq E$

The Gryzinski rate is then obtained by numerical integrating the cross sections as follows

$$K_e(i, j) = \frac{8\pi}{m^{1/2}} \left(\frac{1}{2\pi n k T_e} \right)^{3/2} \left[\int_{\Delta E_{ij}}^{\infty} \sigma_{ij}(E) \exp\left(-\frac{hc}{kT_e} E\right) EdE + \int_{\Delta E_{i(j+1)}}^{\infty} \sigma_{i(j+1)}(E) \exp\left(-\frac{hc}{kT_e} E\right) EdE \right] \quad (4.34)$$

A summary of the above approximate formulas for the electron-impact cross sections are presented in Table 4.1. Although these approximate formulas are relatively old, a review of recent astrophysics (Przybilla et al. [2000], Bhatia and Kastner [1995], Kastner and Bhatia [1997], Fisher et al. [1996], Lemke and Venn [1996]) and plasma physics (Bourdon and Vervisch [1996 and 1998]) literature reveals that in the absence of experimental data or detailed calculations,

these approximate formulas are the best available alternative. One method that has been used frequently (Park [1971], Kunc and Soon [1989], Soon and Kunc [1990]) and was not mentioned here is the method of Sobelman and Vainshtein [1968 and 1981]. This method is complicated because the original reference (Sobelman and Vainshtein [1968]) is in Russian. Although it is explained somewhat in Sobelman and Vainshtein [1981], the necessary procedure for forbidden transitions is not clear. Comparison of the results obtained by the methods in Table 4.1 with Soon and Kunc's [1990] results for oxygen show that the method is not a drastic improvement.

Table 4.1. Summary of Approximate Equations for Electron Impact Excitation Rates

	Name	Transition Type	Equation	Reference
1	Van Regmoter	allowed	(4.30)	Van Regmoter [1962]
2	Park approx.	forbidden	(4.30) times 0.4	Park [1973]
3	Gryzinski	any	(4.32) – (4.34)	Gryzinski [1959]
4	Allen	forbidden	(4.31)	Allen [1962]

a) Choice of Electron-Impact Excitation Rates for Atomic Nitrogen

This sub-section compares the electron-impact excitation rates proposed by various researchers for atomic nitrogen. This comparison is aimed at determining the best available rate for each transition, as well as confirming the validity of the approximate formulas for transitions with no detailed rates available. The detailed rate or approximate formula chosen for each transition is presented at the conclusion of this sub-section.

The two main sources of detailed quantum mechanical calculations for nitrogen are the recent works by Frost [1998] and Tayal [2000]. Frost [1998] presents tabulated values for the transition rates from the lowest three levels ($i = 1, 2, 3$) to the first 21 levels. These rates were obtained using an R-matrix approach and were shown to match available experimental data. Tayal [2000] presents tabulated values for the transition rates from the lowest three levels ($i = 1, 2, 3$) to the first 12 levels. An R-matrix approach was also used in this study, although comparisons with experimental results or other calculations were not made. Figures 4.1(a–e) compare the calculations of Frost and Tayal with the approximate formulas summarized in Table 4.1. Figure 4.1(a) shows that for the 1–5 forbidden transition, the results of Frost and Tayal differ by an order of magnitude, while the approximate expressions are all similar and fall between Frost's and Tayal's results. Figure 4.1(b) shows that for transitions between higher levels (3–20), Allen's approximate formula provides values nearest the values predicted by Frost. Note that Tayal did not present a value for this transition or for the 1–20 transition presented in Figure 4.1(c). Figure 4.1(c) shows that for the allowed 1–20 transition the Van Regmoter and Gryzinski methods produce results that are nearly identical, but significantly lower, than the values predicted by

Frost. Similarly, Figure 4.1(d) shows that again the Van Regmorter and Gryzinski methods produce nearly identical results, although the values of Tayal and Frost disagree with each other. The Park [1990] values in this figure refer to the rates presented in Table 2.1 of Park [1990], though, only transitions between the first five levels can be compared with Park [1990] because of the difference in the atomic level grouping. The significant difference between Park's value and the other detailed studies is surprising, and difficult to explain because Park does not indicate how his values were obtained. Note that the Park [1990] value for the 1-5 transition is not presented in Figure 4.1(a) because it is essentially zero.

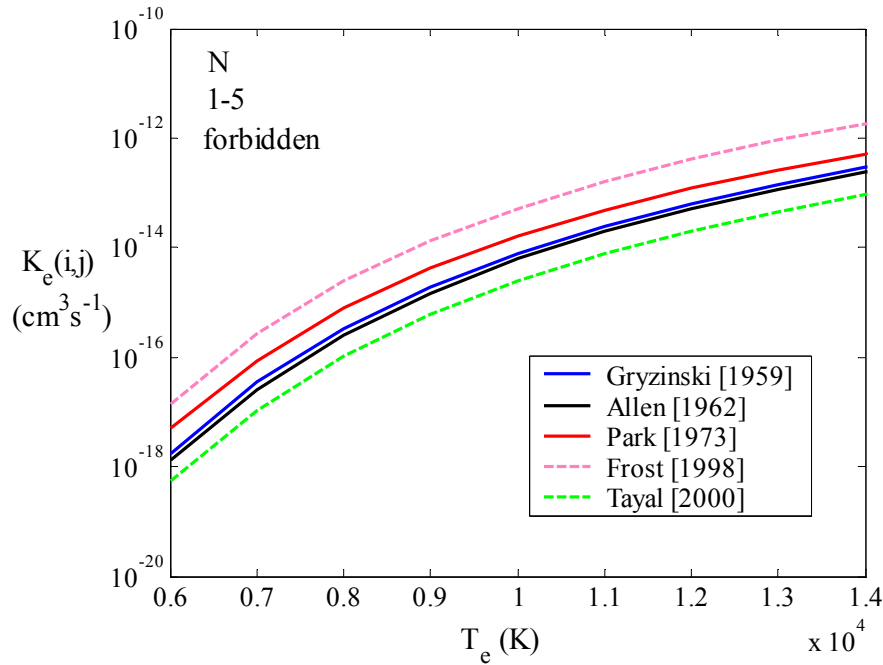


Figure 4.1(a). Comparison of the various approximate electron-impact excitation cross sections with detailed calculations. The two numbers in the top left hand corner refer to the transition $i - j$ with the levels defined in Table 3.1.

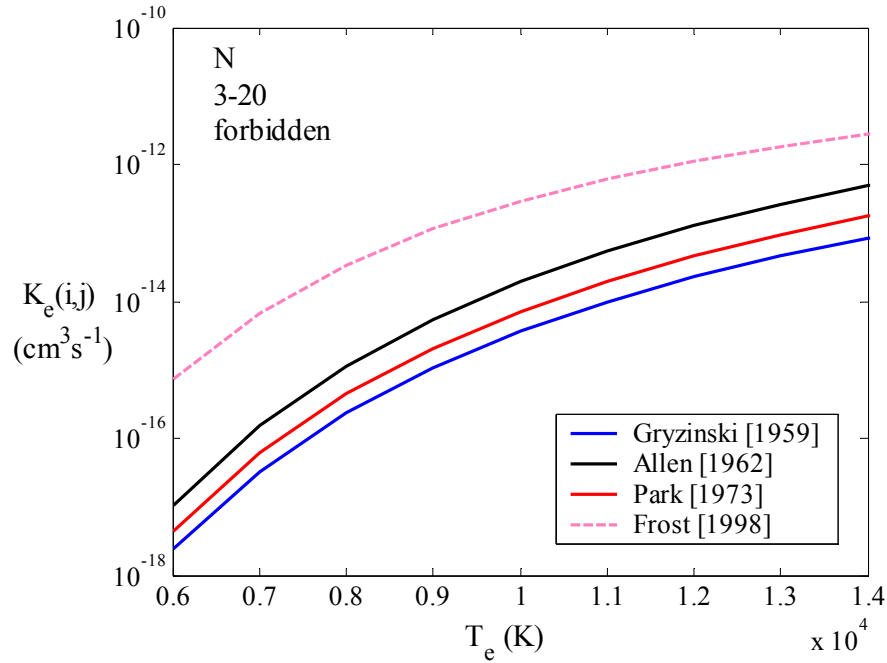


Figure 4.1(b). Comparison of the various approximate electron-impact excitation cross sections with detailed calculations. The two numbers in the top left hand corner refer to the transition $i - j$ with the levels defined in Table 3.1.

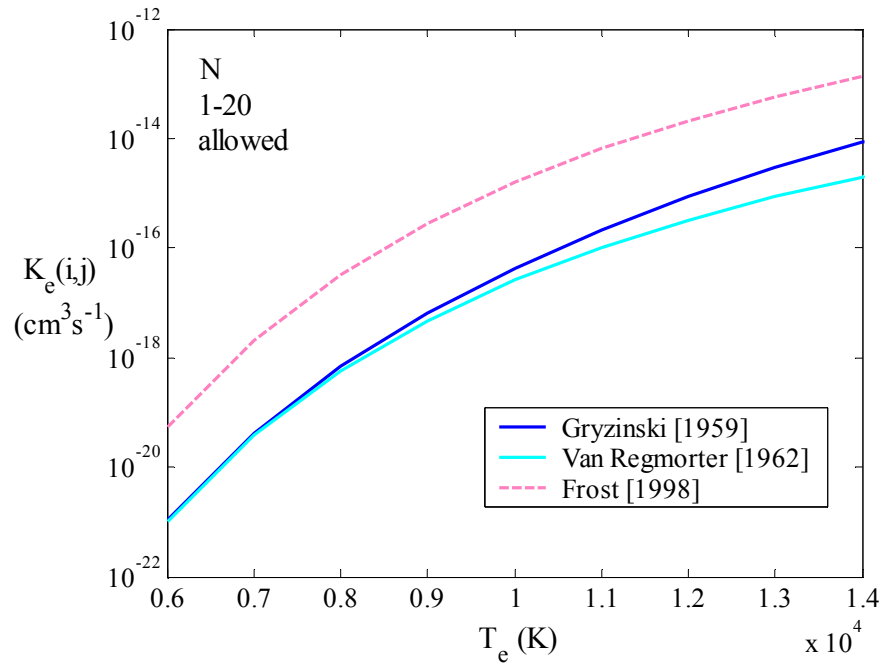


Figure 4.1(c). Comparison of the various approximate electron-impact excitation cross sections with detailed calculations. The two numbers in the top left hand corner refer to the transition $i - j$ with the levels defined in Table 3.1.

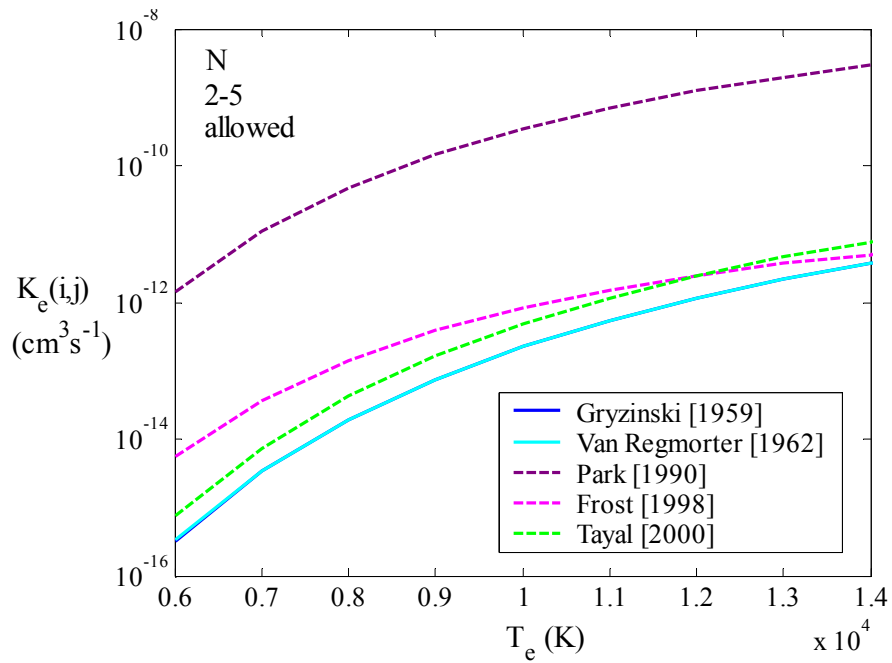
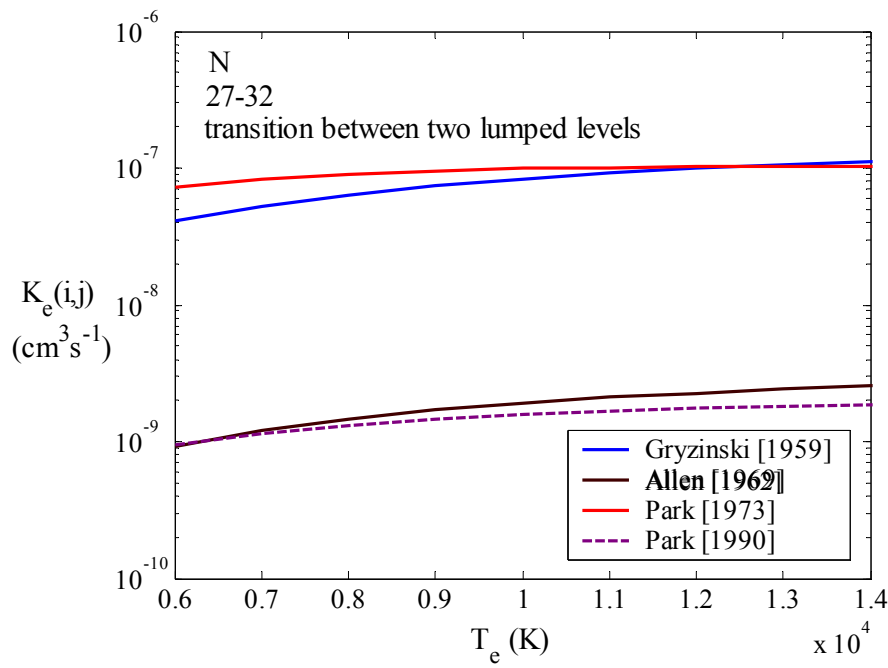


Figure 4.1(d). Comparison of the various approximate electron-impact excitation cross sections with detailed calculations. The two numbers in the top left hand corner refer to the transition $i - j$ with the levels defined in Table 3.1.



Figures 4.1(e). Comparisons of the various approximate electron-impact excitation cross sections with detailed calculations. The two numbers in the top left hand corner refer to the transition $i - j$ with the levels defined in Table 3.1.

From the above comparison, along with the study of many transitions not discussed above, it was concluded that Van Regmoter's expression is the best available approximate expression for *allowed* transitions where the upper level of the transition is less than $j = 22$. Similarly, Allen's formula was concluded to be the best for *forbidden* transitions with j less than 22. For transitions with j greater than 22, Gryzinski's formula is accurate because of the hydrogenic nature of these upper levels, and was therefore applied. A summary of these chosen rate sources for the final nitrogen model is presented in Table 4.2. Note that Frost's detailed calculation values were used for all the transitions considered in that study. These were chosen instead of Tayal's values because Frost considered more transitions, including all of those considered by Tayal.

Table 4.2. Selection of Electron-Impact Excitation Rates for Nitrogen

-
- 1) Frost's rates are used for $i = 1, 2, 3$ and $j = 2$ through 21
 - 2) Remaining *allowed* transitions with $j < 22$ use Van Regmoter's formula
 - 3) Remaining *forbidden* transitions with $j < 22$ use Allen's formula
 - 4) All remaining transitions use Gryzinski's formula
-

b) Choice of Electron-Impact Excitation Rates for Atomic Oxygen

The main sources of detailed electron-impact excitation rates for atomic oxygen are the studies by Laher and Gilmore [1990], Bhatia and Kastner [1995], and Zatsarinny and Tayal [2003]. Laher and Gilmore [1990] obtained rates for transitions from the ground state to the first 19 excited states by reviewing past experimental data and by using a correlation presented by Jackman et al. [1977]. Bhatia and Kastner [1995] used a distorted-wave calculation to obtain rates for most of the transitions between the lowest ten states. Some of the rates presented by Bhatia and Kastner were taken from Laher and Gilmore, although they were not specified. Zatsarinny and Tayal [2003] calculated values for transitions from the lowest 3 states to the first 21 excited states using an R-matrix approach (with many values missing for transitions from the second and third state). Figures 4.2(a-e) compare the rates proposed by these researchers with the approximate equations summarized in Table 4.1. A good agreement is shown for the 1–5 transition in Figure 4.2(a), except for the value given by Park [1990], which is significantly larger. Because Park does not specify the source of his rates, it is difficult to explain this discrepancy. The comparison in Figure 4.2(b) for the 1–10 forbidden transition shows a moderate agreement between the various methods. Note that the Laher and Gilmore result is about an order of magnitude lower than the Zatsarinny and Tayal result. For transitions from the second and third levels, Figures 4.2(c–e) show that Zatsarinny and Tayal's and Bhatia and Kastner's results are many orders of magnitudes less than the other methods. In 4.2(c), the Bhatia and Kastner result is significantly lower than the Zatsarinny and Tayal result. It is difficult to explain the large disagreement between the various

values for this rate, so it will be assumed that the Zatsarinny and Tayal value is the most accurate because it is the most recent. The values labeled Gordillo and Kunc in these figures are from a paper by Gordillo and Kunc [1995]. Note that the set of rates presented by Park [1990] has values of zero for the rates considered in Figures 4.2 (c and e). Table 4.3 lists the sources of the rates chosen for the final model. The statement “where available” in this table means that there were missing values in the range of transitions of interest.

Table 4.3. Selection of Electron-Impact Excitation Rates for Oxygen

-
- 1) Zatsarinny and Tayal rates are used for $i = 1, 2, 3$ and $j = 2$ through 21 where available
 - 2) Bhatia and Kastner for remaining rates with $j < 10$ where available
 - 3) Gordillo and Kunc for remaining rates with $j < 7$
 - 4) Remaining *allowed* transitions with $j < 22$ use Van Regmorter’s formula where available
 - 5) Remaining *forbidden* transitions with $j < 22$ use Allen’s formula
 - 6) All remaining transitions use Gryzinski’s formula
-

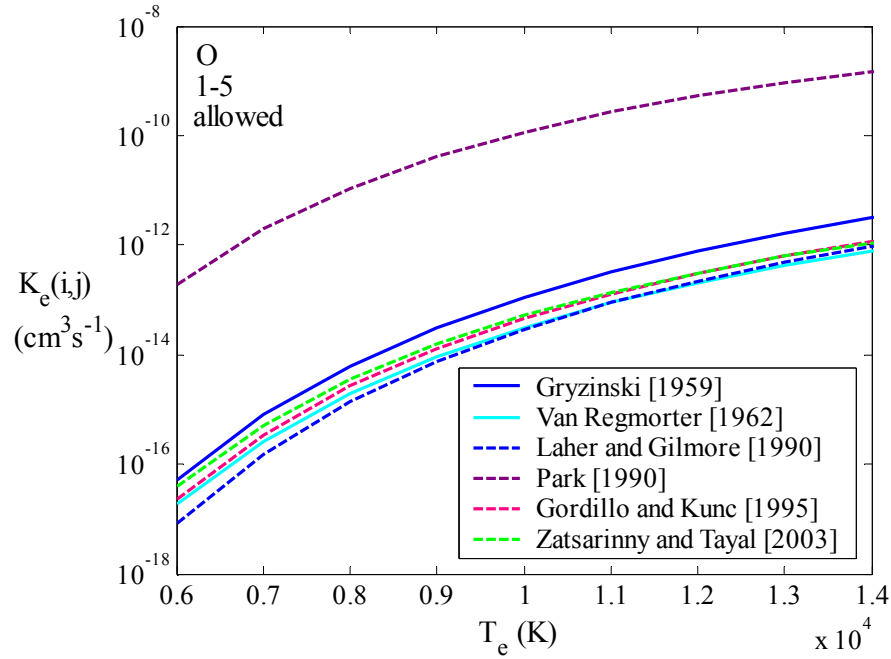


Figure 4.2(a). Comparison of the various approximate electron-impact excitation cross sections with detailed calculations. The two numbers in the top left hand corner refer to the transition $i - j$ with the levels defined in Table 3.2.

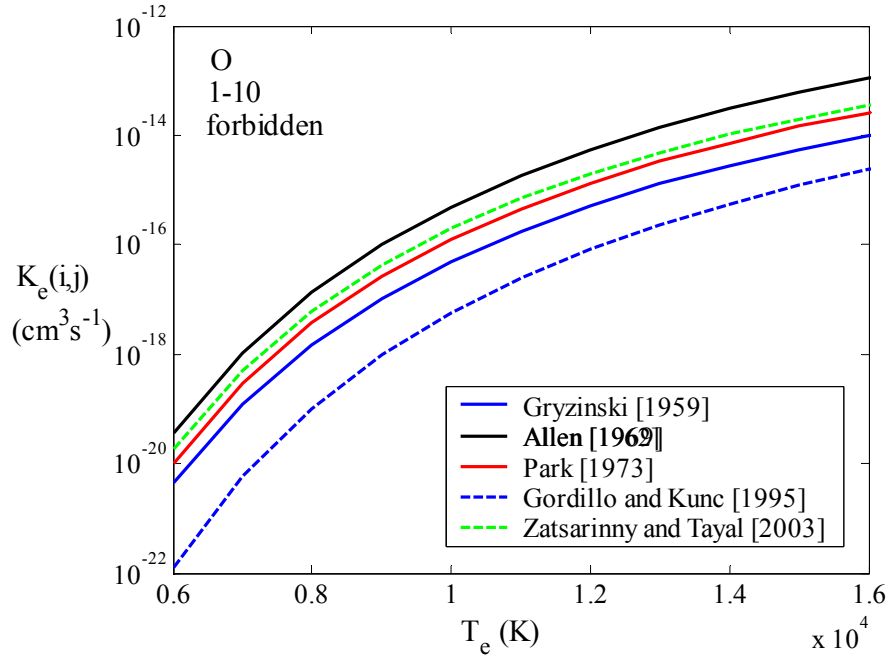


Figure 4.2(b). Comparison of the various approximate electron-impact excitation cross sections with detailed calculations. The two numbers in the top left hand corner refer to the transition $i - j$ with the levels defined in Table 3.2.

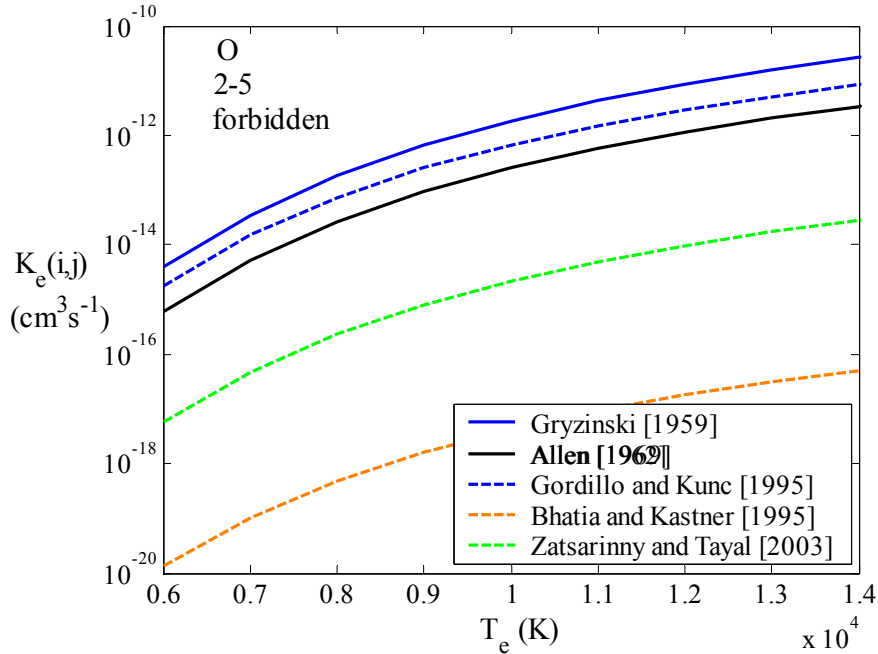


Figure 4.2(c). Comparison of the various approximate electron-impact excitation cross sections with detailed calculations. The two numbers in the top left hand corner refer to the transition $i - j$ with the levels defined in Table 3.2.

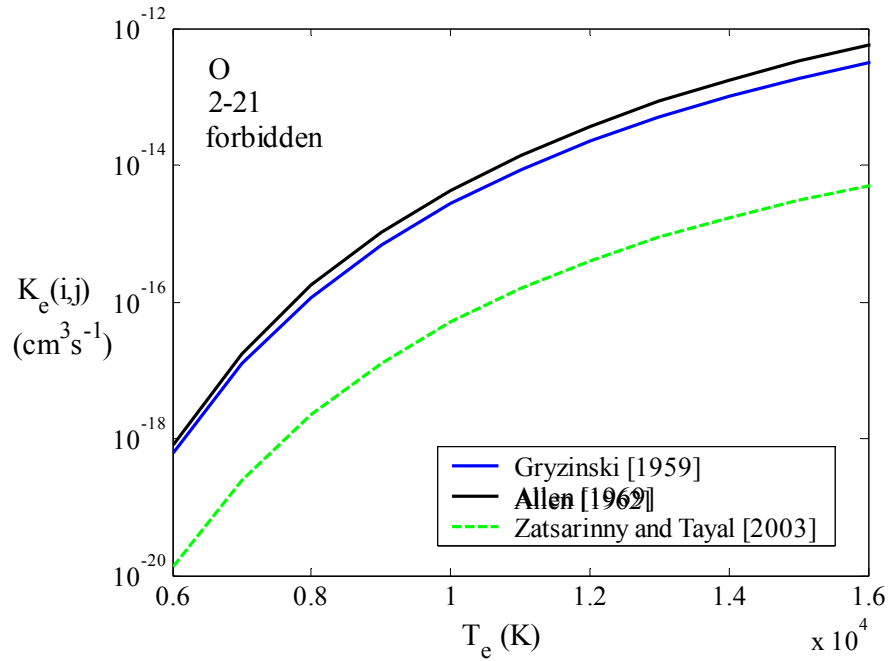


Figure 4.2(d). Comparison of the various approximate electron-impact excitation cross sections with detailed calculations.

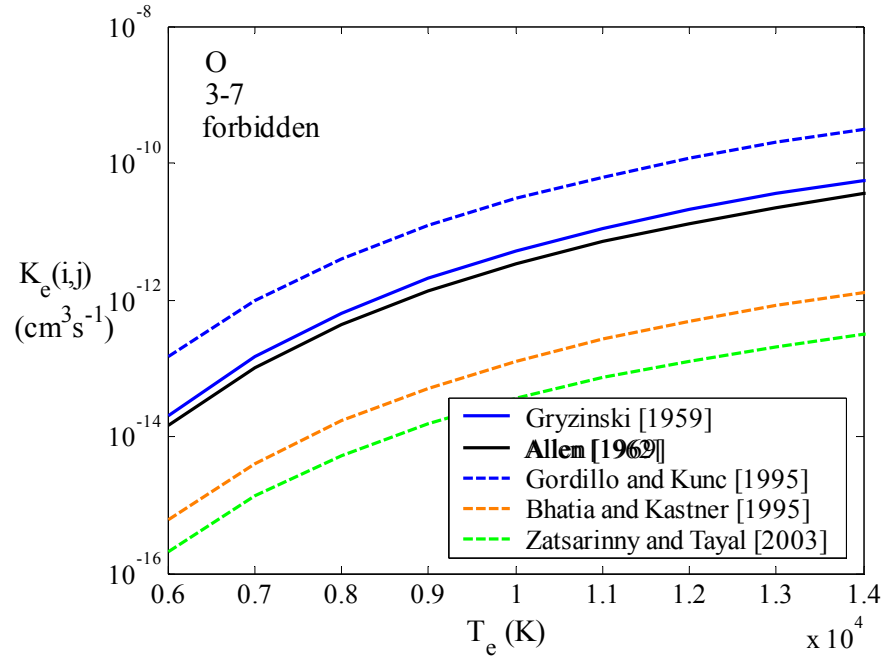


Figure 4.2(e). Comparison of the various approximate electron-impact excitation cross sections with detailed calculations.

II. Electron-Impact Ionization:

The process of electron impact ionization was discussed in general in Section 4.2. This process is of less importance than electron-impact excitation and bound-bound radiative transitions, and

therefore it does not need to be treated as precisely. Also, only one rate is required for each level so that significantly fewer rates are required than the bound-bound processes.

The rate coefficients for electron-impact ionization from excited levels may be calculated accurately with the following formula proposed by Drawin [1968]

$$K(i,c) = 1.46 \times 10^{-10} T_e^{1/2} \left(\frac{E_i^H}{E_{ionize} - E_i} \right)^2 \xi y \psi_1(y) \quad (cm^3 s^{-1}) \quad (4.35)$$

where ξ is the number of equivalent electrons ($\xi = 3$ for the ground state of atomic nitrogen and oxygen and $\xi = 1$ for all excited states) and y is the reduced energy of the incoming electrons, $y = (E_{ionize} - E_i)hc/kT_e$. The function ψ_1 is approximated by the following equation

$$\psi_1(y) = \frac{\exp(-y)}{1+y} \left\{ \frac{1}{20+y} + \ln \left[1.25 \left(1 + \frac{1}{y} \right) \right] \right\} \quad (4.36)$$

For ionization from the lowest two states of oxygen and nitrogen, the rate coefficients proposed by Kunc and Soon [1989] and Soon and Kunc [1990] were used.

III. Bound-Bound Radiative Transitions (Atomic Line Transitions)

The influence of bound-bound radiative transitions on the Master Equation was discussed in Section 4.2. This process was also discussed in Section 3.3, as it related to the spectral modeling of atomic line radiation. The set of atomic lines for nitrogen and oxygen chosen from the NIST database in Chapter 3 are also applied in the present Master Equation model. This data is presented in Appendix A. In general, the transition probabilities are related to the oscillator strengths as follows

$$A(j,i) = \frac{8\pi^2 e^2}{mc^3} \sum_{i',j'} \frac{g_{i'}}{g_{j'}} (w_{CL} c)^2 f_{i'j'} \left[\frac{g_{j'}}{g_j} \exp \left(-\frac{hc}{kT_e} (E_{j'} - E_j) \right) \right] \quad (s^{-1}) \quad (4.37)$$

where the term in brackets accounts for grouped levels, as discussed in Section 3.2. The summation in this equation is over all of the i' and j' individual levels present in the i and j grouped levels. Only optically allowed radiative transitions are considered in the present study. Although Kunc and Soon [1989] and Soon and Kunc [1990] considered various forbidden transitions, they note that their influence is small, especially the relatively large electron number densities present in the hypersonic shock-layers of interest in this study.

IV. Bound-Free Radiative Transitions:

The bound-free radiative transitions, introduced in Section 4.2, are of minor importance for most cases. The approximate expression presented by Drawin [1968], based on the hydrogenic model for the bound-free cross sections, is applied in this study. This is written as follows:

$$A(c,i) = 5.20 \times 10^{-14} Z u_i^{3/2} G_i i^{-3} \bar{K}(u_i) \exp(u_i) \quad (cm^3 s^{-1}) \quad (4.38)$$

where the exponential integral is defined as

$$\bar{K}(u_i) = \int_{t=u_i}^{\infty} \frac{\exp(-t)}{t} dt \quad (4.39)$$

The detailed bound-free cross-section obtained from the TOPbase, which are presented in Chapter 3, could be applied for a more detailed calculation, although this has a negligible influence on the results.

4.6 The Approximate Atomic CR (AACR) Model

Using the detailed CR model described in the previous section as a baseline, an approximate atomic CR (AACR) model was developed, which is significantly simpler to apply than the detailed CR model and is nearly as accurate at predicting the resulting nonequilibrium radiative emission. The details of this method will be presented in the present section and its results compared with the detailed CR model for some relevant shock-layer conditions. Comparisons will also be made to Gally's [1992] 1st order LTNE method, which is the approximate method discussed previously in Section 1.3. Recall that the Gally's method assumed that the three lowest levels were in a Boltzmann distribution with the ground state (Eq. (1.2)) and the upper levels were in a Saha-Boltzmann distribution (Eq. (1.1)).

The approximate atomic CR (AACR) model developed in this study contains the following three main approximations: 1) the \vec{r}_0 and \vec{r}_1 vectors defined in Eq. (4.24) are modeled as single curve fits over a wide range of T_e and N_e values, 2) closely spaced atomic states are assumed to be in a Boltzmann distribution with each other, 3) the three lowest atomic states are assumed populated by a Boltzmann distribution. The only approximate aspect of the first of these approximations is that a single curve fit over a range of T_e and N_e values deviates slightly from the actual data that was curve-fitted. The dependence of \vec{r}_0 and \vec{r}_1 on only T_e and N_e was pointed out in Section 4.3, and is therefore *not* an approximation. The second approximation listed above is apparent from Figure 1.1, which shows groups of closely spaced levels with nearly the same slope (among the levels in the group) as the Boltzmann and Saha-Boltzmann curves. With this assumption, once the

population of a single level in each of these groups is known, then the population of the other levels in the group may be calculated with the following equation

$$N_{i'} = N_i \frac{g_{i'}}{g_i} \exp\left[-\frac{hc}{kT_e}(E_{i'} - E_i)\right] \quad (4.40)$$

where the un-primed values indicate the level whose number density is known. Table 4.4 presents the grouping of levels for N and O, defined in terms of the level model presented in Chapter 3, chosen here for the AACR model. The level in each group whose \bar{r}_0 and \bar{r}_1 values were curve-fit are also listed in this table. These curve-fits, which are presented in Appendix C, were created from the detailed model discussed in the previous section for the following range of conditions: $7,000 < T_e < 14,000$ K and $1 \times 10^{14} < N_e < 1 \times 10^{16}$ particles/cm³. The third assumption that the first three levels are populated by Boltzmann distribution, which can be shown to be a good approximation for all the conditions of interest in the present study, allows the number densities of the curve-fit level for each group to be written in terms of Eqs. (4.14) and (4.29). The procedure for applying the AACR method is as follows:

- 1) Calculate the r_0 and r_1 values for each of the groups listed in Table 4.4 (except the first group) from the curve fits presented in Appendix C. These r_0 and r_1 values belong specifically to the levels listed in the column “*Curve-Fit Level for the Group...*”.
- 2) Calculate the number densities for the levels in the first group listed in Table 4.4 assuming a Boltzmann distribution (Eq. 1.2).
- 3) Calculate the number densities of each curve-fit level using the r_0 and r_1 values calculated in Step 1, the ground state number density from Step 2, and Eqs. (4.14) and (4.29).
- 4) Calculate the number densities for the other levels in each group using Eq. (4.40) and the number densities calculated in Step 3.

Table 4.4. Level Groupings for the AACR Model

<i>Group #</i>	<i>Range of Levels for N from Table 3.1</i>	<i>Curve-Fit Level for the Group for N</i>	<i>Range of Levels for O from Table 3.2</i>	<i>Curve-Fit Level for the Group for O</i>
1	1 – 3	-	1 – 3	-
2	4 – 6	5	4 – 7	5
3	7 – 13	10	8 – 13	10
4	14 – 21	17	14 – 21	17
5	22 – 27	24	22 – 27	24
6	28 – 35	28	28 – 35	28

To examine the accuracy of the proposed AACR model relative to the detailed atomic CR model and the approximate model proposed by Gally, the radiation for the Fire II 1634 second was

calculated using each model and the uncoupled LAURA stagnation-line flowfield presented in Chapter 2. The total wall-directed radiative flux resulting from each model is presented in Figure 4.3. Also presented is a case where the atoms were assumed to be populated in a Boltzmann distribution. The molecular species are treated in each case using the non-Boltzmann model presented later in this chapter. This figure illustrates the significant result that three CR models predict very similar radiative flux values throughout the shock layer, with the AACR and Gally Model within 2% and 5% of the detailed CR model, respectively. Although the AACR model produces better agreement with the detailed CR model than the Gally model, it should be noted that the Gally model is significantly simpler conceptually and in application. The importance of applying a non-Boltzmann model, rather than assuming a Boltzmann distribution, is clearly shown in this figure with the nearly 100% over prediction of the Boltzmann case relative to the various CR model cases. The excessive radiation from the Boltzmann model originates entirely from the region thermochemical nonequilibrium directly behind the shock. The three CR model cases, on the other hand, show that this region contributes only slightly to the radiative flux. The reason for this will be discussed in the next paragraph.

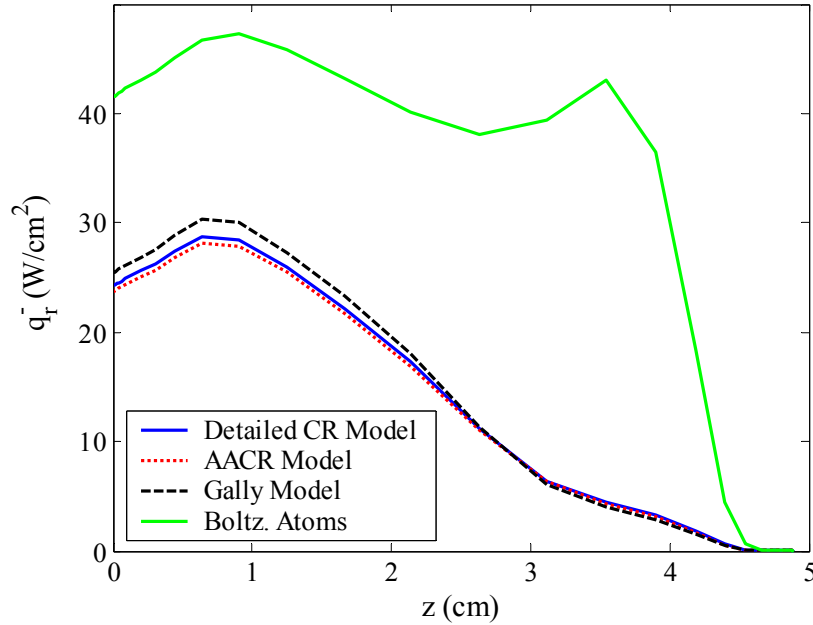


Figure 4.3. Influence of the various atomic CR models on the total wall-directed radiative flux for the Fire 1634 s case, the molecules are treated in all cases with the non-Boltzmann model presented later in this Chapter.

The good agreement between the radiative flux predicted by the two approximate models with that predicted by the detailed CR model was noted in the previous paragraph for the Fire 1634 s case. To investigate this comparison further, two points in the shock layer were studied in detail:

a nearly thermochemical equilibrium point at $z = 2$ cm and a nonequilibrium point near the shock at $z = 4$ cm. The temperature and relevant number densities for these points are presented in Table 4.5.

Table 4.5. Conditions for two points in the Fire 1634 s shock-layer

	$z = 2\text{ cm}$	$z = 4\text{ cm}$
T_e (K)	10,467	12,670
T_t (K)	10,459	19,186
number densities (#/cm ³)		
N	1.74×10^{16}	1.2×10^{16}
N ⁺	3.90×10^{15}	3.5×10^{14}
e ⁻	4.55×10^{15}	4.7×10^{14}

For the nonequilibrium point at $z = 4$ cm, Figure 4.4 compares the number densities, divided by the degeneracy, of the excited states predicted by the three models (the lowest three levels are not shown because the result of all three models are indistinguishable and the values are orders of magnitude larger than those shown). The significant under prediction of the excited state number densities by the Gally model is apparent in this figure, as well as the excellent agreement of the AACR model with the detailed CR model. The under prediction by Gally's model could have been predicted from Figure 1.1, which presents the excited state number densities for similar conditions and illustrates the trend that the Saha-Boltzmann values for the excited states, which in Gally's model are assumed equal to the excited state number densities, are lower than the CR model prediction. Figure 4.5 presents the nitrogen atomic line emission from each level corresponding to the number densities shown in Figure 4.4. The differences in these emission values are consistent with the differences in the number densities of these levels, as they should be since the emission is proportional to the number density of the upper level of the transition. For the detailed CR model case, the total emission from nitrogen lines is 0.065 W/cm³-sr while the overall emission from all radiative processes is 0.844 W/cm³-sr. Thus, the nitrogen lines contribute less than 10% to the emission (most of the emission at this point is due to molecular band systems), which explains why the radiative flux at $z = 4$ cm in Figure 4.3 predicted by the Gally model is similar to the other models, even though it was shown in Figures 4.4 and 4.5 that this model significantly under predicted the nitrogen line emission.

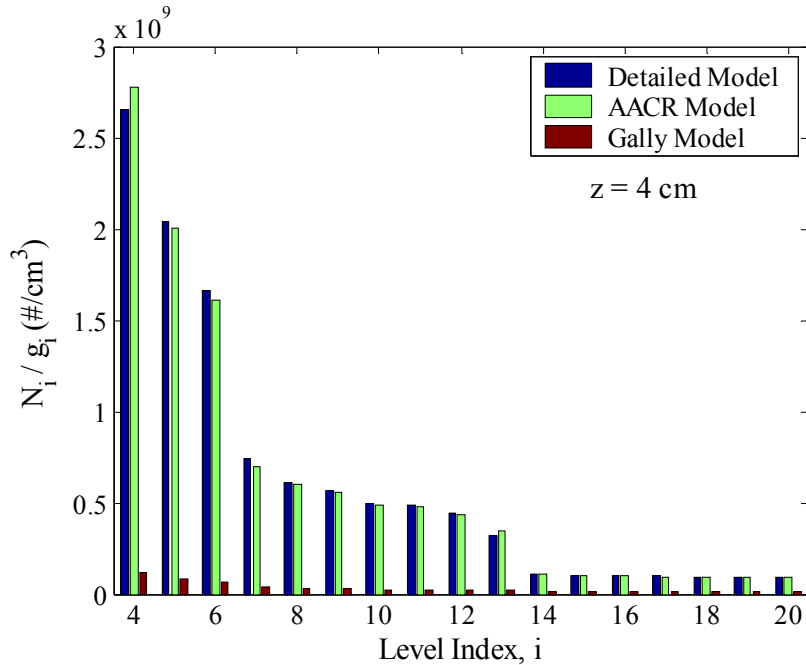


Figure 4.4. Number densities of nitrogen levels for the $z = 4 \text{ cm}$ point predicted by the various models

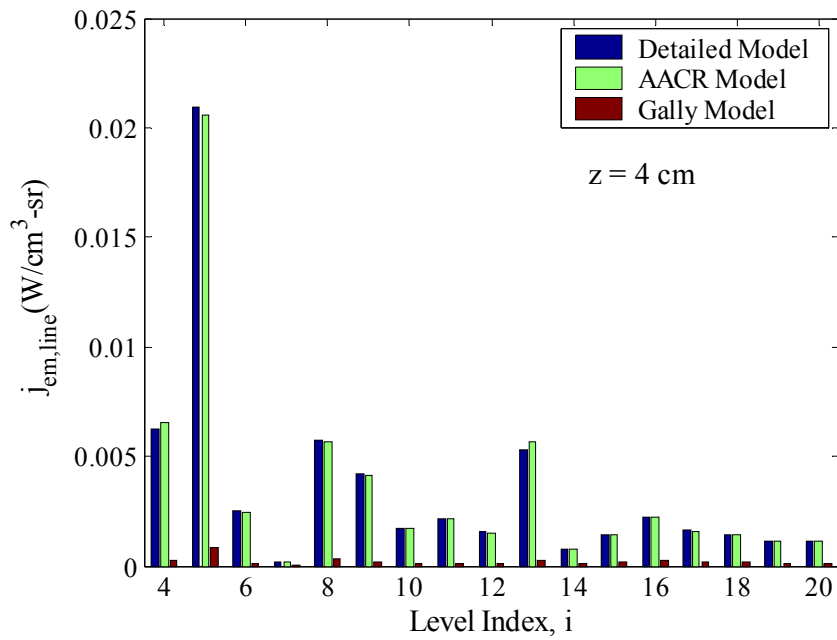


Figure 4.5. Atomic line emission from nitrogen levels for the $z = 4 \text{ cm}$ point predicted by the various CR models

The $z = 2 \text{ cm}$ point listed in Table 4.5 is essentially in chemical equilibrium. This means that the Gally model reduces to a Boltzmann distribution (because the Saha-Boltzmann and Boltzmann

equations are identical for chemical equilibrium conditions). Figure 4.6 compares the excited states number densities for this case, and it is seen that the population of the lower levels predicted by the Detailed and AACR model are noticeably lower than the Gally prediction, or essentially the Boltzmann prediction. These levels do not reduce to their Boltzmann values because they are strongly radiating, meaning they are rapidly depopulated by spontaneous emission of photons and corresponding transitions to lower levels. The characteristic of being a strongly radiating level is a result of being the upper level of atomic line transitions with large transition probabilities, which were defined in Eq. (4.37). Also, it has been assumed that the gas is optically thin, as it applies to the Master Equation, meaning the escape factors have been set equal to one. This maximizes the influence of radiative transitions on the Master Equation. Figure 4.7 compares the nitrogen atomic line radiation for this case. As expected from the number densities, the Gally model over predicts the emission for the lower states, which are seen to be the most strongly radiating, as mentioned. The total (including all radiating mechanisms of all species) emission from this point for the Detailed CR model case is 2.29 W/cm³-sr while that from nitrogen line emission is 1.02 W/cm³-sr. Thus, it is seen that the nitrogen lines contribute a significant fraction of the total emission at this point, unlike for the previous $z = 4$ cm point. The Gally model predicts a 1.22 W/cm³-sr contribution from the nitrogen lines. This larger value explains the larger radiative flux value from the Gally model shown in Figure 4.3.

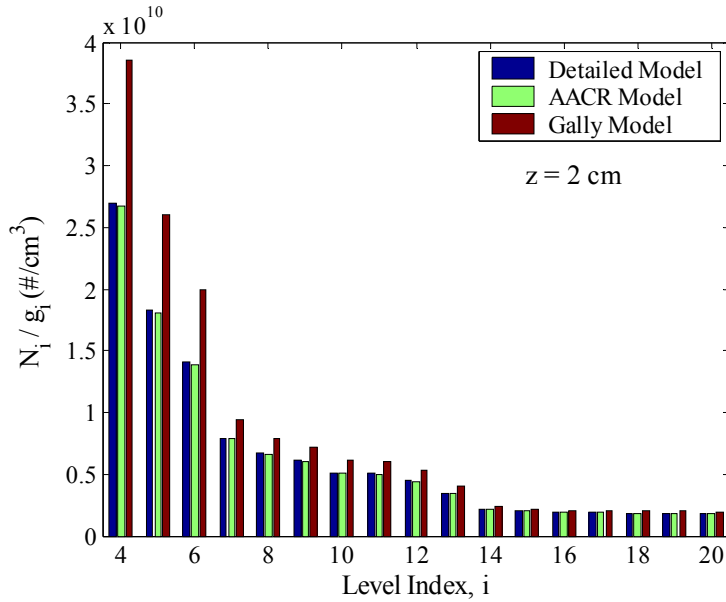


Figure 4.6. Number densities of nitrogen levels for the $z = 2$ cm point predicted by the various models

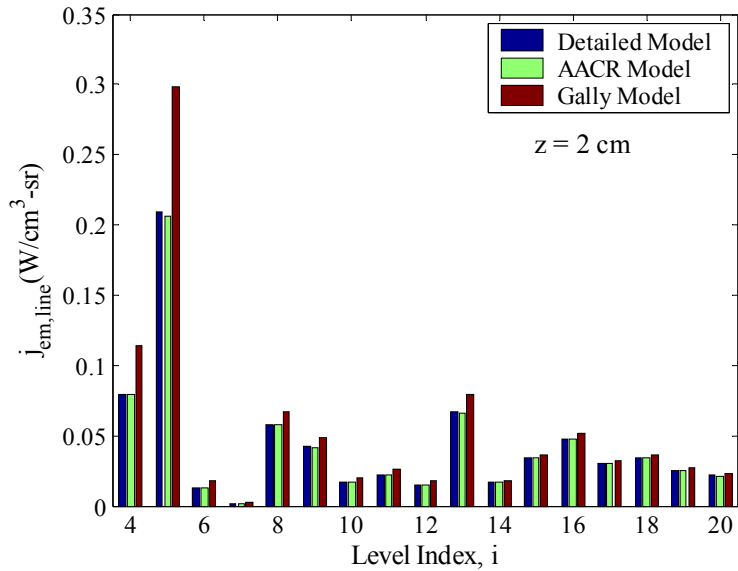


Figure 4.7. Atomic line emission from nitrogen levels for the $z = 2 \text{ cm}$ point predicted by the various CR models

From the present discussion regarding the non-Boltzmann modeling of atomic species, it may be concluded that for the shock layer applications of present interest, the AACR model provides a sufficiently accurate non-Boltzmann model that is both computationally efficient and simple to apply. The six grouped levels used by this model for each species (listed in Table 4.4) essentially means that the 35 and 32 levels listed in Tables 3.1 and 3.2 for nitrogen and oxygen may be reduced to these six grouped levels.

4.7 Non-Boltzmann Modeling for N_2^+ and N_2

For shock layers in air at lunar return conditions and near peak heating (radiative and convective), the N_2^+ and N_2 molecules are the main contributors to the *nonequilibrium* molecular band radiation. The contributions from the NO and O_2 bands discussed in Section 3.9 are limited to the equilibrium regions of the shock-layer. For lower velocity nonequilibrium conditions, such as those studied by Levin et al. [1993], the shock layer temperature is on the order of 6,000 K and the nonequilibrium contribution from NO and O_2 may be large. For such conditions, the model discussed in this section is not sufficient, and instead, the models presented by Levin [1993] and Gorelov [1998] should be applied.

Before the rate models for N_2^+ and N_2 are discussed, it should be mentioned that the upper electronic states of the N_2 VUV band systems (which are identified in Table 3.7) are very high

(above the dissociation limit), and are therefore assumed to be in dissociation equilibrium, which means their population is calculated by Eq. (4.7) (Greendyke and Hartung [1991]). There are no available kinetic models for these states, so that the assumption of dissociation equilibrium is the best available model. When this is implemented for most cases, the N₂ VUV bands do not emit any noticeable amount from the nonequilibrium regions of the shock-layer, although they do absorb significantly in the nonequilibrium boundary layer.

The rate models for the electronic excitation of N₂⁺ and N₂, for the lunar return shock layers of interest here, do not require that all of the processes discussed in Section 4.2 be included. Nevertheless, for completeness, all of the processes will be included in the initial model proposed here, except for the electron-impact ionization process, which was shown to be negligible in the preliminary stage of this study (using the rates presented by Teulet [1999]). Note that this process is not considered in the kinetic model applied for the flowfield chemistry (Park [1993]).

I. The Rate Model for N₂⁺

For N₂⁺, the electronic levels are shown in Table 4.6 and the chosen rates for electron-impact excitation, dissociation, heavy-particle excitation, and radiative transitions are shown in Table 4.7 along with their reference source. The rates are related to the coefficients listed in this table as follows:

$$K_r = a_r T_e^{b_r} \exp(-c_r / T_e)$$

where K_r represents $K_e(i,j)$ for $r = 1$ to 6, $K_e(i,d)$ for $r = 7$ to 10, and $K_M(i,j)$ for $r = 11$ and 12. For many of the rates, the only available values were the theoretical predictions by Teulet et al. [1999]. These values were used when no other values were available. Preference was given to other values because the method used by Teulet et al. was more approximate than the experimental and detailed calculation procedures used by other researchers. The most important rate, and fortunately the most frequently studied rate, is that for the electron impact excitation from the N₂^{+(X)} state to the N₂^{+(B)} state, which is the second rate listed in Table 4.7. This rate is the most significant for determining the population of the N₂^{+(B)} state, which is the upper level of the important N₂⁺⁽¹⁻⁾ band system. Figure 4.8 compares the rates proposed by numerous researchers for this process. The solid lines represent the cases where the actual rates were presented by the researcher, whereas the non-solid lines indicate that the excitation *cross-section* was presented, which was converted to a rate by numerically integrating the following formula:

$$K_e(i,j) = \frac{8\pi}{m^{1/2}} \left(\frac{1}{2\pi n k T_e} \right)^{3/2} \int_0^{\infty} \sigma_{ij}(E) \exp\left(-\frac{hc}{kT_e} E\right) E dE \quad (4.41)$$

This figure indicates the large discrepancy between the various studies, with values ranging many orders of magnitude. Because there is no guidance in choosing the best of these values, the fixed-nuclei result of Nagy [2003] was chosen because it was the most recent and because it was roughly in the middle of the other predictions. The other sources of rates used for N_2^+ in the present study are Gorelov et al. [1998], Flagan and Appleton [1972], and Chernyi and Losev [1993].

Table 4.6. N_2^+ electronic levels treated in the present model (Teulet [1999])

Level	E_e (cm $^{-1}$)	g_e
$X^2\Sigma_g^+$	0.0	2
$A^2\Pi_u$	9,016.4	4
$B^2\Sigma_u^+$	25,461.5	2
$C^2\Sigma_u^+$	64,542.0	2

Table 4.7. Non-Boltzmann rate model for N_2^+

r	Process	a_r	b_r	c_r	Ref.
1	$N_2^+(X) + e^- \Leftrightarrow N_2^+(A) + e^-$	7.1×10^{-11}	0.0	13,300	1
2	$N_2^+(X) + e^- \Leftrightarrow N_2^+(B) + e^-$	2.0×10^{-11}	0.73	36,649	3
3	$N_2^+(X) + e^- \Leftrightarrow N_2^+(C) + e^-$	6.6×10^{-9}	0.41	85,038	2
4	$N_2^+(A) + e^- \Leftrightarrow N_2^+(B) + e^-$	1.0×10^{-9}	0.0	23,500	1
5	$N_2^+(A) + e^- \Leftrightarrow N_2^+(C) + e^-$	1.3×10^{-7}	0.11	78,403	2
6	$N_2^+(B) + e^- \Leftrightarrow N_2^+(C) + e^-$	3.9×10^{-9}	0.34	49,622	2
7	$N_2^+(X) + e^- \Leftrightarrow N + N^+ + e^-$	8.02×10^{-31}	5.54	101,117	2
8	$N_2^+(A) + e^- \Leftrightarrow N + N^+ + e^-$	8.27×10^{-26}	4.38	88,142	2
9	$N_2^+(B) + e^- \Leftrightarrow N + N^+ + e^-$	2.58×10^{-32}	5.81	64,328	2
10	$N_2^+(C) + e^- \Leftrightarrow N + N^+ + e^-$	1.31×10^{-28}	4.93	35,906	2
11	$N_2^+(X) + N_2 \Leftrightarrow N_2^+(A) + N_2$	3.8×10^{-2}	-2.33	12,978	3
12	$N_2^+(X) + N_2 \Leftrightarrow N_2^+(B) + N_2$	1.9×10^{-2}	-2.33	36,600	4
		A_r (s $^{-1}$)			
13	$N_2^+(A) \Rightarrow N_2^+(X) + h\nu$	6.7×10^4			5
14	$N_2^+(B) \Rightarrow N_2^+(X) + h\nu$	1.5×10^7			1
15	$N_2^+(C) \Rightarrow N_2^+(X) + h\nu$	1.4×10^7			5

¹Gorelov, V.A., *Journal of Thermophysics and Heat Transfer*, Vol. 12, pp. 172-179, 1998.

²Teulet, P., Sarrette, J.P., Gomes, A.M., *J. Quant. Spectr. and Rad. Tran.*, Vol. 62, pp. 549-569, 1999.

³Nagy, O., *Chemical Physics*, Vol. 286, pp. 109-114, 2003.

⁴Flagan, R.C., and Appleton, J.P., *Journal of Chemical Physics*, Vol. 56, pp. 1163-1173, 1972.

⁵Chernyi, G.G., and Losev, S.A., *Analysis of Russian Experimental Investigations for Validation of Kinetic Models for Hypersonic Flows in Thermochemical Nonequilibrium*, Moscow State University – Institute of Mechanics, pp. 233, 1993.

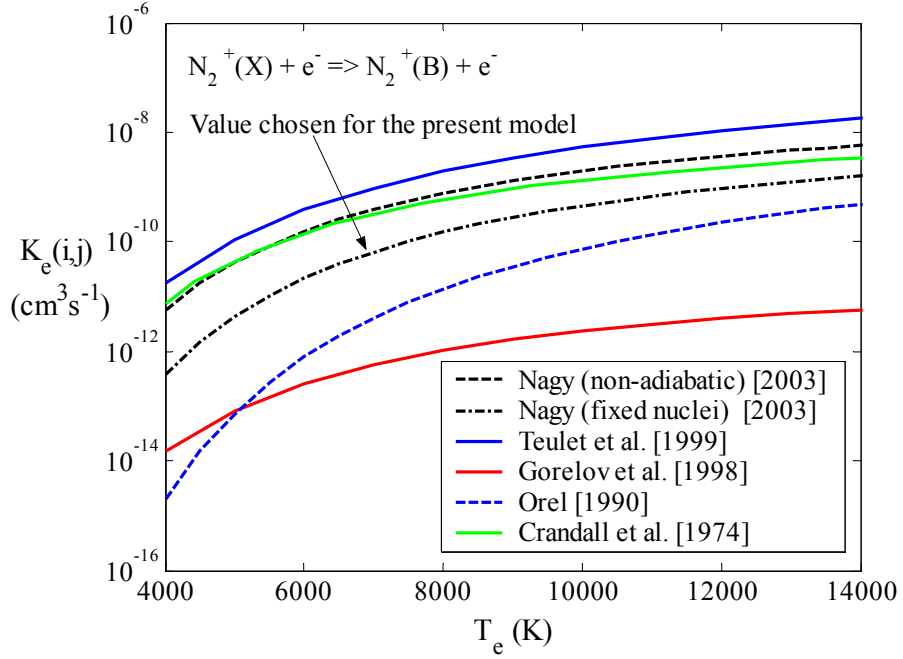


Figure 4.8. Comparison of electron-impact excitation rates for populating the $\text{N}_2^+(B)$ state.

For validation of the above model for N_2^+ , and to examine the influences of the various excitation and de-excitation processes, the Fire II 1634 trajectory point, which was defined in Table 1.1, will be examined using the uncoupled LAURA flowfields presented in Chapter 2. Note that the LAURA flowfields were demonstrated in Chapter 2 to provide radiation results within 5% of the VSL flowfields, so the conclusions made here with the LAURA flowfields also apply to the VSL flowfields.

The first topic to examine for the proposed N_2^+ model is the importance of each of the processes listed in Table 4.7. To aid in this study, it is useful to define the ratio of the inflow and outflow of a level j due to a specific process. For example, the ratio of the outflow from level j due to electron-impact transitions to the total outflow from level j (due to all process) may be written from Eq. (4.12) as follows:

$$\{\text{ratio of } j \text{ outflow due to el-imp-trans}\} = \frac{\sum_{j=1}^m K_e(j,i) N_j N_e}{\left(\frac{\partial N_i}{\partial t}\right)_{\text{outflow}}} \quad (4.42)$$

where the total outflow from level j is written as

$$\begin{aligned} \left(\frac{\partial N_i}{\partial t} \right)_{\text{outflow}} = & \sum_{j=1}^m K_e(j,i) N_j N_e + \sum_{j=1}^m K_M(j,i) N_j N_M + K_e(c,i) N_+ N_e^2 \\ & + K_e(d,i) N_X N_Y N_e + \sum_{j=i+1}^m A_{j,i} A(j,i) N_j + A_{c,i} A(c,i) N_+ N \end{aligned} \quad (4.43)$$

The equations for the outflow and inflow from each of the processes discussed in Section 4.2 may be written analogously. We are interested in the emission from the $\text{N}_2^+(1)$ -band system, which emits from the $\text{N}_2^+(\text{B})$ state, which for the present purposes represents j in Eqs. (4.42) and (4.43). Figures 4.9 and 4.10 present the inflow and outflow, respectively, for the Fire II 1634 s case using the rates listed in Table 4.7. The relative contributors to the inflow, or transition of molecules into the $\text{N}_2^+(\text{B})$ state, are shown in Figure 4.9 to be dominated by electron-impact transitions from the $\text{N}_2^+(\text{X})$ state, which is the important process discussed previously ($r = 2$ in Table 4.7). The other electron-impact transition processes are seen to be much smaller, although not negligible throughout the shock layer. The electron-impact dissociation and heavy-particle impact transitions are seen to only contribute noticeably in narrow regions near the shock and the body. The same trend is apparent in Figure 4.10, which shows the relative contributors to the outflow, or transition of molecules out of the $\text{N}_2^+(\text{B})$ state. The influence of radiative transitions is seen to contribute significantly to the outflow. Note that this calculation assumes that the molecular radiation is optically thin, which means that the radiation transitions have their maximum possible influence on the outflow. Figure 4.11 presents the net inflow, meaning the inflow ratio of Figure 4.9 minus the outflow ratio of Figure 4.10, for the present case. Because the quasi-steady state assumption was applied in solving the Master Equation, meaning the right-hand side of Eq. (4.12) was set to zero, the sum of the various net inflow components equals zero at each point in the shock layer. This figure shows that although the electron-impact inflow and outflow transitions to and from $\text{N}_2^+(\text{A})$ and $\text{N}_2^+(\text{C})$ have noticeable components in Figures 4.9 and 4.10, they are of equal magnitude and cancel out to a negligible amount for the net magnitude shown in Figure 4.11. Therefore, they have little influence on the solution of the Master Equation and the resulting state populations.

The conclusion that the electron-impact dissociation and heavy-particle impact transitions do not contribute significantly to the population of the $\text{N}_2^+(\text{B})$ state is applicable to all of the shock layers examined in this study. If these mechanisms are ignored, then from Eq. (4.23), the solution of the Master Equation becomes dependent upon only the electron number density and the electronic temperature, as mentioned previously. This dependence on only these two variables allows for a curve-fit to be conveniently constructed for the N_2^+ state populations. These curve-fits were constructed using the present rate model, and are presented in Appendix C for the four

N_2^+ levels listed in Table 4.6. Unlike the curve-fits for the atomic species, which consisted of fits for r_0 and r_1 , the number densities of the levels are fit directly for molecules. This is possible for molecules because r_0 is equal to zero, which as seen from Eqs. (4.20) and (4.24) is a result of the electron-impact ionization and bound-free radiation being ignored.

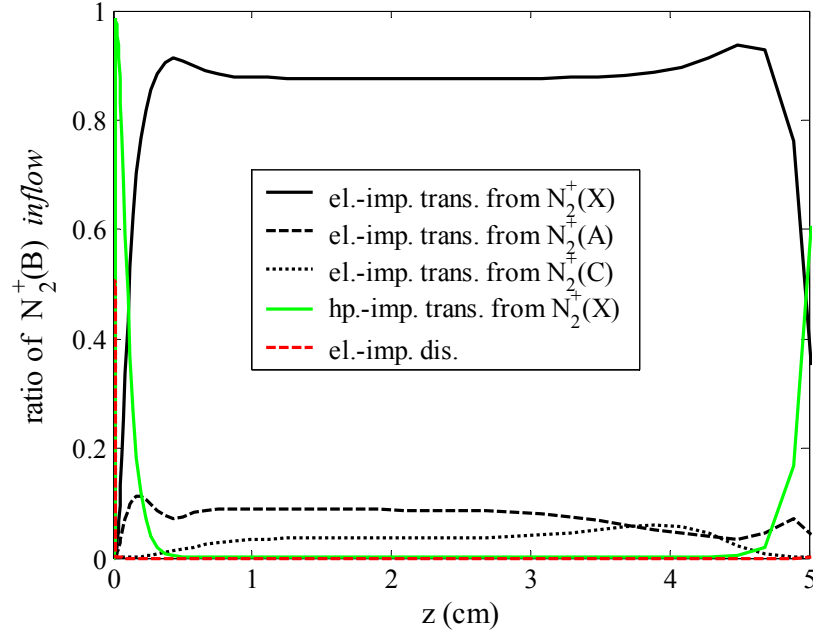


Figure 4.9. The ratio of $\text{N}_2^+(\text{B})$ inflow for various process

for the Fire II 1634 s case, using the Table 4.7 rates.

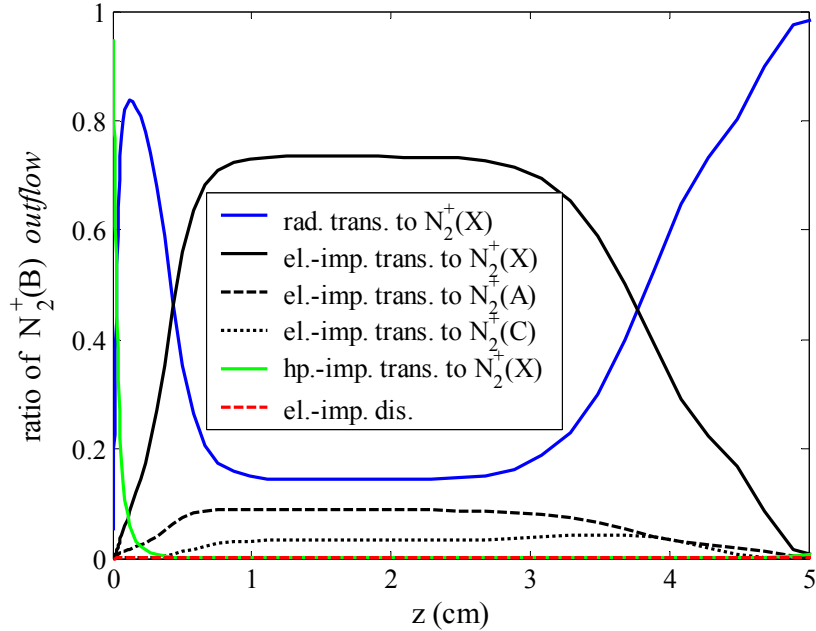


Figure 4.10. The ratio of $\text{N}_2^+(\text{B})$ outflow for various process

for the Fire II 1634 s case, using the Table 4.7 rates.

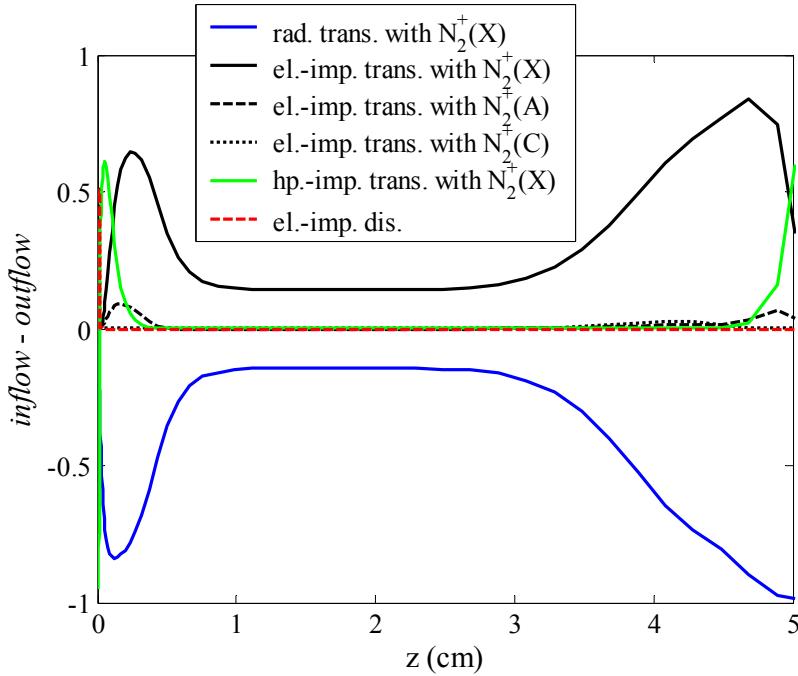


Figure 4.11. The ratio of $\text{N}_2^+(\text{B})$ inflow ratio minus the outflow ratio for each process corresponding to Figures 4.9 and 4.10.

A comparison of the number densities for N_2^+ obtained with the CR model presented here and those obtained with the Boltzmann model are presented in Figure 4.12 for the Fire II 1634 s case. The largest deviation from a Boltzmann distribution is seen to be present for the $\text{N}_2^+(\text{B})$ state. The CR model predicts a much lower number density, which implies that the emission from the $\text{N}_2^+(1)$ band is reduced proportionately. Figure 4.13 illustrated this reduction in emission by comparing the wall directed radiative flux profiles (resulting from all radiation mechanisms) for the Fire II 1634 s case obtained by assuming a Boltzmann distribution of the $\text{N}_2^+(\text{B})$ state or by using the present CR model for this state. This figure also shows the effect of choosing other rate values for the $r = 2$ reaction listed in Figure 4.8. It is seen that the Teulet et al. [1999] value, which was the largest of the rates considered, drives the $\text{N}_2^+(\text{B})$ state to a Boltzmann distribution, while the Gorelov et al. [1998] value, which was the smallest of the rates considered, decreases the flux about 10% below the present rate value.

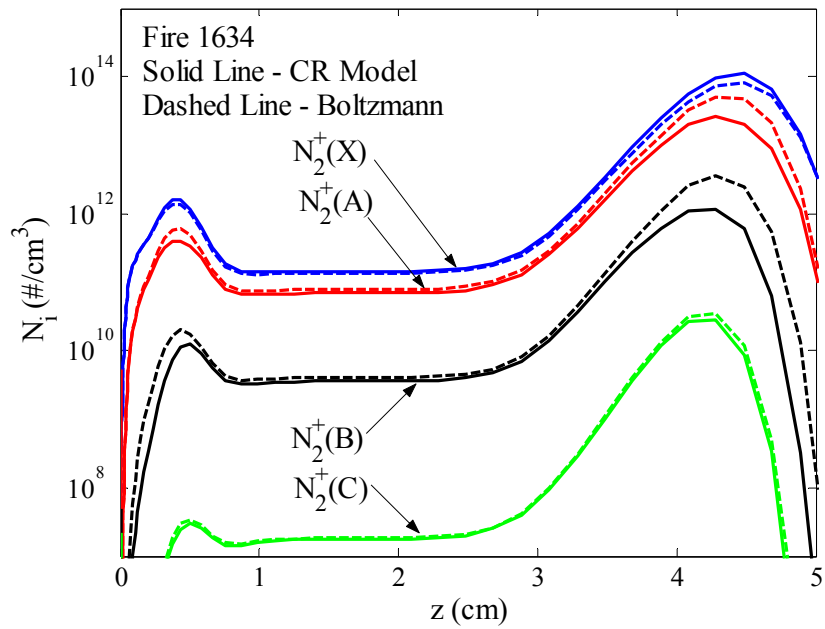


Figure 4.12. Comparison of the electronic state number densities predicted by the Boltzmann and CR Model along the stagnation line for the Fire II 1634 s case

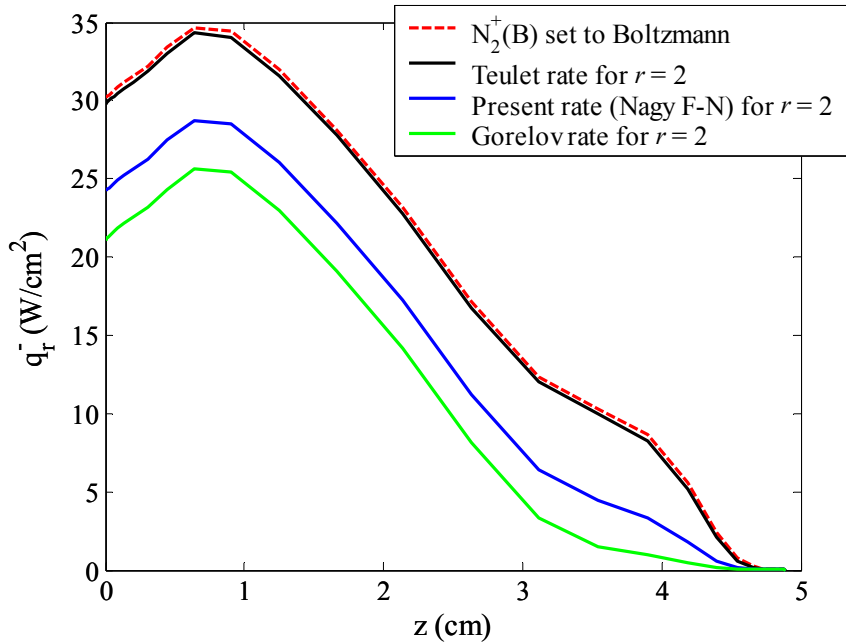


Figure 4.13. Wall directed radiative flux profiles for the Fire II 1634 case for different treatments of the $N_2^+(B)$ state population

II. The Rate Model for N₂

The electronic levels treated for the N₂ model are listed in Table 4.8 and the chosen rates for electron-impact excitation, dissociation, heavy-particle excitation, and radiative transitions are shown in Table 4.7 along with their reference source. These rates were more commonly studied and available than the N₂⁺ rates discussed previously.

Table 4.8. N₂ electronic levels treated in the present model (Teulet [1999])

Level	E _e (cm ⁻¹)	g _e
X ^{1Σ_g⁺}	0.0	1
A ^{3Σ_u⁺}	49,754.8	3
B ^{3Π_g}	59,306.8	6
C ^{3Σ_u}	88,977.8	6

Table 4.9. Non-Boltzmann rate model for N₂

r	Process	a _r	b _r	c _r	Ref.
1	N ₂ (X)+e ⁻ ⇌ N ₂ (A)+e ⁻	4.0x10 ⁻⁹	0.1	71,610	1
2	N ₂ (X)+e ⁻ ⇌ N ₂ (B)+e ⁻	4.6x10 ⁻⁸	-0.1	85,740	1
3	N ₂ (X)+e ⁻ ⇌ N ₂ (C)+e ⁻	3.8x10 ⁻⁹	0.1	127,900	2
4	N ₂ (A)+e ⁻ ⇌ N ₂ (B)+e ⁻	5.0x10 ⁻⁹	0.0	13,495	1
5	N ₂ (A)+e ⁻ ⇌ N ₂ (C)+e ⁻	2.9x10 ⁻⁹	0.28	46.655	3
6	N ₂ (B)+e ⁻ ⇌ N ₂ (C)+e ⁻	1.2x10 ⁻³	-0.99	44,385	3
7	N ₂ (X)+e ⁻ ⇌ 2N+e ⁻	4.11x10 ⁻³³	6.16	113263	3
8	N ₂ (A)+e ⁻ ⇌ 2N+e ⁻	6.61x10 ⁻²⁰	2.98	41,669	3
9	N ₂ (B)+e ⁻ ⇌ 2N+e ⁻	4.50x10 ⁻²³	3.73	55,586	3
10	N ₂ (C)+e ⁻ ⇌ 2N+e ⁻	5.14 x10 ⁻²¹	3.27	12,892	3
11	N ₂ (X)+N ₂ ⇌ N ₂ (A)+N ₂	1.83x10 ⁻¹²	-0.5	71,600	4
12	N ₂ (A)+N ₂ ⇌ N ₂ (B)+N ₂	1.99x10 ⁻¹¹	0.0	13,495	1
13	N ₂ (B)+N ₂ ⇌ N ₂ (C)+N ₂	8.47x10 ⁻¹¹	0.0	42,476	6
		A _r (s ⁻¹)			
14	N ₂ (B)⇒ N ₂ (A)+hv	1.4x10 ⁵			1
15	N ₂ (C)⇒ N ₂ (B)+hv	2.6x10 ⁷			5

¹Chernyi, G.G., and Losev, S.A., *Development of Thermal Protection Systems for Interplanetary Flight*, Final Project Technical Report, ISTC N 036-96, Research Institute of Mechanics, Moscow, 1999.

²Capitelli, C.M., et al., *Plasma Kinetics in Atmospheric Gases*, Springer, Berlin, 2000.

³Teulet, P., Sarrette, J.P., Gomes, A.M., *J. Quant. Spectr. and Rad. Tran.*, Vol. 62, pp. 549-569, 1999.

⁴Kurochkin, Y.M., et al., *High Temperature*, Vol. 16, pp. 1167-1177, 1978.

⁵Pancheshnyi, S.V., et al., *Chemical Physics*, Vol. 262, 2000.

⁶Fresnet, F., et al., *Plasma Sources Science and Technology*, Vol. 11, pp. 152-160, 2002.

The influence of the various processes listed in Table 4.9 may be studied by examining the inflow and outflow of each process as was done for N₂⁺. Figures 4.14 and 4.15 present the inflow and outflow of the N₂(B) state, respectively, along the stagnation line for the Fire II 1634 s case.

There are several differences between the trends shown in these figures and those shown for N_2^+ in Figures 4.9 and 4.10. For the inflow, Figure 4.14 shows that there is contribution from radiative transitions, which was not seen for $\text{N}_2^+(B)$, because the $\text{N}_2(B)$ state is the lower state of a radiative transition, as represented by $r = 15$ in Table 4.9. For the outflow, Figure 4.15 shows that the radiative transitions have a smaller effect than they did for $\text{N}_2^+(B)$. This is a result of the larger radiative lifetime for $\text{N}_2(B)$ relative to that for $\text{N}_2^+(B)$. Also, the effect of electron-impact dissociation is shown to contribute noticeably to the outflow, although the reverse process (three-body recombination), is negligible. This lack of balance for the dissociation process is shown in Figure 4.16 to result in a large net contribution from dissociation, which indicates that it has a significant influence on the solution of the Master Equation. The fact that the recombination process is negligible means that the Master Equation remains a function of T_e and N_e , even with the dissociation contribution. As was done for N_2^+ , curve fits for the N_2 electronic state populations were created for a range of T_e and N_e values, and are presented in Appendix C.

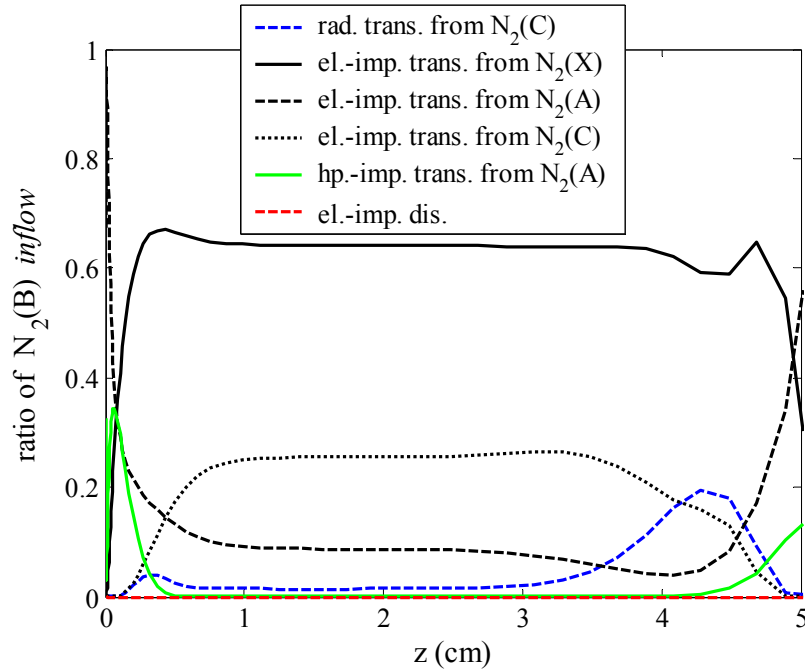


Figure 4.14. The ratio of $\text{N}_2(\text{B})$ inflow for various process

for the Fire II 1634 s case, using the Table 4.9 rates.

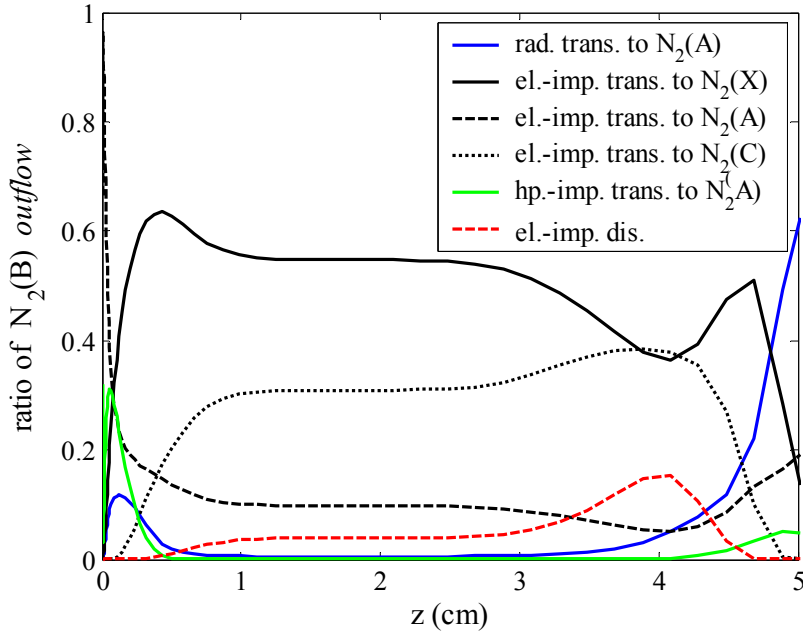


Figure 4.15. The ratio of $N_2(B)$ outflow for various process

for the Fire II 1634 s case, using the Table 4.9 rates.

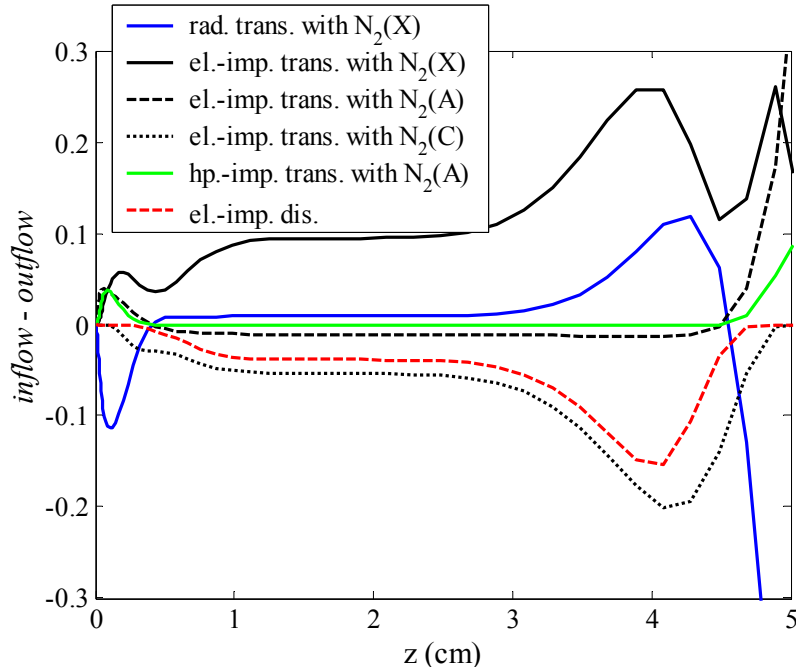


Figure 4.16. The ratio of $N_2(B)$ inflow ratio minus the outflow ratio for each process

corresponding to Figures 4.14 and 4.15.

The populations of the N_2 electronic states predicted by the present CR model and the Boltzmann model are compared in Figure 4.17 for the Fire II shock layer at 1634 seconds. The $N_2(A)$ and $N_2(B)$ states, which are closely spaced in energy, are shown to have similar Boltzmann and non-Boltzmann distributions throughout the layer. The $N_2(C)$ state is seen to diverge most from a

Boltzmann distribution. This is a result of it being the upper state of the $\text{N}_2(2+)$ radiative transition, represented by $r = 15$ in Table 4.9. This transition has a small radiative lifetime, which creates a large outflow from the $\text{N}_2(\text{C})$ state to cause the large difference from the Boltzmann result.

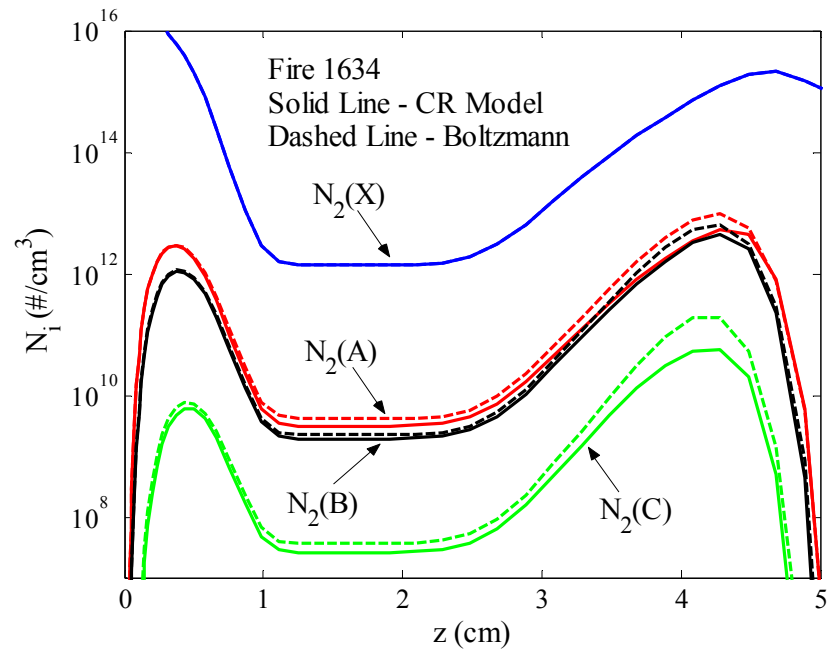


Figure 4.17. Comparison of the electronic state number densities predicted by the Boltzmann and CR Model along the stagnation line for the Fire II 1634 s case

Chapter 5

Coupled Radiative Heating for Lunar-Return Shock-Layers

5.1 Chapter Overview

This chapter combines the VSL flowfield model developed in Chapter 2 with the radiation model developed in Chapters 3 and 4, to produce a detailed and efficient model for calculating radiation-flowfield coupled shock-layers in the stagnation region of a blunt body. This method is applied in this chapter to the Fire II and Apollo 4 vehicles, and the results are compared with flight data and previous studies, both of which were discussed previously in Sections 1.4 and 1.5. The deviations of the present results from the flight data and previous studies are discussed, and the influence of non-Boltzmann radiation and flowfield coupling are assessed. The differences between the radiation predicted by a two-temperature chemical nonequilibrium VSL flowfield and a single temperature chemical equilibrium VSL flowfield are compared, which provides insight into the effect of multiple temperatures and chemical nonequilibrium on the radiative heating predictions and the effect of radiation-flowfield coupling.

The basic concept of radiation-flowfield coupling is presented in Section 5.2. The influence of radiation on the two-temperature formulation of the energy equations is discussed. An explanation is provided for the similarities (seen in Sections 5.4 and 5.5) between the radiation coupling effect for a single-temperature and two-temperature flowfield model. Section 5.3 presents the *uncoupled* radiative heating predictions for the Fire II vehicle. Although the uncoupled assumption is known to be physically unrealistic, these values are presented as baseline results to compare with the coupled values. Section 5.4 presents the coupled values for the Fire II case. These coupled solutions are compared with the flight data and the predictions of

previous studies. Coupled results for both the two-temperature nonequilibrium (NE) VSL method and single-temperature equilibrium (E) VSL results are compared. The Apollo 4 flight vehicle is considered in Section 5.5. Coupled predictions from both the NE and E VSL method are compared with the flight data and the predictions of previous studies.

5.2 Radiation-Flowfield Coupling

The influence of radiation on the governing flowfield equations is represented mostly[†] by the presence of the radiative flux divergence (Q_{rad}) in the total energy equation and the vibrational-electronic-electron energy equation. To examine the influence of this term on the energy equations, it is convenient to subtract the vibrational-electronic-electron energy equation from the total energy equation to obtain the translational-rotational energy equation. These two equations, in the VSL formulation, may be written in dimensional form along the stagnation line as follows:

Vibrational-Electronic-Electron Energy:

$$\begin{aligned} \rho C_{p,ve} v \frac{\partial T_{ve}}{\partial z} = & \left\{ Q_{e-t} + Q_{v-t} + Q_{e,ion} + Q_{v,dis} + Q_{rad} - \sum_{i=1}^{N_s} h_{ve,i} \dot{w}_i \right\} \\ & + \frac{p_e}{\rho} v \frac{\partial \rho}{\partial z} + \frac{\partial}{\partial z} \left[K_{ve} \frac{\partial T_{ve}}{\partial z} \right] + \frac{2}{R_N + z} K_{ve} \frac{\partial T_{ve}}{\partial z} - \sum_{i=1}^{N_s} J_i C_{p,ve}^i \frac{\partial T_{ve}}{\partial z} \end{aligned} \quad (5.1)$$

Translational-Rotational Energy:

$$\begin{aligned} \rho C_{p,tr} v \frac{\partial T_{tr}}{\partial z} - v \frac{\partial p}{\partial z} = & \left\{ -Q_{e-t} - Q_{v-t} - Q_{e,ion} - Q_{v,dis} - \sum_{i=1}^{N_s} h_{tr,i} \dot{w}_i \right\} \\ & - \frac{p_e}{\rho} v \frac{\partial \rho}{\partial z} + \frac{\partial}{\partial z} \left[K_{tr} \frac{\partial T_{tr}}{\partial z} \right] + \frac{2}{R_N + z} K_{tr} \frac{\partial T_{tr}}{\partial z} - \sum_{i=1}^{N_s} J_i C_{p,tr}^i \frac{\partial T_{tr}}{\partial z} \end{aligned} \quad (5.2)$$

The terms in these equations are defined in Chapter 2, although they are written here in dimensional form without the ‘*’, which is used in Chapter 2 to denote dimensional values. Note that Q_{rad} is *not* present in the translational-rotational energy equation. Because of this, the influence of radiation on the translational-rotational energy equation, and the resulting translational-rotational temperature (T_{tr}), is provided mainly by Q_{e-t} , which is the electron-translational energy exchange term discussed in Section 2.4. As seen from Eq. (2.40), this term is proportional to the difference between T_{tr} and T_{ve} , and thus, acts to bring the two temperatures together. For the lunar-return conditions studied here, the ion contributions to this term are dominant (meaning that they are the dominant contributors to the summation present in Eq.

[†] The radiation pressure terms are ignored in the momentum equations, as is commonly done. Also, the influence of radiation on the wall temperature is not accounted for in this study (because the wall temperature is specified for all the cases treated), although the radiation *from* the wall is accounted for in the divergence of the radiative flux.

(2.40)). If the ion contributions are not considered, the T_{tr} and T_{ve} values from the resulting flowfield solution will be different by more than a 1,000 K if radiation-flowfield coupling is considered. This occurs because there is insufficient energy transport between Eqs. (5.1) and (5.2), which results in the two energy equations becoming essentially independent of each other. Specifically, *without* the ion contributions to Q_{e-t} , T_{ve} decreases, relative to the uncoupled value, with the addition of coupling, and T_{tr} increases above its uncoupled value, due to increased electron-impact ionization recombination (which enters Eq. (5.2) through the chemical production term, which is the last term in brackets). The increased value of T_{tr} results in a lower density and larger shock-standoff distance relative to the uncoupled case. On the other hand, if Q_{e-t} is treated properly, a two temperature flowfield behaves nearly the same as a single-temperature equilibrium flowfield, with the addition of coupling. This will be illustrated throughout this chapter by comparing results from the two-temperature nonequilibrium VSL flowfield (NE VSL) with the single temperature equilibrium VSL flowfield (E VSL). The coupling provided by Q_{e-t} is so large, in fact, that Q_{rad} could be distributed between the two energy equations in any proportion, and the coupled solution would be essentially unchanged.

The calculation of the radiative flux through the shock-layer was performed using the tangent-slab approximation, which is discussed in Appendix F. This method was implemented following the methodology outlined by Chambers [1994]. The 150 points applied through the shock-layer for the flowfield solution were reduced to 40 points for the radiation transport calculation. The chosen radiation grid was clustered significantly towards the shock and body to provide sufficient resolution of the possible large number density and temperature gradients in these regions.

5.3 Uncoupled Radiative Heating for Fire II

The Fire II flight experiment was discussed in detail in Section 1.4. Along with presenting the flight data, it was shown in this section that there is a large scatter among the previous theoretical predictions of this data. Furthermore, each prediction failed to compare well throughout both the early nonequilibrium region of the trajectory and in the later mostly equilibrium peak-heating region. It was shown that the more recent and sophisticated prediction methods did not lead to a consistently better comparison with the data relative to older prediction methods. The goal of this section and Section 5.3 is to compare the results of the flowfield and radiation models developed in Chapters 1 – 4 with the flight data and previous predictions. It will be shown that the present model provides a better comparison with the data, on average over the trajectory, than any previous study. Although the uncoupled results are known to be physically inaccurate, they are

presented in this section so that they may be compared with the uncoupled values predicted by previous studies. This allows the differences in the flowfield and radiation models to be examined without the complication of radiation-flowfield coupling. Furthermore, it will be insightful to compare these uncoupled values with the coupled values presented in the next section.

The chemical kinetics and thermophysical properties applied in the present flowfield model were discussed in Section 2.8. The uncoupled Fire II flowfields were also presented in that section, and shown to provide uncoupled radiative heating values consistent with those resulting from a LAURA (Navier-Stokes) flowfield. Table 5.1 lists the various radiative components predicted with the present *uncoupled* nonequilibrium VSL model and the radiation model presented in Chapters 3 and 4. The non-Boltzmann models for atoms and molecules, using the curve fit models presented in Appendix C, were applied for all results presented in this chapter, unless specified otherwise. The q_r^- and I_w values listed here represent the wall-directed radiative flux and wall-directed intensity, respectively, at the wall ($z = 0$). The numbers in parenthesis in the header column represent the spectral range, in eV, included in each value. The αq_r^- values represent the radiation absorbed by the Beryllium calorimeter, which is a quantity required for comparison with the calorimeter data (as mentioned previously in the discussion of Figure 1.6). Also required for the comparison with the calorimeter data is the convective heating (q_c), which is listed in this table and assumes a super-catalytic wall.

Table 5.1. *Uncoupled* convective and radiative heat-flux values (W/cm^2) and radiative intensities ($\text{W}/\text{cm}^2\text{-sr}$) for the Fire II vehicle obtained using the NE VSL flowfield model.

t (s)	q_c	αq_r^-	q_r^- (0-18)	q_r^- (0-6)	q_r^- (6-18)	I_w (0-18)	I_w (0-6)	I_w (6-18)
1634.0	221.0	19.2	25.7	10.9	14.8	4.9	1.8	3.2
1636.0	316.3	71.7	96.1	38.5	57.7	19.5	6.4	13.0
1637.5	398.2	151.5	206.3	85.1	121.2	42.6	14.5	28.1
1640.5	578.2	427.4	615.5	297.0	318.5	129.6	51.8	77.8
1643.0	776.7	499.9	755.5	415.8	339.7	156.2	71.9	84.4
1645.0	834.5	253.1	403.7	256.5	147.2	79.1	42.9	36.3
1648.3	756.3	25.6	41.8	25.2	16.6	7.1	4.0	3.1

The two previous studies that present uncoupled results over the majority of the trajectory are the studies by Olynick et al. [1994] and Greendyke and Hartung [1994]. The flowfield and radiation models applied by these researchers have been summarized in Table 1.2. The comparison between the q_r^- and I_w (0-6) values presented in Table 5.1 and those presented in Table V of Olynick et al. [1994] indicates agreement within 10% over most of the trajectory. The values presented by Greendyke and Hartung [1994] in their Figure 4 and 5, on the other hand, are lower

than the present values by up to 30%. The fact that Olynick's values agree well, while Greendyke's do not, is interesting considering that Olynick applied a Boltzmann model and Greendyke applied a non-Boltzmann model for the electronic state populations. As mentioned previously, the present study also applies a non-Boltzmann model, which was shown in Chapter 4 to result in less radiation than the Boltzmann model, especially in regions of significant chemical nonequilibrium. The flowfields predicted by Greendyke and Olynick were significantly different (see Figure 3 of Olynick [1994]), even though both were nonequilibrium Navier-Stokes solutions. The flowfield presented by Greendyke is closer to the present flowfield than Olynick's. The flowfields presented by Olynick contain smaller regions of chemical equilibrium, which likely explains why his radiation results, obtained assuming a Boltzmann distribution, are not significantly larger than the present values. The lower values predicted by Greendyke are likely a result of the updated atomic line and atomic bound-free data applied in the present model, which was shown in Chapter 3 to predict more radiation than older models. These observed differences in the uncoupled results for these two past studies will have significant influence on their coupled results discussed in the next section.

5.4 Coupled Radiative Heating for Fire II

The radiation components predicted by the present radiation-coupled flowfield model are presented in Table 5.2 for the Fire II case. The column definitions are identical to those of Table 5.1. To illustrate the differences between these values and the uncoupled results discussed previously, Figure 5.1 compares q_c , q_r^- , and αq_r^- between the coupled and uncoupled cases. It is seen that the q_r^- and αq_r^- values are reduced by 20 – 30% throughout the trajectory, except for 1648 s, where the reduction is negligible. This reduction is slightly larger than the 15 – 25 % reduction reported by Olynick et al. [1994] and the 5 – 18% reduction reported by Greendyke and Hartung [1994]. The smaller reduction found by Greendyke and Hartung is most likely a result of their significantly smaller uncoupled radiation prediction, which reduces the coupling effect. The discrepancy with Olynick's result is likely a result of differences in the flowfield modeling. A significant difference between Olynick's flowfield model and the present model is that Olynick obtains the vibrational-electronic-electron temperature by solving the vibrational energy equation, and *not* the vibrational-electronic-electron energy equation, as is done in the present model. The consequence of this treatment by Olynick is that the divergence of the radiative flux does not appear in the vibrational energy equation, even though the temperature obtained from this equation governs the magnitude of the radiation. The influence of radiation on the behavior of the two temperatures is therefore fundamentally different because radiation does not directly effect

the vibrational-electronic-electron temperature. For the high-temperature shock-layers of present interest, the vibrational energy is very small throughout most of the shock-layer because the majority of the molecules are dissociated. Furthermore, the coupling of the vibrational energy mode to the translational energy mode is represented through Q_{v-t} , which is shown in Eq. (2.39) to be proportional to the mass fractions of the molecules. For the present highly-dissociated conditions, this term is small, which results in the vibrational energy mode being weakly coupled to the translational energy mode. This indicates the inadequacy in solving the vibrational energy equation instead of the vibrational-electronic-electron energy equation for the high-temperature shock-layers of present interest.

Table 5.2. *Coupled* convective and radiative heat-flux values (W/cm^2) and radiative intensities ($\text{W}/\text{cm}^2\text{-sr}$) for the Fire II vehicle obtained using the NE VSL flowfield model.

t (s)	q_c	αq_r^-	q_r^- (0-18)	q_r^- (0-6)	q_r^- (6-18)	I_w (0-18)	I_w (0-6)	I_w (6-18)
1634.0	216.5	17.2	23.2	10.3	12.9	4.4	1.7	2.8
1636.0	304.1	59.4	80.7	34.2	46.5	16.2	5.7	10.5
1637.5	377.0	118.9	164.6	72.6	92.0	33.6	12.3	21.3
1640.5	535.2	308.5	454.6	236.1	218.5	94.2	40.8	53.4
1643.0	732.8	365.7	567.3	334.5	232.8	115.1	57.3	57.8
1645.0	807.2	208.4	338.0	222.6	115.4	65.2	37.0	28.3
1648.3	751.5	25.6	41.7	25.1	16.6	7.1	4.0	3.1

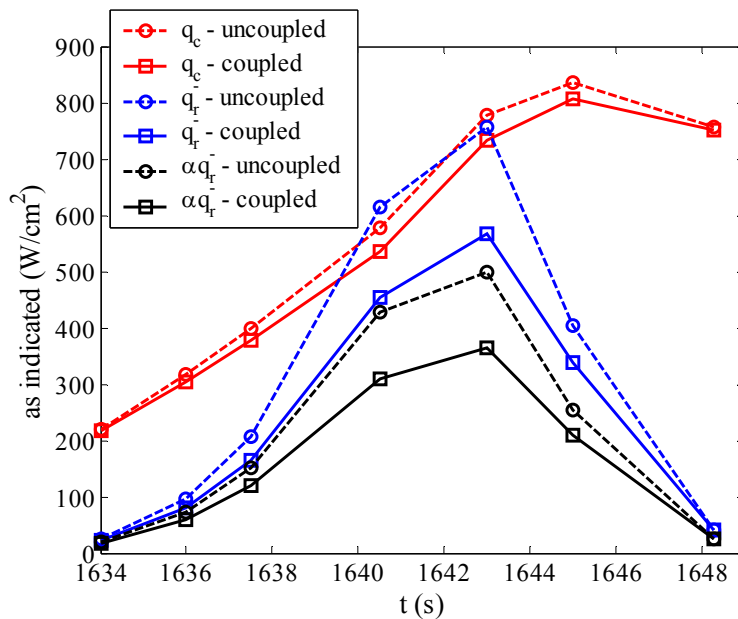


Figure 5.1. Uncoupled and coupled values for the convective and radiative heat flux along the Fire II trajectory. The αq_r values represent the radiative flux absorbed by the calorimeter.

As discussed in Section 5.2, the influence of radiation-flowfield coupling on a two-temperature chemical nonequilibrium flowfield should be similar to that predicted by a single-temperature chemical equilibrium model, assuming that the electron-translational energy exchange term is properly treated (for the two-temperature model). By comparing the present two-temperature chemical nonequilibrium VSL flowfield (NE VSL) with the chemical equilibrium VSL flowfield (E VSL) discussed briefly in Section 2.7, the influence of coupling on the two models may be compared. Figure 5.2 compares the partial intensity (0 – 6.2 eV) at the wall predicted by the uncoupled and coupled NE VSL and E VSL predictions. The decrease in intensity with the addition of coupling is seen to be very similar for both flowfield models. This confirms the previous statement regarding the similarity of the coupling effect for the two flowfield models. Figure 5.3 presents the coupled and uncoupled temperature profiles for the NE VSL and E VSL models at the 1643 s condition. Note that the y-axis on this figure ranges from 10,000 K to 12,000 K, for clarity. Except for the differences in the boundary layer, which is a result of the different diffusion modeling and possible nonequilibrium effects, the NE VSL and E VSL models compare very well for both the coupled and uncoupled cases. The slight separation seen between the models throughout the layer is only 10 to 20 K, which is negligible relative to the temperatures of roughly 11,000 K.

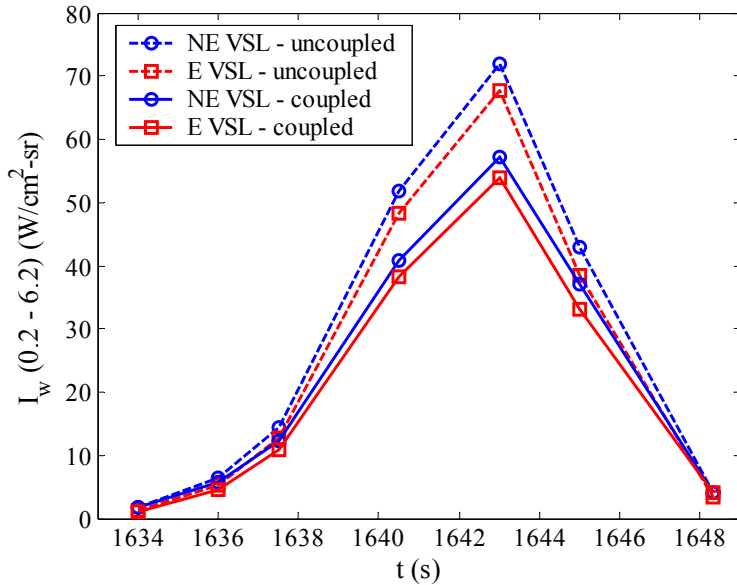


Figure 5.2. Partial wall intensity values (0.2 – 6.2 eV) predicted by the coupled and uncoupled application of the NE and E VSL flowfield models.

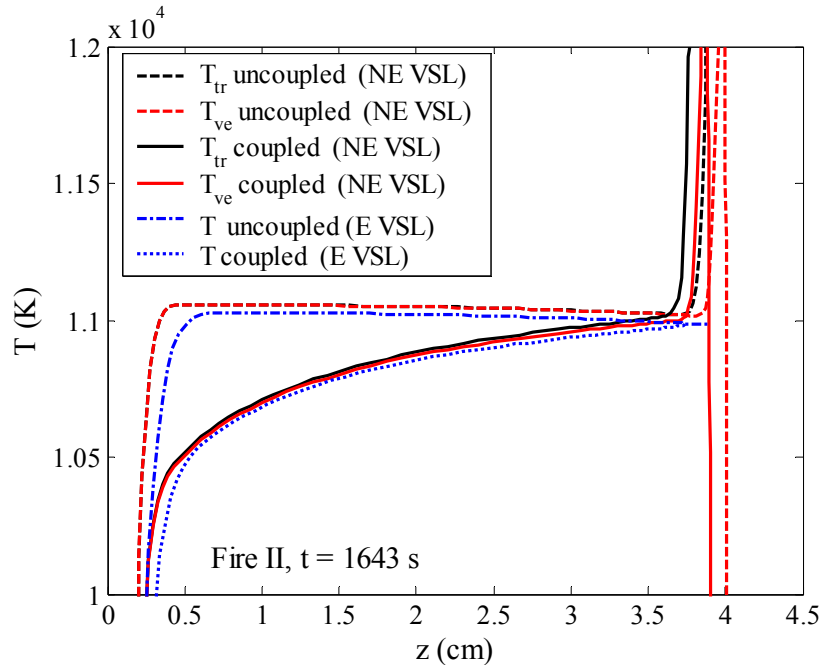


Figure 5.3. Uncoupled and coupled stagnation-line temperature profiles for $t = 1643$ s.

To assess the influence of non-Boltzmann modeling and radiation-flowfield coupling on the radiative flux throughout the shock layer, and on the flux that ultimately reaches the wall, Figures 5.4 through 5.7 present the wall-directed spectrally-integrated radiative flux profiles through the shock-layer and the radiative flux spectrum at the wall. In these figures, both the non-Boltzmann and Boltzmann results are presented for the coupled case, while only the non-Boltzmann result is presented for the uncoupled case. The non-Boltzmann and Boltzmann terminology used here specifies that the atomic *and* molecular electronic states are modeled by their respective Boltzmann or non-Boltzmann models. These models are discussed in detail in Chapter 4. The accumulated flux values presented in Figures 5.5 and 5.7 allow for the contributions from the various radiative mechanisms to be compared (note that the *spectrum* for only the coupled non-Boltzmann case is presented in each figure). For the 1636 s case, the non-Boltzmann influence is seen to be large. This is a result of the relatively large region of nonequilibrium directly behind the shock, which was shown previously in Figures 2.3 and 2.4. From Figure 5.5, the increased flux for the Boltzmann case is seen to come from the atomic lines between 1.3 and 1.8 eV and the N_2^+ first-negative band system located between 2.0 and 5.0 eV. The atomic bound-free continuum located above 12.0 eV also provides some excess radiation for the Boltzmann case. For the 1643 s case, Figure 5.6 shows that the Boltzmann influence is small. This is a result of most of the shock-layer being in equilibrium, which was shown previously in Figures 2.5 and 2.6. The influence of coupling for both the 1636 and 1643 s cases is seen to result mostly from the atomic

lines located between 1.3 and 1.8 eV and the atomic bound-free continuum located above 12.0 eV.

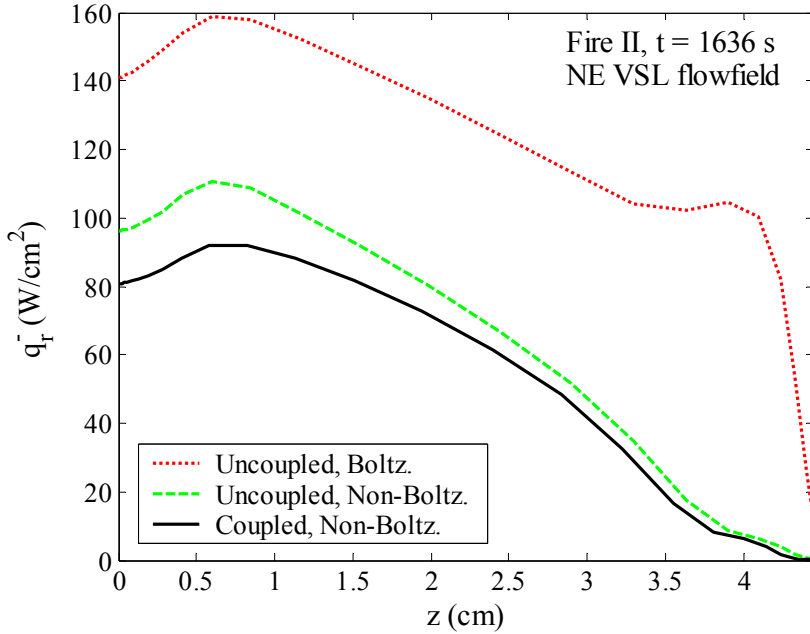


Figure 5.4. Wall-directed radiative flux profiles resulting from the coupled and uncoupled cases for $t = 1636$ s .

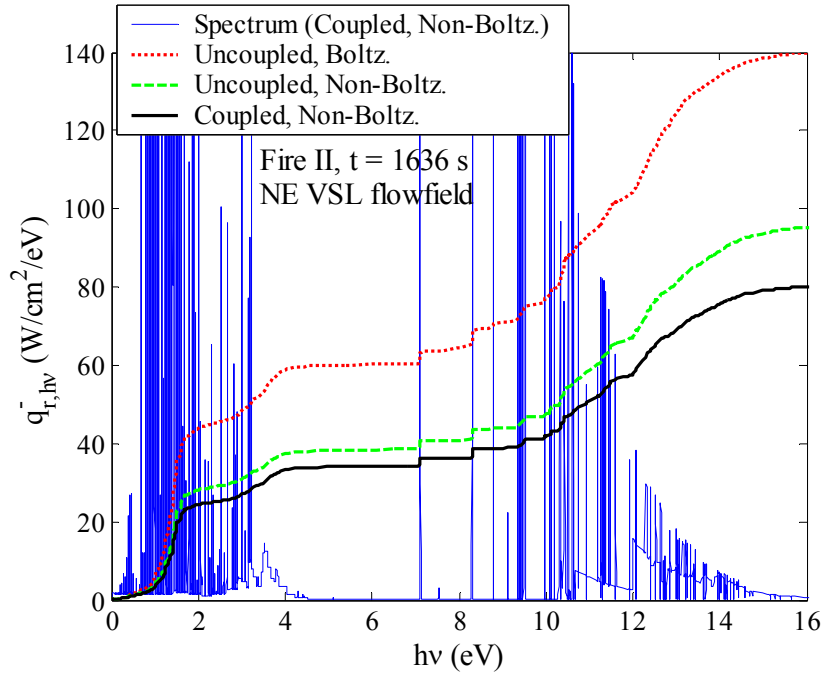


Figure 5.5. Radiative flux spectrum at the wall for $t = 1636$ s resulting from uncoupled and coupled flowfield models.

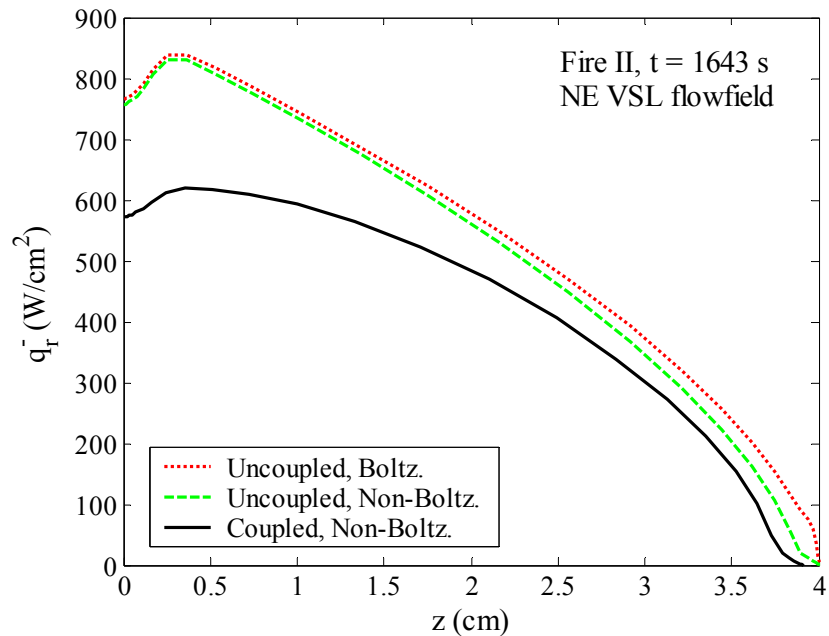


Figure 5.6. Wall-directed radiative flux profiles resulting from the coupled and uncoupled cases for $t = 1643$ s .

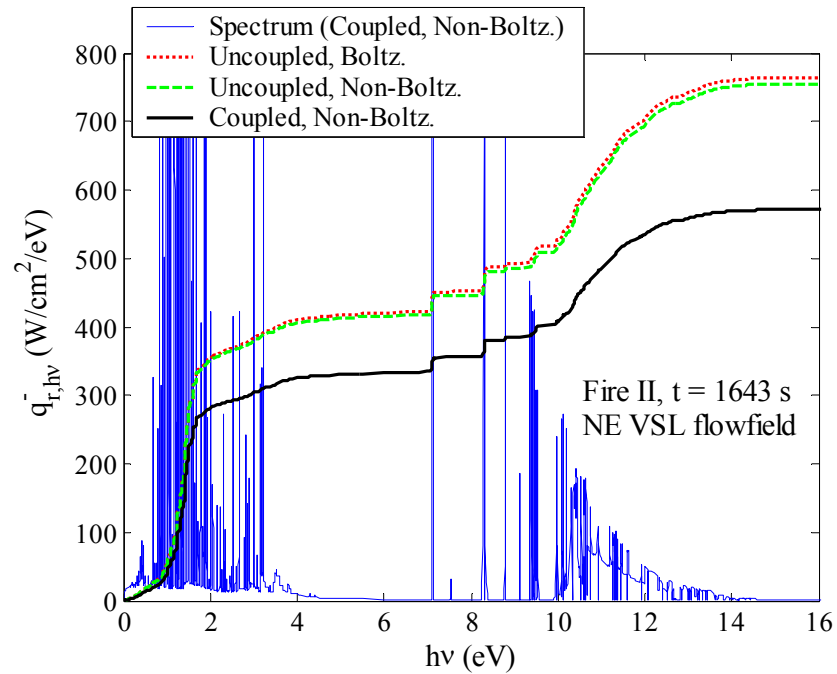


Figure 5.7. Radiative flux spectrum at the wall for $t = 1643$ s resulting from uncoupled and coupled flowfield models..

The Fire II total radiometer data and the theoretical predictions of this data by past studies were presented previously in Section 1.4. This data is compared in Figures 5.8 and 5.9 with the present radiation model coupled to the nonequilibrium (NE VSL) and equilibrium flowfield (E VSL) models. The predictions from past studies are also shown in these figures for comparison. Figure 5.8 shows the values for all trajectory points considered, while Figure 5.9 focuses on the three earliest points, which are important because they contain a significant amount of nonequilibrium radiation. From Figure 5.8, the differences between the flight data, previous predictions, and the present predictions can clearly be seen for the 1643 s point. For this trajectory point, the study by Olynick et al. [1994] is the only previous prediction that is closer to the data than the present NE VSL result. As discussed previously, the Olynick values are erroneously large because of the treatment of radiation-flowfield coupling, and because a Boltzmann distribution was assumed for the electronic state populations. Note that the present equilibrium values (E VSL) are slightly larger than the values predicted by Gupta [1987], who also applied an equilibrium VSL method. Assuming that the flowfield models were nearly equivalent, this trend is consistent with the fact that the present radiation model predicts larger radiation values for a given condition than the RAD/EQUIL code applied by Gupta. The reasonable agreement with Park's [2004] prediction at 1643 s is noted. This agreement may be fortuitous, as will be shown in the next section by comparing the radiative flux profiles (through the shock-layer) for the Apollo 4 case calculated by Park [2004] and calculated in the present study. It should be noted that the under-prediction at the 1637.5 point seen in Figure 5.9 is possibly a result of the radiometer window reaching its melting point, which would have caused the data at this trajectory point to be inaccurate. Of all the data points considered in Figures 5.8 and 5.9, this is the only point that is not considered a "prime" data period by Cauchon [1967]. For the early nonequilibrium points presented in Figure 5.9, the present results provide the most consistent agreement with the data, excluding the results of Olynick. The assumption made by Olynick of a Boltzmann distribution of the electronic state populations should have caused a significant over prediction of the radiation at the early trajectory points, as indicated by the behavior shown in Figure 5.4. Since this behavior was not predicted by Olynick, it may be concluded that his flowfield model is inconsistent with the present nonequilibrium VSL method, as well as past and present results from the LAURA Navier-Stokes code. A surprising result of Figure 5.9 is the relatively close agreement between the NE VSL and E VSL models, even though the shock layer is in considerable chemical nonequilibrium. This is a result of the non-Boltzmann model suppressing the radiation from the regions of chemical nonequilibrium, as shown in Figure 5.4. Note that if the comparison between these methods was made using Boltzmann results, the NE VSL prediction would be significantly

larger than the E VSL prediction, which would be essentially unchanged from the non-Boltzmann prediction. Hence, if nonequilibrium chemistry is accounted for, a non-Boltzmann model must be applied.

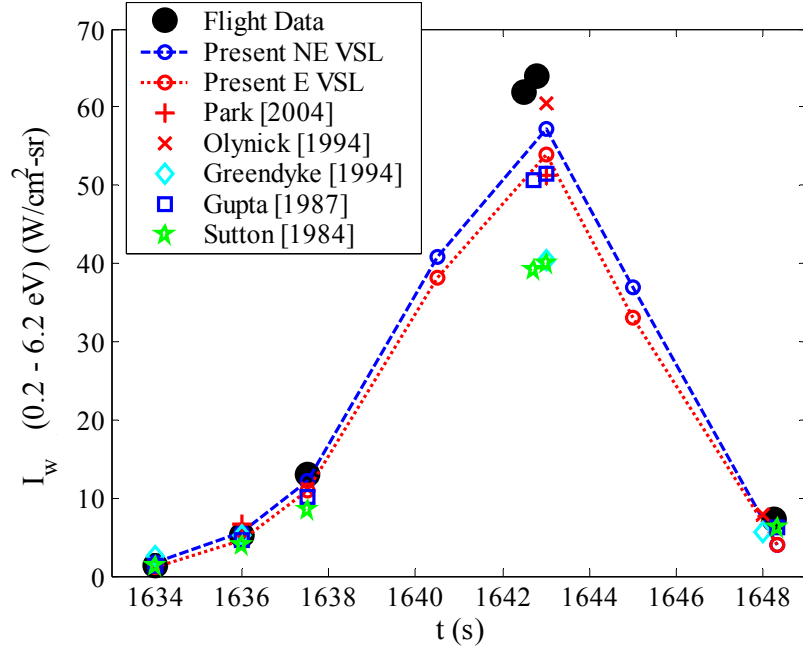


Figure 5.8. Comparison of the measured partial intensity ($0.2 - 6.2$ eV) with various predictions, including the results of the present radiation model applied to the NE and E VSL codes.

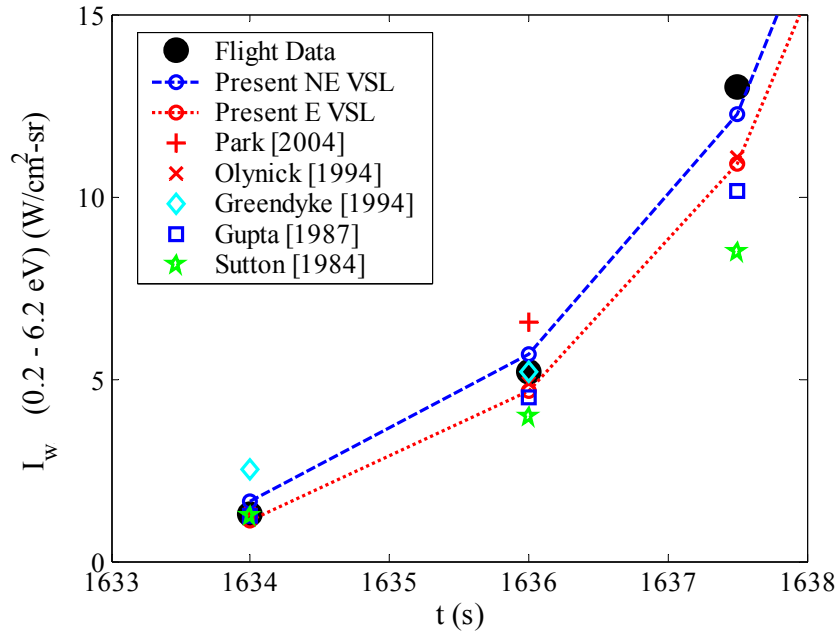


Figure 5.9. The same comparison as shown in Figure 5.8, except that it is focused on the early trajectory points for clarity.

The Fire II spectral radiometer data, which measured the intensity in the 2.2 – 4.1 eV spectral range, was presented and compared with past predictions in Section 1.4. The results of the present radiation model, coupled to the nonequilibrium (NE VSL) and equilibrium flowfield (E VSL) models, are compared with this data in Figure 5.10. The flight data is represented by two lines, representing the upper and lower limit of the data, which contained significant scatter. Good agreement is seen for the NE VSL method throughout the entire trajectory, while the E VSL results are slightly lower than the data. The radiation contained in this limited spectral range is due mostly to the N_2^+ first negative band system. For the 1634 to 1640 s points, this radiation is effected significantly by the rates chosen in Section 4.7 for the excitation of the $N_2^+(B)$ state. The agreement of the present model with the data at these points provides confidence that sufficient rates were chosen. Note that both Sutton's and Gupta's values are larger than the present predictions for the intensity from this 2.2 – 4.1 eV spectral range. Since Figure 5.8 shows that the contribution from the 0 – 6.2 eV range in these studies is actually smaller than the present predictions, then the radiation from the 0 – 2.2 eV range must have been significantly under predicted by Sutton and Gupta relative to the present model. This is likely a result of the increased line radiation in the 1 – 2 eV range resulting from the updated set of the atomic lines applied in the present model, and illustrated in Figures 3.3 and 3.4.

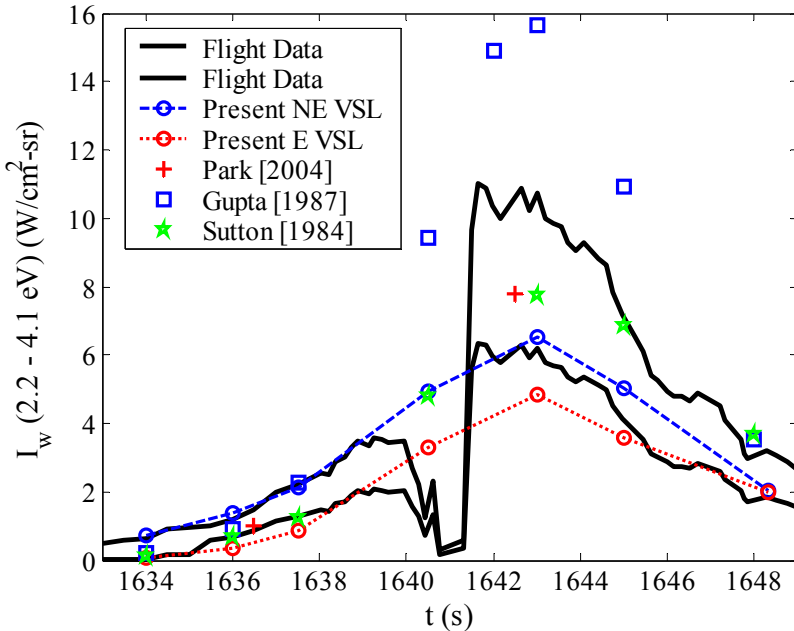


Figure 5.10. Comparison of the partial intensity (2.2 – 4.1 eV) measured by the Fire II spectral radiometer with the present results and previous predictions.

The Fire II total calorimeter measurements presented by Cornette [1965] contain the convective heating component along with the radiation absorbed by the beryllium calorimeter. This measured quantity, which will be labeled q_{total} , may be written as

$$q_{total} = q_c + \alpha q_r^- \quad (5.3)$$

where q_c is the convective heating and αq_r represents the radiation absorbed by the beryllium calorimeter. The absorbed radiation was obtained by multiplying the frequency-dependent radiative flux by the frequency-dependent absorptance (of polished beryllium) presented by Cauchon [1967]. The two components of Eq. (5.3) are presented in Table 5.2. The convective heating presented in this table assumes a super-catalytic wall, meaning the wall boundary condition specifies that the species recombine to their free-stream values at the wall. Figure 5.11 compares these super-catalytic values for q_{total} with the flight data. A consistent over-prediction of flight data is seen to exist at the earlier times. Two possible reasons for this over-prediction are that the wall is not actually super-catalytic and that the tangent-slab approximation, applied for the radiation transport calculation, is not accounting for the shock-layer curvature. Past studies concerning the accuracy of the tangent slab approximation have concluded that a detailed three-dimensional transport calculation produces a flux value about 20% lower than that predicted by the tangent slab approximation (Hartung and Hassan [1992c]). Applying this correction to the present results improves the comparison throughout the trajectory, although the present results are still too large.

The influence of surface catalyticity on the calorimeter predictions was studied by obtaining coupled flowfield solutions with a non-catalytic wall, which provides the opposite catalyticity extreme relative to the super-catalytic case. These results are presented in Figure 5.11 and are seen to compare significantly better with the data than the super-catalytic case. This comparison supports the argument that the beryllium surface of the calorimeter, at temperatures ranging from 600 to 1,600 K, is closer to being non-catalytic than super-catalytic. Both the super-catalytic and the non-catalytic cases predict peak heating at 1643 s, which disagrees with the 1645 s location indicated by the data. As indicated by Figure 1.5, this behavior is consistent with all previous theoretical predictions and has not been explained. Unlike the 1643 s point, the total radiometer data at 1645 s is not accurate enough[‡] to confirm the accuracy of the radiation prediction at this point (between 0.2 and 6.2 eV). Therefore, it is possible that some unknown radiation mechanism contributed to the apparent shift of the peak heating point. Note that Sutton [1984] showed that this shift was *not* due to the value used for the beryllium absorptance.

[‡] This is a result of the heat shield reaching its melting point.

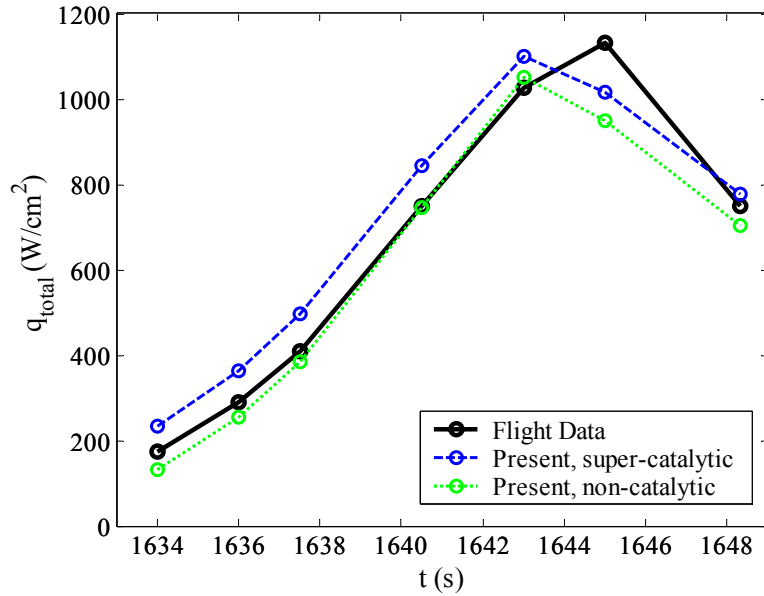


Figure 5.11. Comparison of the present results, assuming a catalytic and non-catalytic wall, with the Fire II calorimeter data. These are coupled values from the nonequilibrium VSL flowfield.

5.5 Radiative Heating Analysis of Apollo 4

A review of the Apollo 4 flight experiment was provided in Section 1.5. Only data for the partial intensity (0 – 6 eV) was obtained in this experiment. Relative to the Fire II case, there have been few theoretical studies of this data, all of which were discussed and compared in Section 1.5. The conclusion reached from this comparison was that the more advanced analysis performed by Park [2004], which included viscosity, two-temperatures, chemical nonequilibrium, non-Boltzmann radiation, and ablation did not compare as well as the inviscid, single-temperature, equilibrium, non-ablating analysis performed by Sutton [1984]. The goal of the present section is to apply the present flowfield and radiation models to the Apollo 4 trajectory, as was done for the Fire II case, and compare these with the flight data. Both the uncoupled and coupled results are presented in this section.

The flowfield kinetics and thermophysical properties applied here are the same as those applied to the Fire II cases in the previous section. A nose radius of 3.05 m was used, which was determined by Reid et al. [1972] to provide the proper shock-standoff distance for the radiometer location. The wall temperature was set equal to a constant value of 1,000 K, and ablation or blowing was not considered. The free-stream conditions for the considered trajectory points were defined previously in Table 1.3. Figures 5.12 through 5.15 present the temperature and number density

profiles along the stagnation-line for the 10 s and 32 s trajectory points obtained from the NE VSL method. The temperature profiles are shown for both the coupled and uncoupled cases, while, for clarity, the number densities are shown for only the uncoupled case. The $t = 10$ s case is seen to have a significant region of nonequilibrium, while the $t = 32$ s case is almost entirely in equilibrium. Because the nose radius for these cases is roughly three times as large as that for the Fire cases, the shock-layers are roughly three times as thick as those for the Fire cases.

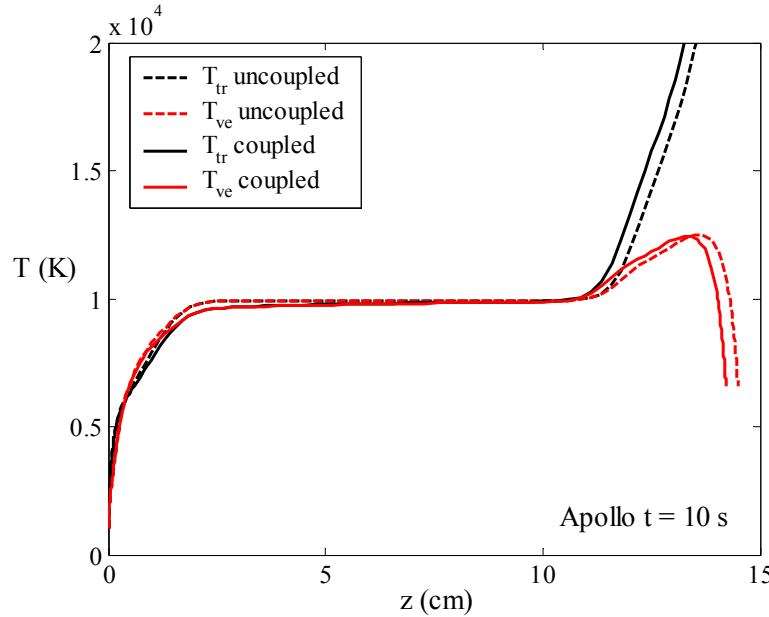


Figure 5.12. Uncoupled and coupled stagnation-line temperature profiles for $t = 10$ s.

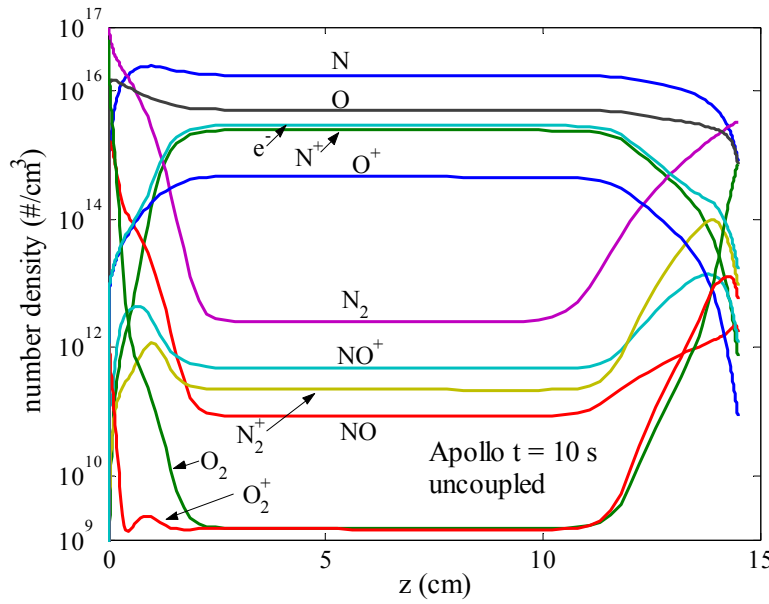


Figure 5.13. Uncoupled stagnation-line number density profiles for $t = 10$ s.

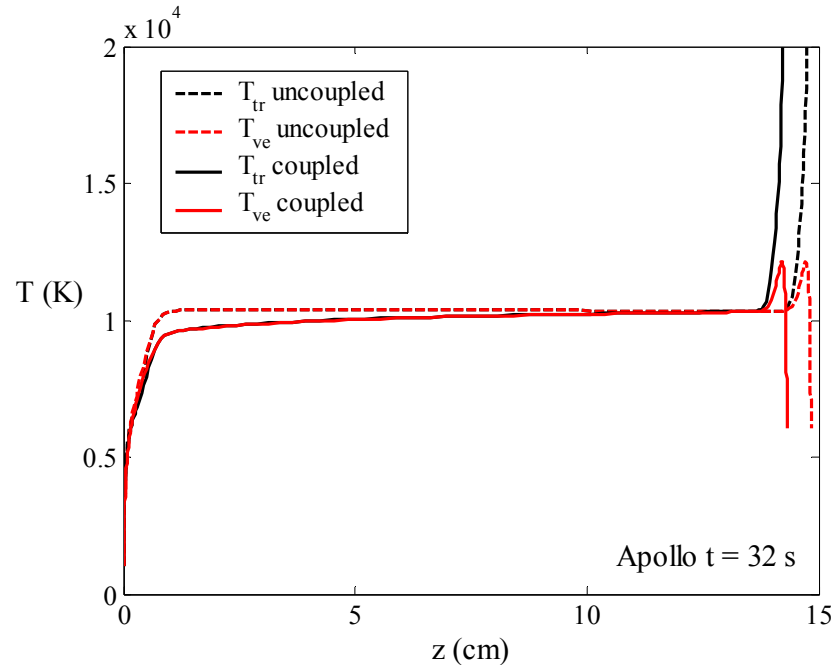


Figure 5.14. Uncoupled and coupled stagnation-line temperature profiles for $t = 32$ s.

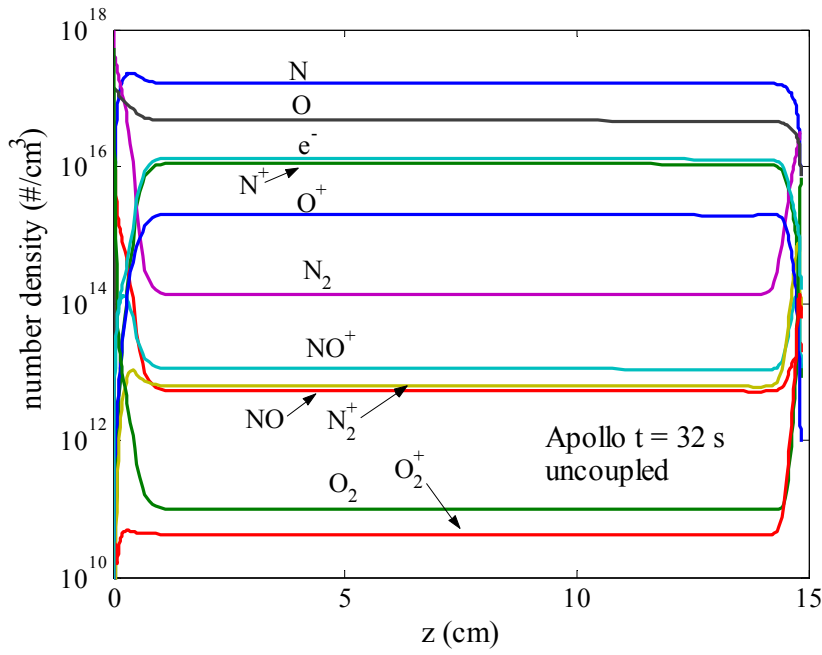


Figure 5.15. Uncoupled stagnation-line number density profiles for $t = 32$ s.

The convective heating, radiative heating, and radiative intensity values at the wall ($z = 0$) are presented in Tables 5.3 and 5.4 for the uncoupled and coupled cases, respectively. At peak radiative heating ($t = 32$ s), the radiative heating is reduced by about 30% while the convective heating is reduced by 8%. The effect of coupling for these cases is similar to that presented in the

previous section for the Fire case. Figure 5.17 illustrates this similarity by plotting the cooling factor (\mathcal{D}), which is the ratio of the coupled and uncoupled radiative heating, as a function of the Goulard factor Γ , which is a similarity parameter defined in the figure (for optically thin, inviscid, equilibrium shock layers), which was originally derived by Goulard [1961] in his study of the “cooling effect”, or decrease in radiation, found for coupled shock-layers. The Apollo and Fire cases are seen to have the same functional dependence on Γ , and they form a distinct band that could be used to estimate the cooling factor for an unknown case.

Table 5.3. *Uncoupled* convective and radiative heat-flux values (W/cm^2) and radiative intensities ($\text{W}/\text{cm}^2\text{-sr}$) for Apollo 4 obtained using the NE VSL flowfield model.

t (s)	q_c	q_r^- (0-18)	q_r^- (0-6)	q_r^- (6-18)	I_w (0-18)	I_w (0-6)	I_w (6-18)
10	96.2	31.3	16.0	15.3	6.1	2.7	3.4
20	161.2	157.5	85.5	72.0	32.1	15.0	17.1
24	191.2	243.6	140.5	103.1	49.9	24.9	25.1
28	219.8	335.6	204.5	131.1	68.6	36.4	32.2
32	246.4	420.7	270.4	150.3	85.5	48.2	37.3
40	260.7	276.3	196.2	80.1	53.7	34.0	19.7
44	250.9	140.4	104.6	35.8	26.2	17.5	8.7
52	210.9	23.7	17.9	5.7	4.2	2.9	1.3

Table 5.4. *Coupled* convective and radiative heat-flux values (W/cm^2) and radiative intensities ($\text{W}/\text{cm}^2\text{-sr}$) for Apollo 4 obtained using the NE VSL flowfield model.

t (s)	q_c	q_r^- (0-18)	q_r^- (0-6)	q_r^- (6-18)	I_w (0-18)	I_w (0-6)	I_w (6-18)
10	92.5	26.2	14.1	12.1	5.0	2.3	2.7
20	150.2	116.6	68.2	48.4	23.3	11.8	11.5
24	177.0	174.9	108.9	66.0	35.1	19.0	16.1
28	203.0	235.7	155.0	80.7	47.2	27.2	20.0
32	227.6	292.8	202.0	90.8	58.1	35.5	22.6
40	247.4	208.5	154.9	53.7	39.7	26.5	13.2
44	243.3	115.9	88.7	27.2	21.3	14.8	6.6
52	209.6	23.1	17.6	5.6	4.1	2.8	1.3

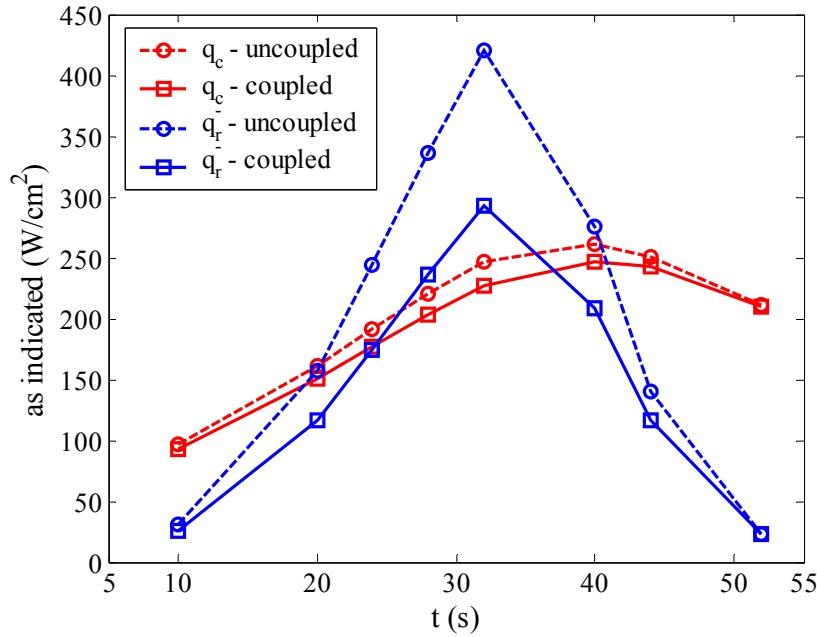


Figure 5.16. Uncoupled and coupled values for the convective and radiative heat flux along the Apollo 4 trajectory obtained from the NE VSL model.

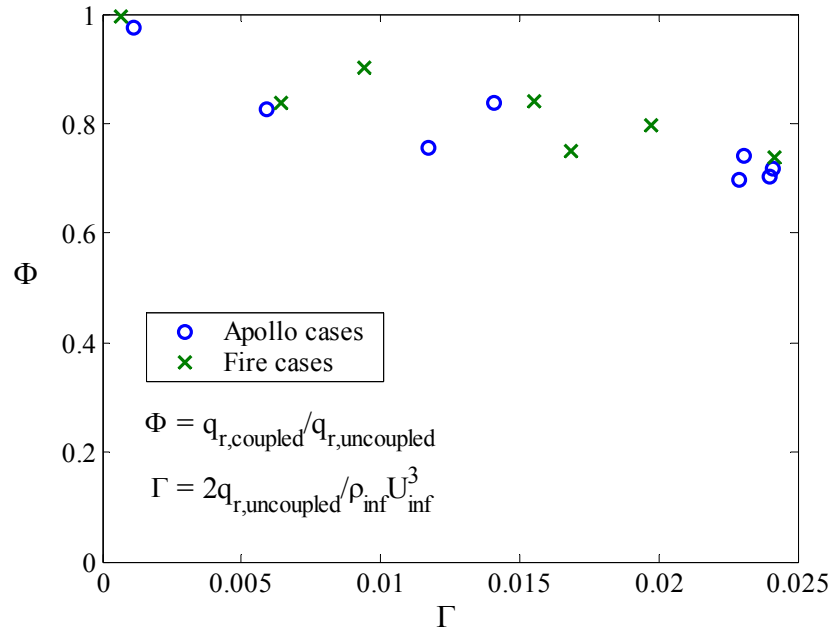


Figure 5.17. Cooling factors derived from the present Apollo and Fire results.

As was done for the Fire cases, the equilibrium VSL (E VSL) cases were run in addition to the nonequilibrium VSL cases (NE VSL). These equilibrium cases provide baseline values that may be compared to the corresponding nonequilibrium values, which allows the effect of

nonequilibrium to be assessed. Figure 5.18 compares the uncoupled and coupled partial intensity values resulting from the NE VSL and E VSL models. The two models are seen to agree throughout the trajectory. As was discussed in Section 5.4, this good agreement would not be present if the Boltzmann distribution of electronic states was applied to the NE VSL model. Figures 5.19 and 5.20 illustrate this point by comparing the wall-directed radiative flux profiles resulting from the NE VSL flowfield with a non-Boltzmann and Boltzmann model for the radiating electronic states, and a E VSL flowfield with a Boltzmann model for the electronic states. For the $t = 10$ s case shown in Figure 5.19, the Boltzmann model results in a 100% over prediction of the flux reaching the wall. For the $t = 32$ s cases, the nonequilibrium region is much smaller, and thus the influence of the non-Boltzmann model is seen to be considerably less.

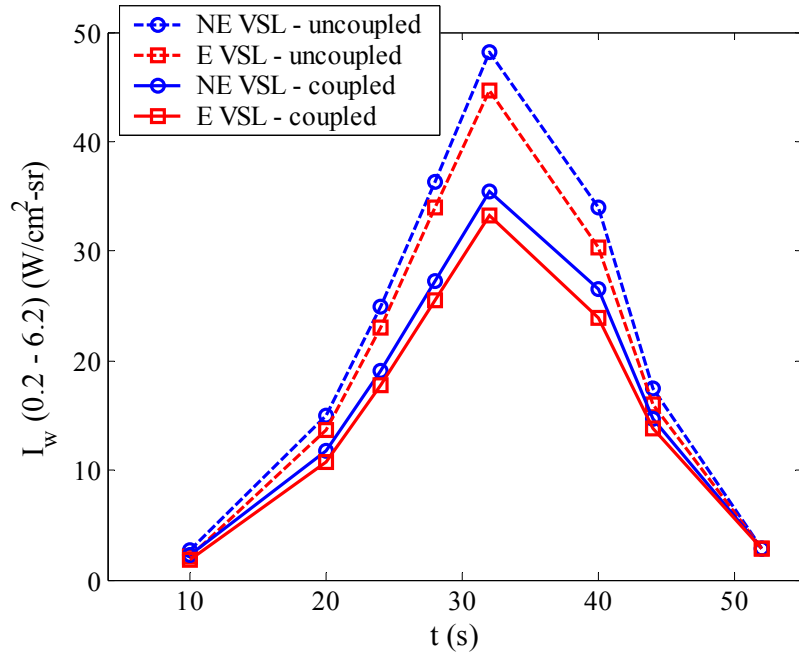


Figure 5.18. Partial wall intensity values (0.2 – 6.2 eV) predicted by the coupled and uncoupled application of the NE and E VSL flowfield models.

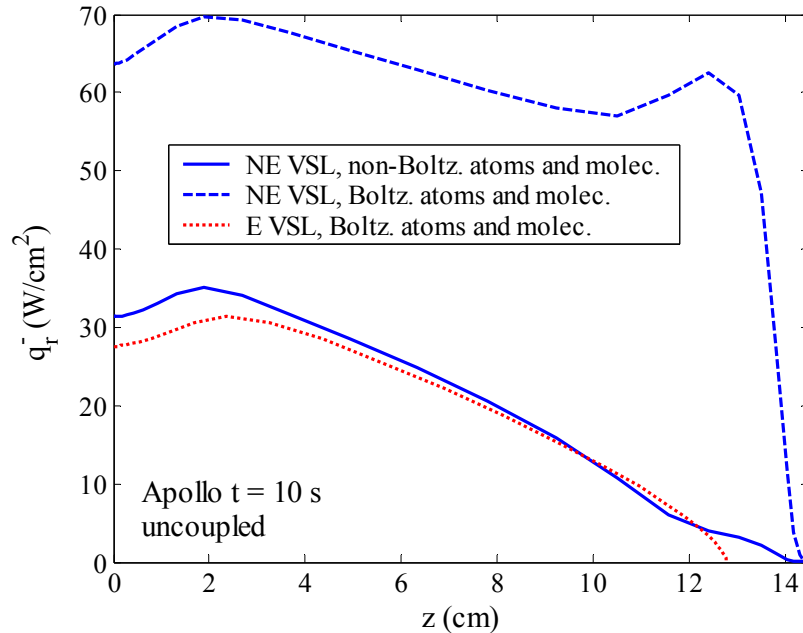


Figure 5.19. Wall-directed radiative flux profiles resulting from the different flowfield models, and treatment of the electronic state populations, for the $t = 10$ s case.

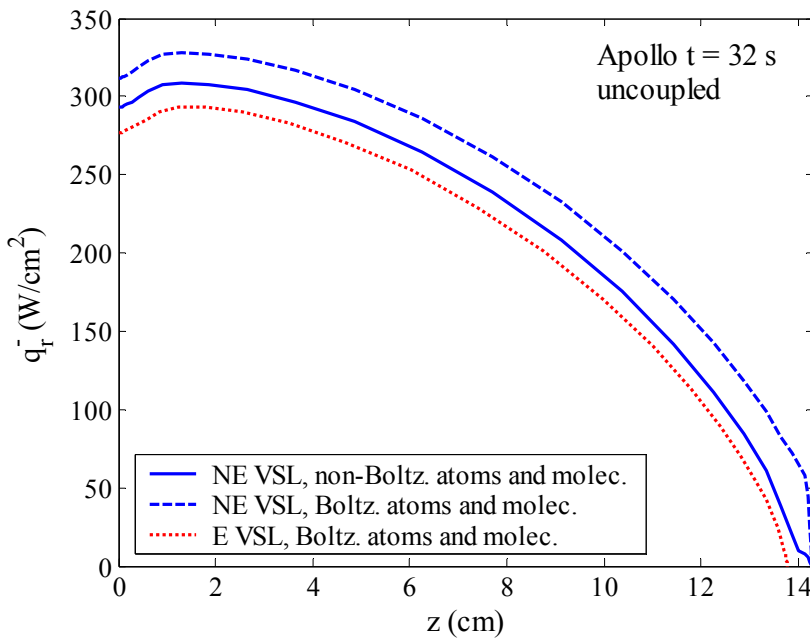


Figure 5.20. Wall-directed radiative flux profiles resulting from the different flowfield models, and treatment of the electronic state populations, for the $t = 32$ s case.

The radiative flux spectrum at the wall for the $t = 10$ and 32 s cases are presented in Figures 5.21 and 5.22. The accumulated flux, from left right, shown in these figures allows the contribution

from the various spectral regions to be seen. The major contributors to the total flux are identified from these figures to be the atomic lines between 1.3 and 1.7 eV, the N_2^+ first negative band system located between 2.0 and 5.0 eV, the strong VUV lines between 7.0 and 12.0 eV, and the atomic bound-free contribution located above 10.0 eV. The VUV N_2 band systems were included in the present study, as discussed in Section 3.9, and their influence on the absorption in the boundary layer was found to be much less than that predicted by Park [2005]. Park predicted that these band systems would absorb nearly all of the radiation located above 8.0 eV, while the present study finds that no more than 10% of the VUV radiation is absorbed by these band systems. This difference may possibly be attributed to the non-catalytic wall and ablation products treated by Park, as well as the different data used for the VUV band systems. The ablation products treated by Park resulted in ten CO and H_2 band systems located in the VUV, which possibly contributed to his strong boundary layer absorption predictions.

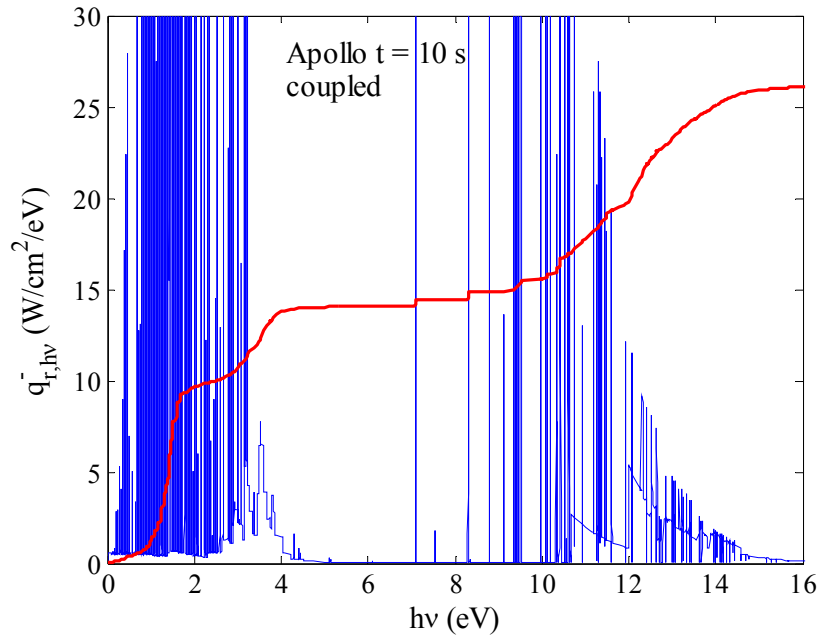


Figure 5.21. Radiative flux spectrum at the wall for the $t = 10$ s case.

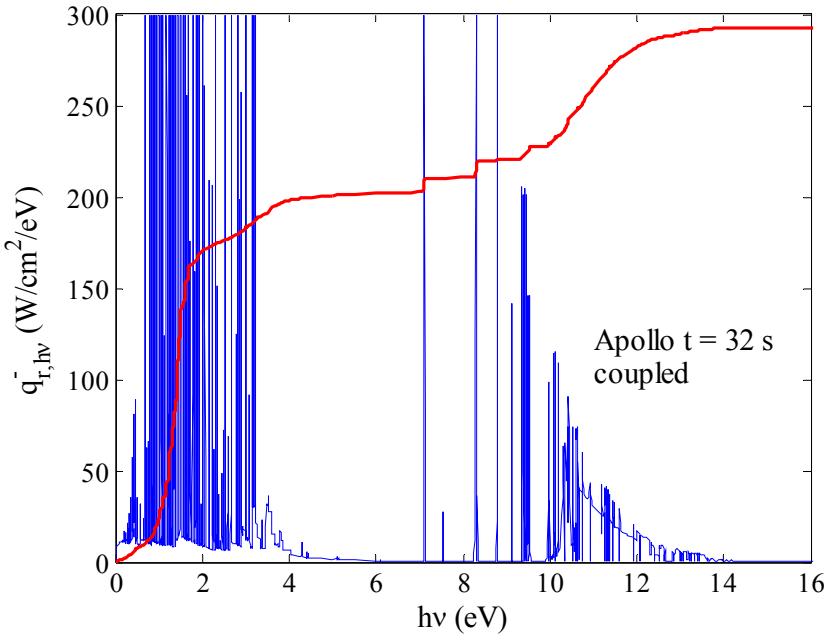


Figure 5.22. Radiative flux spectrum at the wall for the $t = 32$ s case.

The Apollo 4 radiometer data, which was presented previously in Figure 1.8, is compared with the present *coupled* predictions in Figure 5.23. Both the NE VSL and E VSL values are presented, along with the previous predictions by Park [2004] and Sutton [1984]. The present model is seen to over-predict the flight data throughout most of the trajectory. The present values are larger than Sutton's values, which is consistent with the comparison shown in Figure 5.8 for the Fire data. Much of the present over prediction is due to the updated atomic line data applied in the present radiation model (discussed in Section 3.4). Figure 5.24 compares the accumulated intensity, from left to right, resulting from the present line model and the older line model applied by Park [1985]. The actual spectrum is shown for reference in this figure, and corresponds to the present line model. As shown previously in Figures 3.3 and 3.4, this model results in an increased contribution from the 1.3 to 1.7 eV spectral range. The atomic data for the present line model is known to be more accurate than the older values, as indicated in Tables 3.5 and 3.6, and therefore should not be responsible for the present disagreement with the flight data. Although a good agreement between the present results and the values of Park [2004] is shown in Figure 5.23 for the $t = 24$ and 32 s points, the actual profiles of the radiative flux or intensity are quite different. This is seen by comparing Figure 5.20 of this paper with Figure 11 of Park [2004] (although Figure 5.20 presents the uncoupled values, the shape of the coupled curves are similar). Park shows a sharp spike in the flux directly behind the shock, which is likely a result of the relatively large region of nonequilibrium behind the shock predicted by his flowfield model. Note that this

region of nonequilibrium is much larger than that predicted by the present model, which is seen by comparing the temperature profiles shown in Figure 5.14 of this paper with those shown in Figure 7 of Park [2004].

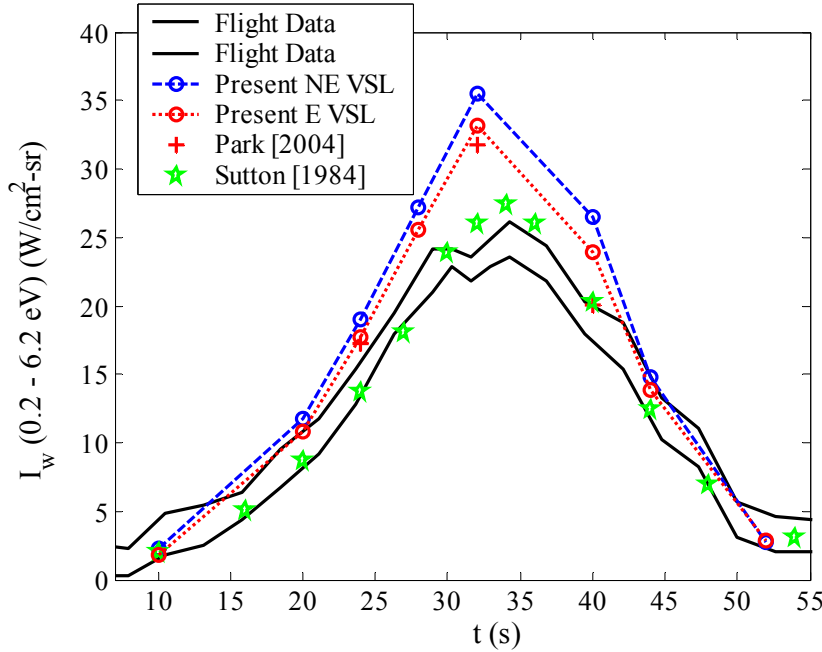


Figure 5.23. Comparison of the measured partial intensity ($0.2 - 6.2$ eV) with various predictions, including the results of the present model.

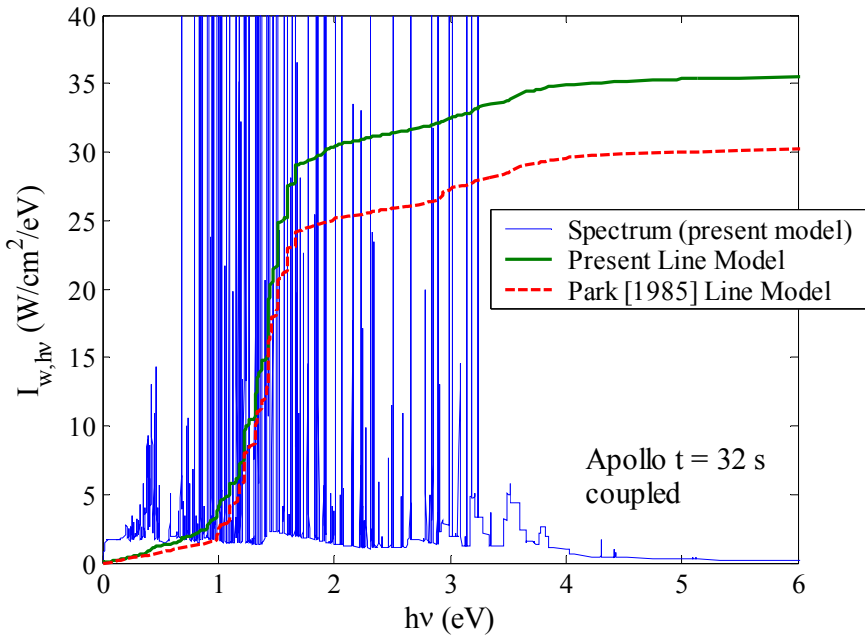


Figure 5.24. Influence of the updated atomic line model on the intensity between 0 and 6 eV.

A possible explanation regarding the poor agreement of the present results with the Apollo 4 flight data is that the flight data was affected significantly by phenomena not accounted for in the present model. Reid et al. [1972] mention that a residue was found in the radiometer cavity upon post-flight inspection, and that the radiometer did not function until this residue was removed. It is suggested in Appendix B of Reid et al. [1972] that this residue was likely deposited after peak heating conditions were reached, and therefore did not affect peak heating measurements. It is also reported, though, that post-flight radiometer performance tests indicated that relatively cool ablation products could have filled the radiometer cavity during flight, which because of their strong absorption characteristics, could have caused a decrease in the measured radiation. This possibility was also discussed by Park [2004], who concluded that this likely did not occur, because the detector window was not found to have any carbon deposit on it in the post-flight inspection. Assuming the window was relatively cold, these deposits would have formed if carbon species were present in the cavity. This argument assumes that the residue found on the window during the post flight inspection was not carbon. The present author could not find any information that specified the chemical composition of this residue. In conclusion, the present over-prediction of the data supports the possibility that the radiometer was contaminated with ablation products, especially considering the good agreement presented in the previous section for the Fire II vehicle, which was non-ablating.

Chapter 6

Radiative Heating for Huygens Entry into Titan

6.1 Chapter Overview

Recent studies concerning the aerothermodynamic environment of the Huygens probe, for entry into Titan, have indicated that significant uncertainty exists in the prediction of shock-layer radiative heating (Hollis et al [2005], Wright et al. [2006]). A review of these studies leads to the conclusion that this uncertainty may be attributed to three primary sources: 1) the accuracy of the CN violet and red molecular band spectral representations (these band systems contribute the majority of the radiation at Huygens entry conditions); 2) the influence of radiation-flowfield coupling; 3) the accuracy of the kinetic scheme required for modeling the CN electronic state populations. The first of these was made clear by Hollis et al. [2005], who showed that two widely used radiation codes, NEQAIR and RAD/EQUIL, disagreed by a factor of two for Huygens conditions. Wright et al. [2006] have since shown agreement between the line-by-line approach of NEQAIR and other similar but independent line-by-line codes, which suggests that the lack of agreement shown by Hollis was due to inadequacies in the molecular band modeling of the RAD/EQUIL code. The uncertainty in the spectral modeling is therefore small if the line-by-line approach is used. The drawback to this approach is that it is very computationally expensive, which makes it very difficult to apply to a coupled radiation-flowfield analysis. Therefore, although it models the spectrum accurately for given flowfield conditions, the inaccuracy due to ignoring coupling remains, which was the second source of uncertainty listed above. The coupling effect has been approximately treated in these past studies using a correction factor developed for Jupiter entry (Tauber and Wakefield [1971]). Unfortunately, this

approximate method has not been validated for Titan entry with non-optically thin radiation. Further complications to the radiation calculation arise from the recent suggestion (Bose et al. [2005]) that the excited electronic states of the CN molecule are not populated by a Boltzmann distribution. Kinetics schemes for CN excitation, similar to those presented in Chapter 4 for air molecules, have been proposed recently by both Raynaud et al. [2005] and Magin et al. [2005] specifically for Titan. Similarly to the air cases studied in Chapter 5, these models are shown to reduce the radiative heating significantly. The influence of radiative absorption on the excitation calculation, as discussed by Bose et al. [2005], complicates the calculation further, especially if the spectrum is modeled using the line-by-line approach.

The aim of the present study is to formulate the Huygens probe radiative heating prediction, including all effects mentioned above, into a manageable calculation. The thermochemical nonequilibrium viscous-shock-layer analysis presented in Chapter 2 will be used for the flowfield calculation. The line-by-line method of calculating the radiative spectrum will be compared with the smeared rotational band (SRB) method (discussed previously in Section 3.8 for application to air molecules) at conditions of interest for the Huygens probe. A new approach to the spectrum calculation, which is a slight modification of the smeared-rotational band approach, will be discussed and validated. The radiative heating to the Huygens probe near peak heating conditions will be calculated using the developed flowfield and radiative models for both the coupled and uncoupled radiation cases. Finally, the collisional-radiative (CR) model formulation presented in Chapter 4 will be applied specifically to the CN molecule, and its effect on the radiative flux at Huygens peak heating conditions will be discussed.

6.2 Spectral Modeling of CN Molecular Band Radiation

The two methods that will be considered here for the modeling of the CN molecular bands are the line-by-line (LBL) approach, as presented by Arnold and Whiting [1969] and used in NEQAIR (Park [1985] and Whiting et al. [1996]), and the smeared-rotational band (SRB) approach, as derived by Patch, Shackleford, and Penner [1962] and extended to higher order accuracy and multiple temperatures by Chambers [1992 and 1994]. The details of the LBL approach for a $^2\Sigma - ^2\Sigma$ transition, which is consistent with the CN violet ($X^2\Sigma^+ - B^2\Sigma^+$) transition, are presented in Appendix D. The details of the SRB approach are presented in Section 3.8. The spectroscopic constants and absorption oscillator strengths ($f_{VV'}$) for the CN violet and red transitions were taken from Laux [1993] for the present study.

The emission coefficients for the CN *red* band, and the resulting radiative flux, presented in this paper are $\frac{1}{2}$ of the values reported in an earlier version of this work (Johnston et al. [2006]). This is a result of the missing $g_{e''}/g_e$ factor in Eq. (3.38) (fortunately, this factor is equal to one for CN violet). The corrected values for the CN red radiation have been included throughout the present paper, including the radiation-coupled cases, although because of the minor importance of the CN red radiation for Huygens entry, this did not change any of the conclusions reached previously in Johnston et al. [2006].

Assuming that it is implemented correctly and that accurate spectroscopic data is used, the LBL approach is considered to provide the theoretically exact radiative spectrum for a molecule. As a result, it provides an accurate value for the spectrally-integrated radiative flux, regardless of the optical depth. The drawback to this method is that it requires an enormous number of spectral points (on the order of 100,000 for the spectral range of the CN violet band). This makes it very difficult to apply in a coupled radiation-flowfield calculation, where many radiation calculations are required. The SRB method, on the other hand, produces an approximate spectrum that captures the average shape of each vibrational band ($V' - V''$). This provides a rough estimate of the spectrum while maintaining an accurate spectrally-integrated radiative flux in the optically thin limit. The accuracy of the SRB method in the optically-thin limit is a result of the method's derivation, which forces this to be true for any molecular band system. Figure 6.1 compares the LBL and SRB values for the integrated emission coefficient, which is proportional to the integrated flux in the optically thin limit, for the CN violet band over a range of temperatures. The contribution from each of the major three vibrational bands is shown separately along with the total. In all cases, good agreement is seen between the SRB and the LBL values. This confirms the statement that the SRB method is a good approximation of the LBL method for an optically thin gas.

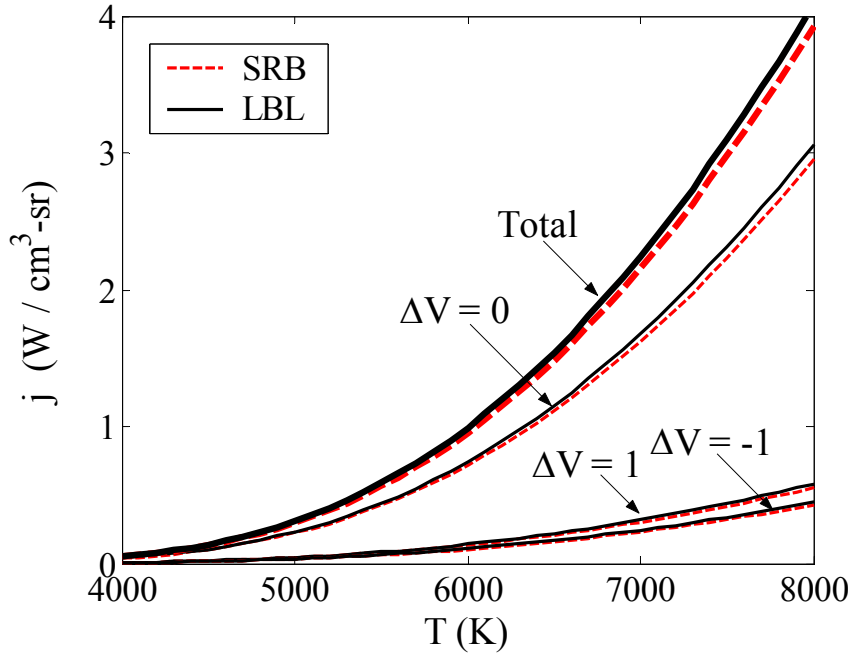


Figure 6.1. Comparison of the LBL and SRB predictions for the *CN violet* integrated emission coefficient for $N_{CN}=1\times10^{15} \text{ cm}^{-3}$

To examine how the methods compare as the gas becomes more optically thick, Table 6.1 compares the integrated intensity from a 1-cm slab of CN in equilibrium at 7000 K in spectral range of 3.176 to 3.444 eV for various pressures. The entire $\Delta V = 0$ band and a small part of the $\Delta V = 1$ band are captured in this spectral range. This comparison was also made by Wright et al. [2006], whose values are shown in the “NEQAIR96” column of the table. The NEQAIR96 values, which are from a line-by-line calculation, compare well with the current LBL results. A comparison was also made between the present LBL results and the NEQAIR96 results for the intensity resulting from spectral intervals of 25 Angstrom. The two values were shown to compare within 5% for each interval. This excellent comparison provides confidence that the present LBL calculation has been implemented correctly. As for the comparison between the LBL and SRB values, Table 6.1 shows that they do *not* compare well for the two higher pressure cases. This suggests that the SRB method is inadequate for modeling a gas with optically thick spectral regions. The optical thickness of a constant property slab is dependent on the term $N_{CN}\Delta z$, where N_{CN} is the CN number density and Δz is the thickness of the slab. This term is a similarity parameter for the radiative flux emitted from a constant property slab of CN in equilibrium. Taking the shock-layer thickness to be about 10-cm from Figure 2.13 and N_{CN} to be about $1\times10^{15} \text{ cm}^{-3}$ from Figure 2.14, a constant property slab representative of Huygens peak heating conditions is found to have a $N_{CN}\Delta z$ equal to about $1\times10^{16} \text{ cm}^{-3}$. Figure 6.2 compares the LBL and

SRB result in a small region of the spectrum (3.19 - 3.21 eV) for the 0.001 and 0.01 atmosphere cases, which correspond to values of $N_{CN}\Delta z$ equal to 1×10^{15} and $1\times 10^{16} \text{ cm}^{-2}$, respectively. It is seen in these comparisons that the SRB model does not capture the intense peaks predicted by the LBL model at each vibrational band head. This has a small influence on the integrated flux for the 0.001 atm case ($N_{CN}\Delta z = 1\times 10^{15} \text{ cm}^{-2}$) because even the largest peaks of the LBL spectrum are less than 75% of the blackbody limit (which is represented by πB_v in the figure) so that the entire spectrum is essentially optically thin. For the 0.01 atm case ($N_{CN}\Delta z = 1\times 10^{16} \text{ cm}^{-2}$), it is seen that the vibrational band heads predicted by the LBL method are suppressed by the blackbody limit, and much of the nearby spectrum is near this limit. These spectral regions are therefore optically thick. The SRB prediction for this case, on the other hand, fails to predict any spectral region that is more than half of the blackbody limit. The predicted spectrum therefore remains optically thin, which means that the absorption and corresponding reduction in flux predicted by the optically thick LBL method is not properly modeled by the SRB method. As a result, the spectrally integrated flux listed in Table 6.1 for the SRB model is larger than the LBL prediction, and the comparison between the two methods gets worse as the optical thickness increases.

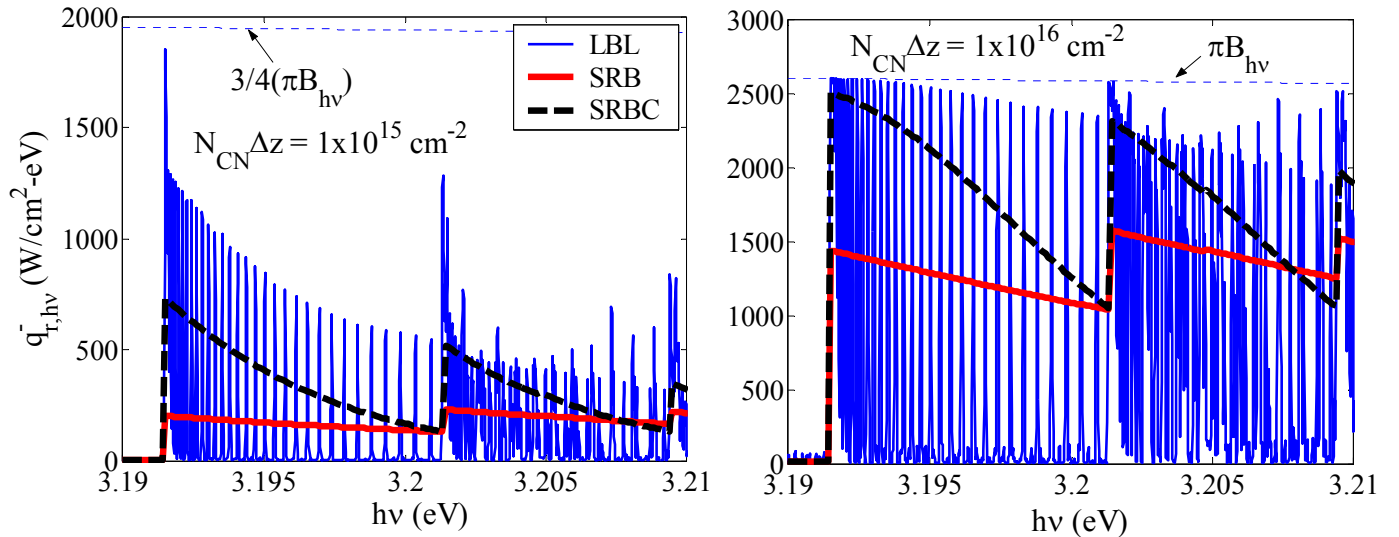


Figure 6.2. Comparison between the various spectrum models for the radiative flux spectrum from a constant property slab of CN at 7000 K. The spectral range shown illustrates the (0-0) and (1-1) band heads.

Table 6.1. Intensity resulting from a 1-cm constant property slab of CN in equilibrium at 7000 K ($\text{W}/\text{cm}^2 \cdot \text{sr}$)

p (atm)	N_{CN} (cm^{-3})	NEQAIR96	Present - LBL	Present - SRB
0.001	1.05×10^{15}	1.67	1.60	1.63
0.01	1.05×10^{16}	11.7	11.6	14.3
0.1	1.05×10^{17}	41.0	39.6	60.3

The previous discussion indicated that the SRB method does not provide a satisfactory model for the spectrum at Huygens peak heating conditions. Through the course of the present work, a simple correction to this model was developed that considerably improves its modeling capability. To rationalize the correction developed for the SRB method, it is first observed from the equations presented in Section 3.8 that decreasing the rotational temperature (T_r) increases the magnitude of each vibrational band head. This implies that the spectrum has larger spikes, which is the behavior required for a better agreement with the LBL results. Since this method is an approximation to begin with, it is justifiable to consider the possibility of choosing a nonphysical value of T_r to improve the method's agreement with the LBL results. This is equivalent to introducing an empirically derived correction factor into the SRB equations wherever T_r appears, and does not imply that the physical value of the rotational temperature is believed to be any different than what is predicted by the flowfield solution (where it is assumed equal to the translational temperature). The initial concern in attempting this approach is that it may reduce the accuracy of the SRB method in the regime in which it is already known to be accurate, which was shown previously in Figure 6.1 to be the optically thin limit. Therefore, for this approach to be valid, it must be shown that the rotational temperature has a small influence on the frequency-integrated emission coefficient (j). The integrated emission coefficient from a single vibrational band ($j_{VV''}$) may be evaluated analytically for the SRB method as follows

$$\begin{aligned} j_{VV''} &= \frac{N_{e'}}{Q_{V'} Q_{J'}} \exp\left(-\frac{hc}{kT_v} E_{V'}\right) \frac{2\pi e^2 h}{c^4 m} \frac{g_{e''}}{g_{e'}} \frac{f_{VV''}}{|B_{e'} - B_{e''}|} \int_{\nu_{VV''}}^{\infty} \nu^3 \exp(-C_r(\nu - \nu_{VV''})) d\nu \quad \left(\frac{\text{erg}}{\text{cm}^3 \cdot \text{s} \cdot \text{sr}} \right) \\ &= \frac{N_{e'}}{Q_{V'}} \exp\left(-\frac{hc}{kT_v} E_{V'}\right) \frac{2\pi e^2 h}{c^3 m} \frac{g_{e''}}{g_{e'}} f_{VV''} \underbrace{\left[\nu_{VV''}^3 - \frac{3}{C_r} \nu_{VV''}^2 - \frac{6}{C_r^3} (C_r \nu_{VV''} - 1) \right]}_{\underline{\nu_{VV''}^3}} \end{aligned} \quad (6.1)$$

where

$$C_r = \frac{B_{V'}}{B_{V'} - B_{V''}} \frac{h}{kT_r} \quad (6.2)$$

and $\nu_{VV''}$ is the frequency of the vibrational band head. The other parameters in this equation are defined in the Nomenclature section of this document. The useful result of this equation is that the underlined terms are the only place where the rotational temperature appears. This is significant because the underlined terms are negligible relative to the $\nu_{VV''}^3$ term for any practical case. This is because $\nu_{VV''}$ is usually much larger than $1/C_r$ ($\nu_{VV''} \sim 25,000 \text{ sec}^{-1}$ for the CN violet band while $1/C_r \sim 170 \text{ sec}^{-1}$). It is therefore shown that the rotational temperature has a very

small influence on the integrated emission, which was the desired result. The next step is to find the value for T_r which provides the best fit to the LBL calculation over a wide range of conditions. By investigating numerous constant property slabs over a range of temperatures and optical depths, the best value was found to be $T_r = 1700$ K. The results obtained using this approach will be referred to throughout this paper as the smeared rotational band corrected model, or SRBC. An example of the spectrum produced by this approach is shown in Figure 6.2. As intended, the vibrational band head peaks are much larger and more closely imitate the LBL spectrum. Figure 6.3 compares the flux from a constant-property slab at various optical depths and two different temperatures. The results consider the radiation from only the CN violet $\Delta V = 0$ region of the spectrum, which is the most optically thick. The success of the SRBC method is clearly seen throughout the entire range of conditions. This result is characteristic of the other conditions investigated, which included temperatures ranging from 3000 to 9000 K. As mentioned previously, the constant property slab characteristic of the shock layer at Huygens peak heating conditions requires a value of $N_{CN}\Delta z$ no larger than $1 \times 10^{16} \text{ cm}^{-2}$. Therefore, the SRBC model is more than adequate for the present application.

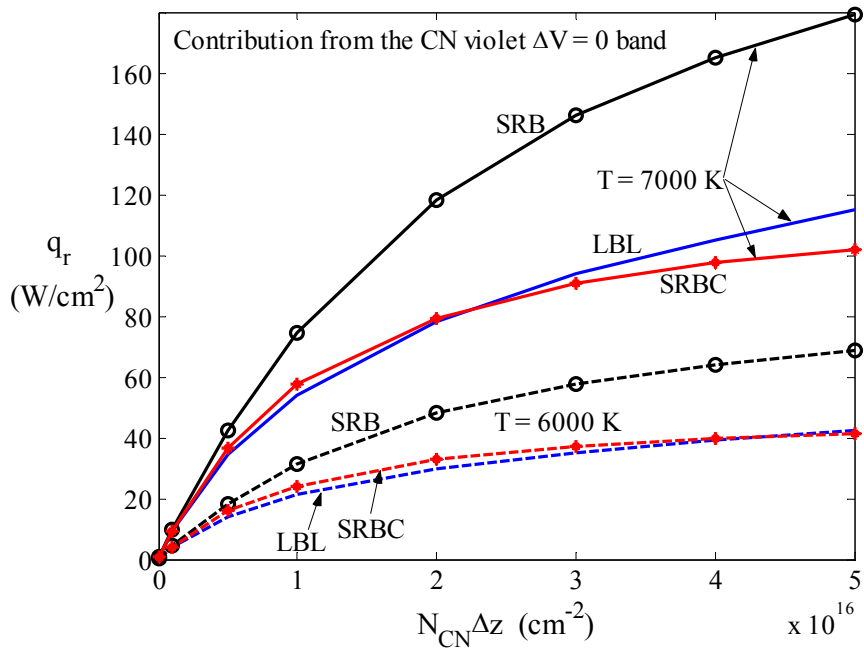


Figure 6.3. Comparison of the radiative flux from a constant property slab for different spectral models.

6.3 Uncoupled and Coupled Radiative Heating Assuming a Boltzmann Distribution

The SRBC model was shown in the previous section to accurately predict the radiative flux for conditions of present interest. The use of the SRBC approach, rather than the LBL approach, results in a significant decrease in the computational burden associated with radiation coupling. But, to be completely sure that the SRBC model is providing accurate results, the SRBC *and* LBL approach will be used here for the *uncoupled* calculations. This allows the accuracy of the SRBC method to be monitored relative to the LBL calculations for an actual shock layer, and not just a constant property slab. For the coupled calculations, only the SRBC approach is used. However, once a converged coupled flowfield is obtained, the LBL approach is used to check the validity of the SRBC in the new flowfield. Note that *no* correction has been included in the presented results to account for shock-layer curvature effects. In the study by Wright et al. [2006], a correction is applied by multiplying the radiative heat flux by 0.8.

Table 6.2 presents a breakdown of the uncoupled radiation spectrum for the three trajectory points considered. The values in parentheses are the LBL results, while the values *not* in parentheses are the SRBC results. This convention will be used throughout the rest of this paper. Note that the CN red spectrum was only calculated using the SRBC approach. This table shows good agreement between the two methods for both the total flux value and the individual components. The distribution through the shock layer of each of these components, predicted by the SRBC approach for the $t = 189$ case, is shown in Figure 6.4. The corresponding radiative flux spectrum at the wall for the CN violet band is shown in Figure 6.5. It is seen that the different ΔV bands do not overlap, which means that they may be treated independently in the spectrum and transport calculation. This is also true for the CN red band as a whole, which is located around 1 eV. The radiative heating values predicted by previous studies (Hollis et al. [2006]) are also listed in Table 6.2 for comparison. The RAD/EQUIL result is much larger than the current prediction is because it models the molecular band spectrum with a curve-fit over frequency, which is even more of an approximation than the SRB model. The blackbody limiting effect is therefore under predicted because the spectrum is too smooth, similarly to the SRB model. The agreement of the current predictions with the NEQAIR results is excellent, especially considering that different flowfield models were applied. The smaller contribution from the CN red band presented here, relative to those presented in the earlier version of this paper, improved the

agreement with the NEQAIR results considerably. Note that the study by Olejniczak et al. [2003], using NEQAIR, ignored the CN red contribution entirely.

Table 6.2. Breakdown of the radiative heat flux towards the wall (q_r) at $z = 0$ for the *uncoupled* case (W/cm^2), values *not* in parenthesis are the SRBC predictions and values *in* parenthesis are the LBL predictions.

t (s)	CN violet $\Delta V = 0$	CN violet $\Delta V = 1$	CN violet $\Delta V = -1$	CN red	Total	NEQAIR*	RAD/EQUIL*
185	46.7 (47.7)	11.6 (12.6)	9.0 (9.5)	4.4	71.7 (74.2)	72.3	118.4
189	50.5 (50.7)	13.5 (14.8)	11.3 (11.8)	7.5	82.8 (84.8)	81.5	143.1
193	39.8 (39.3)	11.3 (12.7)	10.3 (10.7)	10.5	71.9 (73.2)	72.1	147.2

*Values presented by Hollis et al. [2006]

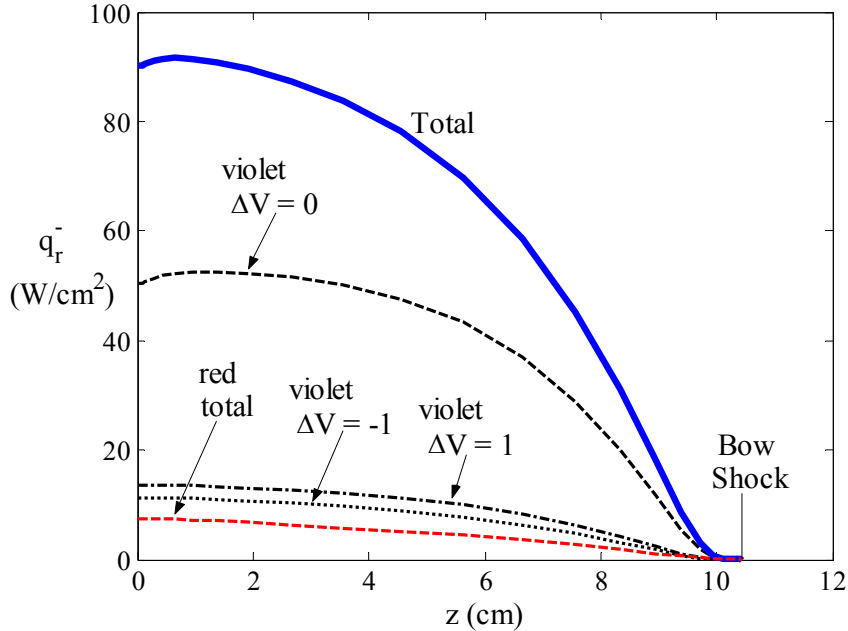


Figure 6.4. The contributions from the various radiative mechanisms to the wall directed radiative flux profile for the $t = 189$ uncoupled case

As mentioned previously, radiation-coupled flowfields were obtained using the SRBC approach for the radiation model. This computationally efficient approach allowed coupled flowfields to be obtained without making any assumptions regarding the optical thickness, as was done in previous studies (Mazoue et al. [2005], Wright et al. [2005]). A discussion and comparison of the coupled flowfields will be presented here, followed by a discussion of the coupling effect on the radiative heating. Figure 6.6 compare the temperature profiles for the $t = 189$ uncoupled and coupled cases. The expected trend for the coupled case of reduced temperature and shock standoff distance is seen. Figure 6.7 compares the CN number density profiles for the coupled

and uncoupled cases. The interesting result of increased CN number density with the addition of coupling is found. The explanation of this phenomenon requires the study of the contribution of each chemical reaction that involves CN to the total mass rate of formation of CN. Figure 6.8 plots the mass rate of formation of CN resulting from three of the main reactions involving CN. Although Gocken's [2004] simplified reaction set contains 6 reactions involving CN, the three not presented here do not contribute significantly to the difference between the coupled and uncoupled cases, although their contribution is included in the "Total" line presented in Figure 6.8. The reason for the increased CN number density for the coupled case is seen from this figure to be a result of the smaller *negative* formation values from reactions 1 and 3. Because these two reactions involve CN as a reactant, the lower temperatures throughout most of the shock layer for the coupled case results in a decreased forward reaction rate, and therefore lower rate of CN destruction. Reaction 2 has the opposite effect, but its influence is overshadowed by reactions 1 and 3. The large positive formation values near the shock reach almost exactly the same peak for the coupled and uncoupled case, which explains the similar number density profiles seen near the shock in Figure 6.7.

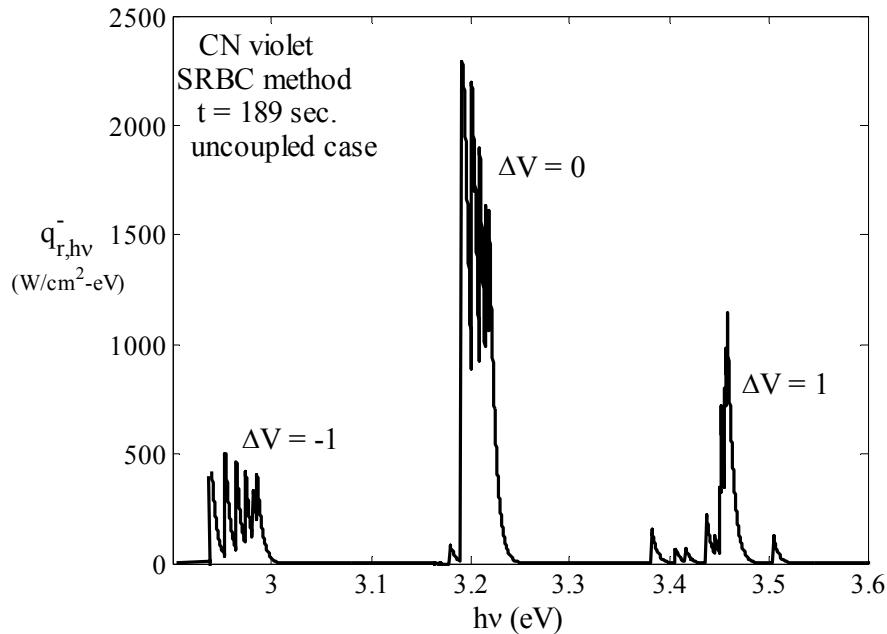


Figure 6.5. The CN violet spectrum at the wall as predicted by the SRBC method for the $t = 189$ coupled case.

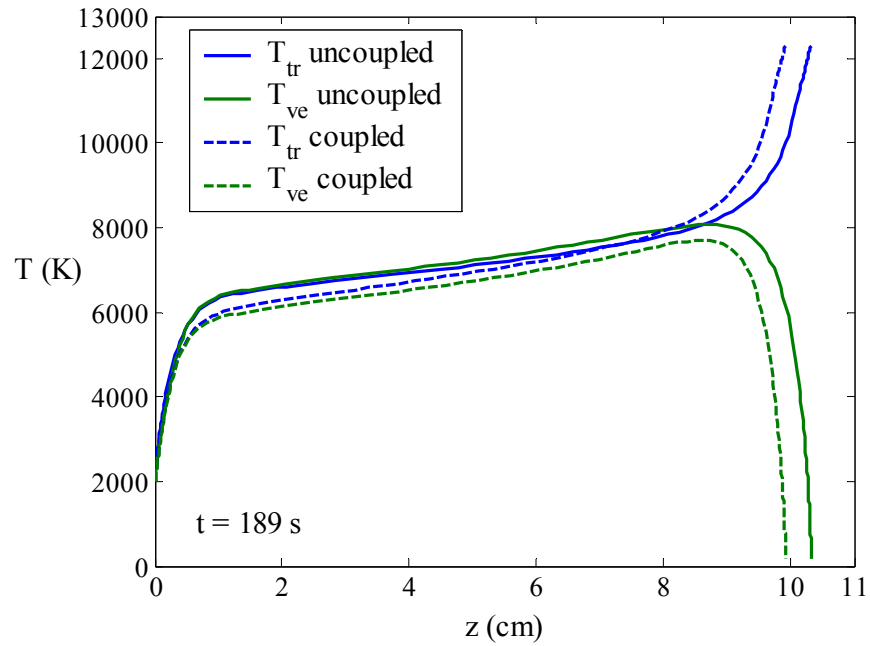


Figure 6.6. Comparison between the coupled and uncoupled temperature profiles for the $t = 189$ case.

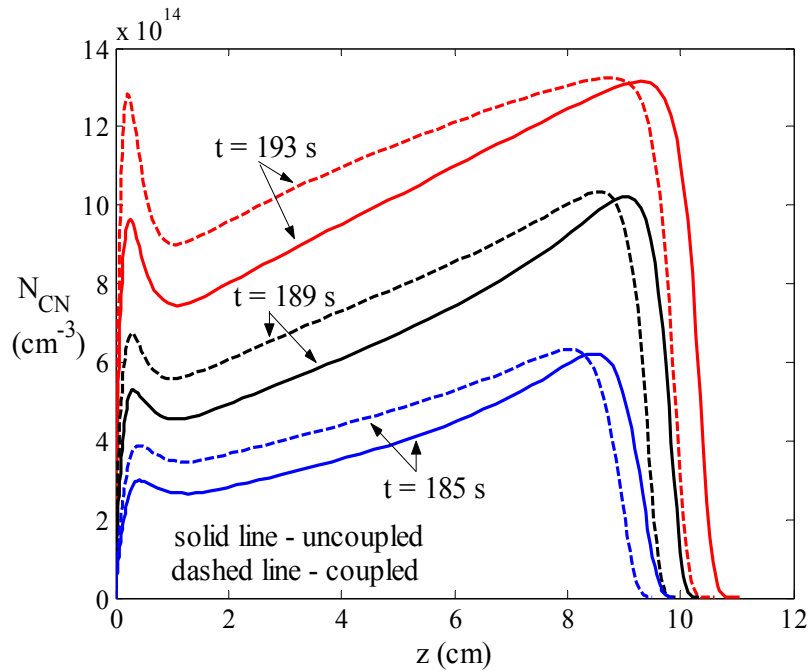


Figure 6.7. Comparison between the coupled and uncoupled CN number density profiles.

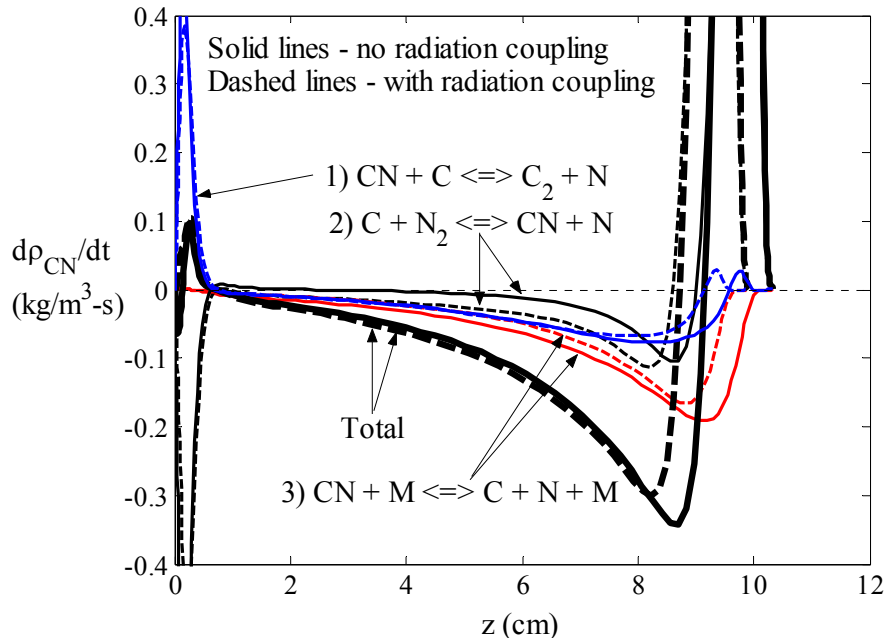


Figure 6.8. Comparison of the mass rate of formation of CN molecules by various reactions for the uncoupled and coupled cases at $t = 189$ s.

Table 6.3 compares the *convective* heat flux at the wall for the coupled and uncoupled cases. A reduction of 11 to 15% is found for the three trajectory points. The influence of radiation on the convective heating is a combination of two competing mechanisms. The absorption of radiation in the boundary layer tends to increase the convective heating, while the emission of radiation out of the shock layer away from the body tends to decrease it. The mild decease in convective heating predicted here is consistent with the previous observation that the shock layer is optically thick only in the small spectral region of the CN violet vibrational band heads. Note that the values for the uncoupled case agree within 5% of the Navier-Stokes results presented by Hollis et al. [2005].

Table 6.3. Comparison of the *convective* heat flux for the uncoupled and coupled cases (W/cm^2)

t (s)	q_c uncoupled	q_c coupled	% difference
185	43.9	37.6	14.4
189	44.5	38.7	13.0
193	37.9	33.7	11.1

Table 6.4 presents the wall radiative heat flux values for the coupled case and compares them with the uncoupled values presented previously. Note that the values in parentheses are the LBL

results that were calculated only after the coupled flowfield solution was obtained using the SRBC approach. An observed reduction in the flux values ranging from 18 to 25 percent indicates the significant influence of coupling on the radiation calculation. This reduction also indicates that although the CN number density was shown to increase with the addition of coupling, its effect on the radiation is overshadowed by the corresponding temperature decrease. This is because the emission coefficient depends exponentially on temperature, assuming a Boltzmann distribution, and only linearly on the CN number density. The column labeled “coupled-TW” presents the coupled radiative heating predicted using the Tauber-Wakefield approximate method (Tauber and Wakefield [1971]). This method depends on the uncoupled radiative heating and a constant, κ , which has been assumed equal to 2 in previous studies (Hollis et al. [2005] and Wright et al. [2006]). The present results show that this method over predicts the effect of coupling for the first two trajectory points. Figure 6.9 shows the difference in the wall directed radiative flux profiles with the addition of coupling. Although the magnitudes of the coupled results are lower than the uncoupled results, the shapes of the profiles are similar. This indicates that the temperature decrease due to the addition of coupling does not introduce any fundamental changes in the radiation spectrum and transport, other than the expected decrease in emission.

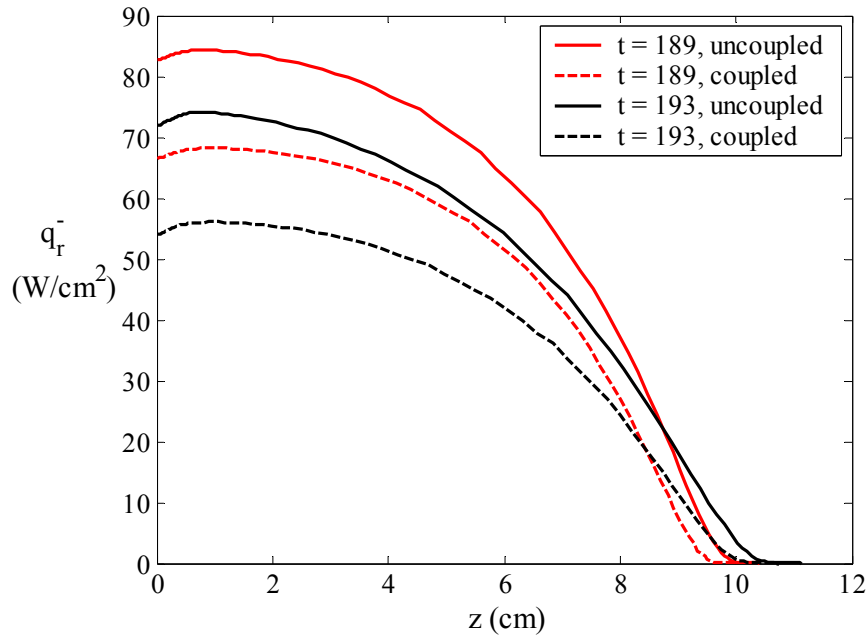


Figure 6.9. Comparison between the coupled and uncoupled wall directed radiative flux profiles

Table 6.4. Comparison of the *radiative* heat flux towards the wall at $z = 0$ for the uncoupled and coupled cases (W/cm^2)

t (s)	q_r uncoupled	q_r coupled	% difference	q_r coupled - TW
185	71.7 (74.2)	59.0 (60.8)	17.7 (18.1)	51.8 (53.2)
189	82.8 (84.8)	66.5 (68.3)	19.7 (19.5)	61.3 (62.5)
193	71.9 (73.2)	54.0 (55.0)	25.0 (25.0)	54.5 (55.3)

6.4 Collisional-Radiative Modeling for Titan Entry

Recent shock-tube experiments by Bose et al. [2005] have shown that near Huygens peak heating conditions, the measured CN(B) population* is an order-of-magnitude less than predicted by a Boltzmann distribution. Since the CN(B) state is the upper level of the CN violet transition, this implies that the radiation from the CN violet band is an order-of-magnitude less than that predicted assuming a Boltzmann distribution. Using excitation rates from previous studies (Zalogin et al. [2001], Kudryavtsev et al. [2001]), Bose et al. formulated a simple collisional-radiative (CR) model that provided a closer prediction to their experimental results than the Boltzmann model. Raynaud et al. [2005] and Magin et al. [2005] have since assembled a more elaborate set of excitation rates and discussed their influence on the predicted CN(B) population. The present study will review the rates suggested by these past studies and consider the effect of using other values found in the literature. Also, the influence of removing the optically thin assumption from the CR model (i.e. applying escape factors other than 1) will be examined. It will be shown that the escape factor can be curve fit as a function of temperature, and therefore implemented easily into the CR model. This avoids the costly iteration procedure used by Bose et al. in their treatment of the escape factor. The details of the CR model as implemented in the present study are discussed below.

The non-Boltzmann treatment of the CN molecule applied in this study is similar to that discussed in Section 4.7 for the N_2^+ and N_2 molecules. Table 6.5 lists the excitation processes and corresponding rates, based on the models presented by Raynaud et al [2005] and Magin et al [2005], which were found to contribute noticeably to the CN(B) population. The main difference between this model and those discussed in Section 4.7 is that heavy-particle collision contribution to the excitation process is significantly larger than the electron-impact contribution. In fact, the electron impact contribution is not required at all for the weakly-ionized cases considered here,

* The notation that CN(B) refers to $\text{CN}(\text{B}^2\Sigma^+)$, CN(X) refers to $\text{CN}(\text{X}^2\Sigma^+)$, and CN(A) refers to $\text{CN}(\text{A}^2\Pi)$ will be used throughout this paper.

although they are listed in Table 6.5 because they may be important for other cases. Note that Magin et al. [2005] found these reactions to have a significant effect at the present flow conditions because their flowfield contained a significantly higher electron number density than what is currently predicted (when the ionized species are considered in the flowfield). This over prediction of electrons was a result of their use of Nelson's (Nelson et al. [1991]) chemical reaction rate set instead of Gocken's recent model. The influence of other possible values for the rates listed in Table 6.5 will be discussed later.

Table 6.5. Excitation reactions considered in the present study

		a_r	b_r	c_r	T_f	T_b	Ref.
<i>Neutral Particle Collisional Deexcitation:</i>							
1	$\text{CN}(\text{X}) + M \leftrightarrow \text{CN}(\text{A}) + M$	1.5e+11	0.5	13300	T_a	T_{tr}	Zagolin
2	$\text{CN}(\text{X}) + M \leftrightarrow \text{CN}(\text{B}) + M$	1.8e+11	0.5	37000	T_a	T_{tr}	Zagolin
<i>Electron Impact Deexcitation:</i>							
3	$\text{CN}(\text{X}) + e^- \leftrightarrow \text{CN}(\text{A}) + e^-$	6.0e+14	0.5	13300	T_{ve}	T_{ve}	Zagolin
4	$\text{CN}(\text{X}) + e^- \leftrightarrow \text{CN}(\text{B}) + e^-$	6.3e+14	0.5	37000	T_{ve}	T_{ve}	Zagolin
<i>Resonant Collisional Deexcitation:</i>							
5	$\text{CN}(\text{X}) + \text{N}_2(\text{X}, V=4) \leftrightarrow \text{CN}(\text{A}) + \text{N}_2(\text{X}, V=0)$	6.0e+13	0	0	-	T_{tr}	Chernyi
6	$\text{CN}(\text{X}) + \text{N}_2(\text{X}, V=11) \leftrightarrow \text{CN}(\text{B}) + \text{N}_2(\text{X}, V=0)$	6.0e+13	0	0	-	T_{tr}	Chernyi
<i>Quenching Reaction:</i>							
7	$\text{N}_2(\text{A}) + \text{CN}(\text{X}) \leftrightarrow \text{N}_2(\text{X}) + \text{CN}(\text{B})$	4.2e+12	0.5	0	T_a	T_{tr}	Pintassilgo

Because the CN molecule is the only significant radiator for the Huygens cases, it practical to consider the task of treating the escape factor in detail (Bose [2005]). For the air cases treated in Chapter 4, this was not practical, and so the escape factor was set equal to one (which was the optical thin assumption). From Eq. (4.9), the rate of excitation of level the CN(B) state due to radiative emission and absorption may be written as

$$\left(\frac{\partial N_{\text{CN}(B)}}{\partial t} \right)_{\text{rad-ex}} = -A_{B,X} A(B, X) N_{\text{CN}(B)} \left(\frac{\text{particles}}{\text{cm}^3 \cdot \text{s}} \right) \quad (6.3)$$

where $A(B, X)$ is the transition probability in s^{-1} , which are listed in Table 6.6 for CN, and $A_{B,X}$ is the escape factor (nondimensional) for the CN(B) to CN(X) transition. This escape factor is shown in Appendix E to be written in general as

$$A_{j,i} = 1 - \frac{1}{A_{j,i} N_j} \int_0^\infty \frac{\kappa_{\nu,j}^*}{h\nu} F_\nu d\nu \quad (6.4)$$

where $\kappa_{\nu,j}^*$ is the absorption coefficient, including induced emission, resulting from the molecular band system with an upper state j , which for the present case is the CN(B) state ($i = \text{CN}(\text{X})$ in Eq.

(6.4) for the CN violet band). The function F_ν is the incoming radiative intensity integrated over all directions, which may be written as

$$F_\nu = 2\pi \int_0^\pi I_\nu(\phi) \sin \phi d\phi \quad \left(\frac{\text{erg}}{\text{cm}^2} \right) \quad (6.5)$$

where I_ν is the directional radiative intensity ($\text{erg}/\text{cm}^2\text{-sr}$) and ϕ is the angle from the vertical axis directed away from the wall. Note that if a $\cos\phi$ was added to the integrand, the conventional radiative flux equation would be obtained. The evaluation of this term, consistent with the tangent-slab approximation, and written in terms of approximate exponential integrals, is presented in Appendix F. A significant property of the escape factor is that it depends on the radiation emitted from every point in the shock layer. Therefore if an exact solution is desired, it is necessary to iterate over the entire flowfield. Fortunately, as written in Eq. (6.4), it is not very dependent on this iteration procedure because of the large value of N_j present in the denominator. After evaluating the escape factor exactly through an iteration procedure for the trajectory points considered in this study, it was found that it could be correlated as a function of only temperature as follows:

$$\begin{aligned} A_{B,X} &= -4.6079 \times 10^{-8} T_{ve}^2 + 8.052 \times 10^{-4} T_{ve} - 2.6814 & 9000K > T_{ve} > 4477K \\ A_{B,X} &= 0.0 & T_{ve} < 4477K \end{aligned} \quad (6.6)$$

This correlation is compared with the computed values in Figure 6.10. Although some error is introduced by using the correlation, it allows for a considerable reduction in computational time and complexity, especially for radiation coupled solutions. A comparison between the radiative flux values computed using the exact values and the correlation is presented in Table 6.7.

Table 6.6. Transition probabilities for the CN radiative transitions.

	$A(s^{-1})$	Ref.
CN(A) \rightarrow CN(X) + $h\nu$	1.54e-5	Zagolin
CN(B) \rightarrow CN(X) + $h\nu$	6.55e-8	Zagolin

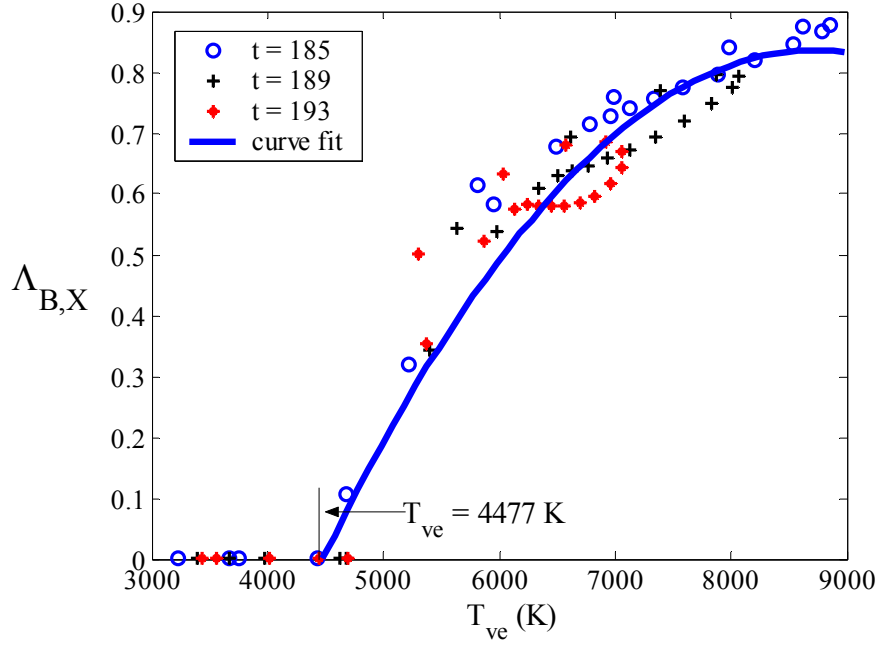


Figure 6.10. Values of the escape factor calculated for the three trajectory points compared with an approximate curve fit.

Applying the excitation mechanisms listed in Tables 6.5 and 6.6, the Master Equation (Eq. (4.12)) may be solved by applying the quasi-steady state assumption (Park [1990]), as discussed in Section 4.3. Both Raynaud et al. and Magin et al. investigated the accuracy of this assumption for Titan and concluded that it was sufficiently accurate. By applying the QSS assumption, Eq. (4.12) may be solved for the B and A states (in terms of the X state) as follows

$$N_{CN(B)} = N_{CN(X)} \left(\frac{k_{f,2}N_M + k_{f,4}N_e + k_{f,6}N_{N_2(X,\nu=11)} + k_{f,7}N_{N_2(A)}}{k_{b,2}N_M + k_{b,4}N_e + k_{b,6}N_{N_2(X,\nu=11)} + k_{b,7}N_{N_2(A)} + \Lambda_{CN(B)}N_a / \tau_{CN(B)}} \right) \quad (6.7)$$

$$N_{CN(A)} = N_{CN(X)} \left(\frac{k_{f,1}N_M + k_{f,3}N_e + k_{f,5}N_{N_2(X,\nu=11)}}{k_{b,1}N_M + k_{b,3}N_e + k_{b,5}N_{N_2(X,\nu=11)} + \Lambda_{CN(A)}N_a / \tau_{CN(A)}} \right) \quad (6.8)$$

Following Section 4.4, the ground state number density (X) may be solved from the requirement that the sum of the various state number densities equals the total CN number density:

$$N_{CN(X)} = N_{CN} - N_{CN(A)} - N_{CN(B)} \quad (6.9)$$

These equations may be set up as a set of three linear equations in terms of three unknowns and solved easily. For the cases considered here, the A and X states are so close to their Boltzmann values that Eqs. (6.8) and (6.9) do not need to be considered. Therefore, only Eq. (6.7) is evaluated assuming $N_{CN(X)}$ is equal to its Boltzmann value, along with all of the N_2 states.

The influence of the various excitation mechanisms on the CN(B) number density profile for the $t = 189$ case are shown in Figure 6.11. The “all reactions” case with $\Lambda_{B,X} = 1$ (which means that absorption is not included) represents the baseline case. The influence of each reaction is then seen by removing each reaction individually from the calculation and observing the deviation of the predicted values of $N_{CN(B)}$ from the baseline case. This is shown in Figure 6.11 for reactions 2, 6, and 7, which are defined in Table 6.5. The most important reaction appears to be reaction 6, which is resonant-collisional deexcitation reaction. Also shown in this figure is the influence of including the absorption term, which implies using an escape factor less than one. The “ $\Lambda_{B,X} = \text{exact}$ ” case implemented the exact escape factor calculation as described previously. The “ $\Lambda_{B,X} = \text{fit}$ ” case applied Eq. (6.6) for the escape factor. It is seen that the “exact” and “fit” cases are in good agreement. This is also true for the other two trajectory points considered in this study, which therefore validates the use of the curve-fit for these conditions.

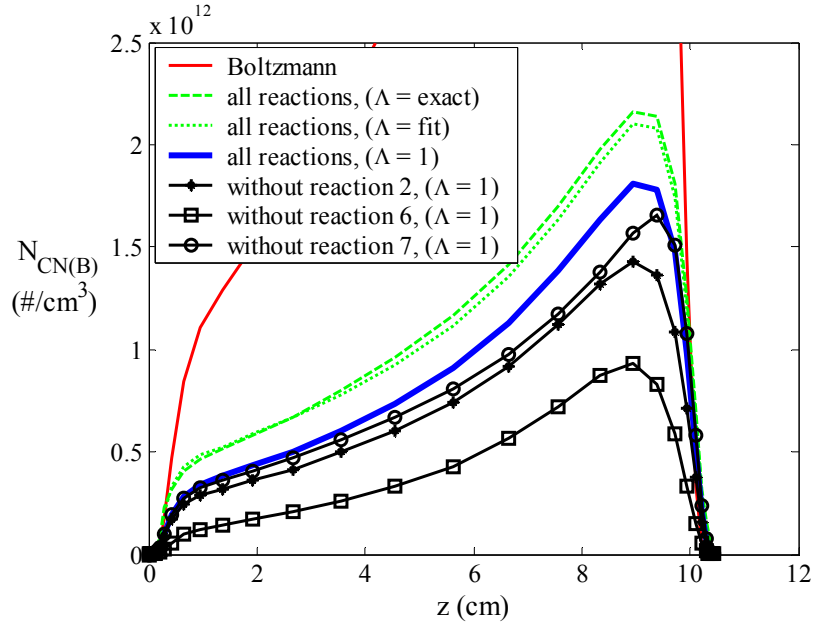


Figure 6.11. The influence of various excitation mechanisms on the CN(B) number density for the $t=189$ case.

The wall radiative heat flux values obtained using the CR model are listed in Table 6.7. The results obtained by using the escape factor curve fit or ignoring absorption ($\Lambda_{B,X} = 1$) may be compared with exact escape factor case. It is seen that, again, good agreement is obtained using the curve fit. The reduction in q_r due to the use of the CR model, rather than a Boltzmann distribution, is found to be as large as 70% at $t = 185$ s. The increase in q_r due to absorption is found to be the largest at $t = 193$ s, where it provides an increase of about 16% above the $\Lambda_{B,X} = 1$

case. The effect of radiation-flowfield coupling on the CR model was also considered and the resulting radiative heating values presented in the last column of Table 6.7. Considering the greatly reduced radiation predicted by the CR model, it is not surprising that the coupling effect is small. Note that the coupled results, which include the curve-fit model for the escape factor, are not even reduced back to the uncoupled cases with no absorption ($A_{B,X} = 1$).

Table 6.7. Comparison of the radiative heat flux towards the wall at $z = 0$ for the various escape factor models (W/cm²)

t (s)	q_r	q_r	q_r	q_r <i>coupled</i> ($A_{B,X}$ fit)
	uncoupled ($A_{B,X}$ exact)	uncoupled ($A_{B,X}$ fit)	uncoupled ($A_{B,X} = 1.0$)	
185	21.0	21.4 (22.0)	18.2	20.8
189	35.3	34.6 (35.4)	29.0	32.8
193	40.3	39.3 (39.9)	31.1	34.9

It was shown in this section that accounting for a non-Boltzmann distribution reduces the radiative heating by about half. This significant reduction is dependent on the rates used for the various collisional excitation processes, which are not very well known. As shown in Figure 6.11, reaction 6 is the most important while reactions 2 and 7 are of roughly equal importance. The rate for reaction 2 used in the present model, following past Titan studies, was taken from Zalogin et al. [2001]. This study conducted experiments in a 9.6% CO₂, 0.3% N₂ and 90.1% Ar free-stream at 1 Torr and chose values for the excitation rates so that their computational and experimental results agreed. A concern in using the rate derived from this study is the large argon concentration present, which essentially implies that the collision partner in their experiment for reaction 2 was argon. The non-Boltzmann results obtained at relatively large initial pressures indicate that Ar may be inefficient, relative to N₂, at exciting CN. Fairbairn [1969] found a similar result for the excitation of CN through collisions with argon. Past studies that have considered the excitation of CN through collisions with N₂ have suggested much larger rate constants (Provencher [1972], Tereshchenko [1975]). Unfortunately, these studies have been at low temperature conditions (around 300 K) so that the derived rate constants are not directly applicable to the present problem. It should be mentioned, however, that the rate for reactions 6 - 8 were obtained from similar low temperature conditions. Thus, it is worth considering the effect of replacing reaction 2 with one of these low temperature rates. If a value of 1.2×10^{13} cm³/mol/s is used for reaction 2, as was suggested by Tereshchenko [1975] (this is also close to value suggested by Provencher [1972]), the resulting CN(B) populations are very close to a Boltzmann distribution for the cases considered here. This conclusion indicates that caution must be used when considering the large decrease in the radiative heating resulting from the present CR model.

Chapter 7

Conclusions

7.1 Accomplishments

An efficient and accurate model for radiation-coupled stagnation region shock-layers was developed. This consists of a new viscous-shock layer (VSL) approach, which models the two-temperature thermochemical nonequilibrium stagnation-region flowfield of a blunt-body. State-of-the-art chemical kinetic models, thermophysical properties, and energy-mode exchange terms are incorporated in this approach, which allows its results to be meaningfully compared with current Navier-Stokes flowfield solvers that apply these same models, such as the LAURA code. For both lunar return conditions (for Earth entry) and Huygens conditions (for Titan entry) the developed VSL approach is shown to predict temperature and number density profiles along the stagnation line that are in relatively good agreement with those predicted by LAURA. This is the first study to confirm, through comparisons with Navier-Stokes results, the applicability of the nonequilibrium VSL flowfield at lunar-return conditions. Also, this is the first study to apply this two-temperature nonequilibrium VSL flowfield to Titan entry, which requires the treatment of more chemical species and reactions than the Earth entry cases. By applying the same radiation model to both the VSL and LAURA flowfields (uncoupled), it is shown that the VSL flowfield produces radiation values within 5% of those resulting from the LAURA flowfields. This result confirms that, for the study of a blunt body (forebody) stagnation region, the present VSL approach is an efficient and convenient alternative to the computationally expensive Navier-Stokes solutions. For coupled radiation-flowfield cases, the VSL method requires orders-of-magnitude less computational time than a Navier-Stokes solution. Thus, use of the VSL approach is justified for the study of coupled radiation-flowfield shock-layers at lunar return and Huygens entry conditions.

A nonequilibrium radiation model was developed for modeling the radiation resulting from air shock-layers at lunar-return conditions. New models for atomic lines, photoionization, and molecular bands were developed. The atomic line model was based on the most recent atomic line data compiled in the NIST database. The influence of these new data on the radiative heating at the conditions of present interest was investigated. It was found that these new atomic line data provided up to a 20% increase in the atomic line radiation resulting from the 1 – 2 eV spectral region (relative to the NEQAIR air model of Park [1985a]). For the spectral region above 6 eV, this new data was shown to result in less radiation. A new atomic photoionization model was applied based on the data compiled in the TOPbase. This new model contains significant spectral detail, which was simplified using a combination of curve-fits and step models. This new photoionization model was shown to provide slightly larger radiation values than the often applied hydrogenic model (Chambers [1994]). The non-Boltzmann modeling of the atomic and molecular species were accounted for in this study by solving the Master Equation, using the best available excitation rates. A comparison of various rates and their influence on the shock-layer radiation was presented. A novel approach of curve-fitting the non-Boltzmann population of the radiating atomic and molecular states was developed. This new approach provides a simple and accurate method for calculating the non-Boltzmann population of atoms and molecules.

The nonequilibrium VSL flowfield and nonequilibrium radiation models developed in this study were applied to the Fire II and Apollo 4 cases, and the resulting radiation predictions were compared with the flight data. For the Fire II case, the present radiation-coupled flowfield model provided intensity values at the wall that predicted the flight data better than any other previous study, on average, throughout the trajectory for the both the 0.2 – 6.0 eV and 2.2 – 4.1 eV spectral ranges. The present method over-predicted the calorimeter total-heating measurements over most of the trajectory, although this was shown to possibly be a result of the super-catalytic assumption, which caused the predicted convective heating to be too high. For the Apollo 4 case, the present model over-predicted the flight data for the wall radiative intensity between 0.2 – 6.2 eV. Unlike the Fire II case, the Apollo 4 vehicle had an ablating heat shield, which was not accounted for in this study. Also, it has been suggested that the Apollo 4 data was influenced by ablation species entering the radiometer cavity, which would have caused significant reduction in the measured radiation. These two influences are likely the cause for the present over-prediction of the data.

An approach to calculating the Huygens probe radiative heating was developed, which included the effects of radiation-flowfield coupling and non-Boltzmann electronic state populations. The

ability to treat radiation-flowfield coupling with reasonable computational requirements was made possible by using a modified smeared rotational band (SRBC) calculation for the radiations spectrum. This approach was shown to provide frequency-integrated heat flux values within 5% of a line-by-line calculation over the range of conditions for Huygens entry. The reduction in radiative heating due to coupling was found to be about 20% for the three peak-heating trajectory points considered. This reduction was less than that estimated in previous studies using the Tauber-Wakefield correction. The convective heating was shown to be reduced by about 15%. Details of implementing a collisional-radiative (CR) model for Titan entry were presented. The use of the CR model for calculating the population of the CN(B) state was shown to reduce the radiative heating by roughly half, with the effect of coupling being small. However, caution is noted in accepting this conclusion because of the uncertainties in the rate data. The detailed treatment of the escape factor was shown to increase the radiation predicted by the CR model by up to 15%.

7.2 Future Work

The non-Boltzmann model applied in the present study for air contains the optically-thin assumption, which means the escape factor was set equal to one. The treatment of the escape factor proposed in Chapter 7 for the CN molecule at Titan conditions could be applied to the atomic and molecular species in air. To the author's knowledge, the influence of the optically-thin assumption on the non-Boltzmann modeling of air shock-layers has not been presented previously in the literature. Another question remaining for the non-Boltzmann air model is the influence of the quasi-steady state assumption, which was applied in the present study. The radiation transport in the present study was modeled using the tangent-slab approximation. The influence of this assumption has been studied by various researchers in the past (Hartung and Hassan [1992c], Sakai and Sawada [2001], and Bose and Wright et al. [2004]), although an efficient and accurate alternative to this assumption (for non optical-thin conditions) has not been presented to date.

References

- Allen, R.A., Rose, P.H., and Camm, J.C., "Nonequilibrium and Equilibrium Radiation at Super-Satellite Re-Entry Velocities," AVCO Research Report 156, 1962.
- Allen, C.W., *Astrophysical Quantities*, London, 1962.
- Anderson, J.D., "An Engineering Survey of Radiating Shock Layers," *AIAA Journal*, Vol. 7, pp. 1665-1675, 1969.
- Anderson, J.D., *Hypersonic and High Temperature Gas Dynamics*, American Institute of Aeronautics and Astronautics, Reston, Virginia, pp. 446-448, 2000.
- Appleton, J. P., and Bray, K. N. C., "The Conservation Equations for a Non-Equilibrium Plasma," *Journal of Fluid Mechanics*, Vol. 20, pp. 659-672, 1964.
- Armaly, B.F., "Continuum Absorption Coefficient of Atoms and Ions," Final Report for NASA Grant NSG 1581, University of Missouri-Rolla, 1979.
- Arnold, J.O., Whiting, E.E., and Lyle, G.C., "Line by Line Calculation of Spectra from Diatomic Molecules and Atoms Assuming a Voight Line Profile," *Journal of Quantitative Spectroscopy and Radiative Transfer*, Vol. 9, pp. 775-798, 1969.
- Arnold, J.O., Cooper, D.M., Park, C., and Prakash, S.G., "Line-by-Line Transport Calculations for Jupiter Entry Probes," AIAA Paper 79-1082, 1979.
- Bacri, J., Lagreca, M., and Medani, A., "Composition of a Quasi-Homogenous Stationary Nitrogen Plasma at Atmospheric Pressure," *Physica C*, Vol. 113, pp. 403-418, 1982.
- Balakrishnan, A., Park, C., and Green, M., J., "Radiative Viscous-Shock-Layer Analysis of Fire, Apollo, and PAET Flight Data," AIAA Paper 85-1064, 1985.

Barnwell, R.W., "Inviscid Radiating Shock-Layers About Spheres Traveling at Hyperbolic Speeds in Air," NASA TR R-311, 1969.

Bates, D.R., Kingston, A.E., and McWhirter, R.W.P., Recombination Between Electrons and Atomic Ions. I. Optically Thin Plasmas," *Proceedings of the Royal Society, Series A*, Vol. 267, pp. 297-312, 1962.

Bates, D.R., and Kingston, A.E., "Properties of a Decaying Plasma," *Planetary and Space Science*, Vol. 11, pp. 1-22, 1963.

Belotserkovskii, O.M., Biberman, L.M., Bronin, S.Y., Lagar'kov, A.N., and Fomin, V.N., "Hypersonic Gas Flow Around a Blunt Object and Heating of the Object, with an Account of Radiation," *High Temperature*, Vol. 7, pp. 529-541, 1969.

Bhatia, A.K., and Kastner, S.O., "The Neutral Oxygen Spectrum. I. Collisionally Excited Level Populations and Line Intensities under Optically Thin Conditions," *The Astrophysical Journal Supplement Series*, Vol. 96, pp. 325-341, 1995.

Biberman, L.M., and Norman, G.E., "On the Calculation of Photoionization Absorption," *Optics and Spectroscopy*, Vol. 8, pp. 230-232, 1960.

Biberman, L.M., Norman, G.E., and Ulyanov, K.N., "On the Calculation of Photoionization Absorption in Atomic Gases," *Optics and Spectroscopy*, Vol. 10, pp. 297-299, 1961.

Biberman, L.M., and Norman, G.E., "Recombination Radiation and Brehmstrahlung," *Journal of Quantitative Spectroscopy and Radiative Transfer*, Vol. 3, pp. 221-245, 1963.

Biberman, L.M., Iakubov, I.T., Norman, G.E., and Vorobyov, V.S., "Radiation Heating Under Hypersonic Flow," *Astronautica Acta*, Vol. 10, pp. 238-253, 1964.

Billig, F. S., "Shock-Wave Shapes around Spherical and Cylindrical-Nosed Bodies," *Journal of Spacecraft and Rockets*, Vol. 4, pp. 822,823, June 1967.

Bird, G.A., "Nonequilibrium Radiation During Re-Entry at 10 km/s," AIAA Paper 87-1543, 1987.

Blottner, F. G., "Viscous Shock Layer at the Stagnation Point with Nonequilibrium Chemistry," *AIAA Journal*, Vol. 7, pp. 2281-2288, December 1969.

Bose, D., and Wright, M.J., "View-Factor Based Radiation Transport in a Hypersonic Shock Layer," *Journal of Thermophysics and Heat Transfer*, Vol. 18, pp. 553-555, 2004.

Bose, D., Wright, M.J., Bogdanoff, D.W., Raiche, G.A., and Allen, G.A., "Modeling and Experimental Validation of CN Radiation Behind a Strong Shock Wave," AIAA Paper 2005-768, Jan. 2005.

Bourdon, A., and Vervisch, P., "Three-Body Recombination Rate of Atomic Nitrogen in Low-Pressure Plasma Flows," *Physical Review E*, Vol. 54, pp. 1888-1898, 1996.

Bourdon, A., Teresiak, Y., and Vervisch, P., "Ionization and Recombination Rates of Atomic Oxygen in High-Temperature Air Plasma Flows," *Physical Review E*, Vol. 57, pp. 4684-4692, 1998.

Callis, L.B., "Solutions of Blunt-Body Stagnation Region Flows with Nongray Emission and Absorption of Radiation by a Time-Asymptotic Technique," NASA TR R-299, 1969.

Camm, J.C., Kivel, B., Taylor, R.L., Teare, J.D., "Absolute Intensity of Nonequilibrium Radiation in Air and Stagnation Heating at High Altitudes," AVCO Research Report 93, 1959.

Carlson, L.A., "Approximations for Hypervelocity Nonequilibrium Radiating, Reacting, and Conducting Stagnation Regions," *Journal of Thermophysics and Heat Transfer*, Vol. 3, pp. 380-388, 1989.

Carlson, L. A., Gally, T. A., "Effect of Electron Temperature and Impact Ionization on Martian Return AOTV Flowfields," *Journal of Thermophysics and Heat Transfer*, Vol. 5, pp. 9-20, Jan. 1991.

Catherinot, A., Sy, A., "Electron Temperature Determination from Non-LTE Populations in a Nitrogen Plasma JET," *Z. Naturforsch.*, Vol. 30, pp. 1143-1155, 1975.

Cauchon, D.L., "Radiative Heating Results from the Fire II Flight Experiment at a Reentry Velocity of 11.4 km/s," NASA TM X-1402, 1967.

Cauchon, D.L., McKee, C.W., Cornette, E.S., "Spectral Measurements of Gas-Cap Radiation During Project Fire Flight Experiment at Reentry Velocities Near 11.4 km/s," NASA TM X-1389, 1967.

Chambers, L.H., "Predicting Radiative Heat Transfer in Thermochemical Nonequilibrium Flow Fields," NASA TM-4564, 1994.

Chauveau, S., Perrin, M.Y., Riviere, P., and Soufiani, A., "Contributions of Diatomic Molecular Electronic Systems to Heated Air Radiation," *Journal of Quantitative Spectroscopy and Radiative Transfer*, Vol. 72, pp. 503-530, 2002.

Chauveau, S., Deron, C., Perrin, M.Y., Riviere, P., and Soufiani, A., "Radiative Transfer in LTE Air Plasmas for Temperatures up to 15,000 K," *Journal of Quantitative Spectroscopy and Radiative Transfer*, Vol. 73, pp. 113-130, 2003.

Cheng, H.K., "The Blunt-Body Problem in Hypersonic Flow at Low Reynolds Number," Cornell Aeronautical Lab, CAL Report No. AF-1285-A-10, 1962.

Chernyi, G.G., and Losev, S.A., *Development of Thermal Protection Systems for Interplanetary Flight*, Research Institute of Mechanics, ISTC Report, Moscow, 1999.

Cohen, I.M., "Strongly Radiating Hypersonic Flow Over a Sphere: An Asymptotic Sketch," *AIAA Journal*, Vol. 5, pp. 501-506, 1967.

Colket, M.B., "Spectroscopic Absorption Model for CN(X²Σ-B²Σ): Comparison of Experiments and Theory," *Journal of Quantitative Spectroscopy and Radiative Transfer*, Vol. 31, pp. 7-13, 1984.

Cornette, E.S., "Forebody Temperature and Calorimeter Heating Rates Measured During Project Fire II Reentry At 11.35 km/s," NASA TM X-1305, 1966.

Crandall, et al., "Absolute Cross-Sections for Electron-Impact Excitation of N₂⁺," *Physical Review A*, Vol. 9, pp. 2545-2551, 1974.

Cunto, W., et al., "TOPbase at the CDS", *Astronomy and Astrophysics*, Vol. 275, pp. L5-L8, 1993 (The TOPbase website is <http://vizier.u-strasbg.fr/topbase/topbase.html>).

Cowley, C.R., "An Approximate Stark Broadening Formula for Use in Spectrum Synthesis," *The Observatory*, Vol. 91, pp. 139-140, 1971.

Davis, R.T.,[1970a], "Numerical Solution of the Hypersonic Viscous Shock-Layer Equations," *AIAA Journal*, Vol. 8, pp. 843-851, 1970.

Davis, R.T.,[1970b], "Hypersonic Flow of a Chemically Reacting Binary Mixture Past a Blunt Body," AIAA Paper 70-805, 1970.

Dimitrijevic, M.S., Konjevic, N., "Simple Formulae for Estimating Stark Widths and Shifts of Neutral Atom Lines, *Astronomy and Astrophysics*, Vol. 163, pp. 297-300, 1986.

Drawin, H.W., "Collision and Transport Cross Sections," in *Plasma Diagnostics* (ed. Lochte-Holtgreven), pp. 842-876, 1968.

Drawin, H.W., Klan, F., and Ringler, H., "Investigation of Excited States of Helium Atoms in Stationary PIG-Discharge," *Z. Naturforsch.*, Vol. 26, pp. 186-197, 1970.

Drawin, H.W., and Emard, F., "Instantaneous Population Densities of the Excited Levels of Hydrogen Atoms and Hydrogen-Like Ions in Plasmas," *Physica C*, Vol. 85, pp. 333-356, 1977.

Dunseath, K.M., et al., "Electron-Impact Excitation of the n<4 Levels of Carbon," *Journal of Physics B*, Vol. 30, pp. 277-287, 1997.

Erdman, P.W., Zipf, E.C., Epsy, P., Howlett, C., Levin, D.A., Loda, R., Collins, R.J., Candler, G., "Flight Measurements of Low-Velocity Bow Shock Ultraviolet Radiation," *Journal of Thermophysics and Heat Transfer*, Vol. 7, pp. 37-41, 1993.

Fairbairn, A.R., "Shock-Tube Study of the Dissociation Rate of CN," *The Journal of Chemical Physics*, Vol. 51, pp. 972-975, August 1969.

Fisher, V., Bernshtam, V., Golten, H., Maron, Y., "Electron-Impact Excitation Cross-Sections for Allowed Transitions in Atoms," *Physical Review A*, Vol. 53, pp. 2425-2431, 1996.

Freudenstein, S.A., Cooper, J., "A Simple Formula for Estimating Stark Widths of Neutral Lines," *The Astrophysical Journal*, Vol. 224, pp. 1079-1084, 1978.

Frost, R.M., *et al.*, "Calculated Cross Sections and Measured Rate Coefficients for Electron-Impact Excitation of Neutral and Singly Ionized Nitrogen," *Journal of Applied Physics*, Vol. 84, pp. 2989-3003, 1998.

Gally, T.A., "Development of Engineering Methods for Nonequilibrium Radiative Phenomena about Aeroassisted Entry Vehicles, Ph.D. Dissertation, Texas A&M University, 1992.

Gally, T. A., and Carlson, L. A., "Nonequilibrium Chemical and Radiation Coupling, Part II: Results for AOTV Flowfields," *Journal of Thermophysics and Heat Transfer*, Vol. 6, pp. 392-399, July-Sept 1992

Gally, T.A., Carlson, L.A., and Green, D., "Flowfield Coupled Excitation and Radiation Model for Nonequilibrium Reacting Flows," *Journal of Thermophysics and Heat Transfer*, Vol. 7, pp. 285-293, 1993.

Garrett, L.B., Smith, G.L., and Perkins, J.N., "An Implicit Finite-Difference Solution to the Viscous Shock Layer, Including the Effects of Radiation and Strong Blowing, NASA TR R-388, 1972.

Gnoffo, P. A., Gupta, R. N., Shinn, J. L., "Conservation Equations and Physical Models for Hypersonic Air Flows in Thermal and Chemical Nonequilibrium," NASA TP-2867, 1989.

Gnoffo, P. A., Weilmuenster, K. J., Hamilton, H. H., Olynick, D. R., Venkatapathy, E., "Computational Aerothermodynamic Design Issues of Hypersonic Vehicles," *Journal of Spacecraft and Rockets*, Vol. 36, pp. 21-43, Jan.-Feb. 1999.

Gocken, T., “N₂-CH₄-Ar Chemical Reaction Model for Simulations of Atmospheric Entry to Titan,” AIAA Paper 2004-2469, Jan. 2004.

Golden, S.A., “Approximate Spectral Absorption Coefficients of Electronic Transitions in Diatomic Molecules,” *Journal of Quantitative Spectroscopy and Radiative Transfer*, Vol. 7, pp. 225-249, 1967.

Gordillo-Vazquez, F. J., and Kunc, J.A., “Diagnostics of Plasmas with Substantial Concentrations of Atomic Oxygen,” *Physical Review E*, Vol. 51, pp. 6010-6015, 1995.

Goulard, R., “The Coupling of Radiation and Convection in Detached Shock Layers,” *Journal of Quantitative Spectroscopy and Radiative Transfer*, Vol. 1, pp. 249-257, 1961.

Goulard, R., “Preliminary Estimates of Radiative Transfer Effects on Detached Shock Layers,” *AIAA Journal*, Vol. 2, pp. 494-502, 1964.

Goulard, R., Boughner, R.E., Burns, R.C., and Nelson, H.F., “Flow of Radiating Gas Around a Probe Entering a Planetary Atmosphere,” *High Temperature*, Vol. 7, pp. 542-565, 1969.

Green, M.J., Balakrishnan, A., and Swenson, B.L., “Aerothermodynamic Environment for A Titan Probe with Deployable Decelerator,” AIAA Paper 85-1063, 1985.

Greendyke, R.B., and Hartung, L.C., “Approximate Method for the Calculation of Nonequilibrium Radiative Heat Transfer,” *Journal of Spacecraft and Rockets*, Vol. 28, pp. 165-171, 1991.

Greendyke, R.B., “Parametric Analysis of Radiative Structure in Aerobrake Shock Layers,” *Journal of Spacecraft and Rockets*, Vol. 30, pp. 51-57, 1993.

Greendyke, R.B., and Hartung, L.C., “Convective and Radiative Heat Transfer Analysis for the Fire II Forebody,” *Journal of Spacecraft and Rockets*, Vol. 31, pp. 986-992, 1994.

Griem, H.R., *Spectral Line Broadening by Plasmas*, Academic Press, New York and London, 1974.

Gruszczynski, J. S., and Warren, W. R., "Study of Equilibrium Air Radiation," *AIAA Journal*, Vol. 5, No. 3, pp. 517-525, March 1967.

Gryzinski, M., "Classical Theory of Electronic and Ionic Inelastic Collisions" *Physical Review*, Vol. 115, pp. 374-383, 1959.

Gupta, R.N., "Navier-Stokes and Viscous Shock-Layer Solutions for Radiating Hypersonic Flows", AIAA Paper 87-1576, 1987.

Gupta, R.N., Yos, J.M., Thompson, R.A., and Lee, K.P., "A Review of Reaction Rates and Thermodynamic and Transport Properties for an 11-Species Air Model for Chemical and Thermal Nonequilibrium Calculations to 30,000 K", NASA RP-1232, 1990.

Gupta, R.N., and Lee, K.P., "Thermo-Chemical Nonequilibrium Analysis of Viscous Shock-Layers," AIAA Paper 95-2083, 1995.

Gupta, R.N., "Viscous Shock-Layer Study of Thermochemical Nonequilibrium," *Journal of Thermophysics and Heat Transfer*, Vol. 10, pp. 257-266, 1996.

Hammerling, P., Teare, J.D., Kivel, B., "Theory of Radiation from Luminous Shock Waves in Nitrogen," AVCO Research Report 49, 1959.

Hartung, L.C., Mitcheltree, R.A., Gnoffo, P.A. [1992a], "Stagnation Point Nonequilibrium Radiative Heating and the Influence of Energy Exchange Models," *Journal Thermophysics and Heat Transfer*, Vol. 6, pp. 412-418, 1992.

Hartung, L.C. [1992b], "Development of a Nonequilibrium Radiative Heating Prediction Method for Coupled Flowfield Solutions," *Journal Thermophysics and Heat Transfer*, Vol. 6, pp. 618-625, 1992.

Hartung, L.C., and Hassan, H.A. [1992c], "Radiation Transport Around Axisymmetric Blunt Body Vehicles Using a Modified Differential Approximation," AIAA Paper 92-0119, 1992.

Henline, W.D., "Documentation of the Detailed Radiation Property Data for the Radiation-Ablation Code RASLE," NASA TM-103848, 1991.

Hofsaess, D., "Photoionization Cross Sections Calculated by Scaled Thomas-Fermi Method ($h\nu < 50$ eV)," *Atomic Data and Nuclear Data Tables*, Vol. 24, pp. 285-321, 1979.

Hollis, B.R., Striepe, S.A., Wright, M.J., Bose, D., Sutton, K., and Takashima, N., "Prediction of the Aerothermodynamic Environment of the Huygens Probe," AIAA Paper 2005-4816, June 2005.

Hoshizaki, H., and Lasher, L.E., "Convective and Radiative Heat Transfer to an Ablating Body," *AIAA Journal*, Vol. 6, pp. 1441-1449, 1968.

Jischke, M.C., "Optically Thin Stagnation-Point Flow," *AIAA Journal*, Vol. 6, pp. 2219-2222, 1968.

Jackman, C.H., Garvey, R.H., and Green, A.E.S., "Electron Impact on Atmospheric Gases I. Updated Cross Sections," *Journal of Geophysical Research*, Vol. 82, pp. 5081-5090, 1977.

Johnston, C.O., Hollis, B.R., and Sutton, K., "Radiative Heating Methodology for the Huygens Probe," AIAA Paper 2006-3426, 2006.

Jones, J.J., "The Rationale for an Aeroassist Flight Experiment," AIAA Paper 87-1508, 1987.

Kastner, S.O., and Bhatia, A.K., "The Neutral Nitrogen Spectrum: Term Populations, Multiplet Intensities, Diagnostic Diagrams, and Comparisons with Observations," *The Astrophysical Journal Supplement Series*, Vol. 109, pp. 241-267, 1997.

Kennet, H., and Strack, S.L., "Radiation Heat Transfer to Hemispherical Noses," *ARS Journal*, Vol. 32, pp. 90-92, 1961.

Kudryavtsev, N.N., Kuznetsova, L.A., Surzhikov, S.T., "Kinetics and Nonequilibrium Radiation of CO₂-N₂ Shock Waves," AIAA Paper 2001-2728, June 2001.

Kunc, J.A., and Soon, W.H., "Collisional-Radiative Nonequilibrium in Partially Ionized Atomic Nitrogen," *Physical Review A*, Vol. 40, pp. 5822-5843, 1989.

Laher R.R., and Gilmore, F.R., "Updated Excitation and Ionization Cross Sections for Electron Impact of Atomic Oxygen," *Journal of Physical and Chemical Reference Data*, Vol. 19, pp. 277-305, 1990.

Laux, C. O., "Optical Diagnostics and Radiative Emission of Air Plasmas," High Temperature Gas Dynamics Lab, Mechanical Engineering Dept., Rept. T-288, Stanford University, 1993.

Lee, J. H., "Basic Governing Equations for the Flight Regimes of Aeroassisted Orbital Transfer Vehicles," AIAA 84-1729, 1984.

Lee, K-P, and Gupta, R.N., "Viscous-Shock-Layer Analysis of Hypersonic Flows Over Long Slender Vehicles," NASA CR-189614, 1991.

Lemke, M., and Venn, K.A., "The Interesting Problem of the NLTE Nitrogen Abundance in Vega," *Astronomy and Astrophysics*, Vol. 309, pp. 558-569, 1996.

Levin, D.A., Candler, G.V., Erdman, P.W., Zipf, E.C., Epsy, P., Howlett, C., "Flight Measurements of Low-Velocity Bow Shock Ultraviolet Radiation," *Journal of Thermophysics and Heat Transfer*, Vol. 7, pp. 30-36, 1993.

Levin, D.A., Candler, G.V., Erdman, P.W., Zipf, E.C., Epsy, P., Howlett, C., "Examination of Theory for Ultraviolet Rocket Experiments - I," *Journal of Thermophysics and Heat Transfer*, Vol. 8, pp. 447-452, 1994.

Liu, Y., *et al.*, "Simple Empirical Analytical Approximation to the Voigt Profile," *Journal of the Optical Society of America B*, Vol. 18, pp. 666-672, 2001.

Magin, T.E., Caillault, L., Bourdon, A., and Laux, C.O., "Nonequilibrium Radiation Modeling for Huygens Entry," 3rd International Planetary Probe Workshop, Anavyssos, Greece, 2005.

Martin, W.C., and Wiese, W.L., "Atomic Spectroscopy," in *Atomic, Molecular, and Optical Physics Handbook*, ed. Drake, G.W.F., AIP Press, New York, 1996.

Matsuyama, S., Ohnishi, N., Sasoh, A., Sawada, K., "Numerical Simulation of Galileo Probe Entry Flowfield with Radiation," *Journal of Thermophysics and Heat Transfer*, Vol. 19, pp. 28-35, 2005.

Mazoue, F., Marraffa, L., "Flow-field/Radiation Coupling Analysis for Huygens Probe Entry into Titan Atmosphere," AIAA Paper 2005-5392, June 2005.

Mcbride, B.J., Zehe, M.J., and Gordon, S., "NASA Glenn Coefficients for Calculating Thermodynamic Properties of Individual Species," NASA TP 2002-211556, Sept. 2002.

Milos, F. S., "Galileo Probe Heat Shield Ablation Experiment" *Journal of Spacecraft and Rockets*, Vol. 34, pp. 705-713, 1997.

Miner, E.W., and Lewis, C.H., "Hypersonic Ionizing Air Viscous Shock-Layer Flows Over Nonanalytic Blunt Bodies," NASA CR-2550, 1975.

Moss, J.N., "Solutions for Reacting and Nonreacting Viscous Shock Layers with Multicomponent Diffusion and Mass Injection," NASA TR R-411, 1974.

Moss, J.N., "Radiative Viscous-Shock-Layer Solutions with Coupled Ablation Injection," *AIAA Journal*, Vol. 9, pp. 1131-1317, 1976.

Moss, J.N., Zoby, E.V., Sutton, K. Anderson, E.C., "Aero thermal Environment for the Pioneer-Venus Multiprobe Mission," AIAA Paper 77-766, 1977.

Moss, J.N., "A Study of the Aero thermal Entry Environment for the Galileo Probe," AIAA Paper 79-1081, 1979.

Murty, S.S.R., "Approximations on Angular Distribution of Intensity of Thermal Radiation," *International Journal of Heat and Mass Transfer*, Vol. 8, pp. 1203-1208, 1965.

Naghizadeh-Kashani, T., Cressault, Y., and Gleizes, A., Net Emission of Air Thermal Plasma," *Journal of Physics D, Applied Physics*, Vol. 35, pp 1925-1934, 2002.

Nagy, O., "Excitation Cross-Sections of N_2^+ Molecular Ion by Electron Impact and the Vibrational Energy Levels of the Three Target States, *Chemical Physics*, Vol. 286, pp. 109-114, 2003.

Nelson, H.F., "Nonequilibrium Radiative Heating during Outer Planet Atmospheric Entry," *Journal of Spacecraft and Rockets*, Vol. 20, pp.407-409, 1983.

Nelson, H.F., Park, C., Whiting, E.E., "Titan Atmospheric Composition by Hypervelocity Shock-Layer Analysis," *Journal of Thermophysics and Heat Transfer*, Vol. 5, pp. 157-165, 1991.

Nicolet, W.E., "Advanced Methods for Calculating Radiation Transport in Ablation-Product Contaminated Boundary Layers," NASA CR-1656, 1970.

Nicolet, W.E., Waterland, L.R., and Kendall, R.M., "Methods for Predicting Radiation Coupled Flowfields About Planetary Entry Probes," AIAA Paper 77-744, 1977.

Olejniczak, J., Wright, M.J., Prabhu, D., Takashima, N., Hollis, B.R., Zoby, E.V., and Sutton, K., "An Analysis of the Radiative Heating Environment for Aerocapture at Titan," AIAA Paper 2003-4953, 2003.

Olivero, J.J., and Longbothum, R.L., "Empirical Fits to the Voigt Line Width: A Brief Review," *Journal of Quantitative Spectroscopy and Radiative Transfer*, Vol. 17, pp. 233, 1977.

Olstad, W.B., "Blunt-Body Stagnation Region Flow with Nongray Radiation Heat Transfer – A Singular Perturbation Problem," NASA TR R-295, 1968.

Olynick, D.R., Henline, W.D., Chamber, L.H., and Candler, G.V., "Comparisons of Coupled Radiative Navier-Stokes Flow Solutions with the Project Fire II Flight Data," AIAA Paper 94-1955, 1994.

Orel, A. E., "Theoretical Study of Electron-Impact Excitation of N_2^+ ," Physical Review A, Vol. 42, pp. 5292-5297, 1990.

Page, W.A., and Woodward, H.T., "Radiative and Convective Heating During Venus Entry," *AIAA Journal*, Vol. 10, pp. 1379-1381, 1972.

Park, C., "Spectral Line Intensities in a Nonequilibrium Nitrogen Plasma," *Journal of Quantitative Spectroscopy and Radiative Transfer*, Vol. 8, pp. 1633-1653, 1968.

Park, C., "Theoretical Population Inversion in a Decaying Nitrogen Plasma Column," AIAA Paper 69-48, 1969

Park, C., "Comparison of Electron and Electronic Temperatures in a Recombining Nozzle Flow of Ionized Nitrogen – Hydrogen Mixture. Part 1. Theory," *Journal of Plasma Physics*, Vol. 9, pp. 187-215, 1973.

Park, C., "Calculation of Radiative Properties of Nonequilibrium Hydrogen Plasma," *J. Quant. Spectrosc. Radiat. Transfer*, Vol. 22, pp. 101-112, 1979.

Park, C., "Radiation Enhancement by Nonequilibrium During Flight through the Titan Atmosphere," AIAA Paper 1982-0878, 1982.

Park, C., "Calculation of Radiation from Argon Shock Layers," *Journal of Quantitative Spectroscopy and Radiative Transfer*, Vol. 28, pp. 29-40, 1982.

Park, C., [1984a], "Calculation of Nonequilibrium Radiation in AOTV Flight Regimes," AIAA Paper 84-0306, 1984.

Park, C., [1984b], "Problems of Rate Chemistry in the Flight Regimes of Aeroassisted Orbital Transfer Vehicles," AIAA 84-1730, 1984.

Park, C., [1985a], "Nonequilibrium Air Radiation (NEQAIR) Program: User's Manual," NASA TM 86707, 1985.

Park, C., [1985b], "Radiation Enhancement by Nonequilibrium in Earth's Atmosphere," *Journal of Spacecraft and Rockets*, Vol. 22, pp. 27-36, 1985.

Park, C., "Assessment of Two-Temperature Kinetic Model for Dissociating and Weakly Ionizing Nitrogen," *Journal of Thermophysics and Heat Transfer*, Vol. 2, pp. 8-16, July 1988.

Park, C., "Assessment of Two-Temperature Kinetic Model for Ionizing Air," *Journal of Thermophysics and Heat Transfer*, Vol. 3, pp. 233-244, July 1989.,

Park, C., *Nonequilibrium Hypersonic Aerothermodynamics*, Wiley, New York, pp. 126-129, 1990.

Park, C., and Ahn, H.K., "Stagnation-Point Heat Transfer Rates for Pioneer-Venus Probes," *Journal of Thermophysics and Heat Transfer*, Vol. 13, pp. 33-41, 1999.

Park, C., "Stagnation-Point Radiation for Apollo 4 – A Review and Current Status," AIAA Paper 2001-3070, 2001.

Park, C., "Stagnation-Point Radiation for Apollo 4," *Journal of Thermophysics and Heat Transfer*, Vol. 18, pp. 349-357, 2004.

Patch, R.W., Shackleford, W.L., Penner, S.S., "Approximate Spectral Absorption Coefficient Calculations for Electronic Band Systems Belonging to Diatomic Molecules," *Journal of Quantitative Spectroscopy and Radiative Transfer*, Vol. 2, pp. 263-271, July-Sept. 1962.

Petschek, H., and Byron, S., "Approach to Equilibrium Ionization Behind Strong Shock Waves in Argon," *Annals of Physics*, Vol. 1, pp. 270-315, 1957.

Pintassilgo, C.D., Cernogore, G., and Loureiro, J., "Spectroscopy Study and Modeling of an Afterglow Created by a Low-Pressure Pulsed Discharge in N₂-CH₄," *Plasma Sources Science and Technology*, Vol. 10, pp. 147-161, 2001.

Prabhu, R.K., Erickson, W.D., "A Rapid Method for the Computation of Equilibrium Chemical Composition of Air to 15,000 K," NASA TP-2792, March 1988.

Provencher, G.M., McKenney, D.J., "CN Emission in Active Nitrogen. II. The Role of Energy Transfer and Atom Transfer Reactions in CN(X²Σ⁺) Excitation," *Canadian Journal of Chemistry*, Vol. 50, pp. 2527-2536, 1972.

Przybilla, N., et al., "Non-LTE Line Formation for Neutral Oxygen: Model Atom and First Results on A-Type Stars," *Astronomy and Astrophysics*, Vol. 359, pp. 1085-1106, 2000.

Ralchenko, Yu, et al., "NIST Atomic Spectra Database, Version 3.1.0," National Institute of Standards and Technology (NIST) Physics Lab, <http://physics.nist.gov/PhysRefData/ASD/index.html>, July 2006 [cited 3 Sept. 2006].

Raynaud, E., Tran, Ph., Soler, J., Baillion, M., "Huygens Aerothermal Environment: Radiative Heating," 3rd International Planetary Probe Workshop, Anavyssos, Greece, 2005.

Reid, R. C., Rochelle, W.C., and Milhoan, J.D., "Radiative Heating to the Apollo Command Module: Engineering Predictions and Flight Measurements," NASA TM X-58091, April 1972.

Rigdon, W.S., Dirling, R.B., and Thomas, M., "Stagnation Point Heat Transfer During Hypervelocity Atmospheric Entry," NASA CR-1462, 1970.

Sakai, T., and Sawada, K., "Calculation of Nonequilibrium Radiation from a Blunt-Body Shock Layer," *Journal of Thermophysics and Heat Transfer*, Vol. 15, pp. 99-105, 2001.

Sedney, R., "Shock-Wave Curvature for Hypersonic Axisymmetric Flow," *Journal of the Aeronautical Sciences*, Vol. 24, pp. 630, August 1957.

Sharma, S., "Assessment of Nonequilibrium Radiation Computational Methods for Hypersonic Flows," NASA TM-103994, 1993.

Sharma, S., "Modeling of Nonequilibrium Radiation Phenomena: An Assessment," *Journal of Thermophysics and Heat Transfer*, Vol. 10, pp. 385-396, 1996.

Sobel'man, I.I., and Vainshtein, L.A., (in Russian), *J. Quant. Spectrosc. Radiat. Transfer*, Vol. 8, pp. 1491-1526, 1968.

Sobel'man, I.I., Vainshtein, L.A., and Yukov, E.A., *Excitation of Atoms and Broadening of Spectral Lines*, Springer-Verlag, New York, 1981.

Soon, W.H., and Kunc, J.A., "Thermal Nonequilibrium in Partially Ionized Atomic Oxygen," *Physical Review A*, Vol. 41, pp. 825-843, 1990.

Stahel, D., Leoni, M., and Dresslar, K., "Nonadiabatic Representations of the $^1\Sigma_u$ and $^1\Pi_u$ States of the N₂ Molecule," *Journal of Chemical Physics*, Vol. 79, pp. 2541-2558, 1983.

Surzhikov, S., et al., Prediction of Nonequilibrium and Equilibrium Radiation for Reentry Conditions, AIAA Paper 2006-1188, 2006.

Suttles, J.T., "Comparison of the Radiation Flux Profiles and Spectral Detail from Three Detailed Nongray Radiation Models at Conditions Representative of Hypervelocity Earth Entry," NASA TMX-2447, 1972.

Sutton, G. W., and Sherman, A., *Engineering Magnetohydrodynamics*, McGraw Hill, New York, pp. 198-201, 1965.

Sutton, K., and Falagna, R.A., "Stagnation Region Radiative Heating with Steady-State Ablation during Venus Entry," *Journal of Spacecraft and Rockets*, Vol. 10, pp. 155-157, 1973.

Sutton, K., "Coupled Nongray Radiating Flow about Ablating Planetary Entry Bodies," *AIAA Journal*, Vol. 12, pp. 1099-1105, 1974.

Sutton, K., "Radiative Heating about Outer Planet Entry Probes," *Journal of Spacecraft and Rockets*, Vol. 13, pp. 294-300, 1976.

Sutton, K., "Air Radiation Revisited," AIAA Paper 84-1733, 1984.

Sutton, K., Gnoffo, P.A., "Multi-Component Diffusion with Application to Computational Aerothermodynamics," AIAA Paper 98-2575, 1998.

Tannehill, J.C., Anderson, D.A., and Pletcher, R.H., *Computational Fluid Mechanics and Heat Transfer*, Taylor and Francis, Philadelphia, pp. 334-335, 1997.

Tauber, M., and Wakefield, R., "Heating Environment and Protection During Jupiter Entry," *Journal of Spacecraft and Rockets*, Vol. 8, pp. 630-636, 1971.

Tayal, S.S., "Effective Collision Strengths for Electron Impact Excitation of N I," *Atomic Data and Nuclear Data Tables*, Vol. 76, pp. 191-212, 2000.

Tereshchenko, E.N., and Dodonova, N.A., "Collisional Deactivation Processes for Electronically Excited CN($B^2\Sigma^+$) Radicals," *Optics and Spectroscopy*, Vol. 39, pp. 435-436, Oct. 1975.

Teulet, P., Sarrette, J.P., and Gomes, A.M., "Calculation of Electron-Impact Inelastic Cross-Sections and Rate Coefficients for Diatomic Molecules. Application to Air Molecules," *Journal of Quantitative Spectroscopy and Radiative Transfer*, Vol. 62, pp. 549-569, 1999.

Thomas, G. M., and Menard, W. A., "Measurements of the Continuum and Atomic Line Radiation from High Temperature Air," *AIAA Journal*, Vol. 5, No. 12, pp. 2214-2223, Dec. 1967.

Thomas, P.D., "Transparency Assumption in Hypersonic Radiative Gas Dynamics," *AIAA Journal*, Vol. 3, pp. 1401-1538, 1965.

Tiwari, S.N., and Szema, K.Y., "Effects of Precursor Heating on Radiative and Chemically Reacting Viscous Flow around a Jovian Body," NASA CR-3186, 1979.

Tiwari, S.N., Chow, H., and Moss, J.N., "Analysis of Aerothermal Environment of a Titan Aerocapture Vehicle," AIAA Paper 1981-1128, 1981.

Tiwari, S.N., and Subramanian, S.V., "Nonequilibrium Radiative Heating of an Ablating Jovian Entry Probe," *AIAA Journal*, Vol. 21, pp. 1338-1344, 1983.

Tiwari, S.N., Szema, K.Y., Moss, J.N., and Subramanian, S.V., "Convective and Radiative Heating of a Saturn Entry Probe," *International Journal of Heat and Mass Transfer*, Vol. 27, pp. 191-205, 1984.

Pitts, W.C., and Wakefield, R.M., "Performance of Entry Heat Shields on Pioneer-Venus Probes," *Journal of Geophysical Research*, Vol. 85, pp. 8333-8537, 1980.

Van Regemorter, H., "Rate of Collisional Excitation in Stellar Atmospheres," *Astrophysical Journal*, Vol. 136, pp. 906-915, 1962.

Walberg, G.D., "A Review of Aeroassisted Orbital Transfer," *Journal of Spacecraft and Rockets*, Vol. 22, pp. 3-18, 1985.

Whang, T.J., Guoxing, Z., Stwalley, W.C., and Wu, C.Y.R., "Franck-Condon Factors of the Transitions of N₂," *Journal of Quantitative Spectroscopy and Radiative Transfer*, Vol. 55, pp. 335-344, 1996.

Whiting, E.E., "An Empirical Approximation to the Voight Profile," *Journal of Quantitative Spectroscopy and Radiative Transfer*, Vol. 8, pp. 1379-1384, 1968.

Whiting, E.E., Arnold, J.O., and Lyle, G.C., "A Computer Program for a Line-by-Line Calculation of Spectra from Diatomic Molecules and Atoms assuming a Voigt Line Profile," NASA TN D-5088, 1969.

Whiting, E. E., et al., "NEQAIR96, Nonequilibrium and Equilibrium Radiative Transport and Spectra Program: User's Manual," NASA RP-1389, 1996.

Wiese, W.L., Smith, M.W., and Glennon, B.M., Atomic Transition Probabilities, Vol. 1, Hydrogen through Neon, NSRDS-NBS 4, National Bureau of Standards, May 1966.

Wiese, W.L., Fuhr, J.R., and Deters, T.M., "Atomic Transition Probabilities of Carbon, Nitrogen, and Oxygen," *Journal of Physical Chemistry Reference Data Monograph*, No. 7, 1996.

Wilson, K.H., and Nicolet, W.E., "Spectral Absorption Coefficients of Carbon, Nitrogen, and Oxygen Atoms," *Journal of Quantitative Spectroscopy and Radiative Transfer*, Vol. 7, pp. 891-941, 1967.

Wilson, K.H., "RATRAP – A Radiation Transport Code," Lockheed Report 6-77-67-12, 1967.

Wiese, W. L., Smith, M. W., and Glennon, B. M., "Atomic Transition Probabilities, Vol. 1. Hydrogen Through Neon," NSRDS-NBS 4, National Bureau of Standards, May 1966.

Wright, M.J., Bose, D., Olejniczak, J., "The Impact of Flowfield-Radiation Coupling on Aeroheating for Titan Aerocapture," *Journal of Thermophysics and Heat Transfer*, Vol. 19, pp. 17-27, Jan.-March 2005.

Wright, M.J., Olejniczak, J., Walpot, L., Raynaud, E., Magin, T., Caillaut, L., and Hollis, B.R., "A Code Calibration Study for Huygens Entry Aeroheating," AIAA Paper 2006-382, Jan. 2006.

Yoshikawa, K.K., and Wick, B.H., "Radiative Heat Transfer During Atmosphere Entry at Parabolic Velocity," NASA TN D-1074, 1961.

Zalogin, G.N., Koslov, P.V., Kuznetsova, L.A., Losev, S.A., Makarov, V.N., Romanenko, Y.P., and Surzhikov, S.T., "Radiation Excited by Shock Waves in a CO₂-N₂-Ar Mixture: Experiment and Theory," *Technical Physics*, Vol. 46, No. 6, 2001.

Zatsarinny, O., and Tayal, S.S., "Electron Collisional Excitation Rates for O I using the B-Spline R-Matrix Approach," *The Astrophysical Journal Supplement Series*, Vol. 148, 2003, pp. 575-582.

Zeldovich, Y.B., and Raizer, Y.P., *Physics of Shock Waves and High Temperature Hydrodynamic Phenomena*, Vol. 1, Academic Press, New York and London, pp. 283-298, 1966.

Zhigulev, V.N., Romishevskii, Y.A., and Vertushkin, V.K., "Role of Radiation in Modern Gasdynamics," *AIAA Journal*, Vol. 1, pp. 1473-1485, 1963.

Zoby, E.V., Sutton, K., Olstad, W.B., and Moss, J.N., "An Approximate Inviscid Radiating Flow-Field Analysis for Outer Planet Entry Probes," AIAA Paper 78-189, 1978.

Zoby, E.V., and Moss, J.N., "Preliminary Thermal Analysis for Saturn Entry," AIAA Paper 1980-359, 1980.

Appendix A. Atomic Line Data

This appendix presents the atomic line data discussed in Chapter 3. For each line, the upper and lower levels of the transition are specified by i and k , respectively, which correspond to the atomic levels defined in Tables 3.1 and 3.2. The value $E_{k'}$ represents the energy of the upper ungrouped level, which may be different than E_k , which is the energy of the upper grouped level. The energy of the lower ungrouped level is obtained by subtracting $h\nu_{CL}$ from $E_{k'}$. The degeneracies of the upper and lower ungrouped levels are shown as $g_{i'}$ and $g_{k'}$, respectively. The transition probability is presented as $A_{k'i'}$, which may be related to the oscillator strength as follows:

$$A_{k'i'} = \frac{8\pi^2 e^2}{mc^3} \frac{g_{i'}}{g_{k'}} (w_{CL} c)^2 f_{i'k'} \quad (s^{-1}) \quad (\text{A-1})$$

The Stark broadening coefficient ($\Delta\lambda_{S,0}$) applied in Eq. (3.13) is presented for each line, and the source of this value is listed under the “Stark Source” column. The values of 1, 2, and 3 indicate that $\Delta\lambda_{S,0}$ was obtained from Griem [1974], Wilson and Nicolet [1967], and Eq. (3.16), respectively.

Table A-1. Data for *nitrogen* lines in the VUV (6 – 18 eV) (note that these are *individual* lines, not multiplet lines).

line index	i	k	$E_{k'}$ (eV)	$g_{i'}$	$g_{k'}$	$h\nu_{CL}$ (eV)	$A_{k'i'}$ (1/s)	$\Delta\lambda_{S,0}$ (Ang.)	Stark Source	conf. i	conf. k	term i	term k
1	1	34	14.330	4	6	14.329	3.74E+06	1.6E-02	3	2p3	9s	4S*	4P
2	1	34	14.320	4	4	14.319	3.74E+06	1.6E-02	3	2p3	9s	4S*	4P
3	1	34	14.314	4	2	14.313	3.73E+06	1.6E-02	3	2p3	9s	4S*	4P
4	1	33	14.261	4	6	14.260	5.56E+06	1.5E-01	2	2p3	8s	4S*	4P
5	1	33	14.251	4	4	14.250	5.55E+06	1.5E-01	2	2p3	8s	4S*	4P
6	1	33	14.245	4	2	14.244	5.54E+06	1.5E-01	2	2p3	8s	4S*	4P
7	1	31	14.165	4	2	14.164	3.40E+07	4.9E-02	2	2p3	6d	4S*	4P
8	1	31	14.159	4	4	14.158	3.39E+07	4.9E-02	2	2p3	6d	4S*	4P
9	1	31	14.158	4	6	14.157	3.39E+07	4.9E-02	2	2p3	6d	4S*	4P
10	1	32	14.152	4	6	14.152	8.81E+06	7.2E-02	2	2p3	7s	4S*	4P
11	1	32	14.143	4	4	14.142	8.79E+06	7.2E-02	2	2p3	7s	4S*	4P
12	1	32	14.138	4	2	14.137	8.78E+06	7.2E-02	2	2p3	7s	4S*	4P
13	1	30	13.994	4	2	13.993	5.58E+07	3.4E-02	2	2p3	5d	4S*	4P
14	1	30	13.990	4	4	13.990	5.58E+07	3.4E-02	2	2p3	5d	4S*	4P
15	1	30	13.988	4	6	13.987	5.58E+07	3.4E-02	2	2p3	5d	4S*	4P
16	1	31	13.971	4	6	13.970	1.51E+07	3.0E-02	2	2p3	6s	4S*	4P
17	1	31	13.962	4	4	13.961	1.51E+07	3.0E-02	2	2p3	6s	4S*	4P
18	1	31	13.956	4	2	13.956	1.51E+07	3.0E-02	2	2p3	6s	4S*	4P
19	1	28	13.682	4	2	13.681	9.99E+07	2.0E-02	2	2p3	4d	4S*	4P
20	1	28	13.678	4	4	13.677	9.99E+07	2.0E-02	2	2p3	4d	4S*	4P
21	1	28	13.675	4	6	13.675	9.98E+07	2.0E-02	2	2p3	4d	4S*	4P
22	1	30	13.629	4	6	13.629	2.93E+07	1.2E-02	2	2p3	5s	4S*	4P
23	1	30	13.620	4	4	13.620	2.92E+07	1.2E-02	2	2p3	5s	4S*	4P
24	1	30	13.615	4	2	13.614	2.92E+07	1.2E-02	2	2p3	5s	4S*	4P

25	1	20	13.019	4	6	13.019	9.19E+06	2.8E-03	3	2p3	3d	4S*	4D
26	1	20	13.018	4	4	13.018	1.25E+07	2.8E-03	3	2p3	3d	4S*	4D
27	1	20	13.016	4	2	13.015	8.82E+06	2.8E-03	3	2p3	3d	4S*	4D
28	1	19	13.004	4	2	13.004	1.93E+08	2.2E-03	2	2p3	3d	4S*	4P
29	1	19	13.001	4	4	13.000	1.83E+08	2.2E-03	2	2p3	3d	4S*	4P
30	1	19	12.997	4	6	12.997	1.70E+08	2.2E-03	2	2p3	3d	4S*	4P
31	1	18	12.995	4	6	12.994	3.30E+07	2.7E-03	3	2p3	3d	4S*	2F
32	1	14	12.862	4	6	12.861	7.07E+07	3.3E-03	2	2p3	4s	4S*	4P
33	1	14	12.853	4	4	12.853	6.76E+07	3.3E-03	2	2p3	4s	4S*	4P
34	1	14	12.848	4	2	12.847	5.76E+07	3.3E-03	2	2p3	4s	4S*	4P
35	2	35	15.027	6	6	12.643	3.33E+08	2.1E-02	3	2p3	2p4	2D*	2D
36	2	35	15.027	4	6	12.642	2.29E+07	2.1E-02	3	2p3	2p4	2D*	2D
37	2	35	14.916	6	4	12.533	9.95E+07	2.1E-02	3	2p3	3d	2D*	2P
38	2	35	14.917	4	2	12.532	1.12E+08	2.1E-02	3	2p3	3d	2D*	2P
39	2	35	14.916	4	4	12.532	1.09E+07	2.1E-02	3	2p3	3d	2D*	2P
40	2	35	14.897	6	4	12.513	2.49E+07	2.1E-02	3	2p3	3d	2D*	2D
41	2	35	14.897	6	6	12.513	2.35E+08	2.1E-02	3	2p3	3d	2D*	2D
42	2	35	14.897	4	4	12.512	2.26E+08	2.1E-02	3	2p3	3d	2D*	2D
43	2	35	14.897	4	6	12.512	1.65E+07	2.1E-02	3	2p3	3d	2D*	2D
44	2	35	14.780	6	6	12.396	3.72E+07	2.2E-02	3	2p3	4s	2D*	2D
45	2	35	14.780	6	4	12.396	3.92E+06	2.2E-02	3	2p3	4s	2D*	2D
46	2	35	14.780	4	4	12.395	3.62E+07	2.2E-02	3	2p3	4s	2D*	2D
47	2	35	14.780	4	6	12.395	2.72E+06	2.2E-02	3	2p3	4s	2D*	2D
48	2	30	13.997	6	8	11.613	3.53E+07	1.1E-02	1	2p3	5d	2D*	2F
49	2	30	13.987	6	6	11.603	2.34E+06	1.1E-02	1	2p3	5d	2D*	2F
50	2	30	13.987	4	6	11.602	3.28E+07	1.1E-02	1	2p3	5d	2D*	2F
51	3	35	15.027	4	6	11.451	1.26E+08	2.6E-02	3	2p3	2p4	2P*	2D
52	3	35	14.948	2	2	11.372	6.55E+07	2.6E-02	3	2p3	3d	2P*	2S
53	3	35	14.948	4	2	11.372	1.31E+08	2.6E-02	3	2p3	3d	2P*	2S
54	3	35	14.917	2	2	11.340	7.88E+07	2.6E-02	3	2p3	3d	2P*	2P
55	3	35	14.917	4	2	11.340	3.85E+07	2.6E-02	3	2p3	3d	2P*	2P
56	3	35	14.916	2	4	11.340	1.99E+07	2.6E-02	3	2p3	3d	2P*	2P
57	3	35	14.916	4	4	11.340	9.96E+07	2.6E-02	3	2p3	3d	2P*	2P
58	3	35	14.897	2	4	11.321	1.15E+06	2.6E-02	3	2p3	3d	2P*	2D
59	3	35	14.897	4	6	11.320	1.40E+06	2.6E-02	3	2p3	3d	2P*	2D
60	2	28	13.683	6	8	11.299	6.35E+07	2.1E-02	2	2p3	4d	2D*	2F
61	2	28	13.674	6	6	11.290	4.23E+06	2.1E-02	2	2p3	4d	2D*	2F
62	2	28	13.674	4	6	11.288	5.91E+07	2.1E-02	2	2p3	4d	2D*	2F
63	2	30	13.651	6	4	11.267	3.60E+07	1.1E-02	1	2p3	5s	2D*	2P
64	2	30	13.651	4	4	11.266	4.00E+06	1.1E-02	1	2p3	5s	2D*	2P
65	2	30	13.643	4	2	11.258	3.99E+07	1.1E-02	1	2p3	5s	2D*	2P
66	3	35	14.780	2	4	11.204	3.04E+06	2.7E-02	3	2p3	4s	2P*	2D
67	3	35	14.780	4	6	11.204	3.52E+06	2.7E-02	3	2p3	4s	2P*	2D
68	3	35	14.780	4	4	11.204	7.39E+05	2.7E-02	3	2p3	4s	2P*	2D
69	1	6	10.932	4	2	10.931	1.58E+08	1.7E-05	2	2p3	2p4	4S*	4P
70	1	6	10.929	4	4	10.929	1.54E+08	1.7E-05	2	2p3	2p4	4S*	4P
71	1	6	10.924	4	6	10.923	1.50E+08	1.7E-05	2	2p3	2p4	4S*	4P
72	2	21	13.036	6	6	10.652	7.52E+07	3.1E-03	1	2p3	3d	2D*	2D
73	2	21	13.036	4	6	10.651	1.27E+06	3.1E-03	1	2p3	3d	2D*	2D
74	2	21	13.033	6	4	10.649	5.17E+06	3.1E-03	1	2p3	3d	2D*	2D
75	2	21	13.033	4	4	10.648	6.94E+07	3.1E-03	1	2p3	3d	2D*	2D
76	2	18	13.004	6	8	10.620	1.29E+08	2.8E-03	1	2p3	3d	2D*	2F
77	2	19	12.997	4	6	10.611	2.36E+07	4.1E-03	3	2p3	3d	2D*	4P
78	2	18	12.995	6	6	10.611	4.24E+06	2.8E-03	1	2p3	3d	2D*	2F
79	2	18	12.995	4	6	10.610	1.24E+08	2.8E-03	1	2p3	3d	2D*	2F
80	2	16	12.975	4	2	10.590	5.31E+07	2.7E-03	2	2p3	3d	2D*	2P

81	2	16	12.971	6	4	10.587	5.60E+07	2.7E-03	2	2p3	3d	2D*	2P
82	2	16	12.971	4	4	10.585	2.84E+06	2.7E-03	2	2p3	3d	2D*	2P
83	2	15	12.922	6	4	10.538	9.22E+07	5.0E-03	1	2p3	4s	2D*	2P
84	2	15	12.922	4	4	10.537	1.02E+07	5.0E-03	1	2p3	4s	2D*	2P
85	2	15	12.912	4	2	10.527	1.02E+08	5.0E-03	1	2p3	4s	2D*	2P
86	3	30	14.003	4	6	10.427	2.48E+07	5.7E-01	2	2p3	5d	2P*	2D
87	3	30	14.001	2	4	10.425	2.07E+07	5.7E-01	2	2p3	5d	2P*	2D
88	3	30	14.001	4	4	10.425	4.13E+06	5.7E-01	2	2p3	5d	2P*	2D
89	3	30	13.986	2	2	10.410	1.46E+07	5.7E-01	2	2p3	5d	2P*	2P
90	3	30	13.986	4	2	10.410	7.30E+06	5.7E-01	2	2p3	5d	2P*	2P
91	3	30	13.986	2	4	10.409	3.65E+06	5.7E-01	2	2p3	5d	2P*	2P
92	3	30	13.986	4	4	10.409	1.82E+07	5.7E-01	2	2p3	5d	2P*	2P
93	1	4	10.336	4	6	10.335	4.01E+08	6.9E-04	1	2p3	3s	4S*	4P
94	1	4	10.330	4	4	10.330	3.99E+08	6.9E-04	1	2p3	3s	4S*	4P
95	1	4	10.326	4	2	10.325	3.98E+08	6.9E-04	1	2p3	3s	4S*	4P
96	3	28	13.697	4	6	10.120	4.41E+07	2.6E-02	2	2p3	4d	2P*	2D
97	3	28	13.694	2	4	10.118	3.67E+07	2.6E-02	2	2p3	4d	2P*	2D
98	3	28	13.694	4	4	10.118	7.34E+06	2.6E-02	2	2p3	4d	2P*	2D
99	3	28	13.669	2	2	10.092	2.70E+07	2.6E-02	2	2p3	4d	2P*	2P
100	3	28	13.669	4	2	10.092	1.35E+07	2.6E-02	2	2p3	4d	2P*	2P
101	3	28	13.666	2	4	10.089	6.76E+06	2.6E-02	2	2p3	4d	2P*	2P
102	3	28	13.666	4	4	10.089	3.38E+07	2.6E-02	2	2p3	4d	2P*	2P
103	2	13	12.357	6	4	9.973	3.34E+07	7.9E-04	1	2p3	3s	2D*	2D
104	2	13	12.357	6	6	9.973	3.21E+08	7.9E-04	1	2p3	3s	2D*	2D
105	2	13	12.357	4	4	9.972	3.09E+08	7.9E-04	1	2p3	3s	2D*	2D
106	2	13	12.357	4	6	9.971	2.35E+07	7.9E-04	1	2p3	3s	2D*	2D
107	3	21	13.036	4	6	9.460	8.42E+07	3.9E-03	1	2p3	3d	2P*	2D
108	3	21	13.033	2	4	9.457	6.68E+07	3.9E-03	1	2p3	3d	2P*	2D
109	3	21	13.033	4	4	9.457	1.89E+07	3.9E-03	1	2p3	3d	2P*	2D
110	3	19	12.997	4	6	9.421	4.04E+04	5.2E-03	3	2p3	3d	2P*	4P
111	3	18	12.995	4	6	9.419	1.42E+06	3.5E-03	1	2p3	3d	2P*	2F
112	3	16	12.975	2	2	9.399	5.62E+07	3.3E-03	1	2p3	3d	2P*	2P
113	3	16	12.975	4	2	9.399	2.76E+07	3.3E-03	1	2p3	3d	2P*	2P
114	3	16	12.971	2	4	9.395	2.02E+07	3.3E-03	1	2p3	3d	2P*	2P
115	3	16	12.971	4	4	9.394	6.33E+07	3.3E-03	1	2p3	3d	2P*	2P
116	3	15	12.922	2	4	9.346	1.79E+06	6.4E-03	1	2p3	4s	2P*	2P
117	3	15	12.922	4	4	9.346	8.95E+06	6.4E-03	1	2p3	4s	2P*	2P
118	3	15	12.912	2	2	9.336	7.14E+06	6.4E-03	1	2p3	4s	2P*	2P
119	3	15	12.912	4	2	9.336	3.57E+06	6.4E-03	1	2p3	4s	2P*	2P
120	3	13	12.357	2	4	8.781	4.25E+07	1.0E-03	1	2p3	3s	2P*	2D
121	3	13	12.357	4	4	8.781	9.59E+06	1.0E-03	1	2p3	3s	2P*	2D
122	3	13	12.357	4	6	8.781	5.10E+07	1.0E-03	1	2p3	3s	2P*	2D
123	2	5	10.690	6	4	8.306	3.13E+08	1.3E-03	1	2p3	3s	2D*	2P
124	2	5	10.690	4	4	8.305	3.51E+07	1.3E-03	1	2p3	3s	2D*	2P
125	2	5	10.680	4	2	8.295	3.72E+08	1.3E-03	1	2p3	3s	2D*	2P
126	3	5	10.690	2	4	7.114	2.34E+07	1.7E-03	1	2p3	3s	2P*	2P
127	3	5	10.690	4	4	7.114	1.16E+08	1.7E-03	1	2p3	3s	2P*	2P
128	3	5	10.680	2	2	7.104	9.22E+07	1.7E-03	1	2p3	3s	2P*	2P
129	3	5	10.680	4	2	7.104	4.45E+07	1.7E-03	1	2p3	3s	2P*	2P

Table A-2. Nitrogen lines in the 0 – 6 eV spectral range (note that these are *multiplet* lines).

line index	<i>i</i>	<i>k</i>	$E_{k'}$ (eV)	g_i	$g_{k'}$	$\hbar\nu_{CL}$ (eV)	$A_{k'y}$ (1/s)	$\Delta\lambda_{s,0}$ (Ang.)	Stark Source	conf. <i>i</i>	conf. <i>k</i>	term <i>i</i>	term <i>k</i>
130	4	8	11.758	12	20	1.426	2.47E+07	4.5E-02	1	3s	3p	4P	4D*
131	4	9	11.842	12	12	1.509	3.10E+07	4.4E-02	1	3s	3p	4P	4P*
132	4	10	11.996	12	4	1.663	3.77E+07	4.8E-02	1	3s	3p	4P	4S*
133	4	26	13.322	12	4	2.989	1.90E+06	8.1E-02	1	3s	4p	4P	4S*
134	5	7	11.603	6	2	0.916	9.83E+06	1.1E-01	2	3s	3p	2P	2S*
135	5	11	12.006	6	10	1.319	2.63E+07	7.2E-02	1	3s	3p	2P	2D*
136	5	12	12.125	6	6	1.438	3.15E+07	7.3E-02	1	3s	3p	2P	2P*
137	5	22	13.202	6	2	2.515	2.57E+06	1.0E-01	1	3s	4p	2P	2S*
138	5	27	13.343	6	6	2.656	9.73E+05	1.0E-01	2	3s	4p	2P	2P*
139	5	28	13.705	6	10	3.018	4.00E+06	6.7E-02	2	3s	3p	2P	2D*
140	5	30	13.770	6	2	3.083	1.72E+06	2.7E-01	2	3s	5p	2P	2S*
141	5	30	13.872	6	10	3.185	2.50E+06	2.7E-01	2	3s	5p	2P	2D*
142	5	30	13.925	6	6	3.238	5.57E+06	6.7E-02	2	3s	3p	2P	2P*
143	6	8	11.758	12	20	0.831	9.56E+05	1.4E-01	3	2p4	3p	4P	4D*
144	6	9	11.842	12	12	0.915	7.20E+05	1.3E-01	3	2p4	3p	4P	4P*
145	6	10	11.996	12	4	1.068	4.04E+06	1.1E-01	3	2p4	3p	4P	4S*
146	6	23	13.244	12	20	2.317	2.03E+05	1.4E-01	3	2p4	4p	4P	4D*
147	6	24	13.268	12	12	2.341	1.23E+05	1.4E-01	3	2p4	4p	4P	4P*
148	7	15	12.919	2	6	1.316	1.64E+05	3.4E-01	2	3p	4s	2S*	2P
149	7	16	12.972	2	6	1.370	2.97E+07	1.9E-01	1	3p	3d	2S*	2P
150	7	28	13.667	2	6	2.064	3.60E+06	8.4E-01	2	3p	4d	2S*	2P
151	7	30	13.986	2	6	2.383	1.87E+06	2.4E+00	1	3p	5d	2S*	2P
152	8	14	12.856	20	12	1.098	1.35E+07	4.6E-01	1	3p	4s	4D*	4P
153	8	17	12.984	20	28	1.225	3.75E+07	2.2E-01	1	3p	3d	4D*	4F
154	8	18	13.000	20	14	1.241	2.46E+06	3.0E-01	3	3p	3d	4D*	2F
155	8	19	12.999	20	12	1.241	4.37E+06	3.0E-01	3	3p	3d	4D*	4P
156	8	20	13.019	20	20	1.261	9.34E+06	2.3E-01	1	3p	3d	4D*	4D
157	8	30	13.624	20	12	1.865	4.36E+06	5.2E-01	3	3p	5s	4D*	4P
158	8	28	13.670	20	28	1.911	4.90E+06	9.9E-01	2	3p	4d	4D*	4F
159	8	28	13.688	20	20	1.929	1.56E+06	9.9E-01	2	3p	4d	4D*	4D
160	8	30	13.986	20	28	2.228	1.42E+06	1.3E+00	3	3p	5d	4D*	4F
161	8	30	13.999	20	20	2.241	5.08E+05	1.4E+00	3	3p	5d	4D*	4D
162	9	14	12.856	12	12	1.015	9.62E+06	5.4E-01	1	3p	4s	4P*	4P
163	9	18	13.000	12	14	1.158	4.41E+05	3.5E-01	3	3p	3d	4P*	2F
164	9	19	12.999	12	12	1.158	7.21E+06	2.2E-01	1	3p	3d	4P*	4P
165	9	20	13.019	12	20	1.177	2.43E+07	2.6E-01	1	3p	3d	4P*	4D
166	9	30	13.624	12	12	1.782	2.53E+06	5.7E-01	3	3p	5s	4P*	4P
167	9	28	13.677	12	12	1.836	1.16E+06	1.1E+00	2	3p	4d	4P*	4P
168	9	28	13.688	12	20	1.846	3.57E+06	1.1E+00	2	3p	4d	4P*	4D
169	9	30	13.999	12	20	2.157	1.07E+06	1.5E+00	3	3p	5d	4P*	4D
170	10	14	12.856	4	12	0.861	1.24E+06	7.1E-01	2	3p	4s	4S*	4P
171	10	19	12.999	4	12	1.004	1.29E+07	2.9E-01	1	3p	3d	4S*	4P
172	10	30	13.624	4	12	1.628	6.94E+05	6.8E-01	3	3p	5s	4S*	4P
173	10	28	13.677	4	12	1.682	1.31E+06	1.3E+00	2	3p	4d	4S*	4P
174	10	31	13.965	4	12	1.970	3.72E+05	1.6E+00	3	3p	6s	4S*	4P
175	10	30	13.990	4	12	1.994	2.78E+05	1.7E+00	3	3p	5d	4S*	4P
176	10	32	14.147	4	12	2.151	2.19E+05	7.2E-01	3	3p	7s	4S*	4P
177	10	31	14.159	4	12	2.164	8.87E+04	7.2E-01	3	3p	6d	4S*	4P
178	10	33	14.255	4	12	2.259	1.38E+05	6.6E-01	3	3p	8s	4S*	4P
179	10	34	14.324	4	12	2.328	9.33E+04	6.2E-01	3	3p	9s	4S*	4P
180	11	13	12.357	10	10	0.351	1.32E+04	1.5E+00	3	3p	3s	2D*	2D
181	11	15	12.919	10	6	0.913	6.11E+06	7.3E-01	2	3p	4s	2D*	2P

182	11	16	12.972	10	6	0.966	2.91E+06	4.8E-01	3	3p	3d	2D*	2P
183	11	18	13.000	10	14	0.994	2.27E+07	4.1E-01	1	3p	3d	2D*	2F
184	11	21	13.035	10	10	1.029	6.02E+06	4.5E-01	1	3p	3d	2D*	2D
185	11	30	13.648	10	6	1.642	2.30E+06	7.2E-01	3	3p	5s	2D*	2P
186	11	28	13.667	10	6	1.661	8.93E+05	1.3E+00	2	3p	4d	2D*	2P
187	11	28	13.679	10	14	1.673	1.63E+06	1.3E+00	2	3p	4d	2D*	2F
188	11	28	13.695	10	10	1.689	5.97E+05	1.3E+00	2	3p	4d	2D*	2D
189	11	30	13.993	10	14	1.987	2.81E+05	1.7E+00	3	3p	5d	2D*	2F
190	11	30	14.003	10	10	1.997	1.34E+05	1.8E+00	3	3p	5d	2D*	2D
191	11	35	14.855	10	14	2.849	2.91E+06	4.1E-01	3	3p	3d	2D*	2F
192	11	35	14.897	10	10	2.891	5.57E+06	4.0E-01	3	3p	3d	2D*	2D
193	11	35	14.917	10	6	2.911	2.52E+06	4.0E-01	3	3p	3d	2D*	2P
194	11	35	15.027	10	10	3.021	7.86E+05	3.7E-01	3	3p	2p4	2D*	2D
195	12	13	12.357	6	10	0.232	2.68E+03	3.5E+00	3	3p	3s	2P*	2D
196	12	15	12.919	6	6	0.794	5.87E+06	9.8E-01	2	3p	4s	2P*	2P
197	12	16	12.972	6	6	0.847	2.79E+06	1.9E-01	2	3p	3d	2P*	2P
198	12	21	13.035	6	10	0.910	1.40E+07	5.0E-01	2	3p	3d	2P*	2D
199	12	30	13.648	6	6	1.523	1.40E+06	8.3E-01	3	3p	5s	2P*	2P
200	12	28	13.695	6	10	1.570	8.21E+05	1.2E+00	2	3p	4d	2P*	2D
201	12	30	13.986	6	6	1.861	2.04E+05	1.9E+00	3	3p	5d	2P*	2P
202	12	30	14.003	6	10	1.878	1.09E+05	2.0E+00	3	3p	5d	2P*	2D
203	12	35	14.780	6	10	2.655	1.81E+06	4.8E-01	3	3p	4s	2P*	2D
204	12	35	14.897	6	10	2.772	2.47E+04	4.4E-01	3	3p	3d	2P*	2D
205	12	35	14.917	6	6	2.791	4.51E+06	4.3E-01	3	3p	3d	2P*	2P
206	12	35	14.948	6	2	2.823	2.64E+06	4.2E-01	3	3p	3d	2P*	2S
207	12	35	15.027	6	10	2.902	4.97E+05	4.0E-01	3	3p	2p4	2P*	2D
208	13	25	13.294	10	10	0.937	4.51E+05	9.2E-01	3	3s	4p	2D	2D*
209	13	27	13.343	10	6	0.986	1.81E+05	9.2E-01	3	3s	4p	2D	2P*
210	13	28	13.705	10	10	1.348	2.61E+07	1.3E+00	3	3s	3p	2D	2D*
211	13	28	13.727	10	14	1.370	2.80E+07	1.3E+00	3	3s	3p	2D	2F*
212	13	30	13.788	10	6	1.431	6.06E+06	1.5E+00	3	3s	5p	2D	2P*
213	13	30	13.872	10	10	1.515	1.40E+07	1.8E+00	3	3s	5p	2D	2D*
214	13	30	13.925	10	6	1.568	3.14E+07	2.1E+00	3	3s	3p	2D	2P*
215	14	23	13.244	12	20	0.388	3.06E+06	4.9E+00	3	4s	4p	4P	4D*
216	14	24	13.268	12	12	0.412	3.94E+06	4.5E+00	3	4s	4p	4P	4P*
217	14	26	13.322	12	4	0.465	4.14E+06	4.0E+00	3	4s	4p	4P	4S*
218	14	30	13.789	12	20	0.932	6.03E+04	3.5E+00	3	4s	5p	4P	4D*
219	14	30	13.800	12	12	0.943	2.16E+05	3.5E+00	3	4s	5p	4P	4P*
220	14	30	13.824	12	4	0.968	4.84E+05	3.7E+00	3	4s	5p	4P	4S*
221	15	22	13.202	6	2	0.283	7.53E+05	8.4E+00	3	4s	4p	2P	2S*
222	15	25	13.294	6	10	0.376	2.52E+06	5.7E+00	3	4s	4p	2P	2D*
223	15	27	13.343	6	6	0.424	4.37E+06	5.0E+00	3	4s	4p	2P	2P*
224	15	28	13.705	6	10	0.786	9.49E+04	3.7E+00	3	4s	3p	2P	2D*
225	15	30	13.770	6	2	0.851	1.91E+05	3.9E+00	3	4s	5p	2P	2S*
226	15	30	13.788	6	6	0.869	8.98E+04	4.0E+00	3	4s	5p	2P	2P*
227	15	30	13.872	6	10	0.953	1.02E+06	4.5E+00	3	4s	5p	2P	2D*
228	15	30	13.925	6	6	1.006	3.46E+05	5.0E+00	3	4s	3p	2P	2P*
229	16	22	13.202	6	2	0.229	1.01E+06	1.3E+01	3	3d	4p	2P	2S*
230	16	25	13.294	6	10	0.322	2.46E+05	7.8E+00	3	3d	4p	2P	2D*
231	16	27	13.343	6	6	0.370	2.36E+04	6.6E+00	3	3d	4p	2P	2P*
232	16	28	13.705	6	10	0.732	4.12E+04	4.3E+00	3	3d	3p	2P	2D*
233	16	30	13.788	6	6	0.816	4.97E+04	4.5E+00	3	3d	5p	2P	2P*
234	16	30	13.872	6	10	0.900	9.70E+04	5.1E+00	3	3d	5p	2P	2D*
235	16	30	13.925	6	6	0.953	6.07E+04	5.6E+00	3	3d	3p	2P	2P*
236	17	23	13.244	28	20	0.261	7.26E+05	1.1E+01	3	3d	4p	4F	4D*
237	17	30	13.789	28	20	0.805	1.16E+05	4.7E+00	3	3d	5p	4F	4D*

238	18	25	13.294	14	10	0.294	9.04E+05	9.4E+00	3	3d	4p	2F	2D*
239	18	30	13.872	14	10	0.872	4.14E+05	5.4E+00	3	3d	5p	2F	2D*
240	19	23	13.244	12	20	0.245	4.43E+04	1.2E+01	3	3d	4p	4P	4D*
241	19	24	13.268	12	12	0.269	1.19E+05	1.1E+01	3	3d	4p	4P	4P*
242	19	26	13.322	12	4	0.322	1.85E+06	8.3E+00	3	3d	4p	4P	4S*
243	19	30	13.800	12	12	0.801	6.02E+04	4.9E+00	3	3d	5p	4P	4P*
244	19	30	13.824	12	4	0.825	3.60E+05	5.0E+00	3	3d	5p	4P	4S*
245	20	23	13.244	20	20	0.225	9.28E+04	1.4E+01	3	3d	4p	4D	4D*
246	20	24	13.268	20	12	0.249	5.95E+05	1.2E+01	3	3d	4p	4D	4P*
247	20	30	13.800	20	12	0.781	9.54E+04	5.2E+00	3	3d	5p	4D	4P*
248	21	25	13.294	10	10	0.259	1.30E+05	1.2E+01	3	3d	4p	2D	2D*
249	21	27	13.343	10	6	0.308	9.43E+05	9.5E+00	3	3d	4p	2D	2P*
250	21	28	13.705	10	10	0.670	6.90E+04	5.1E+00	3	3d	3p	2D	2D*
251	21	30	13.788	10	6	0.753	1.08E+05	5.3E+00	3	3d	5p	2D	2P*
252	22	28	13.667	2	6	0.465	4.07E+06	9.4E+00	3	4p	4d	2S*	2P
253	22	30	13.986	2	6	0.784	1.28E+06	1.1E+01	3	4p	5d	2S*	2P
254	23	30	13.624	20	12	0.379	2.71E+06	1.3E+01	3	4p	5s	4D*	4P
255	23	28	13.670	20	28	0.425	5.67E+06	1.1E+01	3	4p	4d	4D*	4F
256	23	28	13.677	20	12	0.433	4.31E+05	1.1E+01	3	4p	4d	4D*	4P
257	23	28	13.688	20	20	0.443	1.50E+06	1.1E+01	3	4p	4d	4D*	4D
258	23	30	13.986	20	28	0.742	1.40E+06	1.2E+01	3	4p	5d	4D*	4F
259	23	30	13.990	20	12	0.746	1.47E+05	1.2E+01	3	4p	5d	4D*	4P
260	23	30	13.999	20	20	0.755	4.17E+05	1.2E+01	3	4p	5d	4D*	4D
261	24	30	13.624	12	12	0.356	2.19E+06	1.4E+01	3	4p	5s	4P*	4P
262	24	28	13.677	12	12	0.409	1.63E+06	1.3E+01	3	4p	4d	4P*	4P
263	24	28	13.688	12	20	0.420	4.22E+06	1.2E+01	3	4p	4d	4P*	4D
264	24	30	13.990	12	12	0.722	3.48E+05	1.3E+01	3	4p	5d	4P*	4P
265	24	30	13.999	12	20	0.731	1.05E+06	1.3E+01	3	4p	5d	4P*	4D
266	25	30	13.648	10	6	0.354	1.90E+06	1.5E+01	3	4p	5s	2D*	2P
267	25	28	13.667	10	6	0.372	9.46E+05	1.5E+01	3	4p	4d	2D*	2P
268	25	28	13.679	10	14	0.385	4.70E+06	1.4E+01	3	4p	4d	2D*	2F
269	25	28	13.695	10	10	0.401	1.24E+06	1.4E+01	3	4p	4d	2D*	2D
270	25	30	13.986	10	6	0.692	3.43E+05	1.4E+01	3	4p	5d	2D*	2P
271	25	30	13.993	10	14	0.698	9.20E+05	1.4E+01	3	4p	5d	2D*	2F
272	25	30	14.003	10	10	0.708	2.79E+05	1.4E+01	3	4p	5d	2D*	2D
273	26	30	13.624	4	12	0.302	2.87E+05	2.0E+01	3	4p	5s	4S*	4P
274	26	28	13.677	4	12	0.356	2.54E+06	1.7E+01	3	4p	4d	4S*	4P
275	26	31	13.965	4	12	0.644	1.34E+05	1.5E+01	3	4p	6s	4S*	4P
276	26	30	13.990	4	12	0.668	4.95E+05	1.5E+01	3	4p	5d	4S*	4P
277	26	32	14.147	4	12	0.825	7.68E+04	4.9E+00	3	4p	7s	4S*	4P
278	26	31	14.159	4	12	0.838	1.77E+05	4.8E+00	3	4p	6d	4S*	4P
279	26	33	14.255	4	12	0.933	4.83E+04	3.9E+00	3	4p	8s	4S*	4P
280	26	34	14.324	4	12	1.002	3.23E+04	3.3E+00	3	4p	9s	4S*	4P
281	27	30	13.648	6	6	0.306	2.34E+06	2.1E+01	3	4p	5s	2P*	2P
282	27	28	13.667	6	6	0.324	3.90E+05	1.9E+01	3	4p	4d	2P*	2P
283	27	28	13.695	6	10	0.353	3.14E+06	1.8E+01	3	4p	4d	2P*	2D
284	27	30	14.003	6	10	0.660	5.13E+05	1.7E+01	3	4p	5d	2P*	2D
285	27	35	14.948	6	2	1.606	2.06E+06	1.3E+00	3	4p	3d	2P*	2S
286	30	30	13.789	12	20	0.165	7.07E+05	1.1E+02	3	5s	5p	4P	4D*
287	30	30	13.800	12	12	0.176	9.84E+05	1.0E+02	3	5s	5p	4P	4P*
288	30	30	13.824	12	4	0.200	8.64E+05	8.5E+01	3	5s	5p	4P	4S*
289	30	28	13.705	6	10	0.056	1.36E+04	7.2E+02	3	5s	3p	2P	2D*
290	30	30	13.770	6	2	0.121	9.32E+04	1.9E+02	3	5s	5p	2P	2S*
291	30	30	13.788	6	6	0.140	4.66E+05	1.5E+02	3	5s	5p	2P	2P*
292	30	30	13.872	6	10	0.224	6.47E+05	8.2E+01	3	5s	5p	2P	2D*
293	30	30	13.925	6	6	0.276	3.55E+05	6.6E+01	3	5s	3p	2P	2P*

294	28	30	13.789	28	20	0.119	3.03E+05	2.1E+02	3	4d	5p	4F	4D*
295	28	28	13.705	6	10	0.038	1.42E+03	1.6E+03	3	4d	3p	2P	2D*
296	28	30	13.770	6	2	0.103	4.21E+05	2.7E+02	3	4d	5p	2P	2S*
297	28	30	13.788	6	6	0.121	9.52E+02	2.0E+02	3	4d	5p	2P	2P*
298	28	30	13.872	6	10	0.205	1.60E+05	9.7E+01	3	4d	5p	2P	2D*
299	28	30	13.925	6	6	0.258	3.78E+03	7.6E+01	3	4d	3p	2P	2P*
300	28	28	13.705	14	10	0.025	2.01E+03	3.5E+03	3	4d	3p	2F	2D*
301	28	30	13.872	14	10	0.193	4.05E+05	1.1E+02	3	4d	5p	2F	2D*
302	28	30	13.789	12	20	0.111	1.85E+04	2.4E+02	3	4d	5p	4P	4D*
303	28	30	13.800	12	12	0.122	4.76E+04	2.1E+02	3	4d	5p	4P	4P*
304	28	30	13.824	12	4	0.147	7.78E+05	1.6E+02	3	4d	5p	4P	4S*
305	28	30	13.789	20	20	0.101	3.66E+04	3.0E+02	3	4d	5p	4D	4D*
306	28	30	13.800	20	12	0.112	2.35E+05	2.5E+02	3	4d	5p	4D	4P*
307	28	30	13.788	10	6	0.093	1.09E+05	3.5E+02	3	4d	5p	2D	2P*
308	28	30	13.872	10	10	0.176	6.45E+04	1.3E+02	3	4d	5p	2D	2D*
309	28	30	13.925	10	6	0.229	1.20E+05	9.6E+01	3	4d	3p	2D	2P*
310	28	30	13.986	10	6	0.281	2.59E+05	8.4E+01	3	3p	5d	2D*	2P
311	28	30	13.993	10	14	0.288	1.27E+06	8.3E+01	3	3p	5d	2D*	2F
312	28	30	14.003	10	10	0.298	3.00E+05	8.1E+01	3	3p	5d	2D*	2D
313	28	35	14.780	10	10	1.075	1.27E+05	2.9E+00	3	3p	4s	2D*	2D
314	28	35	14.855	10	14	1.150	1.23E+07	2.5E+00	3	3p	3d	2D*	2F
315	28	35	14.897	10	10	1.192	2.22E+07	2.4E+00	3	3p	3d	2D*	2D
316	28	35	14.917	10	6	1.212	8.93E+06	2.3E+00	3	3p	3d	2D*	2P
317	28	35	15.027	10	10	1.322	8.73E+06	1.9E+00	3	3p	2p4	2D*	2D
318	28	35	14.780	14	10	1.053	1.16E+07	3.0E+00	3	3p	4s	2F*	2D
319	28	35	14.855	14	14	1.128	6.04E+06	2.6E+00	3	3p	3d	2F*	2F
320	28	35	14.897	14	10	1.170	2.08E+06	2.4E+00	3	3p	3d	2F*	2D
321	28	35	15.027	14	10	1.300	1.81E+05	2.0E+00	3	3p	2p4	2F*	2D
322	30	30	13.986	2	6	0.216	1.08E+06	1.4E+02	3	5p	5d	2S*	2P
323	30	30	13.986	20	28	0.198	1.46E+06	1.7E+02	3	5p	5d	4D*	4F
324	30	30	13.990	20	12	0.201	1.18E+05	1.7E+02	3	5p	5d	4D*	4P
325	30	30	13.999	20	20	0.210	4.05E+05	1.6E+02	3	5p	5d	4D*	4D
326	30	30	13.986	6	6	0.198	1.14E+05	1.7E+02	3	5p	5d	2P*	2P
327	30	30	14.003	6	10	0.214	1.15E+06	1.6E+02	3	5p	5d	2P*	2D
328	30	35	14.417	6	2	0.629	2.27E+04	8.5E+00	3	5p	3s	2P*	2S
329	30	35	14.948	6	2	1.160	6.75E+06	2.5E+00	3	5p	3d	2P*	2S
330	30	30	13.990	12	12	0.190	3.93E+05	1.9E+02	3	5p	5d	4P*	4P
331	30	30	13.999	12	20	0.199	1.14E+06	1.8E+02	3	5p	5d	4P*	4D
332	30	31	13.965	4	12	0.141	8.92E+04	3.0E+02	3	5p	6s	4S*	4P
333	30	30	13.990	4	12	0.166	6.74E+05	2.5E+02	3	5p	5d	4S*	4P
334	30	32	14.147	4	12	0.322	4.05E+04	3.2E+01	3	5p	7s	4S*	4P
335	30	31	14.159	4	12	0.335	1.85E+05	3.0E+01	3	5p	6d	4S*	4P
336	30	33	14.255	4	12	0.430	2.44E+04	1.8E+01	3	5p	8s	4S*	4P
337	30	34	14.324	4	12	0.499	1.61E+04	1.3E+01	3	5p	9s	4S*	4P
338	30	30	13.986	10	6	0.114	1.34E+05	5.1E+02	3	5p	5d	2D*	2P
339	30	30	13.993	10	14	0.121	4.35E+05	4.7E+02	3	5p	5d	2D*	2F
340	30	30	14.003	10	10	0.131	1.37E+05	4.2E+02	3	5p	5d	2D*	2D
341	30	30	13.986	6	6	0.061	1.19E+03	1.8E+03	3	3p	5d	2P*	2P
342	30	30	14.003	6	10	0.078	7.07E+04	1.2E+03	3	3p	5d	2P*	2D
343	30	35	14.417	6	2	0.492	8.85E+04	1.4E+01	3	3p	3s	2P*	2S
344	30	35	14.780	6	10	0.855	6.23E+06	4.6E+00	3	3p	4s	2P*	2D
345	30	35	14.897	6	10	0.972	1.66E+05	3.5E+00	3	3p	3d	2P*	2D
346	30	35	14.917	6	6	0.992	1.59E+07	3.4E+00	3	3p	3d	2P*	2P
347	30	35	14.948	6	2	1.023	1.55E+07	3.2E+00	3	3p	3d	2P*	2S

Table A-3. Data for *oxygen* lines in the VUV (6 – 18 eV) (note that these are individual lines, not multiplet lines).

line index	<i>i</i>	<i>k</i>	$E_{k'}$ (eV)	g_r	$g_{k'}$	$\hbar\nu_{CL}$ (eV)	$A_{k'r}$ (1/s)	$\Delta\lambda_{S,0}$ (Ang.)	Stark Source	conf. <i>i</i>	conf. <i>k</i>	term <i>i</i>	term <i>k</i>
1	1	32	17.775	5	7	17.729	2.05E+07	1.1E-02	3	2p4	4d	3P	3D*
2	1	32	17.775	5	5	17.729	5.30E+06	1.1E-02	3	2p4	4d	3P	3D*
3	1	32	17.775	5	3	17.729	6.02E+05	1.1E-02	3	2p4	4d	3P	3D*
4	1	32	17.775	3	5	17.729	1.58E+07	1.1E-02	3	2p4	4d	3P	3D*
5	1	32	17.775	3	3	17.729	8.97E+06	1.1E-02	3	2p4	4d	3P	3D*
6	1	32	17.775	1	3	17.729	1.19E+07	1.1E-02	3	2p4	4d	3P	3D*
7	1	32	17.105	5	7	17.109	4.60E+07	1.1E-02	3	2p4	3d	3P	3D*
8	1	32	17.105	5	5	17.109	1.19E+07	1.1E-02	3	2p4	3d	3P	3D*
9	1	32	17.105	5	3	17.109	1.35E+06	1.1E-02	3	2p4	3d	3P	3D*
10	1	32	17.105	3	5	17.109	3.53E+07	1.1E-02	3	2p4	3d	3P	3D*
11	1	32	17.105	3	3	17.109	2.01E+07	1.1E-02	3	2p4	3d	3P	3D*
12	1	32	17.105	1	3	17.109	2.66E+07	1.2E-02	3	2p4	3d	3P	3D*
13	1	32	16.115	5	3	16.117	8.84E+07	1.3E-02	3	2p4	4d	3P	3P*
14	1	32	16.114	5	5	16.117	1.59E+08	1.3E-02	3	2p4	4d	3P	3P*
15	1	32	16.116	3	1	16.117	2.11E+08	1.3E-02	3	2p4	4d	3P	3P*
16	1	32	16.115	3	3	16.117	5.29E+07	1.3E-02	3	2p4	4d	3P	3P*
17	1	32	16.114	3	5	16.117	5.29E+07	1.3E-02	3	2p4	4d	3P	3P*
18	1	32	16.115	1	3	16.117	7.04E+07	1.3E-02	3	2p4	4d	3P	3P*
19	1	32	16.085	5	3	16.117	2.58E+07	1.3E-02	3	2p4	4d	3P	3S*
20	1	32	16.081	5	3	16.117	4.83E+05	1.3E-02	3	2p4	4d	3P	3D*
21	1	32	16.080	5	5	16.117	4.40E+06	1.3E-02	3	2p4	4d	3P	3D*
22	1	32	16.080	5	7	16.117	1.79E+07	1.3E-02	3	2p4	4d	3P	3D*
23	1	32	16.085	3	3	16.117	1.54E+07	1.3E-02	3	2p4	4d	3P	3S*
24	1	32	16.081	3	3	16.117	7.20E+06	1.3E-02	3	2p4	4d	3P	3D*
25	1	32	16.080	3	5	16.117	1.31E+07	1.3E-02	3	2p4	4d	3P	3D*
26	1	32	16.085	1	3	16.117	5.12E+06	1.3E-02	3	2p4	4d	3P	3S*
27	1	32	16.081	1	3	15.993	9.58E+06	1.3E-02	3	2p4	4d	3P	3D*
28	1	32	15.664	5	3	15.621	2.75E+08	1.4E-02	3	2p4	2p5	3P	3P*
29	1	32	15.655	5	5	15.621	4.94E+08	1.4E-02	3	2p4	2p5	3P	3P*
30	1	32	15.670	3	1	15.621	6.59E+08	1.4E-02	3	2p4	2p5	3P	3P*
31	1	32	15.664	3	3	15.621	1.64E+08	1.4E-02	3	2p4	2p5	3P	3P*
32	1	32	15.664	1	3	15.621	2.19E+08	1.4E-02	3	2p4	2p5	3P	3P*
33	1	32	15.655	3	5	15.621	1.64E+08	1.4E-02	3	2p4	2p5	3P	3P*
34	1	32	15.416	5	3	15.373	7.02E+07	1.4E-02	3	2p4	3d	3P	3S*
35	1	32	15.407	5	3	15.373	1.21E+06	1.4E-02	3	2p4	3d	3P	3D*
36	1	32	15.406	5	5	15.373	1.10E+07	1.4E-02	3	2p4	3d	3P	3D*
37	1	32	15.405	5	7	15.373	4.47E+07	1.4E-02	3	2p4	3d	3P	3D*
38	1	32	15.416	3	3	15.373	4.21E+07	1.4E-02	3	2p4	3d	3P	3S*
39	1	32	15.416	1	3	15.373	1.40E+07	1.4E-02	3	2p4	3d	3P	3S*
40	1	32	15.407	3	3	15.373	1.80E+07	1.4E-02	3	2p4	3d	3P	3D*
41	1	32	15.406	3	5	15.373	3.29E+07	1.4E-02	3	2p4	3d	3P	3D*
42	1	32	15.407	1	3	15.373	2.40E+07	1.4E-02	3	2p4	3d	3P	3D*
43	1	32	15.294	5	3	15.249	1.37E+07	1.4E-02	3	2p4	3d	3P	3P*
44	1	32	15.287	5	5	15.249	2.46E+07	1.4E-02	3	2p4	3d	3P	3P*
45	1	32	15.298	3	1	15.249	3.27E+07	1.4E-02	3	2p4	3d	3P	3P*
46	1	32	15.294	3	3	15.249	8.17E+06	1.4E-02	3	2p4	3d	3P	3P*
47	1	32	15.287	3	5	15.249	8.15E+06	1.4E-02	3	2p4	3d	3P	3P*
48	1	32	15.294	1	3	15.249	1.09E+07	1.4E-02	3	2p4	3d	3P	3P*
49	1	32	15.181	5	3	15.125	1.63E+06	1.5E-02	3	2p4	4s	3P	3D*
50	1	32	15.180	5	5	15.125	1.47E+07	1.5E-02	3	2p4	4s	3P	3D*

51	1	32	15.178	5	7	15.125	5.89E+07	1.5E-02	3	2p4	4s	3P	3D*
52	1	32	15.181	3	3	15.125	2.44E+07	1.5E-02	3	2p4	4s	3P	3D*
53	1	32	15.180	3	5	15.125	4.40E+07	1.5E-02	3	2p4	4s	3P	3D*
54	1	32	15.181	1	3	15.125	3.25E+07	1.5E-02	3	2p4	4s	3P	3D*
55	2	32	16.730	5	5	14.753	1.03E+07	1.5E-02	3	2p4	8d	1D	1D*
56	2	32	16.730	5	7	14.753	1.12E+07	1.5E-02	3	2p4	8d	1D	1F*
57	2	32	16.665	5	5	14.753	1.51E+07	1.6E-02	3	2p4	7d	1D	1D*
58	2	32	16.665	5	7	14.753	1.63E+07	1.6E-02	3	2p4	7d	1D	1F*
59	2	32	16.652	5	5	14.629	9.09E+06	1.6E-02	3	2p4	8s	1D	1D*
60	2	32	16.563	5	7	14.629	2.49E+07	1.6E-02	3	2p4	6d	1D	1F*
61	2	32	16.563	5	5	14.629	2.33E+07	1.6E-02	3	2p4	6d	1D	1D*
62	2	32	16.542	5	5	14.629	1.46E+07	1.6E-02	3	2p4	7s	1D	1D*
63	2	32	16.396	5	7	14.381	4.06E+07	1.6E-02	3	2p4	5d	1D	1F*
64	2	32	16.395	5	5	14.381	3.82E+07	1.6E-02	3	2p4	5d	1D	1D*
65	2	32	16.391	5	3	14.381	1.10E+07	1.6E-02	3	2p4	5d	1D	1P*
66	2	32	16.358	5	5	14.381	2.58E+07	1.6E-02	3	2p4	6s	1D	1D*
67	1	32	14.124	5	3	14.133	2.85E+08	1.7E-02	3	2p4	3s	3P	3P*
68	1	32	14.123	5	5	14.133	5.12E+08	1.7E-02	3	2p4	3s	3P	3P*
69	2	32	16.085	5	7	14.133	7.05E+07	1.7E-02	3	2p4	4d	1D	1F*
70	2	32	16.085	5	5	14.133	6.68E+07	1.7E-02	3	2p4	4d	1D	1D*
71	2	32	16.079	5	3	14.133	1.70E+07	1.7E-02	3	2p4	4d	1D	1P*
72	1	32	14.125	3	1	14.133	6.81E+08	1.7E-02	3	2p4	3s	3P	3P*
73	1	32	14.124	3	3	14.133	1.70E+08	1.7E-02	3	2p4	3s	3P	3P*
74	1	32	14.123	3	5	14.133	1.70E+08	1.7E-02	3	2p4	3s	3P	3P*
75	1	32	14.124	1	3	14.133	2.26E+08	1.7E-02	3	2p4	3s	3P	3P*
76	2	32	16.010	5	5	14.009	5.22E+07	1.7E-02	3	2p4	5s	1D	1D*
77	2	32	15.415	5	7	13.390	1.23E+08	1.9E-02	3	2p4	3d	1D	1F*
78	2	32	15.414	5	5	13.390	1.17E+08	1.9E-02	3	2p4	3d	1D	1D*
79	2	32	15.408	5	3	13.390	2.04E+07	1.9E-02	3	2p4	3d	1D	1P*
80	1	30	13.404	5	7	13.390	7.22E+06	4.9E-01	2	2p4	8d	3P	3D*
81	1	30	13.404	5	5	13.390	1.81E+06	4.9E-01	2	2p4	8d	3P	3D*
82	1	30	13.404	5	3	13.390	2.01E+05	4.9E-01	2	2p4	8d	3P	3D*
83	1	30	13.404	3	5	13.390	5.39E+06	4.9E-01	2	2p4	8d	3P	3D*
84	1	30	13.404	3	3	13.390	3.00E+06	4.9E-01	2	2p4	8d	3P	3D*
85	1	30	13.404	1	3	13.390	3.99E+06	4.9E-01	2	2p4	8d	3P	3D*
86	1	29	13.339	5	7	13.390	1.06E+07	3.2E-01	2	2p4	7d	3P	3D*
87	1	29	13.339	5	5	13.390	2.66E+06	3.2E-01	2	2p4	7d	3P	3D*
88	1	29	13.339	5	3	13.390	2.96E+05	3.2E-01	2	2p4	7d	3P	3D*
89	1	30	13.328	5	3	13.266	6.90E+06	1.9E-02	3	2p4	8s	3P	3S*
90	1	29	13.339	3	5	13.266	7.95E+06	3.2E-01	2	2p4	7d	3P	3D*
91	1	29	13.339	3	3	13.266	4.42E+06	3.2E-01	2	2p4	7d	3P	3D*
92	1	29	13.339	1	3	13.266	5.88E+06	3.2E-01	2	2p4	7d	3P	3D*
93	1	30	13.328	3	3	13.266	4.12E+06	1.9E-02	3	2p4	8s	3P	3S*
94	1	30	13.328	1	3	13.266	1.37E+06	1.9E-02	3	2p4	8s	3P	3S*
95	2	32	15.225	5	5	13.266	1.33E+08	1.9E-02	3	2p4	4s	1D	1D*
96	1	28	13.237	5	7	13.266	1.66E+07	1.6E-01	2	2p4	6d	3P	3D*
97	1	28	13.237	5	5	13.266	4.15E+06	1.6E-01	2	2p4	6d	3P	3D*
98	1	28	13.237	5	3	13.266	4.61E+05	1.6E-01	2	2p4	6d	3P	3D*
99	1	29	13.220	5	3	13.266	1.11E+07	1.9E-02	3	2p4	7s	3P	3S*
100	1	28	13.237	3	5	13.266	1.24E+07	1.6E-01	2	2p4	6d	3P	3D*
101	1	28	13.237	3	3	13.266	6.88E+06	1.6E-01	2	2p4	6d	3P	3D*
102	1	28	13.237	1	3	13.266	9.16E+06	1.6E-01	2	2p4	6d	3P	3D*
103	1	29	13.220	3	3	13.142	6.63E+06	1.9E-02	3	2p4	7s	3P	3S*
104	1	29	13.220	1	3	13.142	2.21E+06	1.9E-02	3	2p4	7s	3P	3S*
105	1	25	13.069	5	5	13.018	7.02E+06	4.8E-02	2	2p4	5d	3P	3D*
106	1	25	13.069	5	3	13.018	7.80E+05	4.8E-02	2	2p4	5d	3P	3D*

107	1	25	13.069	5	7	13.018	2.81E+07	4.8E-02	2	2p4	5d	3P	3D*
108	1	25	13.069	3	5	13.018	2.10E+07	4.8E-02	2	2p4	5d	3P	3D*
109	1	25	13.069	3	3	13.018	1.16E+07	4.8E-02	2	2p4	5d	3P	3D*
110	1	25	13.069	1	3	13.018	1.55E+07	4.8E-02	2	2p4	5d	3P	3D*
111	1	28	13.039	5	3	13.018	1.94E+07	4.9E-03	2	2p4	6s	3P	3S*
112	1	28	13.039	3	3	13.018	1.16E+07	4.9E-03	2	2p4	6s	3P	3S*
113	1	28	13.039	1	3	13.018	3.85E+06	4.9E-03	2	2p4	6s	3P	3S*
114	1	19	12.759	5	3	12.770	1.62E+06	1.8E-02	2	2p4	4d	3P	3D*
115	1	19	12.759	5	5	12.770	1.46E+07	1.8E-02	2	2p4	4d	3P	3D*
116	1	19	12.759	5	7	12.770	5.85E+07	1.8E-02	2	2p4	4d	3P	3D*
117	1	19	12.759	3	5	12.770	4.37E+07	1.8E-02	2	2p4	4d	3P	3D*
118	1	19	12.759	3	3	12.770	2.42E+07	1.8E-02	2	2p4	4d	3P	3D*
119	1	19	12.759	1	3	12.770	3.23E+07	1.8E-02	2	2p4	4d	3P	3D*
120	1	17	12.728	5	5	12.770	1.10E+05	1.2E-02	3	2p4	3s	3P	1D*
121	1	17	12.728	3	5	12.770	2.22E+04	1.2E-02	3	2p4	3s	3P	1D*
122	1	16	12.697	5	3	12.646	3.86E+07	5.8E-03	2	2p4	5s	3P	3S*
123	1	16	12.697	3	3	12.646	2.30E+07	5.8E-03	2	2p4	5s	3P	3S*
124	1	16	12.697	1	3	12.646	7.66E+06	5.8E-03	2	2p4	5s	3P	3S*
125	1	14	12.542	5	3	12.522	6.47E+06	4.2E-04	1	2p4	3s	3P	3D*
126	1	14	12.541	5	5	12.522	5.77E+07	4.2E-04	1	2p4	3s	3P	3D*
127	1	14	12.539	5	7	12.522	2.26E+08	4.2E-04	1	2p4	3s	3P	3D*
128	1	14	12.542	3	3	12.522	9.47E+07	4.2E-04	1	2p4	3s	3P	3D*
129	1	14	12.541	3	5	12.522	1.68E+08	4.2E-04	1	2p4	3s	3P	3D*
130	1	14	12.542	1	3	12.522	1.25E+08	4.2E-04	1	2p4	3s	3P	3D*
131	2	32	14.372	5	3	12.398	5.06E+08	2.2E-02	3	2p4	3s	1D	1P*
132	1	11	12.087	5	7	12.088	7.66E+07	2.4E-03	1	2p4	3d	3P	3D*
133	1	11	12.087	5	5	12.088	1.91E+07	2.4E-03	1	2p4	3d	3P	3D*
134	1	11	12.087	5	3	12.088	2.11E+06	2.4E-03	1	2p4	3d	3P	3D*
135	1	11	12.087	3	3	12.063	3.17E+07	2.4E-03	1	2p4	3d	3P	3D*
136	1	11	12.087	3	5	12.063	5.71E+07	2.4E-03	1	2p4	3d	3P	3D*
137	1	11	12.087	1	3	12.063	4.22E+07	2.4E-03	1	2p4	3d	3P	3D*
138	1	9	11.930	5	3	11.927	9.43E+07	1.2E-03	2	2p4	4s	3P	3S*
139	1	9	11.930	3	3	11.914	5.64E+07	1.2E-03	2	2p4	4s	3P	3S*
140	1	9	11.930	1	3	11.902	1.88E+07	1.2E-03	2	2p4	4s	3P	3S*
141	2	17	12.728	5	5	10.761	5.28E+08	6.5E-04	1	2p4	3s	1D	1D*
142	2	14	12.542	5	3	10.575	4.98E+04	1.1E-02	3	2p4	3s	1D	3D*
143	2	14	12.541	5	5	10.575	3.66E+02	1.1E-02	3	2p4	3s	1D	3D*
144	2	14	12.539	5	7	10.575	7.97E+03	1.1E-02	3	2p4	3s	1D	3D*
145	3	32	14.372	1	3	10.179	2.06E+08	3.2E-02	3	2p4	3s	1S	1P*
146	1	5	9.521	5	3	9.521	3.41E+08	8.2E-04	1	2p4	3s	3P	3S*
147	1	5	9.521	3	3	9.497	2.03E+08	8.2E-04	1	2p4	3s	3P	3S*
148	1	5	9.521	1	3	9.497	6.76E+07	8.2E-04	1	2p4	3s	3P	3S*
149	1	4	9.146	5	5	9.150	4.20E+03	3.4E-04	3	2p4	3s	3P	5S*
150	1	4	9.146	3	5	9.125	1.36E+03	3.5E-04	3	2p4	3s	3P	5S*
151	3	14	12.542	1	3	8.356	9.05E+03	1.7E-02	3	2p4	3s	1S	3D*
152	2	5	9.521	5	3	7.550	1.83E+03	6.4E-04	3	2p4	3s	1D	3S*
153	2	4	9.146	5	5	7.178	5.32E-03	5.6E-04	3	2p4	3s	1D	5S*
154	7	32	17.775	3	5	6.782	1.52E+05	7.3E-02	3	3p	4d	3P	3D*
155	7	32	17.775	3	3	6.782	7.79E+04	7.3E-02	3	3p	4d	3P	3D*
156	7	32	17.775	5	7	6.782	1.96E+05	7.3E-02	3	3p	4d	3P	3D*
157	7	32	17.775	1	3	6.782	1.12E+05	7.3E-02	3	3p	4d	3P	3D*
158	7	32	17.775	5	5	6.782	4.32E+04	7.3E-02	3	3p	4d	3P	3D*
159	7	32	17.105	3	5	6.112	2.82E+05	9.0E-02	3	3p	3d	3P	3D*
160	7	32	17.105	3	3	6.112	1.05E+05	9.0E-02	3	3p	3d	3P	3D*
161	7	32	17.105	5	7	6.112	3.70E+05	9.0E-02	3	3p	3d	3P	3D*
162	7	32	17.105	1	3	6.112	1.92E+05	9.0E-02	3	3p	3d	3P	3D*

163	7	32	17.105	5	5	6.112	4.85E+04	9.0E-02	3	3p	3d	3P	3D*
-----	---	----	--------	---	---	-------	----------	---------	---	----	----	----	-----

Table A-4. Oxygen lines in the 0 – 6 eV spectral range (note that these are multiplet lines).

line index	i	k	$E_{k'}$ (eV)	g_i	$g_{k'}$	$\hbar\nu_{CL}$ (eV)	$A_{k''}$ (1/s)	$\Delta\lambda_{S,0}$ (Ang.)	Stark Source	conf. i	conf. k	term i	term k
164	3	5	9.521	1	3	5.331	4.61E+00	1.3E-03	3	2p4	3s	1S	3S*
165	4	6	10.741	5	15	1.594	3.69E+07	3.2E-02	1	3s	3p	5S*	5P
166	4	7	10.989	5	9	1.843	8.70E+02	3.4E-02	3	3s	3p	5S*	3P
167	4	12	12.286	5	15	3.140	4.89E+05	6.3E-02	1	3s	4p	5S*	5P
168	5	6	10.741	3	15	1.219	1.60E+02	6.2E-02	3	3s	3p	3S*	5P
169	5	7	10.989	3	9	1.467	3.22E+07	5.1E-02	1	3s	3p	3S*	3P
170	5	13	12.359	3	9	2.837	7.58E+05	8.0E-02	1	3s	4p	3S*	3P
171	5	23	12.878	3	9	3.357	9.30E+04	1.2E-01	2	3s	5p	3S*	3P
172	6	8	11.838	15	5	1.097	2.67E+07	3.8E-01	1	3p	4s	5P	5S*
173	6	10	12.079	15	25	1.338	4.45E+07	2.2E-01	1	3p	3d	5P	5D*
174	6	11	12.087	15	15	1.346	7.75E+02	2.6E-01	3	3p	3d	5P	3D*
175	6	15	12.661	15	5	1.920	8.25E+06	4.9E-01	1	3p	5s	5P	5S*
176	6	18	12.754	15	25	2.013	7.62E+06	1.2E+00	1	3p	4d	5P	5D*
177	6	19	12.759	15	15	2.018	4.49E+02	4.0E-01	2	3p	4d	5P	3D*
178	6	28	13.021	15	5	2.280	3.86E+06	1.0E+00	1	3p	6s	5P	5S*
179	6	24	13.066	15	25	2.325	2.71E+06	1.3E+00	2	3p	5d	5P	5D*
180	6	29	13.210	15	5	2.469	2.14E+06	5.5E-01	3	3p	7s	5P	5S*
181	6	28	13.235	15	25	2.495	1.27E+06	1.0E+00	1	3p	6d	5P	5D*
182	6	30	13.322	15	5	2.581	1.31E+06	5.0E-01	3	3p	8s	5P	5S*
183	6	29	13.337	15	25	2.597	7.00E+05	5.0E-01	3	3p	7d	5P	5D*
184	6	30	13.403	15	25	2.663	4.30E+05	4.7E-01	3	3p	8d	5P	5D*
185	7	9	11.930	9	3	0.941	2.14E+07	5.5E-01	1	3p	4s	3P	3S*
186	7	10	12.079	9	25	1.090	3.31E+02	4.0E-01	3	3p	3d	3P	5D*
187	7	11	12.087	9	15	1.098	3.09E+07	2.9E-01	1	3p	3d	3P	3D*
188	7	14	12.540	9	15	1.551	5.61E+04	5.0E-01	3	3p	3s	3P	3D*
189	7	16	12.697	9	3	1.709	6.72E+06	6.6E-01	1	3p	5s	3P	3S*
190	7	19	12.759	9	15	1.770	3.53E+06	1.7E+00	1	3p	4d	3P	3D*
191	7	28	13.039	9	3	2.050	3.15E+06	1.3E+00	1	3p	6s	3P	3S*
192	7	25	13.069	9	15	2.080	9.07E+05	1.6E+00	2	3p	5d	3P	3D*
193	7	29	13.220	9	3	2.231	1.75E+06	6.7E-01	3	3p	7s	3P	3S*
194	7	28	13.237	9	15	2.248	3.58E+05	1.3E+00	1	3p	6d	3P	3D*
195	7	30	13.328	9	3	2.339	1.07E+06	6.1E-01	3	3p	8s	3P	3S*
196	7	29	13.339	9	15	2.350	1.76E+05	6.1E-01	3	3p	7d	3P	3D*
197	7	30	13.404	9	15	2.415	9.98E+04	5.7E-01	3	3p	8d	3P	3D*
198	7	32	14.124	9	9	3.135	3.09E+05	3.4E-01	3	3p	3s	3P	3P*
199	7	32	15.291	9	9	4.301	1.47E+06	1.8E-01	3	3p	3d	3P	3P*
200	7	32	15.406	9	15	4.416	4.31E+05	1.7E-01	3	3p	3d	3P	3D*
201	7	32	15.416	9	3	4.427	1.45E+06	1.7E-01	3	3p	3d	3P	3S*
202	7	32	16.080	9	15	5.091	3.09E+05	1.3E-01	3	3p	4d	3P	3D*
203	7	32	16.085	9	3	5.096	1.11E+06	1.3E-01	3	3p	4d	3P	3S*
204	7	32	16.115	9	9	5.126	2.98E+05	1.3E-01	3	3p	4d	3P	3P*
205	8	12	12.286	5	15	0.448	4.30E+06	3.4E+00	3	4s	4p	5S*	5P
206	8	22	12.848	5	15	1.010	2.35E+05	2.8E+00	3	4s	5p	5S*	5P
207	8	28	13.116	5	15	1.278	4.54E+04	2.1E+00	3	4s	6p	5S*	5P
208	9	12	12.286	3	15	0.356	3.01E+01	5.4E+00	3	4s	4p	3S*	5P
209	9	13	12.359	3	9	0.428	4.10E+06	4.3E+00	3	4s	4p	3S*	3P
210	9	23	12.878	3	9	0.948	2.86E+05	3.6E+00	3	4s	5p	3S*	3P
211	10	12	12.286	25	15	0.207	4.97E+05	1.2E+01	2	3d	4p	5D*	5P

212	10	20	12.766	25	35	0.688	1.48E+07	4.4E+00	2	3d	4f	5D*	5F
213	10	22	12.848	25	15	0.769	4.04E+04	2.2E+00	2	3d	5p	5D*	5P
214	10	26	13.073	25	35	0.994	4.97E+06	3.9E+00	2	3d	5f	5D*	5F
215	10	28	13.116	25	15	1.037	2.09E+04	3.1E+00	3	3d	6p	5D*	5P
216	10	28	13.240	25	35	1.161	2.37E+06	2.5E+00	3	3d	6f	5D*	5F
217	10	29	13.340	25	35	1.261	1.34E+06	2.1E+00	3	3d	7f	5D*	5F
218	11	12	12.286	15	15	0.199	5.70E+00	1.3E+01	2	3d	4p	3D*	5P
219	11	13	12.359	15	9	0.272	9.86E+05	1.3E+01	2	3d	4p	3D*	3P
220	11	21	12.766	15	21	0.679	1.47E+07	4.5E+00	2	3d	4f	3D*	3F
221	11	23	12.878	15	9	0.791	1.83E+05	2.3E+00	2	3d	5p	3D*	3P
222	11	27	13.073	15	21	0.986	4.82E+06	3.9E+00	2	3d	5f	3D*	3F
223	11	28	13.131	15	9	1.044	8.52E+04	3.1E+00	3	3d	6p	3D*	3P
224	11	28	13.240	15	21	1.153	2.28E+06	2.5E+00	3	3d	6f	3D*	3F
225	11	29	13.340	15	21	1.253	1.28E+06	2.1E+00	3	3d	7f	3D*	3F
226	11	32	14.047	15	15	1.960	2.41E+04	8.7E-01	3	3d	3p	3D*	3D
227	12	15	12.661	15	5	0.375	5.51E+06	1.2E+01	3	4p	5s	5P	5S*
228	12	18	12.754	15	25	0.468	6.45E+06	9.8E+00	3	4p	4d	5P	5D*
229	12	19	12.759	15	15	0.473	4.26E+02	9.7E+00	3	4p	4d	5P	3D*
230	12	28	13.021	15	5	0.735	1.99E+06	1.0E+01	3	4p	6s	5P	5S*
231	12	24	13.066	15	25	0.780	1.93E+06	1.1E+01	3	4p	5d	5P	5D*
232	12	29	13.210	15	5	0.924	1.04E+06	3.9E+00	3	4p	7s	5P	5S*
233	12	28	13.235	15	25	0.949	8.65E+05	3.7E+00	3	4p	6d	5P	5D*
234	12	30	13.322	15	5	1.035	6.19E+05	3.1E+00	3	4p	8s	5P	5S*
235	12	29	13.337	15	25	1.051	4.70E+05	3.0E+00	3	4p	7d	5P	5D*
236	12	30	13.403	15	25	1.117	2.87E+05	2.7E+00	3	4p	8d	5P	5D*
237	13	16	12.697	9	3	0.339	4.83E+06	1.6E+01	3	4p	5s	3P	3S*
238	13	18	12.754	9	25	0.395	2.24E+02	1.4E+01	3	4p	4d	3P	5D*
239	13	19	12.759	9	15	0.400	5.04E+06	1.4E+01	3	4p	4d	3P	3D*
240	13	28	13.039	9	3	0.680	1.70E+06	1.3E+01	3	4p	6s	3P	3S*
241	13	25	13.069	9	15	0.710	1.18E+06	1.4E+01	3	4p	5d	3P	3D*
242	13	29	13.220	9	3	0.861	8.88E+05	4.5E+00	3	4p	7s	3P	3S*
243	13	28	13.237	9	15	0.878	4.65E+05	4.3E+00	3	4p	6d	3P	3D*
244	13	30	13.328	9	3	0.969	5.31E+05	3.6E+00	3	4p	8s	3P	3S*
245	13	29	13.339	9	15	0.980	2.34E+05	3.5E+00	3	4p	7d	3P	3D*
246	13	30	13.404	9	15	1.045	1.36E+05	3.1E+00	3	4p	8d	3P	3D*
247	13	32	14.124	9	9	1.765	3.21E+04	1.1E+00	3	4p	3s	3P	3P*
248	13	32	15.291	9	9	2.931	5.41E+05	3.9E-01	3	4p	3d	3P	3P*
249	13	32	15.406	9	15	3.046	2.33E+05	3.6E-01	3	4p	3d	3P	3D*
250	13	32	15.416	9	3	3.057	8.19E+05	3.6E-01	3	4p	3d	3P	3S*
251	13	32	16.080	9	15	3.721	2.72E+04	2.4E-01	3	4p	4d	3P	3D*
252	13	32	16.085	9	3	3.726	6.53E+05	2.4E-01	3	4p	4d	3P	3S*
253	13	32	16.115	9	9	3.756	1.43E+05	2.4E-01	3	4p	4d	3P	3P*
254	13	32	17.105	9	15	4.746	1.66E+05	1.5E-01	3	4p	3d	3P	3D*
255	13	32	17.775	9	15	5.416	1.45E+05	1.1E-01	3	4p	4d	3P	3D*
256	14	21	12.766	15	21	0.226	1.56E+04	4.3E+01	3	3s	4f	3D*	3F
257	14	23	12.878	15	9	0.338	2.58E+04	2.8E+01	3	3s	5p	3D*	3P
258	14	27	13.073	15	21	0.533	4.35E+04	2.5E+01	3	3s	5f	3D*	3F
259	14	28	13.240	15	21	0.699	2.51E+04	6.9E+00	3	3s	6f	3D*	3F
260	14	29	13.340	15	21	0.800	1.55E+04	5.2E+00	3	3s	7f	3D*	3F
261	14	32	14.047	15	15	1.507	3.25E+07	1.5E+00	3	3s	3p	3D*	3D
262	14	32	15.781	15	15	3.241	7.47E+05	3.2E-01	3	3s	3p	3D*	3D
263	17	32	14.036	5	3	1.307	2.34E+07	2.0E+00	3	3s	3p	1D*	1P
264	17	32	14.134	5	7	1.405	2.93E+07	1.7E+00	3	3s	3p	1D*	1F
265	17	32	14.460	5	5	1.732	5.05E+07	1.1E+00	3	3s	3p	1D*	1D
266	17	32	15.829	5	3	3.100	2.41E+06	3.5E-01	3	3s	3p	1D*	1P
267	17	32	15.944	5	5	3.215	1.63E+06	3.2E-01	3	3s	3p	1D*	1D

268	18	20	12.766	25	35	0.013	2.40E+02	1.4E+04	3	4d	4f	5D*	5F
269	18	22	12.848	25	15	0.094	2.02E+05	3.3E+02	3	4d	5p	5D*	5P
270	18	26	13.073	25	35	0.319	2.68E+06	7.0E+01	3	4d	5f	5D*	5F
271	18	28	13.116	25	15	0.362	1.35E+04	2.6E+01	3	4d	6p	5D*	5P
272	18	28	13.240	25	35	0.486	1.37E+06	1.4E+01	3	4d	6f	5D*	5F
273	18	29	13.340	25	35	0.586	7.88E+05	9.8E+00	3	4d	7f	5D*	5F
274	19	21	12.766	15	21	0.007	4.68E+01	4.0E+04	3	4d	4f	3D*	3F
275	19	23	12.878	15	9	0.119	3.62E+05	2.3E+02	3	4d	5p	3D*	3P
276	19	27	13.073	15	21	0.314	2.72E+06	7.2E+01	3	4d	5f	3D*	3F
277	19	28	13.131	15	9	0.372	6.75E+04	2.4E+01	3	4d	6p	3D*	3P
278	19	28	13.240	15	21	0.481	1.34E+06	1.5E+01	3	4d	6f	3D*	3F
279	19	29	13.340	15	21	0.581	7.60E+05	9.9E+00	3	4d	7f	3D*	3F
280	19	32	14.047	15	15	1.288	2.09E+05	2.0E+00	3	4d	3p	3D*	3D
281	20	24	13.066	35	25	0.300	6.44E+04	7.7E+01	3	4f	5d	5F	5D*
282	20	28	13.235	35	25	0.469	2.81E+04	1.5E+01	3	4f	6d	5F	5D*
283	20	29	13.337	35	25	0.571	1.50E+04	1.0E+01	3	4f	7d	5F	5D*

Appendix B. Photoionization Cross-Section Data

This appendix presents the step-models and curve-fits created for the photoionization cross-section, which were presented in Section 3.7. Tables B-1 and B-3 present the step models, which are used for the first three levels of nitrogen and oxygen. These models are defined by $h\nu_{A,i}$ and $h\nu_{B,i}$, which are minimum and maximum $h\nu$ values for each step, and σ_i^{bf} , which is the constant value of the cross-section across the step. For the curve-fitted levels, the value presented in Tables B-2 and B-4 are applied to Eq. (3.36).

Nitrogen

Table B-1. Step model for *nitrogen* photoionization cross sections

$(i = 1)$		
$h\nu_{A,i}$ (eV)	$h\nu_{B,i}$ (eV)	$\sigma_i^{bf} \times 10^{18}$ (cm 2)
14.5627	15.0000	12.87
15.0000	15.5000	13.25
15.5000	16.0000	13.60
16.0000	16.2559	13.90
16.2559	18.9518	14.00

$(i = 2)$		
$h\nu_{A,i}$ (eV)	$h\nu_{B,i}$ (eV)	$\sigma_i^{bf} \times 10^{18}$ (cm 2)
11.9897	12.2900	6.90
12.2900	12.3300	50.00
12.3300	12.7750	6.90
12.7750	12.7900	600.00
12.7900	13.1400	6.90
13.1400	13.1700	60.00
13.1700	13.8100	6.90
13.8100	13.8450	240.00
13.8450	13.8760	6.90
13.8760	13.8765	14.00
13.8765	13.8775	6.90
13.8775	16.7166	14.10
16.7166	18.8565	15.40

$(i = 3)$		
$h\nu_{A,i}$ (eV)	$h\nu_{B,i}$ (eV)	$\sigma_i^{bf} \times 10^{18}$ (cm 2)
10.6867	11.4670	6.50
11.4670	11.4850	170.00
11.4850	12.4400	6.50

12.4400	12.4355	140.00
12.4355	12.5744	6.50
12.5744	13.3610	10.10
13.3610	13.9800	9.40
13.9800	14.0120	180.00
14.0120	14.3000	9.40
14.3000	14.3186	190.00
14.3186	14.5845	9.40
14.5845	14.5865	250.00
14.5865	14.7260	9.40
14.7260	15.2900	16.00
15.2900	15.9340	14.92
15.9340	16.4758	20.00
16.4758	18.9899	26.80

Table B-2. Curve-fit parameters for the upper level photoionization cross-sections of nitrogen

Level Index i	$h\nu_{thresh,i}$ (eV)	$\sigma_{thresh,i}^{bf} \times 10^{18}$ (cm 2)	θ_i
4	4.0751	0.120	-2.4896
5	3.6631	0.794	0.3095
6	3.5961	1.090	-1.2292
7	2.7792	5.410	1.8625
8	2.6197	3.740	1.4786
9	2.5293	3.200	1.4868
10	2.3843	2.310	0.8060
11	2.3703	2.020	0.9084
12	2.2474	1.520	0.6732
13	1.6677	4.800	1.6969
14	1.5343	0.868	1.1667
15	1.4771	5.550	1.8842
16	1.4206	25.900	3.0528
17	1.4114	27.900	2.9575
18	1.3973	25.300	2.4588
19	1.3962	26.900	3.4935
20	1.3775	25.600	3.3806
21	1.3613	24.100	3.3403
22	1.1977	18.100	2.3407
23	1.1549	13.500	2.9829
24	1.1311	12.100	2.9187
25	1.0995	9.270	2.7892
26	1.2184	16.426	3.0000
27	1.1974	16.692	3.0000
28	0.8635	22.434	3.0000
29	0.8423	22.937	3.0000
30	0.5791	30.990	3.0000
31	0.3697	42.100	3.0000
32	0.2694	51.179	3.0000
33	0.2044	60.134	3.0000
34	0.1598	69.091	3.0000
35	0.1279	78.076	3.0000

Oxygen

Table B-3. Step model for *oxygen* photoionization cross sections

$(i = 1)$		
$h\nu_{A,i}$ (eV)	$h\nu_{B,i}$ (eV)	$\sigma_i^{bf} \times 10^{18}$ (cm 2)
13.5445	15.2350	3.84
15.2350	15.2500	15.00
15.2500	18.9518	5.21

$(i = 2)$		
$h\nu_{A,i}$ (eV)	$h\nu_{B,i}$ (eV)	$\sigma_i^{bf} \times 10^{18}$ (cm 2)
14.7738	15.0800	8.00
15.0800	15.0900	140.00
15.0900	15.7000	7.50
15.7000	15.7100	50.00
15.7100	18.8565	8.74

$(i = 3)$		
$h\nu_{A,i}$ (eV)	$h\nu_{B,i}$ (eV)	$\sigma_i^{bf} \times 10^{18}$ (cm 2)
12.4071	12.5400	0.01
12.5400	12.5500	100.00
12.5500	12.7100	4.00
12.7100	12.7400	200.00
12.7400	13.3000	0.03
13.3000	13.3400	210.00
13.3400	14.0940	0.40
14.0940	17.7500	9.50
17.7500	18.9899	9.24

Table B-4. Curve-fit parameters for the upper level photoionization cross-sections of *oxygen*

Level Index i	$h\nu_{thresh,i}$ (eV)	$\sigma_{thresh,i}^{bf} \times 10^{18}$ (cm 2)	θ_i
4	13.5445	3.8490	-0.8858
5	14.7738	7.5580	-0.5701
6	12.4071	0.0248	-13.8111
7	4.2674	0.0324	-1.9522
8	3.8902	0.0110	-2.5187
9	2.7243	5.3990	2.0511
10	2.4763	2.5510	1.0492
11	1.6509	0.0695	-0.2865
12	1.5565	0.1025	-0.1245
13	1.4189	24.6200	3.0927
14	2.3703	2.0200	0.6997

15	2.2474	1.5200	0.6247
16	1.6677	4.8000	1.1384
17	1.5343	0.8680	1.0608
18	1.4771	5.5500	1.3870
19	1.4206	25.9000	2.4937
20	1.1977	18.1000	2.0637
21	1.4114	27.9000	2.7457
22	1.3973	25.3000	2.4689
23	1.3962	26.9000	2.9524
24	1.3775	25.6000	2.9514
25	1.3613	24.1000	2.5351
26	1.1549	13.5000	1.7161
27	1.0764	7.5400	1.4713
28	1.0523	5.0500	1.2143
29	0.5469	33.1689	3.0000
30	0.5469	33.1693	3.0000
31	0.3992	40.7996	3.0000
32	0.2822	50.3915	3.0000

Appendix C. Curve-Fit Coefficients for Calculating Electronic State Populations

This appendix presents the curve fit parameters discussed in Chapter 4 for calculating the non-Boltzmann population of the atomic and molecular electronic states.

a) Atomic Species

For the atomic electronic states, the AACR model presented in Section 4.6 is applied. This model treats the population of the grouped levels defined in Table 4.4. For each of these levels, the r_0 and r_1 values defined in Eq. (4.24) are curve-fit as a function of the electronic temperature and the electron number density as follows:

$$r_j = (A_1 T_e^3 + A_2 T_e^2 + A_3 T_e + A_4) (\ln N_e)^3 + (B_1 T_e^3 + B_2 T_e^2 + B_3 T_e + B_4) (\ln N_e)^2 + (C_1 T_e^3 + C_2 T_e^2 + C_3 T_e + C_4) (\ln N_e) + (D_1 T_e^3 + D_2 T_e^2 + D_3 T_e + D_4) \quad (C-1)$$

where r_j represents either r_0 or r_1 . The coefficients for these curve fits are defined in Table C-1 through C-4 for each of the grouped levels defined in Table 4.4. These curve fits are valid for $7,000 < T_e < 14,000$ K and $1 \times 10^{14} < N_e < 1 \times 10^{16}$ particles/cm³, for values of T_e and N_e outside of these limits, it is sufficient for shock layer applications to evaluate the curve-fit using the value at the limit. The procedure for calculating the number density of each of these levels from r_0 and r_1 is described in Section 4.6.

Table C-1. r_0 Curve fit parameters for N

	i	$n = 5$	$n = 10$	$n = 17$	$n = 24$	$n = 28$
A_i	1	2.943570E-14	-3.679405E-16	-5.037113E-15	-5.120039E-15	-2.288411E-15
	2	-5.147823E-10	2.285901E-10	2.453762E-10	2.438074E-10	9.171901E-11
	3	-6.438555E-07	-5.241023E-06	-3.684047E-06	-3.625877E-06	-1.221548E-06
	4	1.916187E-02	2.635927E-02	1.771452E-02	1.724069E-02	5.574363E-03
B_i	1	-2.832276E-12	1.592970E-13	5.626748E-13	5.686106E-13	2.450118E-13
	2	4.597198E-08	-2.740468E-08	-2.655411E-08	-2.631983E-08	-9.732332E-09
	3	1.442056E-04	5.781335E-04	3.910989E-04	3.845806E-04	1.287422E-04
	4	-2.221186E+00	-2.828919E+00	-1.865546E+00	-1.815010E+00	-5.865804E-01
C_i	1	9.047477E-11	-9.262384E-12	-2.054545E-11	-2.067410E-11	-8.676670E-12
	2	-1.343415E-06	1.058720E-06	9.457423E-07	9.357567E-07	3.420989E-07
	3	-7.485024E-03	-2.097987E-02	-1.371628E-02	-1.348132E-02	-4.501622E-03
	4	8.416979E+01	1.004119E+02	6.513526E+01	6.336287E+01	2.052166E+01
D_i	1	-9.594647E-10	1.452198E-10	2.465091E-10	2.472921E-10	1.019330E-10
	2	1.278121E-05	-1.330525E-05	-1.112152E-05	-1.099141E-05	-3.993965E-06
	3	1.129798E-01	2.511408E-01	1.593260E-01	1.565859E-01	5.235146E-02
	4	-1.046966E+03	-1.180407E+03	-7.549593E+02	-7.344588E+02	-2.382878E+02

Table C-2. r_I Curve fit parameters for **N**

	i	$n = 5$	$n = 10$	$n = 17$	$n = 24$	$n = 28$
A_i	1	-2.626055E-14	-1.846197E-14	-9.663253E-15	-9.135009E-15	-1.978273E-15
	2	8.637611E-10	5.955747E-10	3.081625E-10	2.910957E-10	6.251448E-11
	3	-9.193450E-06	-6.209887E-06	-3.175193E-06	-2.996687E-06	-6.374943E-07
	4	3.052449E-02	2.032648E-02	1.030960E-02	9.720360E-03	2.047928E-03
B_i	1	2.644065E-12	1.840146E-12	9.535923E-13	9.007351E-13	1.929803E-13
	2	-8.669291E-08	-5.914172E-08	-3.028145E-08	-2.857953E-08	-6.067513E-09
	3	9.179482E-04	6.129970E-04	3.099295E-04	2.922233E-04	6.138313E-05
	4	-3.017573E+00	-1.984677E+00	-9.943669E-01	-9.364655E-01	-1.944156E-01
C_i	1	-8.872526E-11	-6.116079E-11	-3.139896E-11	-2.963502E-11	-6.282883E-12
	2	2.900148E-06	1.958576E-06	9.929428E-07	9.363318E-07	1.965449E-07
	3	-3.055363E-02	-2.018260E-02	-1.009594E-02	-9.509975E-03	-1.972476E-03
	4	9.946406E+01	6.464327E+01	3.200784E+01	3.010881E+01	6.157075E+00
D_i	1	9.922082E-10	6.777690E-10	3.448984E-10	3.252696E-10	6.825329E-11
	2	-3.233527E-05	-2.162787E-05	-1.086249E-05	-1.023449E-05	-2.124370E-06
	3	3.389887E-01	2.216013E-01	1.097294E-01	1.032609E-01	2.114725E-02
	4	-1.093060E+03	-7.022353E+02	-3.437618E+02	-3.229790E+02	-6.502926E+01

Table C-3. r_θ Curve fit parameters for **O**

	i	$n = 5$	$n = 10$	$n = 17$	$n = 24$	$n = 28$
A_i	1	4.132316E-14	-1.416982E-15	-1.586395E-15	-9.654976E-16	-3.353768E-16
	2	-1.189059E-09	7.911049E-11	7.236652E-11	3.937384E-11	1.313401E-11
	3	9.183833E-06	-1.489709E-06	-1.187711E-06	-5.746902E-07	-1.818368E-07
	4	-1.785406E-02	1.010859E-02	7.672146E-03	3.208160E-03	9.429539E-04
B_i	1	-4.180985E-12	1.620474E-13	1.763893E-13	1.057675E-13	3.656618E-14
	2	1.194754E-07	-8.812612E-09	-7.967026E-09	-4.296543E-09	-1.428584E-09
	3	-9.078648E-04	1.633736E-04	1.296922E-04	6.247206E-05	1.972972E-05
	4	1.713399E+00	-1.098593E+00	-8.326357E-01	-3.475876E-01	-1.020800E-01
C_i	1	1.408795E-10	-6.158291E-12	-6.536075E-12	-3.864203E-12	-1.329838E-12
	2	-3.998526E-06	3.270531E-07	2.924787E-07	1.563877E-07	5.183447E-08
	3	2.989970E-02	-5.974666E-03	-4.723923E-03	-2.265465E-03	-7.141499E-04
	4	-5.471878E+01	3.982782E+01	3.014623E+01	1.256353E+01	3.686638E+00
D_i	1	-1.580988E-09	7.828571E-11	8.101484E-11	4.719059E-11	1.616061E-11
	2	4.457589E-05	-4.060832E-06	-3.590763E-06	-1.902377E-06	-6.283688E-07
	3	-3.280852E-01	7.306106E-02	5.751641E-02	2.744884E-02	8.634930E-03
	4	5.815185E+02	-4.814657E+02	-3.636103E+02	-1.506642E+02	-4.346274E+01

Table C-4. r_I Curve fit parameters for O

	i	$n = 5$	$n = 10$	$n = 17$	$n = 24$	$n = 28$
A_i	1	-1.367478E-14	-2.824874E-15	-1.643003E-15	-5.549855E-16	-1.431444E-16
	2	4.887061E-10	9.475275E-11	5.496342E-11	1.850579E-11	4.762388E-12
	3	-5.820836E-06	-1.055202E-06	-6.101017E-07	-2.046165E-07	-5.251636E-08
	4	2.250760E-02	3.901741E-03	2.246874E-03	7.500921E-04	1.919176E-04
B_i	1	1.392785E-12	2.988173E-13	1.732659E-13	5.849303E-14	1.508118E-14
	2	-4.969809E-08	-1.001826E-08	-5.793639E-09	-1.949602E-09	-5.015473E-10
	3	5.904136E-04	1.115029E-04	6.427451E-05	2.154533E-05	5.528002E-06
	4	-2.271019E+00	-4.120122E-01	-2.365500E-01	-7.893165E-02	-2.018957E-02
C_i	1	-4.725788E-11	-1.056215E-11	-6.107090E-12	-2.060649E-12	-5.311271E-13
	2	1.683785E-06	3.539594E-07	2.041256E-07	6.865678E-08	1.765723E-08
	3	-1.995406E-02	-3.937584E-03	-2.263485E-03	-7.583996E-04	-1.945352E-04
	4	7.637201E+01	1.454155E+01	8.325821E+00	2.776997E+00	7.101477E-01
D_i	1	5.341639E-10	1.244671E-10	7.178974E-11	2.421106E-11	6.238437E-12
	2	-1.900513E-05	-4.169354E-06	-2.398583E-06	-8.063716E-07	-2.073251E-07
	3	2.246938E-01	4.635810E-02	2.658492E-02	8.903576E-03	2.283250E-03
	4	-8.559413E+02	-1.711043E+02	-9.773794E+01	-3.258618E+01	-8.331198E+00

b) Molecular Species

The number density of a molecular electronic state (N_j), divided by the species number density of the particular species (N_a), was curve-fit in the following form

$$\frac{N_j}{N_a} = \left(A_1 T_e^3 + A_2 T_e^2 + A_3 T_e + A_4 \right) (\ln N_e)^3 + \left(B_1 T_e^3 + B_2 T_e^2 + B_3 T_e + B_4 \right) (\ln N_e)^2 + \left(C_1 T_e^3 + C_2 T_e^2 + C_3 T_e + C_4 \right) (\ln N_e) + \left(D_1 T_e^3 + D_2 T_e^2 + D_3 T_e + D_4 \right) \quad (C-2)$$

where T_e is the electronic temperature (K) and N_e is the electron number density (particles/cm³).

The A_i , B_i , C_i , and D_i values are the curve-fit parameters tabulated in Tables C-5 through C-12 for each state of present interest. These curve fits are valid for $7,000 < T_e < 14,000$ K and $1 \times 10^{14} < N_e < 1 \times 10^{16}$ particles/cm³, for values of T_e and N_e outside of these limits, it is sufficient for shock layer applications to evaluate the curve-fit using the value at the limit. For example, this is required in the boundary layer for most shock layers.

Table C-5. Curve fit parameters for the N₂⁺(X) state

	$i = 1$	$i = 2$	$i = 3$	$i = 4$
A_i	5.396812E-14	-1.726705E-09	1.724788E-05	-5.141657E-02
B_i	-5.712549E-12	1.822726E-07	-1.814746E-03	5.395767E+00
C_i	2.011901E-10	-6.400983E-06	6.350960E-02	-1.883384E+02
D_i	-2.357183E-09	7.476941E-05	-7.391945E-01	2.187317E+03

Table C-6. Curve fit parameters for the $\text{N}_2^+(\text{A})$ state

	$i = 1$	$i = 2$	$i = 3$	$i = 4$
A_i	-5.399528E-14	1.727188E-09	-1.722235E-05	5.126986E-02
B_i	5.714617E-12	-1.822912E-07	1.811819E-03	-5.379862E+00
C_i	-2.012305E-10	6.400344E-06	-6.339751E-02	1.877626E+02
D_i	2.357248E-09	-7.474585E-05	7.377692E-01	-2.179374E+03

Table C-7. Curve fit parameters for the $\text{N}_2^+(\text{B})$ state

	$i = 1$	$i = 2$	$i = 3$	$i = 4$
A_i	1.909662E-17	-2.749765E-13	-2.726340E-08	1.514464E-04
B_i	-1.208817E-15	-3.454860E-12	3.109647E-06	-1.640155E-02
C_i	9.864642E-15	1.416583E-09	-1.185081E-04	5.931615E-01
D_i	2.935892E-13	-3.263338E-08	1.499790E-03	-7.143675E+00

Table C-8. Curve fit parameters for the $\text{N}_2^+(\text{C})$ state

	$i = 1$	$i = 2$	$i = 3$	$i = 4$
A_i	8.061409E-18	-2.080982E-13	1.737354E-09	-4.737351E-06
B_i	-8.597091E-16	2.204320E-11	-1.830759E-07	4.970557E-04
C_i	3.054573E-14	-7.774826E-10	6.420562E-06	-1.734947E-02
D_i	-3.592414E-13	9.078005E-09	-7.453387E-05	2.004046E-01

Table C-9. Curve fit parameters for the $\text{N}_2(\text{X})$ state

	$i = 1$	$i = 2$	$i = 3$	$i = 4$
A_i	5.464115E-17	-1.668237E-12	1.614529E-08	-5.027658E-05
B_i	-6.046955E-15	1.832330E-10	-1.764440E-06	5.474624E-03
C_i	2.231820E-13	-6.712248E-09	6.430835E-05	-1.987993E-01
D_i	-2.716708E-12	8.087165E-08	-7.699105E-04	3.369936E+00

Table C-10. Curve fit parameters for the $\text{N}_2(\text{A})$ state

	$i = 1$	$i = 2$	$i = 3$	$i = 4$
A_i	6.088805E-17	-1.996931E-12	1.972836E-08	-6.145452E-05
B_i	-6.531968E-15	2.140591E-10	-2.113395E-06	6.579671E-03
C_i	2.335589E-13	-7.647696E-09	7.545416E-05	-2.347766E-01
D_i	-2.808958E-12	9.190987E-08	-9.060716E-04	2.817098E+00

Table C-11. Curve fit parameters for the $\text{N}_2(\text{B})$ state

	$i = 1$	$i = 2$	$i = 3$	$i = 4$
A_i	-1.184562E-16	3.729569E-12	-3.634327E-08	1.128643E-04
B_i	1.289415E-14	-4.041555E-10	3.927264E-06	-1.217180E-02
C_i	-4.680584E-13	1.460364E-08	-1.414940E-04	4.376239E-01
D_i	5.660715E-12	-1.756566E-07	1.696121E-03	-5.233276E+00

Table C-12. Curve fit parameters for the N₂(C) state

	$i = 1$	$i = 2$	$i = 3$	$i = 4$
A_i	2.926952E-18	-6.439972E-14	4.696176E-10	-1.133174E-06
B_i	-3.152308E-16	6.863452E-12	-4.942952E-08	1.175057E-04
C_i	1.131751E-14	-2.436915E-10	1.731443E-06	-4.048059E-03
D_i	-1.350499E-13	2.875042E-09	-2.013917E-05	4.624250E-02

Appendix D. Line-by-Line Calculation of Molecular Band Radiation

The internal energy of a molecule is the sum of its electronic (E_e), vibrational (E_V), and rotational (E_J) components, which is written as

$$E(e, V, J) = E_e(e) + E_V(e, V) + E_J(e, V, J) \quad (cm^{-1}) \quad (D-1)$$

where e , V , and J are the electronic, vibrational, and rotational quantum numbers, respectively. The vibrational and rotational energies are expressed in terms of V and J as follows:

$$E_V(V) = \omega_e \left(V + \frac{1}{2} \right) - \omega_e x_e \left(V + \frac{1}{2} \right)^2 + \omega_e y_e \left(V + \frac{1}{2} \right)^3 + \omega_e z_e \left(V + \frac{1}{2} \right)^4 + \dots \quad (D-2)$$

$$E_J(V, J) = \left[B_e - \alpha_e \left(V + \frac{1}{2} \right) + \gamma_e \left(V + \frac{1}{2} \right)^2 + \delta_e \left(V + \frac{1}{2} \right)^3 \right] J(J+1) - \left[D_e + \beta_e \left(V + \frac{1}{2} \right) \right] J^2(J+1)^2 + \dots \quad (D-3)$$

where ω_e , $\omega_e x_e$, $\omega_e y_e$, $\omega_e z_e$, B_e , α_e , γ_e , δ_e , D_e , and β_e are the Klein-Dunham coefficients, which are specific to a given electronic level e . The radiative transitions of interest in the present study are those for which a change in the electronic energy level occurs, as well as possible vibrational and rotational level changes. The upper state of the transition, which is defined by e' , V' , and J' , will be referred to as u , and similarly the lower state, which is defined by e'' , V'' , and J'' , will be referred to as l (note that, by definition, $e' > e''$). The absorption coefficient resulting from a transition from u to l is written as

$$\kappa_{\nu, ul} = N_l \frac{S_{J'J''}}{g_l} \frac{\pi e^2}{mc} f_{V'V''} b_\nu \quad (cm^{-1}) \quad (D-4)$$

where N_l is the lower state number density (particles/cm³), g_l is the lower state degeneracy, $f_{V'V''}$ is the band absorption oscillator strength (nondimensional), $S_{J'J''}$ is the line-intensity factor (nondimensional), and b_ν is the line shape function (s). The relationship between N_l and the number density of the lower electronic state ($N_{e''}$) may be written by assuming a Boltzmann distribution of the rotational and vibrational states

$$N_l = N_{e''} \frac{(2J''+1)}{Q_{V''} Q_{J''}} \exp\left(-\frac{hc}{kT_v} E_{V''} - \frac{hc}{kT_r} E_{J''}\right) \quad \left(\frac{\text{particles}}{\text{cm}^3}\right) \quad (D-5)$$

The lower state degeneracy in Eq. (D-4) may be expressed as

$$g_l = g_{e''}(2J''+1) \quad (D-6)$$

Substituting Eqs. (D-5) and (D-6) into (D-4) results in the following expression for the absorption coefficient of a single rotational line

$$\kappa_{v,ul} = N_{e''} \frac{1}{Q_{V''} Q_{J''}} \exp\left(-\frac{hc}{kT_v} E_{V''} - \frac{hc}{kT_r} E_{J''}\right) \frac{1}{g_{e''}} \frac{\pi e^2}{mc} f_{V'V''} S_{J'J''} b_v \quad (cm^{-1}) \quad (\text{D-7})$$

The selection rules for rotational transitions require that $\Delta J = -1, 0$, or 1 , which correspond to lines belonging to the P, Q, and R branches, respectively. Ignoring spin-splitting and assuming a ${}^2\Sigma - {}^2\Sigma$ transition, the $S_{J'J''}$ terms may be written as

$$\begin{aligned} S_{J'J''}^P &= 2(J'+1) \\ S_{J'J''}^Q &= 0 \\ S_{J'J''}^R &= 2J' \end{aligned} \quad (\text{D-8})$$

These values obey the following normalization convention

$$\begin{aligned} \sum_{J''} S_{J'J''} &= S_{J'J''}^P + S_{J'J''}^Q + S_{J'J''}^R \\ &= g_{e'} g_{J'} \\ &= 2(2J'+1) \end{aligned} \quad (\text{D-9})$$

where the electronic degeneracy is equal to 2 for the ${}^2\Sigma$ states considered here. The emission coefficient may be written in terms of these parameters as

$$j_{v,ul} = N_u \frac{2\pi e^2 h}{g_u c^3 m} \nu_{CL}^3 f_{V'V''} S_{J'J''} b_v \quad \left(\frac{\text{erg}}{\text{cm}^3 \cdot \text{sr}}\right) \quad (\text{D-10})$$

which may be written in terms of the upper electronic state number density ($N_{e'}$) as

$$j_{v,ul} = N_{e'} \frac{1}{Q_{V'} Q_{J'}} \exp\left(-\frac{hc}{kT_v} E_{V'} - \frac{hc}{kT_r} E_{J'}\right) \frac{1}{g_{e'}} \frac{2\pi e^2 h}{c^3 m} \nu_{CL}^3 f_{V'V''} S_{J'J''} b_v \quad \left(\frac{\text{erg}}{\text{cm}^3 \cdot \text{sr}}\right) \quad (\text{D-11})$$

The line shape function (b_v) appearing in the equations for the absorption and emission coefficient defines the spectral variation of the respective coefficient. The approximate formula proposed by Liu et al. [2001] will be applied in the present work. This formula is written as

$$b_v = C_1 \frac{\lambda_{CL}^2}{\pi c} \frac{\Delta\lambda_V}{\bar{\lambda}^2 + \Delta\lambda_V^2} + C_2 \frac{\lambda_{CL}^2}{c} \frac{\sqrt{\ln(2)}}{\Delta\lambda_V \sqrt{\pi}} \exp\left[-\frac{\ln(2)\bar{\lambda}^2}{\Delta\lambda_V^2}\right] \quad (s) \quad (\text{D-12})$$

where

$$\bar{\lambda} = |\lambda - \lambda_{CL}| \quad (cm) \quad (\text{D-13})$$

and λ_{CL} is the wavelength of the line center. The weighting between the Lorentzian and Gaussian line shapes are represented by the following functions

$$C_1 = 0.68188 + (0.61293)d - (0.18384)d^2 - (0.11568)d^3 \quad (\text{D-14})$$

$$C_2 = 0.32460 - (0.61825)d + (0.17681)d^2 + (0.12109)d^3 \quad (\text{D-15})$$

where

$$d = \frac{\Delta\lambda_L - \Delta\lambda_G}{\Delta\lambda_L + \Delta\lambda_G} \quad (\text{D-16})$$

These equations are functions of the Voigt ($\Delta\lambda_V$), Lorentzian ($\Delta\lambda_L$), and Gaussian ($\Delta\lambda_G$) half-widths at half-height, or (half) half widths. The Voigt (half) half-width is calculated from the approximation presented by Olivero and Longbothom [1977]:

$$\Delta\lambda_V = \left\{ 1 - 0.18121(1 - d^2) - [0.023665 \exp(0.6d) + 0.00418 \exp(-1.9d)] \sin(\pi d) \right\} (\Delta\lambda_L + \Delta\lambda_G) \quad (\text{D-17})$$

The Gaussian half-width at half-height may be written as (Arnold et al. [1979])

$$\Delta\lambda_G = 2\lambda_{CL} \sqrt{\frac{2kT_t \ln 2N_A}{M_s}} \quad (\text{cm}) \quad (\text{D-18})$$

where M_s is the molecular weight of the specie (kg/kg-mole) and N_A is Avogadro's number (particles/kg-mole). The Lorenztian half-width at half-height may be written as (Colket [1984])

$$\Delta\lambda_L = \frac{\lambda_{CL}^2}{2} 0.04687 \sigma(\text{nm})^2 p(\text{Torr}) \sqrt{\frac{2}{T_t M_s}} \quad (\text{cm}) \quad (\text{D-19})$$

where σ is optical collision diameter in nm, which taken to equal 0.5 nm, and p is the total gas pressure in Torr.

Appendix E. Derivation of the Escape-Factor for Molecular Band Radiation

It is desired to develop an equation for the number of transitions from a lower electronic state to a higher electronic state due to the absorption of incoming radiation. The function F_ν defined in Eq. (6.10) represents the incoming frequency-dependent radiative intensity to a point integrated over all directions. Note that F_ν is dependent on the radiation emitted from every radiative mechanism from every other point in the flowfield. The fraction of this energy that contributes to the excitation of a lower electronic state to a higher state is determined by multiplying F_ν by an absorption coefficient $\kappa_{\nu,j}$ (1/cm). This absorption coefficient is the sum of all those resulting from transitions with an upper level j , where j is the level for which the population is being calculated. Integrating this quantity over frequency, the radiative energy absorbed per-unit volume per-unit second may be written as

$$E^j = \int_0^\infty \kappa_{\nu,j}^* F_\nu d\nu \quad \left(\frac{\text{erg}}{\text{cm}^3 \cdot \text{s}} \right) \quad (\text{E-1})$$

To determine the desired transition rate from the lower to upper electronic state due to this absorbed energy, it is recognized that each absorbed photon, which produces a single electronic transition, contains energy equal to $h\nu$. Therefore the number of transitions per-unit volume per-unit second from the lower to upper electronic state is obtained by dividing Eq. (E-1) by $h\nu$, which results in the following

$$\sigma = \int_0^\infty \frac{\kappa_{\nu,j}^*}{h\nu} F_\nu d\nu \quad \left(\frac{\text{particles}}{\text{cm}^3 \cdot \text{s}} \right) \quad (\text{E-2})$$

This equation could be obtained more rigorously by considering each rotational line and assuming the rotational and vibrational levels followed a Boltzmann distribution. The escape factor ($A_{j,i}$) is obtained using this term by subtracting it from the number of transitions leaving the upper level due to spontaneous emission and nondimensionalizing the resulting equation with $N_j A(j,i)$ which results in the following

$$A_{j,i} = 1 - \frac{1}{A(j,i)N_j} \int_0^\infty \frac{\kappa_{\nu,j}^*}{h\nu} F_\nu d\nu \quad (\text{E-3})$$

This is the form of the escape factor implemented in the present study.

Appendix F. The Calculation of F_ν and q_ν in the Tangent-Slab Approximation

The function F_ν in Eq. (6.10) represents the incoming intensity at a point resulting from all directions surrounding that point. Applying the tangent-slab approximation, this function may be written as follows

$$F_\nu = 2\pi \int_0^\pi I_\nu(\phi) \sin \phi d\phi \quad (\text{F-1})$$

where ϕ is defined in Figure F-1 and the 2π is a result of the symmetry assumed by the tangent-slab approximation in the plane tangent to the paper.

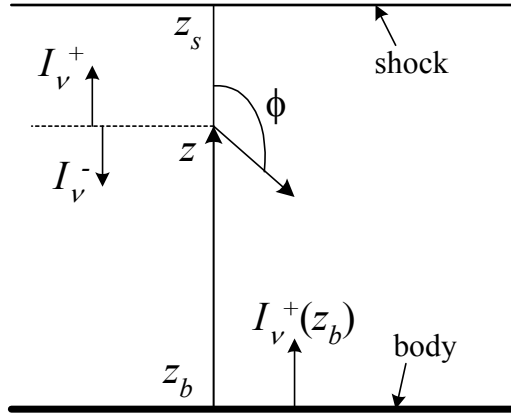


Figure F-1. Geometry and notation for the tangent-slab model

From the notation defined in Figure F-1, Eq. (F-1) may be written as

$$F_\nu(z) = 2\pi \left[\int_0^{\pi/2} I_\nu^+(z, \phi) \sin \phi d\phi + \int_{\pi/2}^\pi I_\nu^-(z, \phi) \sin \phi d\phi \right] \quad (\text{F-2})$$

where the one-sided radiative intensities are written as (see Appendix D in Barnwell [1969])

$$I_\nu^+(z, \phi) = I_\nu^+(z_b) \exp[-\sec \phi \tau_\nu(z_b, z)] + \sec \phi \int_{s=z_b}^{s=z} j_\nu(s) \exp[-\sec \phi \tau_\nu(s, z)] ds \quad (\text{F-3})$$

$$I_\nu^-(z, \phi) = -\sec \phi \int_{s=z}^{s=z_s} j_\nu(s) \exp[\sec \phi \tau_\nu(z, s)] ds \quad (\text{F-4})$$

In these equations, the optical thickness $\tau_\nu(a, b)$ is defined as

$$\begin{aligned}\tau_\nu(a, b) &= \int_a^b \kappa_\nu dz \\ &= \int_0^b \kappa_\nu dz - \int_0^a \kappa_\nu dz\end{aligned}\tag{F-5}$$

and j_ν is the emission coefficient in units of erg-s/cm³-sr. Substituting Eqs. (F-2) through (F-4) into Eq.(F-1) and making the following substitutions

$$\omega = \sec \phi \tag{F-6}$$

$$d\omega = \frac{\sin \phi}{\cos^2 \phi} d\phi = \omega^2 \sin \phi d\phi \tag{F-7}$$

results in the following

$$\begin{aligned}F_\nu(z) &= 2\pi \left\{ \int_1^\infty \left[\frac{1}{\omega^2} I_\nu^+(z_b) \exp[-\omega \tau_\nu(z_b, z)] + \frac{1}{\omega} \int_{s=z_b}^{s=z} j_\nu(s) \exp[-\omega \tau_\nu(s, z)] ds \right] d\omega \right. \\ &\quad \left. + \int_1^\infty \left[\frac{1}{\omega} \int_{s=z}^{s=z_s} j_\nu(s) \exp[\omega \tau_\nu(z, s)] ds \right] d\omega \right\} \end{aligned}\tag{F-8}$$

The integrals in this equation may be written in terms of first and second order exponential integrals, which are defined as

$$E_n(x) = \int_1^\infty \omega^{-n} \exp(-\omega x) d\omega \tag{F-9}$$

From this definition, Eq. (F-8) may be rewritten as

$$F_\nu(z) = 2\pi \left\{ I_\nu^+(z_b) E_2[\tau_\nu(z_b, z)] + \int_{s=z_b}^{s=z} j_\nu(s) E_1[\tau_\nu(s, z)] ds + \int_{s=z}^{s=z_s} j_\nu(s) E_1[\tau_\nu(z, s)] ds \right\} \tag{F-10}$$

Note that an alternative form of this equation may be written by applying the following identity

$$\left| \frac{dE_n}{dx}(x) \right| = -E_{n-1}(x) \tag{F-11}$$

The following approximate expressions for the exponential integrals were obtained by curve fitting the exact functions

$$E_1(x) = 2.591e^{-18.7x} + 1.708e^{-2.11x} \tag{F-12}$$

$$E_2(x) = 0.2653e^{-8.659x} + 0.7347e^{-1.624x} \tag{F-13}$$

$$E_3(x) = 0.0929e^{-4.08x} + 0.4071e^{-1.33x} \tag{F-14}$$

Figure F-2 compares the accuracy of these expressions with the exact function and other often used approximations. The expression for E_2 is similar to the theoretically derived approximation

presented by Murty [1965]. Note that Eq. (F-12) does not properly model the fact that E_1 approaches infinity as x goes to zero, though, this has a negligible influence on the numerical evaluation of Eq. (F-10). Also, it is seen that the often used approximation that $E_2 = \exp(-2x)$ is not very accurate, and is noticeably improved upon by the new approximation (Eq. F-13). This is significant for the calculation of the radiative heat flux (q_ν), which is written similarly to Eq. (F-10) as

$$q_\nu(z) = 2\pi \left\{ I_\nu^+(z_b) E_3[\tau_\nu(z_b, z)] + \int_{s=z_b}^{s=z} j_\nu(s) E_2[\tau_\nu(s, z)] ds - \int_{s=z}^{s=z_s} j_\nu(s) E_2[\tau_\nu(z, s)] ds \right\} \quad (\text{F-15})$$

The use of Eq. (F-13) instead of $\exp(-2x)$ has been found to reduce the wall radiative heating by as much as 7% for Titan conditions.

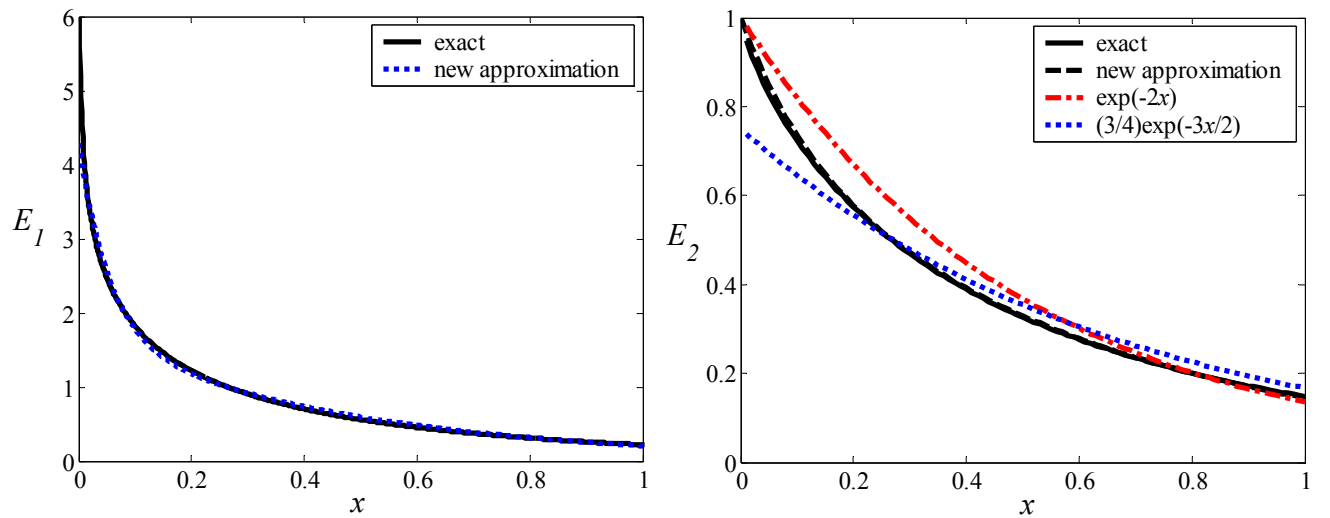


Figure F-2. Comparison of the exact functions and approximate expressions for E_1 and E_2

Appendix G. Fundamental Concepts of Shock-Layer Radiative Heating

This appendix provides a brief overview of the fundamental concepts of shock-layer radiative heating, which is intended for readers unfamiliar with the subject. This overview is meant as a supplement to other recent discussions of this topic, such as that presented by Anderson [2000], and is therefore not complete by itself. Because of the basic nature of this discussion, no references will be cited. Refer to Section 1.2 of this report for references to numerous papers.

There are four distinctive steps to the calculation of the radiative flux from a shock layer, which are listed as follows (It is assumed in this brief discussion that there is no coupling between the flowfield and the radiation, this topic is discussed further in Chapter 5):

- 1) Flowfield calculation (Chapter 2)
- 2) Calculation of the electronic state populations (Chapter 4)
- 3) Spectrum calculation (Chapter 3)
- 4) Radiation transport calculation (Appendix F)

The chapters of this thesis in which these topics are discussed are listed in parenthesis. The flowfield calculation provides the species number densities and temperature at every spatial point in the shock-layer. The number of atoms or molecules in a particular electronic state is required for the spectrum calculation. Using the temperature and number densities from the flowfield solution, these population values may be calculated in two ways. The simplest way is to assume that a Boltzmann distribution exists for each species. This assumption is not valid in regions of chemical or thermodynamic nonequilibrium. For such cases, a non-Boltzmann calculation must be applied. This calculation, also called a collisional-radiative model, requires the solution of the Master Equation for each electronic state. For atomic species, this calculation requires the simultaneous solution of up to 35 coupled equations. Furthermore, hundreds of rates are required for the implementation of these equations, with most being highly uncertain. Once the electronic state population is calculated at each spatial point using one of these methods, the frequency-dependent emission and absorption coefficients at each spatial point may be calculated. These coefficients are the result of atomic bound-bound (atomic lines), atomic bound-free (photoionization), atomic free-free (Bremsstrahlung), and molecular bound-bound (molecular band) transitions. The bound-bound emission and absorption coefficients are proportional to the upper and lower electronic state number density, respectively, which were calculated in the previous step. Each of the radiative processes listed here is independent of the others. The complete frequency-dependent emission and absorption coefficients are linear sums of each radiative process from each species. For the numerical evaluation of these frequency dependent

coefficients, a sufficient number of closely spaced spectral points must be applied to model the details of each radiative process from each species. Once the frequency-dependent emission and absorption coefficients are evaluated at each spatial point in the shock-layer, the actual radiation *transport* calculation may begin. This involves the application of the radiation transport equation to each frequency-point independently. The transport equation may be evaluated by first numerically integrating over space at each spectral point, and then integrating over frequency wherever a frequency-integrated flux value is desired (such as at the wall of a vehicle).

Vita

Christopher O. Johnston was born on September 5, 1980 to Paul and Kaleen Johnston in Prairie Village, Kansas. At the age of 3, he and his family moved to their present home in Manassas, Virginia. He graduated from Osbourn High School in 1998 and began his undergraduate studies that fall at West Virginia University. After his sophomore year, he transferred to Virginia Tech where he obtained his B.S. degree in Aerospace Engineering, Magna cum Laude, in 2002. Following graduation, he immediately began work towards his M.S. degree with funding from the Center for Intelligent Material Systems and Structures (CIMSS) at Virginia Tech. His work on the aerodynamics of biologically-inspired “morphing” aircraft led to the completion of his M.S. degree in December of 2003. After completing most of his course requirements for a Ph.D., Chris relocated to the NASA Langley Research Center in Hampton, VA in August 2004 to begin his Ph.D. research in the field of aerothermodynamics. This led to the work presented in this dissertation, and ultimately his graduation with a Ph.D. degree in Aerospace Engineering in December 2006. Upon graduation, Chris plans to continue working at NASA Langley Research Center.